Semiconductor Quantum Nanostructures for Optoelectronic Applications

Sumanta Bose

School of Electrical and Electronic Engineering

A thesis submitted to the Nanyang Technological University
in partial fulfillment of the requirement for the degree of
Doctor of Philosophy

2018

Approved by:

Assoc. Professor Rusli (Chairman)
School of Electrical & Electronic Engineering, College of Engineering
Nanyang Technological University

Assoc. Professor Wang Hong
School of Electrical & Electronic Engineering, College of Engineering
Nanyang Technological University

Asst. Professor Luo Yu
School of Electrical & Electronic Engineering, College of Engineering
Nanyang Technological University

Supervised by:

Assoc. Professor Fan Weijun (Supervisor)
School of Electrical & Electronic Engineering, College of Engineering
Nanyang Technological University

Professor Zhang Dao Hua (Co-Supervisor)
School of Electrical & Electronic Engineering, College of Engineering
Nanyang Technological University

Acknowledgment

THANK YOU, dear reader, I acknowledge you for reading my thesis! It adds value to the many hours spent writing this, and my journey of over four years leading to it.

A great many people have had immense contributions directly or indirectly, in the evolution of this thesis to its current form and shaping my doctoral career in general.

My deepest gratitude is to my supervisor, Assoc. Prof. Fan Weijun. I have been amazingly fortunate to have a supervisor who believed in me and gave the freedom to explore uncharted waters, but at the same time extended timely guidance to recover whenever my steps faltered. His patience and support has helped me evolve as an independent researcher.

My co-supervisor, Prof. Zhang Dao Hua, has been a support figure with invaluable research insights. I am deeply grateful to him for the discussions during meetings, supporting my cause to access reserved characterization tools, and ready financial support.

Prof. Hilmi Volkan Demir, Prof. Cuong Dang (Steve), Dr. Vijay Kumar Sharma, Dr. Savas Delikanli and Mr. Sushant Shendre – my research collaborators from the *Luminous!* lab have always been a motivation to my work. Their insightful comments and constructive criticisms at different stages of my doctoral career were thought-provoking and often led to significant research improvements. I am grateful to all of them for helping me furnish the very many experimental data reported in this thesis, while enforcing strict validations on every result, thus inculcating in me a meticulous approach of conducting research.

A special thank you to Dr. Zhigang Song, my colleague and friend who has been a valuable collaborator. Our combined works are represented by a respectable portion of the results reported in this thesis. Witnessing his research acumen and perseverance to solve problems with extensive scientific rigor has been a learning experience on its own. *Xiè Xiè!*

It's about time I thank all my co-authors whose contributions have materialized into published contents enabling the successful compilation and defense of my thesis.

Dr. Chen Jian was the first to introduce me to modeling and numerical simulation of semiconductors. His guidance during the initial phase has been invaluable and I express my gratitude for his efforts. Dr. Ma Baoshan, Dr. Liu Zhihong and Dr. Xu Zhengji who trained me on various semiconductor characterization tools have been very helpful too.

I have been fortunate to learn from Prof. Zhang Qing and my supervisor, from whom I took the course *Advanced Semiconductor Physics*. The theory and practice from the course proved to be a foundation stone for my doctoral research on many fronts.

My research and the works reported in this thesis have also been shaped by the numerous stimulating discussions on directly and remotely related topics, that have helped me expand my domain knowledge or develop an alternate paradigm of tackling research problems. In this context, I would like to acknowledge Dr. Landobasa Y. M. Tobing, Dr. Pedro L. H. Martinez and Dr. Soumyabrata Dev in addition to the aforementioned personals.

I am also thankful to my lab-mates at the *Nanophotonics Lab* who have been excellent co-workers striving to maintain a balanced lab environment conducive for productive research. Thank you Aaron Mueller, Hu Hao, Tong Jinchao, Ni Peinan and Qian Li.

Thanks are also due to all the system staff, office staff and administrative staff whose concerted efforts engendered a support system that enabled me to focus solely on my research without having to worry about operational issues. Thank you Mr. Desmond Lim, Mr. Muhd. F. B. Abdullah, Ms. Christina Wong, Ms. Tay Ting Fang, Mr. Alex Chuah, Ms. Seet Lye Ping, Mr. Yeoh Tiow Koon, Ms. Jennifer Chua and the rest of the team!

Financial assistance from various organizations and institutes have supported my Ph.D. program and facilitated the research work conducted (or parts of) that are reported in this thesis. In no particular order they are: NTU Research Scholarship Award, NTU start-up grant, Ministry of Education Singapore (RG 182/14 and RG 86/13), A*STAR Singapore (1220703063), Economic Development Board Singapore (NRF 2013SAS-SRP001-019), Asian Office of Aerospace Research and Development (FA 2386-17-1-0039), National Research Foundation (NRF-RF-2009-09/CRP-6-2010-02), ESF-EURYI and TUBA-GEBIP.

I would also like to acknowledge my Ph.D. defense panel – Assoc. Prof. Rusli, Assoc. Prof. Wang Hong and Asst. Prof. Luo Yu; my thesis advisory committee – Assoc. Prof. Tang Xiaohong and Assoc. Prof. Sun Handong; and my qualifying examination panel – Prof. Liu Aiqun and Assoc. Prof. Sun Changqing, all of whom proved to be a patient audience and shared insightful feedback, thus making my thesis an improved work in its subsequent iterations. In this regard, I also extend a vote of thanks to the three anonymous reviewers for their careful reading of my thesis and their helpful comments and suggestions.

This thesis was written using LaTeX on the *Overleaf* web platform. Thanks to such an amazingly powerful enabler, which simplified the task by orders of magnitude.

Friends have been an integral part of this journey, and I am truly indebted to them for their support. Thank you Soumya, Abhishek, Faye, Zishan, Sushant, Deval, Arijit, Siarhei, Subhrajit, Tanaya, Jhilik, Stephanie, Maria, Astri, Cá, Hesy, Laavi, Echo, Esha, Deepjyoti, Shafquat, Sonia, Anu, Kalpesh, Ashok, Raunaq and the so many more of you. I've missed mentioning the names of many who were beside me at happy times and sad. Life is good because of you!

Finally, yet most importantly, I thank my family for their love, support, belief and patience. I would particularly like to express my heart-felt gratitude towards my mother, Mrs. Shibani Bose and father, Mr. Chandan Bose. Thank you for all you have done, and continue to do!

Sumanta Bose
February 26, 2018

Abstract

SEMICONDUCTOR quantum nanostructures, such as 0D quantum dots (QDs), 1D nanorods and 2D nanoplatelets (NPLs), quantum rings (QRs) and quantum wells (QWs) exhibit unique quantum mechanical and optoelectronic properties due to spatial confinement of excitons in one or more dimensions ($\sim 10^{-9}$ m). They have received increasing research interest in recent years owing to their intriguing fundamental properties that can be leveraged for potential applications in optoelectronic and display devices as cost-effective and quantum-efficient luminophores. They have been successfully used to implement and design light-emitting diodes (LEDs), lasers, photodetectors, solar cells, biomedical imagers, etc. This is owing to their morphological bandgap tunability, fast fluorescence lifetime and unique optical characteristics supporting tunable pure-color or wide spectral emission.

Among the wide range of available and newly studied semiconductor quantum nanostructures, firstly (*i*) NPLs and QRs of II-VI materials and alloys thereof, and secondly (*ii*) QDs and QWs of III-V dilute nitride/bismide alloy materials are two families of nanostructures that have emerged as very promising candidates for novel semiconductor device and optoelectronic applications.

In this thesis, we report studies on the aforementioned two families of semiconductor quantum nanostructures. The first part of the thesis focuses on the study of II-VI (CdSe and CdS) NPLs and optoelectronic properties thereof under varying physical conditions such as geometrical dimensions, temperature, material composition, topology and optical polarization. NPLs are a unique class of atomically flat quasi-2D quantum confined nanocrystals, often synthesized using wide bandgap II-VI materials, having well-defined thicknesses of several monolayers (MLs). Their sizes enable them to be colloidally suspended in solution. Recent advancements in colloidal chemistry has led to the efficient synthesis of high quality single crystal NPL samples having reduced nonradiative recombination paths and enhanced optical properties. They exhibit strong 1D confinement as their thickness is very

small compared to the Bohr radius. NPLs possess the wide bandgap tunability of QDs and the short exciton decay time of QWs bringing together advantageous features from two domains. Compared to QDs, they typically have narrower emission spectra, reduced inhomogeneous broadening and suppressed Auger recombination.

Furthermore, the second part of the thesis focuses on the study of quaternary dilute nitride/bismide III-V (InNBiAs, InNBiSb and GaNBiAs) QDs and QWs for their optoelectronic properties and application. Dilute nitride/bismide doped III-V alloys promises increased engineering flexibility in the design of advanced compound semiconductor heterostructure devices. Increased control over key device parameters such as lattice constant, bandgap and band offsets opens the door to improved performance for a wide range of electronic and optoelectronic devices. In dilute nitride alloys, the resonant states couples with the conduction band (CB) states and produces the band anticrossing (BAC) effects. This causes the CB band edge to get lowered compared to the unalloyed case. Similarly, for dilute bismide alloys, the valence band (VB) edge is lifted due to the valence band anticrossing (VBAC) resulting from coupling between its resonant states and VB states. In addition, the spin-orbital-splitting energy can exceed the bandgap in dilute bismuth alloy which can inhibit the Auger recombination, making it an excellent candidate for optoelectronic device applications, particularly suited for optical fiber telecommunication applications.

The core machinery of our modeling and simulation study of semiconductor quantum nanostructures uses an effective-mass envelope function theory based on the 8-band and 16-band $\boldsymbol{k}\cdot\boldsymbol{p}$ models with strain effect considerations. The optical properties calculations are based on the density-matrix equation and takes into consideration the excitonic effects with intraband scattering and temperature effects. For each of the nanostructure studied, we have performed a comprehensive study on a range of optoelectronic characteristics such as the strain tensor profiles, excitonic transition energies, optical transition matrix elements, Fermi factors, spatial change densities, electron-hole wavefunctions, electronic bandstructure/band lineups, band-mixing probabilities, photoluminescence emission spectra, optical gain/absorption spectra, maximum and differential gains and transparency properties. These findings have important implications for the application of II-VI NPLs and QRs; and dilute nitride/bismide III-V QDs and QWs in optoelectronic devices, such as LEDs, lasers, solar cells etc. They serve as an enabler for designing experiments and predicting optoelectronic characteristics in tandem with measurements and fabrication and can be used to tune reiterations parameters to reduce time and cost of device production.

Contents

List of Figures

List of Tables

List of Abbreviations

0D, 1D, 2D, 3D	Zero-, One-, Two-, Three-dimensional
A.U. (a.u.)	Arbitrary units
AE	Atomic Elasticity
BAC	Band anticrossing
CB	Conduction Band
CE	Continuum Elasticity
CHCC	Conduction-heavy hole-conduction-conduction
CHLH	Conduction-heavy hole-light hole-heavy hole
CHSH	Conduction-heavy hole-split off hole-heavy hole
DOS	Density of states
FWHM	Full width at half maximum
GOST	Giant oscillator strength transition
GUI	Graphical user interface
HH (hh)	Heavy hole
IC	Integrated circuit
K	Kelvin
LED	Light-emitting diode
LH (lh)	Light hole
LL	Landau level
LO	Longitudinal optic
MQW	Multiple quantum well
ML	Monolayer
NPL	Nanoplatelet
ODE	Octadecene
PL	Photoluminescence

QCL	Quantum cascade laser
QD	Quantum Dot
QR	Quantum Ring
QSH	Quantum spin Hall
QW	Quantum Well
RSS	Rashba spin splitting
RT	Room Temperature
SO (so)	Spin-orbit / Split-off
TE	Transverse electric
TEM	Transmission electron microscopy
TI	Topological insulator
TM	Transverse magnetic
TME	Transition matrix element
TRPL	Time-Resolved Photoluminescence
VB	Valence Band
VBAC	Valence band anticrossing
VCA	Virtual crystal approximation
VCSEL	Vertical-cavity surface-emitting laser
VFF	Valence Force Field
ZB	Zinc-blende

Semiconductor Materials

Cd(S,Se)	Cadmium sulfide selenide
CdS	Cadmium sulfide
CdSe	Cadmium selenide
GaAs	Gallium arsenide
GaN	Gallium nitride
GaNBiAs	Gallium nitride bismide arsenide
InAs	Indium arsenide
InN	Indium nitride
InNBiAs	Indium nitride bismide arsenide
InNBiSb	Indium nitride bismide antimonide
InP	Indium phosphide
InSb	Indium antimonide

List of Physical Constants

Speed of light in vacuum	c	=	$2.997\ 924\ 58 \times 10^{8}$ ms^{-1} (exact)
Elementary electric charge	e	=	$1.602\ 176\ 565(35) \times 10^{-19}$ C
Planck's constant	h	=	$4.135\ 667\ 516(91) \times 10^{-15}$ eV·s
Reduced Planck's constant	$\hbar$	=	$6.582\ 119\ 28(15) \times 10^{-16}$ eV·s
Boltzmann Constant	k_B	=	$8.617\ 3324(78) \times 10^{-5}$ eV·K^{-1}
Thermal Energy ($T = 300$K)	k_BT	=	25.853 meV
Free electron rest mass	m_0	=	$9.109\ 382\ 15(45) \times 10^{-31}$ kg
Permeability of free space	μ_0	=	$1.2566370614 \times 10^{-6}$ N·A^{-2}
Permittivity of free space	ϵ_0	=	$8.854\ 187\ 817 \times 10^{-12}$ F/m

List of Symbols and Notations

a (a_0)	Crystal lattice constant
a_{ep}	Exciton-phonon coupling constant
a_B	Bohr radius
a_c	Hydrostatic deformation potential for conduction band
a_s	Substrate lattice constant
a_v	Hydrostatic deformation potential for valence band
a, $a^\dagger$	Ladder operator
$\mathbf{A}$	Vector potential
b	Shear deformation potential
$\mathbf{B}$	Magnetic field vector
c	Velocity of light
C_{11}	Material elastic constant
C_{12}	Material elastic constant
C_{44}	Material elastic constant
d	NPL or QW layer thickness
d	Shear deformation potential
d_0	Ideal bond length
e	Fundamental electronic charge
E ($= \hbar\omega$)	Photon energy
$\mathbf{E}$	Electric field vector
E1 (CB1)	Ground state of conduction band
E_b^{ex}	Exciton binding energy
E_{exc}	Exciton energy
E_{exc} (0)	Exciton energy at temperature 0 Kelvin

$E_{exc}\ (T)$	Exciton energy at temperature T Kelvin
E_{f_c}	Quasi Fermi energy levels for electrons
E_{f_v}	Quasi Fermi energy levels for holes
E_g	Band gap energy
E_g^{eff}	Effective Band gap energy
$E_g\ (0)$	Band gap energy at temperature 0 Kelvin
$E_g\ (T)$	Band gap energy at temperature T Kelvin
$\text{E}_n\ (\text{CB}_n)$	n^{th} state of conduction band
E_{strain}	Total strain energy
f	Fermi distribution function
f_c	Fermi distribution function for electrons
f_v	Fermi distribution function for holes
$\mathscr{G}\left(\cdot\right)$	Optical Gain
G	Two-terminal conductance
$G^{r/a}$	Retarded/advanced Green's function
h	Planck's constant
h_{ij}	Hamiltonian term in the i^{th} row and j^{th} column
$\hbar$	Reduced Planck's constant $\hbar = h/2\pi$
$\hbar\omega_b$	Exciton binding energy
$\hat{H}$	Hamiltonian Operator
H1 (VB1)	Ground state of valence band
H_ε	Strain Hamiltonian Matrix
H_k	Kinetic Hamiltonian Matrix
H_n	Hermite polynomials
$\text{H}_n\ (\text{VB}_n)$	n^{th} state of valence band
I	Photoluminescence/Absorption Intensity
I_{cv}	Overlap integral between electron and hole wavefunction
$k_{\|\|}$	In-plane momentum
k_B	Boltzmann constant
k_x, k_y, k_z	Wave vector components in the reciprocal space
$\mathbf{k}$	Wave vector
$\mathscr{L}\left(\cdot\right)$	Lorentz function
l_B	Magnetic length
L_x, L_y, L_z	Nanocrystal dimensions along x, y and z directions

L, M, N	Modified Luttinger Parameters
m_0	Electron rest mass
m_e^*	Effective Electron Mass
m_h^*	Effective Hole Mass
m_r	Reduced mass of electron-hole pair
n_r	Refractive Index
n_x, n_y, n_z	Plane wave numbers
$\mathbf{p}$	Momentum vector
$\lvert\mathcal{P}_{cv}\rvert^2$	Squared optical transition matrix element
$\mathcal{P}_{cv,x}$	Optical transition matrix elements along the x direction
$\mathcal{P}_{cv,y}$	Optical transition matrix elements along the y direction
$\mathcal{P}_{cv,z}$	Optical transition matrix elements along the z direction
$\mathbf{r}$	Position vector
$\mathscr{R}(\cdot)$	Spontaneous emission rate
R_y	Excitonic Rydberg energy
S	Vibronic electron-phonon coupling constant
$\lvert S\uparrow\downarrow\rangle$	Spin-up and spin-down orbital wavefunction of the bottom of CB
$S_{2D}(\cdot)$	2D Sommerfeld enhancement factor
T	Temperature (Kelvin)
U	Electric potential
V	Nanocrystal volume in real space
V_0	Nanocrystal confining potential
x	Coordinate in the Cartesian system
$\lvert X\uparrow\downarrow\rangle$	Spin-up and spin-down orbital wavefunction of the top of VB
y	Coordinate in the Cartesian system
$\lvert Y\uparrow\downarrow\rangle$	Spin-up and spin-down orbital wavefunction of the top of VB
z	Coordinate in the Cartesian system
$\lvert Z\uparrow\downarrow\rangle$	Spin-up and spin-down orbital wavefunction of the top of VB

$\alpha\,(\cdot)$	Optical absorption
α_{i-j}	VFF bond stretching force constant of the $i-j$ bond
α, β	Varshni Parameters
β_{j-i-k}	VFF bond bending force constant of the $j-i-k$ bond
γ_1, γ_2, γ_3	Luttinger Parameters
γ_{AC}	Exciton-acoustical phonon interaction coefficient
Γ	Center of the Brillouin zone at $\mathbf{k}=0$
Γ_0	Inhomogeneous Photoluminescence linewidth
Γ_{LO}	Exciton-longitudinal optical phonon Fröhlich interaction coefficient
$\Gamma\ (T)$	Photoluminescence linewidth at temperature T Kelvin
$\Gamma^{r/a}_{S(D)}$	Retarded/advanced self-energies due to the source (drain)
Δ_F	Fermi energy separation
Δ_{so}	Spin-orbit Splitting Energy
∇	Del or Nabla operator
ε	Strain tensor matrix
$\varepsilon_{\parallel}$	In-plane strain component
$\varepsilon_{\perp}$	Vertical strain component
ϵ_0	Permittivity of free space
ε_{xx}, ε_{yy}, ε_{zz}	Main diagonal terms of the strain tensor matrix
η	Quantum efficiency
Θ	Average phonon temperature
i	Iota, imaginary unit $i=\sqrt{-1}$
μ_0	Permeability of free space
τ_{in}	Intraband relaxation time
τ_1, τ_2 ...	Photoluminescence decay lifetime components
$\Phi\ (\phi)$	Electron/Hole envelope wavefunction
$\Psi\ (\psi)$	Electron/Hole Wavefunction
ω	Angular optical frequency $\omega=2\pi\nu$
ω_{LO}	Exciton-longitudinal optical phonon angular optical frequency

"If quantum mechanics hasn't profoundly shocked you,
you haven't understood it yet."

– Niels Bohr (1885–1962)

To Humanity

Chapter 1

Introduction and Literature Review

1.1 History, Background and Motivation

SEMICONDUCTORS are materials whose electrical conductivity is intermediate between that of an electrical conductor and an insulator. They have forwarded humanity and revolutionized the way humans interact in ways beyond imagination. It would only be fair to assert that they have shaped modern society – ubiquitous amenities and facilities such as computers, cellular phones, televisions, data storage, display technologies, broadband Internet, mobile telephony, satellite communication and laser-assisted manufacturing are only possible today, thanks to semiconductors![1]

The term *semiconductors* was used for the first time by Alessandro Volta in his report to the Royal Society of London in 1782 [1]. Over half-a-century later, Michael Faraday was the first to observe and report semiconductor effect in 1833, who noticed that the resistance of silver sulfide decreased with temperature, a behavior different than that observed in metals [2]. In the time to follow, the field of semiconductors matured – in 1914 Johan Koenigsberger categorized solid-state materials based on their conductivity: metals, insulators and 'variable conductors'. In 1928 Ferdinand Bloch developed the theory of electrons in lattices, and couple of years later, in 1930 Rudolf Peierls proposed the idea of forbidden energy gaps, which was applied to realistic solids by Léon Brillouin. In the same year, Kronig and Penney formulated the first analytical model of periodic potential in semiconductor lattices. Then, the band theory of solids based on the notion of empty and filled energy bands was proposed by Alan Wilson in 1931. Concurrently, Werner Heisenberg developed

[1] Thanks are also due to all the scientists and engineers who made it happen.

the concept of hole. Pioneering developments were made in 1938 by Walter Schottky, who developed the first model of the potential barrier in a metal-semiconductor junction. In 1945 William Shockley introduced the concept of a semiconductor amplifier, and in 1947 Shockley along with John Bardeen and Walter Brattain invented the first semiconductor transistor in the Bell Laboratory, for which they were combinedly honored with the Nobel Prize in Physics in 1956 [3]. This path-breaking development of the transistor furthered the understanding of the process of the electron mobility in semiconductors, and facilitated the emergence of newer semiconductor devices. In 1958, Jack Kilby and Robert Noyce realized the first integrated circuit (IC) while working at Texas Instruments. It was also at Texas Instruments, where the first light-emitting diode (LED) was developed jointly by James Biard and Gary Pittman in 1961.[2] A year later, in 1962 the first semiconductor laser diode was jointly demonstrated by Robert Hall at General Electric and Marshall Nathan at IBM. This was the inception of the field of *optoelectronics*, which is the study and application of semiconductor devices and systems that generate, detect and control light (photons). The modern understanding of optoelectronics is based on the quantum mechanical effects of *light-matter interaction* and movement of charge carriers in the crystal lattice of semiconductors. And when we talk of light-matter interaction, we refer to the quantum mechanical interaction between photons and electrons occurring at deep sub-wavelength nanometer (10^{-9} m) scale beyond the diffraction limit (Rayleigh criterion). It was serendipitous, but quite essentially so that the fields of semiconductor physics and quantum mechanics evolved hand-in-hand through the course of the 20^{th} century. Pioneers like Werner Heisenberg, Albert Einstein, Erwin Schrödinger, Paul Dirac, Enrico Fermi, Wolfgang Pauli, David Hilbert, Satyendra Nath Bose and others advanced the field of semiconductor physics and quantum mechanics. The theoretical quantum mechanical treatment was a key enabler in the understanding of light-matter interactions. Squeezing light into the nanometer scale opened avenues for exploring new emergent behaviors, whose study came to be known as *nanophotonics*, the principal facilitator of which is semiconductor *nanocrystals*.[3] Nanocrystals are material particles made of semiconductors that have at least one dimension smaller than 100 nanometers. They have garnered much scientific interest as they exhibit intermediate physical properties between that of bulk materials and atomic or molecular structures. Bulk materials have constant physical properties regardless of their size, but as their size

[2]Biard and Pittman developed the first infrared (900 nm) LED in 1961, however the first visible-spectrum (red) LED was developed in 1962 by Nick Holonyak, Jr. at General Electric.

[3]Nanocrystals may also be referred to as nanoparticles, nanostructures, artificial atoms, etc.

approaches the nanometer scale, new and interesting size-dependent properties start to emerge. This is because nanocrystals have a significantly high surface area to volume ratio compared to bulk materials. The size of nanoparticles enables them to confine their electrons and produce quantum mechanical effects, often exhibiting unexpected optoelectronic properties. One of the emergent differences is in their density of states (DOS). The DOS of a system is a quantification of the number of states available per interval of energy at each energy level to be occupied by the charge carriers. In bulk materials (three-dimensional crystals), the charge carriers are free to exists at any given energy. But as the dimensionality starts reducing, the DOS evolves. If the system is confined (i.e. bound to the nanometer scale) along one direction, it is called a quantum well (QW) system; if it is confined along two directions, a quantum wire system; and if along three directions, a quantum dot (QD) system. Fig. 1.1 shows the DOS for bulk, quantum well, wire and dot systems.

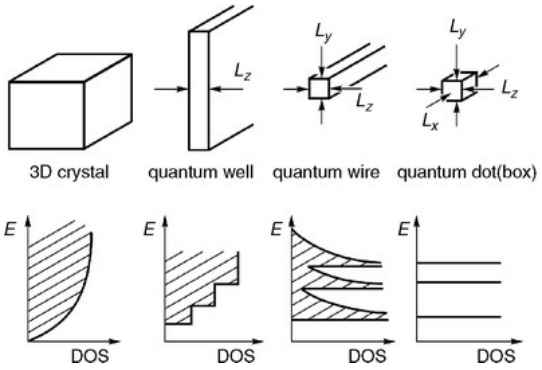

Figure 1.1: Density of states (DOS) in low dimensional semiconductor nanostructures compared with the DOS of bulk material. Reprinted from "J. Kováčč *et al.*, *Optoelectronics*, 2009" with the permission of Springer US [4].

Among the several classes of nanocrystals, one of the popularly studied class with dimensions in the range of ∼1–10 nm are the so-called quantum dots (QDs) [5]. First discovered in the early 1980s [6], QDs display unique electronic and optical properties, which are technologically leveraging for a number of important applications. QDs are considered as zero-dimensional entities with discrete delta-like density of states as seen in Fig. 1.1; and they have high surface-to-volume ratio. The electrons and holes in a QD experiences 3D quantum confinement, so the energy levels become discretely quantized instead of being continuous [5] as illustrated in Fig. 1.2.

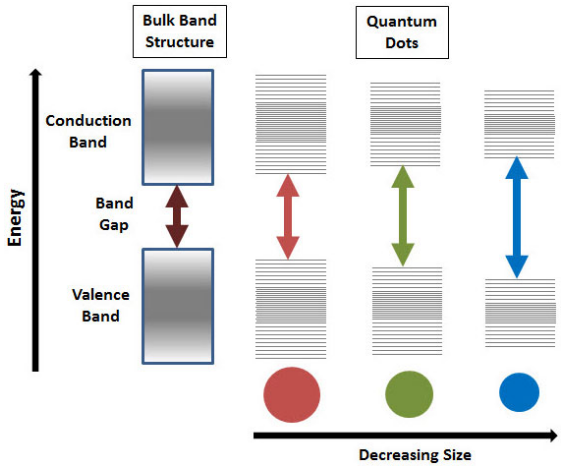

Figure 1.2: Energy level splitting in QDs with size effect on the energy band. (sigmaaldrich.com)

Smaller QDs have widely spaced energy bands, and the photons they generate are towards the blue end of the spectrum. Contrastingly, relatively larger QDs with squeezed energy bands generate photons towards the red end of the spectrum. This holds for QDs with the same semiconductor. However, for QDs of a different semiconductor material, the photon emission wavelength would greatly vary even for QDs of the same size. This technique of tuning the photon emission properties based on the energy bands is called bandgap engineering and forms a crucial basis of the nanophotonics revolution. The concept of bandgap engineering is not only limited to QDs but applies to a range of other nanocrystals too. In recent years, the wide proliferation of nanofabrication techniques such as electron beam lithography, nanoimprinting, ion beam milling, colloidal synthesis etc coupled with diagnostic characterization techniques such as a near-field scanning imaging, X-ray powder diffraction, spectroscopy etc have made the realization of engineered nanocrystals a reality for a whole gamut of applications.

From the above-mentioned key ideas of engineering nanocrystals, we draw the motivation of the work done and presented in this thesis. Among the wide range of available and studied semiconductor nanocrystals, two families have emerged, in the past decade, as very promising candidates for novel semiconductor device applications. They are (*i*) nanoplatelets and quantum rings of II-VI semiconductors and alloys thereof; and (*ii*) quantum dots and quantum wells of dilute nitride/bismide III-V semiconductors. In the sections to follow, we answer the *whats*, *whys* and *hows* critical to the understanding of this research domain, and also identify the contributions extended through this thesis.

1.2 Literature Review

Here we provide a review of the relevant literature of the work reported in this thesis, and give a general account of the current state-of-the-art practices concerning the related research aspects, broadly under two categories: (*i*) nanoplatelets and quantum rings of II-VI semiconductors and alloys thereof, spanning Chapters 3, 4, 5, 6 and 7; and (*ii*) quantum dots and quantum wells of dilute nitride/bismide III-V semiconductors, spanning Chapters 8, 9, 10 and 11.

1.2.1 II-VI Nanoplatelets and Quantum Rings

NPL Dimensions, Operating Temperature and Composition Alloying

Semiconductor nanoplatelets (NPLs) are a recently developed class of atomically flat quasi two-dimensional (2D) quantum confined nanocrystals, often synthesized using wide bandgap II-VI semiconductors such as Cd(Zn)-S(Se)(Te) or ternary/quarternary alloys thereof [7–10]. Low-dimensional wide-bandgap II-VI semiconductor nanocrystals have received increasing research interest owing to their intriguing fundamental properties that can be leveraged for potential applications in optoelectronic and display devices [11–13], wherein they form the active region of semiconductor lasers and light emitting diodes (LEDs) [13]. Recent advances in nanofabrication technology has enabled us to colloidally synthesize NPLs. Other methods of ultra-thin epitaxial layer growth such as molecular beam epitaxy are generally more complicated, and suffer from process-induced defects deteriorating the crystal quality [11]. Colloidal synthesis, on the other hand, is one of the most cost-effective ways to prepare high quality single-crystal NPL samples [14]. It is assisted by the saturation of dangling bonds on the surface, as the organic ligands block further growth [15]. This reduces nonradiative recombination paths enhancing their optical properties. They have attracted increasing interest as they can act as cost-effective and efficient luminophores in display devices, LEDs and lasers [9]. They are excellent candidates for such applications owing to their morphological bandgap tunability, fast fluorescence lifetime and unique optical characteristics supporting bright and tunable spectral emission with narrow full-width-at-half-maxima (FWHM) spanning the entire visible to near IR spectral range [9, 10]. An isolated ideal NPL has a vertical thickness much less than the lateral edge dimensions. NPLs remarkably differ from QDs – NPLs show strong 1D confinement due to their small thickness (typically few monolayers) compared to the Bohr radius [16] while QDs offer 3D

confinement to the excitons. Solution processed NPLs also differ from vacuum-deposited epitaxial quantum wells (QWs) as they have an enhanced splitting between bright and dark excitons due to dielectric confinement [17] and also exhibit giant oscillator strength [10]. NPLs possess the wide bandgap tunability of QDs and the short exciton decay time of QWs bringing together advantageous features from two domains [18]. Also, they have smaller fluorescent lifetimes than colloidal QDs as a result of fast band-edge exciton recombination, and particularly at cryogenic temperatures, their fluorescent lifetime is almost two magnitude orders smaller than that of typical colloidal QDs [10]. This results in fast band-edge excitons recombination leading to high quantum yield up to 80 to ∼100%, at cryogenic ranges [16]. Compared to QDs, they typically have narrower emission spectra, reduced inhomogeneous broadening, suppressed Auger recombination, lower Coulomb blockade and efficient carrier injection [9]. NPLs exhibit femtosecond electron cooling dynamics [19] and are excellent candidates for pure color lasing as NPL lasers have been reported with emission threshold as low as 41 $\mu J/cm^2$ and photoluminescence full width at half maximum (FWHM) as low as 2 nm [8]. Recently for the first time colloidal NPLs have demonstrated the continuous wave laser operation [20]. Owing to such properties NPLs find application in photovoltaics [21], photodetectors [22], laser [23], solar cells [24] etc.

The optoelectronic properties of II-VI semiconductor NPLs are dictated by their electronic bandstructure and band mixing probabilities, which is strongly geometry dependent. The most widely studied CdSe and CdS NPLs however have been reported to be characterized by their thickness alone [10, 25] claiming that they emit at discrete wavelengths depending on atomic-layer thickness. The lateral sizes often vary among these observations but are commonly neglected. To address this problem, in **Chapter 3** of this thesis, we study of the effect of vertical thickness and lateral size in tandem for both CdSe and CdS NPLs.

Furthermore, with the recent developments and potential applications of NPLs in commercial optoelectronic devices [20, 26], it is imperative to study how-and-why their characteristics and performances are influenced by temperature variations, particularly at elevated temperature – when both reversible and irreversible luminescence quenching processes come into the picture [27]. In **Chapter 4** of this thesis, we theoretically study and experimentally characterize the underlying physical phenomena determining the optoelectronic characteristics of CdSe NPLs across varying temperature, above the room temperature (RT).

NPL dimensions and operating temperature are not the only parameters governing their optoelectronic characteristics – they also strongly dependent on the NPL material

composition. By alloying the NPL composition we can obtain continuously tunable emission [28]. In this **Chapter 5** of this thesis, we study the optoelectronic properties of CdS_xSe_{1-x} NPLs for varying alloy compositions in contrasting sizes, thicknesses and temperature.

Polarized Excitonic Absorption in NPLs

The strong 1D vertical confinement in NPLs induces a large exciton binding energy, while the increased exciton center-of-mass extension results in giant oscillator strength transition (GOST) in NPLs [25, 29]. This significantly enhances the NPL's absorption cross-section [29]. A study of the absorption cross-section of NPLs can be an important enabler in quantifying certain fundamental optoelectronic properties of NPLs. For example, with the knowledge of the absorption cross-section, the number of excitons generated due to each photon absorbed by an NPL can be estimated; and the NPL fluorescence quantum yield can also be quantified. [29] The absorption cross-section results can also help to explain low amplified spontaneous emission threshold of NPLs, [30] and determine the concentration of NPLs in solution/films [31].

The absorption spectra of NPLs have been well studied in literature and has a well recognized signature [8, 10] – a higher intensity electron/heavy-hole (HH) absorption peak with a small stokes shift from the emission spectra, and a blue-shifted lower intensity electron/light-hole (LH) absorption peak. However, recently Achtstein *et al.* discovered anomalous absorption spectral properties in ultrathin sub-nanometer (2 ML) CdSe NPLs characterized by increased intrinsic absorption and inverted HH and LH relative peak intensities. [31] They discounted its study in comparison with thicker NPLs due to fundamental physical reasons.[4] In **Chapter 6** of this thesis, we have experimentally verified their observations and theoretically studied the exciton dynamics in NPLs of varying thickness to understand how-and-why the electronic bandstructure and polarization dependent excitonic absorption of CdSe NPLs are affected by the thickness dependent quantum confinement. Ours is a first account of the theoretical treatment of the anomalous absorption spectral characteristics observed in sub-nanometer (2 ML) CdSe NPLs.

[4]Owing to the ultra-strong transversal quantization in 2 ML CdSe NPLs, the exciton wavefunction extends significantly into the neighboring ligand region where the carriers experience a different dielectric environment and effective mass. This affects their electronic structure and exciton dynamics.

Topologically Inverted NPLs: Quantum Rings

Topologically inverted Type-I core/crown NPL heterostructure are commonly referred to as quantum rings (QRs) [32]. They are a very recently developed class of nanocrystals in which a traditionally used active material of lower bandgap (*e.g.* CdSe) is laterally grown around a traditionally used barrier material of higher bandgap (*e.g.* CdS) [32, 33]. Traditional CdSe/CdS core/crown NPLs exhibit good confinement and rapid transfer of excitons from CdS crown to CdSe core [34], but their emission is mostly governed by the core dimensions. However, in QRs the emission window is extended, which originates from the excitonic recombinations in the CdSe QR crown, as expected from the band alignment [32]. In a QR, the laterally grown ring may be rectangular [32, 33] or toroid-like [35], depending on the synthesis techniques. Recently, Fedin *et al.* have demonstrated the colloidal synthesis of luminescent CdSe QRs via controlled etching of NPLs [35]. Other synthesis methods include the use of a one-pot synthesis technique [32] and another using a thick CdS seed [36]. Owing to the non-trivial topology of semiconductor QRs, they exhibit interesting optoelectronic properties. They have high optical tunability and their emission characteristics can be spectrally tuned by varying the extent of lateral confinement. They exhibit high charge injection efficiency and enhanced absorption range [36]. Delikanli *et al.* have shown that the Type-I core/crown CdS/CdSe QRs of a particular thickness is capable of exhibiting a range of peak emission wavelengths – from that of core only CdS NPLs to that of core only CdSe NPLs having the same thickness [36]. These CdS/CdSe QRs have already found application as phosphors for color conversion in white light LEDs [36]. They are also potential candidates for magneto-optical device applications (using Aharonov-Bohm effect) [35]. Colloidal QRs could also be used as charge separator for solar cells and for light harvesting, light-emitting diode, active medium for laser and luminescent probe for biomedical imaging [8, 32]. QRs are also intriguing from a fundamental theoretical physics point-of-view and for light-matter interactions. To understand the physics of QRs for such applications, it is important to study how-and-why its optoelectronic properties can be tailored by varying the QR dimensions and ring size. In **Chapter 7** of this thesis, we will study the electronic structure along with strain profile and charge density, plus the optical gain characteristics for QRs of varying core and crown widths.

This concludes the commentary on the first part of the thesis focusing on the study II-VI NPLs and QRs. Moving on, in the next subsection we will continue the commentary on dilute nitride/bismide III-VI QDs and QWs concerning the remainder of the thesis.

1.2.2 III-V Dilute Nitride/Bismide Quantum Dots and Wells

GaNBiAs/GaAs and InNBiAs QDs and QWs

Dilute nitride/bismide doped III-V semiconductors has attracted much research attention recently due to its potential applications in the near- and mid-infrared photonic devices [37–42]. For example, GaNBiAs, particularly is suited for the 1.55 μm GaAs-based laser diodes for fiber optical communication systems [43, 44]. Per % of bismuth (Bi) incorporation in GaAs reduces the effective bandgap by $\sim$ 60–80 meV [45]. Incorporation of nitrogen (N) also reduced the bandgap, but while Bi induces compressive strain, N helps to achieve lattice matching by inducing an opposite tensile strain. The dilute-N-Bi quantum structures are expected to have better electron and hole quantum confinement. Such fundamental properties of their electronic structure render these materials much suited for telecommunication laser applications compared to conventional III-V materials such as InP based InGaAsP devices, particularly at high temperature [46].

However, to achieve this, a significant count of As atoms must be replaced with Bi atoms. This leads to lattice mismatching and other interface defects. This effect can be compensated for, by an appropriate incorporation of N into the alloy. It has been found that, in GaNBiAs semiconductor alloy, when the N : Bi composition ratio is 0.58 we can obtain lattice matching with GaAs [47]. Co-alloying N and Bi opens up avenues for bandstructure engineering and precise strain control in the GaNBiAs quaternary alloy [48]. In dilute-Bi alloys, the bandgap reduction is caused due to coupling between Bi-resonant state and the valence band (VB) state; while on the other hand, in dilute-N alloys, this effect is induced due to N-resonant state coupling with conduction band (CB) state [49]. In GaNBiAs alloy, both these effects work independently and simultaneously. The origins of such behavior in dilute-N-Bi alloys can be described using a band anticrossing (BAC) model. Since dilute-N alloys predominantly affect the CB, we use the conduction BAC model. Contrastingly, for dilute-Bi alloys we use the valence BAC (VBAC) model in which the VB is most affected [45]. Note that, for the main non-radiative recombination process a conduction electron and a heavy hole (HH) recombine while exciting a spin-split-off hole from valence band. CHSH Auger recombination [50] could be suppressed by a large splitting between HH and spin-orbital coupling (SO) introduced from the VBAC. This is essential for real device system. Therefore, if nitrogen and bismuth are doped simultaneously in GaAs [43, 51], the tuning of the electronic structure will be more controllable and CHSH Auger recombination will be inhibited.

Both bulk and QWs of GaBiAs have attracted lot of interest recently. From the experimentalist's aspect, GaBiAs QWs are well studied [37–42]. Most of them use molecular beam epitaxy followed by related optical characterization of the bandedge [52, 53].

Some theoretical works [54, 55] have also been done since the 12-band effective mass Hamiltonian method [56–60] was proposed by O'Reilly based on the VBAC model. However, not much progress has been made on the study of GaBiAs QDs. Forwarding this research area, in **Chapter 8** of this thesis, we use an improved 16-band effective mass Hamiltonian method to theoretically study and investigate about the electronic bandstructure and optical gain of $GaN_xBi_yAs_{1-x-y}$/GaAs pyramidal QDs, and observe that we could tune the emission wavelength to span within the 1.3–1.55 μm range, suitable for device application in fiber technology. Adding onto that, in this **Chapter 9**, we study various cases of lattice matched GaNBiAs QWs grown on GaAs substrate using another 16-band effective mass Hamiltonian method capable of incorporating the effects of N and Bi doping. This was aimed towards application in the 1.55 μm GaAs-based laser for optical fiber communication systems. A recent work [61] by the O'Reilly group has reported GaBiAs/GaAs QWs, while our work focuses on GaNBiAs QWs, which has better electron confinement due to repulsion between N and the host material's band edge.

The theories and concepts of dilute nitride/bismide III-V semiconductors are not limited to GaNBiAs alone, but is also applicable to other III-V materials such as InAs, InSb, etc. Bulk InAs has a much lower room temperature bandgap of 0.354 eV compared to 1.424 eV of bulk GaAs [62], which implies that InAs based devices would have comparatively longer operating wavelengths. Dilute N and Bi doping in InAs would open new avenues of bandstructure engineering in a similar fashion to that discussed for GaNBiAs in the preceding paragraphs. InNBiAs in particular is a promising candidate for mid-infrared emission device applications. In view of this, in **Chapter 10** of this thesis we study the electronic bandstructure and optical gain of InNBiAs/InP pyramidal QDs investigated using a 16-band effective mass Hamiltonian method. Our objective is to tune the emission wavelength in the range of 2–5 μm suitable for mid-infrared device applications, such as guided missile technology, spectroscopy of trace gases and more recent medical applications such as less-invasive, high-precision, laser surgery [63], by appropriate choices of N and Bi doping compositions.

InNBiSb/InSb QWs: Topological Insulators

Doping of dilute nitride and bismide in III-V semiconductors is known to reduce the bandgap, as already discussed in the preceding subsection. Also, they induce opposite kinds of strain to attain a near-lattice-matching conducive for lattice growth. Particularly, for InSb, however, with the simultaneous incorporation of nitrogen and bismuth we can see new emerging properties such as Quantum spin Hall (QSH) effect, which enables topological phase transitions to be realized in $InN_xBi_ySb_{1-x-y}$/InSb semiconductor QWs. Phase diagram for bandgap shows that as we increase the QW thickness, at a critical thickness, the electronic bandstructure switches from a normal to an inverted type. Such transitions, as we will examine in **Chapter 11** of this thesis, are indeed topological phase transitions between a traditional insulator and a topological insulator exhibiting QSH effect.

Topological insulators (TIs) are a recently discovered class of electronic material that have a bulk bandgap similar to that of an ordinary insulator, but have gapless conducting states on their surface or edge that are topologically protected [64]. These topological surface states are facilitated by the time-reversal symmetry and they are robust against nonmagnetic impurity scattering [64, 65]. They have a Dirac-type energy-momentum relation, unusual spin texture with a Berry's phase of π and exhibit non-dissipative conduction channels that are counter-propagating and fully spin-polarized [64, 65]. In current research, TIs have been successfully realized in both two-dimensional (2D) and three-dimensional (3D) structures. In Chapter 11 of this thesis, we focus on the 2D TIs, which is a quantum spin Hall (QSH) insulator, and is closely related to the integer quantum Hall state [64]. Apart from their intriguing fundamental physical properties which has stirred a lot of research interest in the condensed-matter community recently, they are a candidate with immense potential for application in new electronic, spintronic and quantum computation devices with low power dissipation [66] – for which a specific term *topotronics* [5] has been newly coined [65].

In 2006, for the first time Bernevig *et al.* [67] theoretically predicted QSH effect to exist in 2D semiconductor HgTe/CdSe quantum wells (QW) having an uniform strain gradient. It was experimentally confirmed a year later through transport experiments by Konig *et al.* [68]. Thereafter, researchers paid increased attention on finding more TI materials in traditional semiconductor systems. The InAs/GaSb/AlSb Type-II QW was theoreti-

[5] Topotronics stands for Topological Electronics. A recent article in *Science News* has cited ref. [66] (https://www.sciencenews.org/article/weird-materials-could-make-faster-computers) on how TIs can enable efficient electrical manipulation of magnetic materials for memory and logic applications.

cally proposed [69] and confirmed through the transport experiments [70]. By 2009, other second-generation TIs such as Bi_2Se_3, Bi_2TSe_3 and Sb_2Te_3 were experimentally identified [71]. Later, other semiconductor systems exhibiting QSH effect were proposed, such as 2D GaAs with hexagonal symmetry [72], InN/GaN QW [73] and Ge/GaAs QW [74]. He *et al.* have recently demonstrated magnetic TIs coupled through an antiferromagnetic layer using Cr-doped $(Bi,Sb)_2Te_3$ [75]. InSb has also been explored theoretically, and it has been demonstrated that normal bulk InSb can be converted to exhibit a topologically nontrivial phase by inducing a biaxial lattice expansion of 2–3% based on the density functional theory and tight-binding calculation [76]. A recent proposal designs a *p*-*n* junction QW [77] to invert the band utilizing the built in electric field. Both the schemes claim that InSb is indeed a promising material to realize TIs.

Based on the aforementioned premise, we propose and verify as a proof-of-concept that $InN_xBi_ySb_{1-x-y}$/InSb QW grown along the [001] direction as a semiconductor system can effectively realize QSH effect and topological phase transition. The presence of both N and Bi doped impurities in InSb makes the band inversion easier to realize, and has a twofold advantage: (*i*) Firstly, the conduction band (CB) edge has a negative shift (lowering of CB edge) due to N doping, while the valence band (VB) edge has a positive shift (lifting of VB edge) due to Bi doping. These two phenomenon occur simultaneously and independently of each other [78], which greatly increases the possibility of band inversion, if appropriate proportion of N and Bi were doped. (*ii*) Secondly, the doping of N alone induces tensile strain ($\varepsilon_{\parallel} > 0$), while Bi alone induces compressive strain ($\varepsilon_{\parallel} < 0$), both of which are a concern for lattice growth by molecular beam epitaxy or metal organic chemical vapor deposition. However, with the ideal extent of incorporating both N and Bi, we can significantly reduce the strain or even attain lattice-matching, essential for high quality material growth. Thus N-and-Bi doping in InSb opens avenues for stain-engineering and bandgap-engineering simultaneously. It has been experimentally shown that, by varying the composition of N and Bi, the band gap of InN_xSb_{1-x} can be tuned to be near zero and even negative [79, 80]. This can be theoretically explained by the band anticrossing (BAC) model. The N-related resonant states couple with the CB and lowers the CB edge [81]. Similarly, the reduction of the bandgap in $InBi_ySb_{1-y}$ has been observed in experiments [82–85] and explained by the valence band anticrossing (VBAC) model [86]. The Bi-related resonant states couple with the VB and lifts the VB edge [86]. Therefore, the incorporation of N and Bi in InSb simultaneously offers a promising avenue to realize TIs.

1.3 Thesis Outline and Major Contributions

- **Chapter 1: Introduction and Literature Review**
  In this chapter, we begin by discussing the history, and laying down the background and motivation of the work done and reported in this thesis. Thereafter, we provide an in-depth review of the relevant literature giving a general account of the current state-of-the-art practices concerning the various aspects covered in this thesis, broadly under two categories: firstly (*i*) NPLs and QRs of II-VI materials and alloys thereof, spanning Chapters 3, 4, 5, 6 and 7; and secondly (*ii*) QDs and QWs of III-V dilute nitride/bismide alloy materials, spanning Chapters 8, 9, 10 and 11.

- **Chapter 2: Optoelectronic Theory of Semiconductors**
  In this chapter, we give a mathematical account of the various optoelectronic processes in semiconductors. We introduce, under fair mathematical rigor, the $\boldsymbol{k}\cdot\boldsymbol{p}$ perturbation theory and multi-band variants thereof to calculate the bandstructure of semiconductors. This is followed by a mathematical treatment of the photon generation process in semiconductors and the influence excitonic interactions has on them.

- **Chapter 3: CdSe and CdS Nanoplatelets: Dimension Effect**
  In this chapter, we use a variant of the 8-band $\boldsymbol{k}\cdot\boldsymbol{p}$ model to study of the effect of vertical thickness and lateral size of NPL for both CdSe and CdS, and investigate its influence on their electronic bandstructure and optical properties. The most widely studied CdSe and CdS NPLs however have been reported to be characterized by their thickness alone claiming that they emit at discrete wavelengths depending on atomic-layer thickness. The lateral sizes often vary among these observations but have been commonly neglected. This necessitates the need for such a work.

- **Chapter 4: CdSe Nanoplatelets: Temperature Effect**
  In this chapter, we study in tandem using theoretical modeling and experimental measurements, the underlying physical phenomena determining the optoelectronic characteristics of CdSe NPLs across varying temperature, above the room temperature (RT). Such a study is imperative because at elevated operating temperature both reversible and irreversible luminescence quenching processes come into effect and it becomes important to understand how-and-why the characteristics and performances of NPLs are influenced by varying temperature.

- **Chapter 5: Cd(S,Se) Nanoplatelets: Alloying Effect**
  In this chapter, we study CdS_xSe_{1-x} NPLs for varying alloy compositions in contrasting sizes, thicknesses and temperature for their electronic bandstructure and other optical properties. The basis of such a study is that NPL dimensions and operating temperature are not the only parameters governing their optoelectronic characteristics – they also strongly dependent on the NPL material composition; and by alloying the NPL composition we can obtain continuously tunable emission suitable for device applications.

- **Chapter 6: CdSe Nanoplatelets: Polarized Excitonic Absorption**
  In this chapter, we study the exciton dynamics in CdSe NPLs of varying thickness to understand how-and-why the electronic bandstructure and polarization dependent excitonic absorption of NPLs are affected by the thickness dependent quantum confinement. We provide a first account of the theoretical treatment of certain anomalous absorption spectral characteristics observed in sub-nanometer CdSe NPLs. This study of the absorption cross-section of NPLs has emerged as an important enabler in quantifying several fundamental optoelectronic properties of NPLs.

- **Chapter 7: Inverted CdS/CdSe Nanoplatelets: Quantum Ring**
  In this chapter, we study topologically inverted Type-I CdS/CdSe core/crown NPL heterostructure that are commonly referred to as quantum rings (QRs). Their electronic structure along with strain profile and charge density, plus the optical gain characteristics are examined for varying core and crown widths. Owing to the non-trivial topology of semiconductor QRs, they have high optical tunability and their emission characteristics can be spectrally tuned by varying the extent of lateral confinement. They exhibit high charge injection efficiency and enhanced absorption range.

  This concludes the first part of the thesis on the study of NPLs and QRs of II-VI materials and alloys thereof.

- **Chapter 8: GaNBiAs/GaAs Dilute Nitride-Bismide Quantum Dots**
  In this chapter, we investigate the electronic bandstructure and optical gain of pyramidal $GaN_xBi_yAs_{1-x-y}$/GaAs QDs aimed towards tuning the emission wavelength to span within 1.3–1.55 μm, for device application in fiber technology. A variant of the 16-band $\boldsymbol{k}\cdot\boldsymbol{p}$ model suited for dilute nitride/bismide doped semiconductors is used. Previous studies on dilute nitride/bismide were done using 12- and 14-band models,

and we explain how we have improved upon theirs to obtain a complete represenation of the nitrogen and bismuth orbital resonant states.

- **Chapter 9: GaNBiAs/GaAs Dilute Nitride-Bismide Quantum Wells**
  In this chapter, we study various cases of lattice matched $GaN_xBi_yAs_{1-x-y}$ QWs grown on GaAs barrier, aiming for applications in the 1.55 μm GaAs-based laser for fiber optical communication systems. There have been several works reported on GaBiAs/GaAs QWs, GaInAsBi/GaAs QWs, etc but sufficient literature on GaNBiAs/GaAs QWs are lacking, and this work is timely in that regard.

- **Chapter 10: InNBiAs/InP Dilute Nitride-Bismide Quantum Dots**
  In this chapter, we study the electronic bandstructure and optical gain of pyramidal $InN_xBi_yAs_{1-x-y}$/InP QDs investigated, with an objective of achieving emission wavelength in the range of 2–5 μm suitable for mid-infrared device applications. The concepts of dilute nitride/bismide III-V semiconductors are not limited to GaNBiAs alone, but is also applicable to other III-V materials such as InAs. Here, we also demonstrate bandgap engineering in InNBiAs QDs to obtain mid-infrared emission around the $\sim 250 - 650$ meV range.

- **Chapter 11: InNBiSb/InSb Dilute Nitride-Bismide Quantum Wells**
  In this chapter, we study $InN_xBi_ySb_{1-x-y}$/InSb semiconductor QWs and observe that with the simultaneous incorporation of nitrogen and bismuth new properties such as Quantum spin Hall (QSH) effect, which enables topological phase transitions. Bandgap phase diagrams shows that as the QW thickness increases, the electronic bandstructure switches from a normal to an inverted type. Such transitions are topological phase transitions between a traditional insulator and a topological insulator exhibiting QSH effect.

- **Chapter 12: Thesis Summary and Conclusions**
  In this chapter, we begin with a brief thesis summary spanning the motivation, scope, methodologies and findings of the work. This is followed by a detailed account of the thesis conclusions in a structured fashion enlisting the major findings of every chapter and their related appendices. Then we identify three novel areas having promising future research scope, with the potential to not only unravel new physical phenomena and theory but also provide us with an understanding for efficient optoelectronic device design and applications. Finally, we end the thesis with the closing remark.

- **Appendix A:Semiconductor Material Parameters**
  In this appendix, we enlist the material parameters of CdSe, CdS, GaAs, InAs and InSb; and VC, BAC and VBAC parameters of dilute nitride bismide III-VI semiconductors used for the calculation done and results reported in this thesis.

- **Appendix B: KdotPsoft: Modelling and Simulation of Semiconductor Physics**
  In this appendix, we introduce our in-house software simulation platform called *KdotPsoft*, to model and simulate semiconductor quantum nanostructure systems developed during the course of the work done for this thesis.

- **Appendix C: Nanoplatelets Synthesis and Characterization**
  In this appendix, we describe the NPL synthesis techniques, purification and film preparation methods, TEM/optical characterizations and TRPL response function.

- **Appendix D: Low Temperature NPL Photoluminescence Characterization**
  In this appendix, we study in tandem and validate our theoretical calculations and experimental photoluminescence measurements of 4 ML CdSe NPLs with existing low-temperature results in literature.

- **Appendix E: Anomalous Spectral Characteristics of sub-nm CdSe NPLs**
  In this appendix, we study the photoluminescence spectrum and the relative strength of the HH and LH/SO absorption peaks of the ultrathin sub-nm 2ML CdSe NPLs; and observe anomalous spectral characteristics dependant on the NPL aspect ratio.

- **Appendix F: Inverted Type-I CdS/CdSe Core/Crown Quantum Ring**
  In this appendix, we study the photoluminescence spectra, absorption spectra and spatial charge distributions of 3 ML CdS/CdSe QRs at different phases of crown growth having contrasting characteristics for thin and thick crowns.

Following this, a list of the author's relevant publications and vita, best reflected on the date of the submission of this thesis (February 26, 2018) is furnished; and finally the list of references is enlisted in the bibliography.

Chapter 2

Optoelectronic Theory of Semiconductors

2.1 Theory of Electronic Bandstructures

The solution of an energy-eigenvalue problem of a semiconductor crystal yields its bandstructure, which is more commonly knows as the E–$\mathbf{k}$ diagram or the dispersion curve of the semiconductor material. Fig. 2.1 shows the bandstructure of InAs, as an example.

The highest point of the valence band is knows as the Γ-point, and constitutes the $(k_x = 0, k_y = 0, k_z = 0)$ point in the **k**-space. In most semiconductors, the maximum of valence band and the minimum of conduction band occur as the same point in the **k**-space: at the Γ-point. Such semiconductors are called direct-gap semiconductors and form the backbone of most optical devices. However, if the minimum of conduction band occurs at some other point in the **k**-space, it is an indirect-gap semiconductor. Examples of the former include InAs, GaAs, etc., while that of the latter are Si, Ge, etc. Irrespective of the type of semiconductor, the study of a small portion of the bandstructure near the Γ-point can reveal insights to a number of physical phenomenon (electronic, magnetic, optical, etc.). The framework of such a study involves the use of $\boldsymbol{k}\cdot\boldsymbol{p}$ perturbation theory to appreciate which, it is important to understand the Bloch theorem.

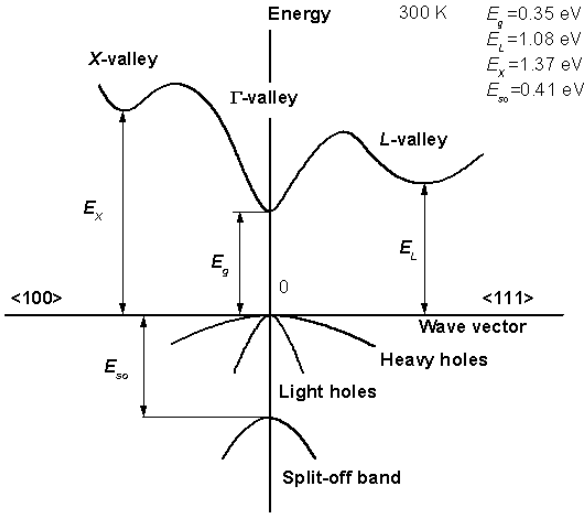

Figure 2.1: The bandstructure (E–$\mathbf{k}$ diagram/dispersion curve) of InAs.

2.2 Bloch Theorem

A periodic potential appears in a crystal lattice because the ions are arranged with a periodicity $\mathbf{R}$ of their Bravais lattice, given by lattice vectors $\mathbf{a}_1$, $\mathbf{a}_2$, $\mathbf{a}_3$ as

$$U(\mathbf{r}+\mathbf{R}) = U(\mathbf{r}) \tag{2.1}$$

where $\mathbf{R} = n_1\mathbf{a}_1 + n_2\mathbf{a}_2 + n_3\mathbf{a}_3$. This potential $U(\mathbf{r})$ is used in the Schrödinger equation

$$\hat{H}\psi(\mathbf{r}) = \left(-\frac{\hbar^2}{2m_0}\nabla^2 + U(\mathbf{r}) \right)\psi(\mathbf{r}) = E(\mathbf{k})\psi(\mathbf{r}) \tag{2.2}$$

where $\mathbf{r}$ is the position vector, $\mathbf{k}$ is the crystal wavevector. The electrons in this periodic lattice can be called as Bloch electrons. The Bloch theorem applies on such a system and states that the solution of the Schrödinger equation for this lattice is of the form [87]

$$\psi_{n\mathbf{k}}(\mathbf{r}) = \exp(i\mathbf{k}\cdot\mathbf{r})u_{n\mathbf{k}}(\mathbf{r}) \tag{2.3}$$

where n is the band index, $\psi(\mathbf{k},\mathbf{r})$ is the Bloch wavefunction, and $u(\mathbf{k},\mathbf{r})$ represents the Bloch lattice (periodic) function with the same periodicity as the lattice i.e. $\mathbf{R}$ as

$$u_{n\mathbf{k}}(\mathbf{r} + \mathbf{R}) = u_{n\mathbf{k}}(\mathbf{r}) \tag{2.4}$$

2.3 $\boldsymbol{k}\cdot\boldsymbol{p}$ Perturbation Theory

Most physical phenomena in semiconductors can be understood by studying the charge carriers' behaviour at the neighborhoods of various energy band extrema, and qualitatively its properties are governed by the shape of these energy surfaces, which is obtainable from symmetry arguments, as observed by Bir and Pikus [88]. In this regard, the $\boldsymbol{k}\cdot\boldsymbol{p}$ perturbation theory is a useful method to analyze the bandstructure near a particular point $\mathbf{k}_0$ in the $\mathbf{k}$-space, specially when it is near an extremum of the bandstructure. The Schrödinger equation for an electron wavefunction $\psi_{n\mathbf{k}}$ in the n^{th} band with a wavevector $\mathbf{k}$ is given by Eq. 2.5 [62].

$$\hat{H}\psi_{n\mathbf{k}}(\mathbf{r}) = \left(\frac{\boldsymbol{p}^2}{2m_0} + U(\mathbf{r})\right)\psi_{n\mathbf{k}}(\mathbf{r}) = E_n(\mathbf{k})\psi_{n\mathbf{k}}(\mathbf{r}) \tag{2.5}$$

When this is written in terms of the Bloch function $u_{n\mathbf{k}}(\mathbf{r})$, it becomes

$$\hat{H}\psi_{n\mathbf{k}}(\mathbf{r}) = \left(\frac{\boldsymbol{p}^2}{2m_0} + \frac{\hbar}{m_0}\boldsymbol{k}\cdot\boldsymbol{p} + U(\mathbf{r})\right)u_{n\mathbf{k}}(\mathbf{r}) = \left(E_n(\mathbf{k}) - \frac{\hbar^2\boldsymbol{k}^2}{2m_0}\right)u_{n\mathbf{k}}(\mathbf{r}) \tag{2.6}$$

The above equation can be expanded near a particular point $\mathbf{k}_0$ in the $\mathbf{k}$-space of the bandstructure. For $\mathbf{k}_0 = 0$, the above equation holds for $E_n(0)$.

$$\hat{H}\psi_{n\mathbf{k}}(\mathbf{r}) = \left(H_0 + \frac{\hbar}{m_0}\boldsymbol{k}\cdot\boldsymbol{p}\right)u_{n\mathbf{k}}(\mathbf{r}) = \left(E_n(\mathbf{k}) - \frac{\hbar^2\boldsymbol{k}^2}{2m_0}\right)u_{n\mathbf{k}}(\mathbf{r}) \tag{2.7}$$

where $H_0 = \frac{\boldsymbol{p}^2}{2m_0} + U(\mathbf{r})$ is the Hamiltonian and $H_0\ u_{n\mathbf{k}}(\mathbf{r}) = E_n(0)\ u_{n\mathbf{k}}(\mathbf{r})$. The procedure thereafter is to determine the eigenvalue $E_n(\boldsymbol{k})$ by solving the Hamiltonian. The inception of this method is from the works of Bardeen [89] and Seitz [90]. Further fundamental developments were done by by Kittel [91] and Kane [92,93] in the 1950s wherein the latter accounted for the spin-orbit interaction calculations. Luttinger and Kohn [94] introduced the concepts of degenerate bands, method of invariants and symmetry arguments. The $\boldsymbol{k}\cdot\boldsymbol{p}$ theory has evolved as an empirical band-structure method with a basis of band states. It

is quite useful and effective for band edge calculation and study with successful application to semiconductor nanostructures [44, 95, 96]. Variations of this method include one-, four-, and six-, eight-, ten- and higher band $\boldsymbol{k}\cdot\boldsymbol{p}$ calculations, which have been compared by Pryor in a seminal work [97].

In this thesis, we will use the two variations of the 8-band model, and two variations of the 16-band model to study II-VI and dilute nitride/bismide III-V semiconductors, as will be explained in the subsections to follow. Material parameters, i.e. constants for a given semiconductor material are essential in the calculation of the various optoelectronic characteristics. Appendix A gives a comprehensive list of the various material parameters that will be used for the various calculation and results reported in this thesis.

Here, we would like to draw the attention of the reader to our in-house semiconductor modeling and simulation software package platform called *KdotPsoft*. During the course of the work done for this thesis, the source code for the various multi-band $\boldsymbol{k}\cdot\boldsymbol{p}$ models that will be described further in this chapter were developed using Fortran and Python. Finally, they were packaged under the name *KdotPsoft*, an end-to-end modeling and simulation software platform for semiconductor quantum nanostructures with a friendly graphical user interface. After further developments and beta-testing, *KdotPsoft* holds the potential of being rolled out as a commercial software package suitable for both academia and industry and the research community at large. Appendix B explains further about *KdotPsoft*, its internal modules, connectivities, dependencies and working flow.

2.3.1 8-band model: First Basis Type

Here we lay down the mathematical framework of our first 8-band $\boldsymbol{k}\cdot\boldsymbol{p}$ model, suited to study the electronic bandstructure of binary semiconductor nanocrystals. It uses an effective mass envelope function theory approach accounting for the nonparabolicity of the coupled conduction band (CB) and valence band (VB) simultaneously, including the orbit-splitting bands to obtain its electronic structure by solving for its eigenenergy in the Γ-point vicinity of the Brillouin zone. The 8-band Hamiltonian, $\mathscr{H}_{8\times8}$ is represented in the Bloch function basis of $|\mathrm{S}\rangle\uparrow$, $|1+1\rangle\uparrow$, $|1,0\rangle\uparrow$, $|1-1\rangle\uparrow$ and $|\mathrm{S}\rangle\downarrow$, $|1+1\rangle\downarrow$, $|1,0\rangle\downarrow$, $|1-1\rangle\downarrow$ as given by Eq. (2.8) [96]. Here $|1,\pm1\rangle\uparrow\downarrow = \left(|X\rangle \pm i|Y\rangle\right)/\sqrt{2}\uparrow\downarrow$ and $|1,0\rangle\uparrow\downarrow = |Z\rangle\uparrow\downarrow$.

$$\mathscr{H}_{8\times8} = \begin{bmatrix} h_{11} & h_{12} & h_{13} & h_{14} & 0 & 0 & 0 & 0 \\ & h_{22} & h_{23} & h_{24} & 0 & 0 & 0 & 0 \\ & & h_{33} & h_{34} & 0 & 0 & 0 & 0 \\ & & & h_{44} & 0 & 0 & 0 & 0 \\ & & & & h_{11} & h_{12} & h_{13} & h_{14} \\ & & & & & h_{22} & h_{23} & h_{24} \\ & & & & & & h_{33} & h_{34} \\ & & & & & & & h_{44} \end{bmatrix} + \frac{\Delta_{so}}{3} \begin{bmatrix} 0 & 0 & 0 & 0 & 0 & 0 & 0 & 0 \\ 0 & 0 & 0 & 0 & 0 & 0 & 0 & 0 \\ 0 & 0 & -1 & 0 & 0 & -\sqrt{2} & 0 & 0 \\ 0 & 0 & 0 & -2 & 0 & 0 & \sqrt{2} & 0 \\ 0 & 0 & 0 & 0 & 0 & 0 & 0 & 0 \\ 0 & 0 & -\sqrt{2} & 0 & 0 & -2 & 0 & 0 \\ 0 & 0 & 0 & \sqrt{2} & 0 & 0 & -1 & 0 \\ 0 & 0 & 0 & 0 & 0 & 0 & 0 & 0 \end{bmatrix} + V_0 \tag{2.8}$$

where the first Hamiltonian matrix contains all the independent terms and terms linearly or quadratically dependent on the wavevector, with $h_{ij} = h_{ji}^{*}$. The second Hamiltonian matrix accounts for the valence band spin-orbit coupling, where Δ_{so} is the spin-orbit splitting energy [96]. V_0 is the nanocrystal confining potential from environment. The individual Hamiltonian elements (h_{ij}) of Eq. 2.8 are expressed below.

$$h_{11} = E_g - \frac{\hbar^2}{2m_0}\cdot\gamma_c\left(k_x^2+k_y^2+k_z^2\right) + a_c\left[tr\left(\varepsilon\right)\right] \tag{2.9a}$$

$$h_{12} = \frac{i\hbar\sqrt{E_p}\left(k_x'+ik_y'\right)}{2\sqrt{m_0}} \tag{2.9b}$$

$$h_{13} = i\hbar\sqrt{\frac{E_p}{2m_0}}k'_z \tag{2.9c}$$

$$h_{14} = \frac{i\hbar\sqrt{E_p}\left(k'_x - ik'_y\right)}{2\sqrt{m_0}} \tag{2.9d}$$

$$h_{22} = h_{44} = -\frac{\hbar^2}{2m_0}\left[\frac{L'+M'}{2}\left(k_x^2+k_y^2\right)+M'k_z^2\right] + a_v\left[tr\left(\varepsilon\right)\right] + \frac{b}{2}\left[tr\left(\varepsilon\right) - 2\varepsilon_{zz}\right] \tag{2.9e}$$

$$h_{23} = h_{34} = -\frac{\hbar^2}{2m_0}\left[\frac{N'\left(k_x - ik_y\right)k_z}{\sqrt{2}}\right] + \sqrt{6}d\left(\varepsilon_{xz} - i\varepsilon_{yz}\right) \tag{2.9f}$$

$$h_{24} = -\frac{\hbar^2}{2m_0}\left[\frac{L'-M'}{2}\left(k_x^2-k_y^2\right) - iN'k_xk_y\right] + \frac{3b}{2}\left(\varepsilon_{xx} - \varepsilon_{yy}\right) - i\sqrt{12}d\varepsilon_{xy} \tag{2.9g}$$

$$h_{33} = -\frac{\hbar^2}{2m_0}\left[M'\left(k_x^2+k_y^2\right)+L'k_z^2\right] + a_v\left[tr\left(\varepsilon\right)\right] + b\left[3\varepsilon_{zz} - tr\left(\varepsilon\right)\right] \tag{2.9h}$$

$$\gamma_c = -\frac{E_p}{3}\left[\frac{1}{E_g+\Delta_{so}} + \frac{2}{E_g}\right] + \frac{m_0}{m_e^*} \tag{2.9i}$$

$$\begin{pmatrix} k'_x \\ k'_y \\ k'_z \end{pmatrix} = \left(I_3 - \varepsilon\right)\begin{pmatrix} k_x \\ k_y \\ k_z \end{pmatrix} \tag{2.9j}$$

Here, a_c and a_v are the hydrostatic deformation potential for conduction and valence band, respectively. b and d are the shear deformation potentials.

Using the Luttinger-Kohn effective mass parameters γ_1, γ_2, γ_3, we have can derive the modified Luttinger parameters for our calculation, as follows.

$$L' = L - \frac{E_p}{E_g} = -\frac{\hbar^2}{2m_0}(\gamma_1 + 4\gamma_2 + 1) \tag{2.10a}$$

$$M' = M = -\frac{\hbar^2}{2m_0}(\gamma_1 - 2\gamma_2 + 1) \tag{2.10b}$$

$$N' = N - \frac{E_p}{E_g} = -\frac{\hbar^2}{2m_0}(6\gamma_3) \tag{2.10c}$$

Considering the nanocrystal periodicities to be L_x, L_y, L_z along the x, y and z directions, we use plane waves to expand the eight-dimensional hole and electron envelope wave function as [49]

$$\Phi_m = \left\{\Phi_m^j\right\} \qquad (j = 1, 2, ..., 8) \tag{2.11a}$$

with

$$\Phi_m^j = \frac{1}{\sqrt{V}} \sum_{n_x, n_y, n_z} a^j_{m, n_x, n_y, n_z} \exp[i(k_{nx}x + k_{ny}y + k_{nz}z)] \tag{2.11b}$$

where $k_{nx} = 2\pi n_x/L_x$, $k_{ny} = 2\pi n_y/L_y$, $k_{nz} = 2\pi n_z/L_z$ and n_x, n_y, n_z are the plane wave numbers. And $V = L_x L_y L_z$. The indices of the basis and energy subbands are given by j and m respectively.

Now we calculate the squared optical transition matrix element (TME), given by $|\mathcal{P}_{cv}|^2$. It quantifies the strength of transition between the electron- and hole-subband [98]. We calculate it using the momentum operator, $\mathbf{p}$ and the real electron and hole wavefunctions, $\Psi_{c,\mathbf{k}}$ and $\Psi_{v,\mathbf{k}}$ respectively, as follows.

$$\mathcal{P}_{cv,i} = \langle \Psi_{c,\mathbf{k}} | \, \hat{\mathrm{e}} \cdot \mathbf{p}_i \, | \Psi_{v,\mathbf{k}} \rangle \quad , \quad i = x, y, z \tag{2.12}$$

Expressions for $\mathcal{P}_{cv,i}$ along the x, y and z directions are given below [99].

$$\mathcal{P}_{cv,x} = \frac{p_0}{\sqrt{2}} \sum_{n_x,n_y,n_z} \big[(a^2_{v,n_x,n_y,n_z} + a^4_{v,n_x,n_y,n_z})a^{1*}_{c,n_x,n_y,n_z} + (a^6_{v,n_x,n_y,n_z} + a^8_{v,n_x,n_y,n_z})a^{5*}_{c,n_x,n_y,n_z} + (a^{2*}_{c,n_x,n_y,n_z} + a^{4*}_{c,n_x,n_y,n_z})a^{1}_{v,n_x,n_y,n_z} + (a^{6*}_{c,n_x,n_y,n_z} + a^{8*}_{c,n_x,n_y,n_z})a^{5}_{v,n_x,n_y,n_z}\big] \tag{2.13a}$$

$$\mathcal{P}_{cv,y} = \frac{ip_0}{\sqrt{2}} \sum_{n_x,n_y,n_z} \big[(a^2_{v,n_x,n_y,n_z} - a^4_{v,n_x,n_y,n_z})a^{1*}_{c,n_x,n_y,n_z} + (a^6_{v,n_x,n_y,n_z} - a^8_{v,n_x,n_y,n_z})a^{5*}_{c,n_x,n_y,n_z} + (a^{2*}_{c,n_x,n_y,n_z} - a^{4*}_{c,n_x,n_y,n_z})a^{1}_{v,n_x,n_y,n_z} + (a^{6*}_{c,n_x,n_y,n_z} - a^{8*}_{c,n_x,n_y,n_z})a^{5}_{v,n_x,n_y,n_z}\big] \tag{2.13b}$$

$$\mathcal{P}_{cv,z} = p_0 \sum_{n_x,n_y,n_z} \big[a^3_{v,n_x,n_y,n_z} a^{1*}_{c,n_x,n_y,n_z} + a^7_{v,n_x,n_y,n_z} a^{5*}_{c,n_x,n_y,n_z} + a^{3*}_{c,n_x,n_y,n_z} a^{1}_{v,n_x,n_y,n_z} + a^{7*}_{c,n_x,n_y,n_z} a^{5}_{v,n_x,n_y,n_z}\big] \tag{2.13c}$$

where $p_0 = \langle S|p_x|X\rangle = \langle S|p_y|Y\rangle = \langle S|p_z|Z\rangle$, and is normally expressed in term of energy units as $p_0 = \hbar\sqrt{\dfrac{E_p}{2m_0}}$ where E_p is the optical Kane matrix element. a_{c,n_x,n_y,n_z} and a_{v,n_x,n_y,n_z} are the plane wave expanding coefficient. In a laser, with light propagating along the nanocrystal layers, there are two distinct optical polarizations – (i) one with the optical electric vector parallel to the NPL layers, called the 'transverse electric' or TE mode polarization and (ii) the other with the optical electric vector perpendicular to the NPL layers, called the 'transverse magnetic' or TM mode polarization. The average of $\mathcal{P}_{cv,x}$ and $\mathcal{P}_{cv,y}$ (TMEs along x and y directions) contributes to the transverse electric (TE) mode optical emission, while $\mathcal{P}_{cv,z}$ (TME along the z direction) contributes to the transverse magnetic (TM) mode optical emission. The TE mode emission is x-y plane polarized, while the TM mode emission is z direction polarized.

2.3.2 8-band model: Second Basis Type

In Sec. 2.3.1 we explained the first 8-band $\boldsymbol{k}\cdot\boldsymbol{p}$ Hamiltonian. Here, we will explain the framework of the second 8-band $\boldsymbol{k}\cdot\boldsymbol{p}$ Hamiltonian, suited for binary semiconductor nanocrystals. We have used the Kane's 8-band Hamiltonian for zinc-blende (ZB) strained semiconductor, containing both kinetic terms H_k (independent, linear and quadratic dependence on k) and strain terms H_ε [44, 100], and is given by Eq. 2.14. It takes into account the energy levels from conduction band (CB), heavy hole (HH), light hole (LH), and spin-orbit split-off-hole (SO) bands which can be seen in the main diagonal terms ($H_{cb}, H_{hh}, H_{lh}, H_{so}$). The off-diagonal terms account for the coupling effects. Under the [001] orientation the basis used for this 8-band Hamiltonian is $|S\uparrow\rangle$, $|S\downarrow\rangle$, $-\frac{i}{\sqrt{2}}|(X+iY)\uparrow\rangle$, $-\frac{i}{\sqrt{6}}|[(X+iY)\downarrow -2Z\uparrow]\rangle$, $\frac{i}{\sqrt{6}}|[(X-iY)\uparrow +2Z\downarrow]\rangle$, $\frac{i}{\sqrt{2}}|(X-iY)\downarrow\rangle$, $\frac{i}{\sqrt{3}}|[(X+iY)\downarrow +Z\uparrow]\rangle$, $\frac{i}{\sqrt{3}}|[(X-iY)\uparrow -Z\downarrow]\rangle$.

$$H_k + H_\varepsilon = \begin{bmatrix} H_{cb} & c.c. & c.c. & c.c. & c.c. & c.c. & c.c. & c.c. \\ 0 & H_{cb} & c.c. & c.c. & c.c. & c.c. & c.c. & c.c. \\ \frac{1}{\sqrt{2}}P_- & 0 & H_{hh} & c.c. & c.c. & c.c. & c.c. & c.c. \\ -\sqrt{\frac{2}{3}}P_z & \frac{1}{\sqrt{6}}P_- & S^* & H_{lh} & c.c. & c.c. & c.c. & c.c. \\ -\frac{1}{\sqrt{6}}P_+ & -\sqrt{\frac{2}{3}}P_z & -R^* & 0 & H_{lh} & c.c. & c.c. & c.c. \\ 0 & -\frac{1}{\sqrt{2}}P_+ & 0 & -R^* & -S^* & H_{hh} & c.c. & c.c. \\ -\frac{1}{\sqrt{3}}P_z & -\frac{1}{\sqrt{3}}P_- & \frac{S^*}{\sqrt{2}} & -D & -\sqrt{\frac{3}{2}}S & \sqrt{2}R & H_{so} & c.c. \\ -\frac{1}{\sqrt{3}}P_+ & \frac{1}{\sqrt{3}}P_z & -\sqrt{2}R^* & -\sqrt{\frac{3}{2}}S^* & D & \frac{S}{\sqrt{2}} & 0 & H_{so} \end{bmatrix} \tag{2.14}$$

The terms in the 8-band $\boldsymbol{k}\cdot\boldsymbol{p}$ Hamiltonian of Eq. 2.14 are as follows [44, 100].

$$H_{cb} = E_g + \frac{\hbar^2}{2m_0}\gamma_c\left(k_x^2 + k_y^2 + k_z^2\right) + E_{c1} \tag{2.15a}$$

$$H_{hh} = -\frac{\hbar^2}{2m_0}\left[(\gamma_1+\gamma_2)\left(k_x^2+k_y^2\right) + (\gamma_1 - 2\gamma_2)\,k_z^2\right] + E_{v1} + E_{v1} \tag{2.15b}$$

$$H_{lh} = -\frac{\hbar^2}{2m_0}\left[(\gamma_1 - \gamma_2)\left(k_x^2 + k_y^2\right) + (\gamma_1 + 2\gamma_2)\,k_z^2\right] + E_{v1} - E_{v1} \tag{2.15c}$$

$$H_{so} = -\frac{\hbar^2}{2m_0}\left[\gamma_1\left(k_x^2 + k_y^2 + k_z^2\right)\right] - \Delta_{so} + E_{v1} \tag{2.15d}$$

$$\begin{bmatrix} P_+ \\ P_- \\ P_z \end{bmatrix} = p_0 \begin{bmatrix} k_x & ik_y & 0 \\ k_x & -ik_y & 0 \\ 0 & 0 & k_z \end{bmatrix} \begin{bmatrix} 1-\varepsilon_{xx} \\ 1-\varepsilon_{yy} \\ 1-\varepsilon_{zz} \end{bmatrix} \tag{2.15e}$$

$$S = -\frac{\hbar^2}{2m_0} 2\sqrt{3}\gamma_3\left(-k_x + ik_y\right)k_z \tag{2.15f}$$

$$R = -\frac{\hbar^2}{2m_0}\sqrt{3}\left[\gamma_2\left(k_x^2 - k_y^2\right) - 2\gamma_3 i k_x k_y\right] \tag{2.15g}$$

$$D = -\frac{\hbar^2}{2m_0}\sqrt{2}\gamma_2\left(k_x^2 + k_y^2 - 2k_z^2\right) + \sqrt{2}E_{v2} \tag{2.15h}$$

$$\gamma_c = \frac{1}{m_e^*} - \frac{E_p}{3}\left(\frac{2}{E_g} + \frac{1}{E_g + \Delta_{so}}\right) \tag{2.15i}$$

$$E_{c1} = 2a_c\left(1 - \frac{c_{12}}{c_{11}}\right)\varepsilon_{xx} \tag{2.15j}$$

$$E_{v1} = 2a_v\left(1 - \frac{c_{12}}{c_{11}}\right)\varepsilon_{xx} \tag{2.15k}$$

$$E_{v2} = b\left(1 + 2\frac{c_{12}}{c_{11}}\right) \tag{2.15l}$$

Here, E_g is the unstrained bandgap, Δ_{so} is the spin-orbit splitting energy. c_{11} and c_{12} are

the elastic stiffness constants of the material, which relates the in-plane and perpendicular strains, as $\varepsilon_{zz} = -2\frac{c_{12}}{c_{12}}\varepsilon_{xx}$. k_x, k_y, k_z are the wavevector operators. The term p_0 in Eq. 2.15e is the same used in Eq. 2.13 in Sec. 2.3.1. The modified Luttinger parameters $(\gamma_1, \gamma_2, \gamma_3)$ related to Luttinger parameters $\left(\gamma_1^L, \gamma_2^L, \gamma_3^L\right)$ in the following manner.

$$\gamma_1 = \gamma_1^L - \frac{1}{3}\frac{E_p}{E_g} \tag{2.16a}$$

$$\gamma_2 = \gamma_2^L - \frac{1}{6}\frac{E_p}{E_g} \tag{2.16b}$$

$$\gamma_3 = \gamma_3^L - \frac{1}{6}\frac{E_p}{E_g} \tag{2.16c}$$

The total Hamiltonian, however, is given by $H_{8\times8} = H_k + H_\varepsilon + V_0$, where V_0 is the conduction and valence band offset (or the confining potential).

The eight dimensional hole and electron envelope wave function for the QWs is expanded as

$$\Phi_m = \left\{\Phi_m^j\right\} (j = 1, 2, ..., 16) \tag{2.17}$$

where

$$\Phi_m^j = \exp\left[i\left(k_x x + k_y y\right)\right] \sum_m a_{n,m}^j \frac{1}{\sqrt{L}} \exp\left[i\left(k_z + m\frac{2\pi}{L}\right)z\right] \tag{2.18}$$

The QW period is $L = l + d$, where the width of the well is l while the barrier width is d. k_i $(i = x, y, z)$ are the wavevectors, $a_{n,m}^j$ is the expansion coefficient while n is the energy subband index [101].

However for 0D QDs or 2D NPLs, we expand as follows.

$$\Phi_m^j = \frac{1}{\sqrt{L_x L_y}} \exp\left[i\left(k_x x + k_y y\right)\right] \sum_m a_{n,m}^j \frac{1}{\sqrt{L_z}} \exp\left[i\left(k_z + m\frac{2\pi}{L_z}\right)z\right] \tag{2.19}$$

where L_z is the NPL thickness or QD thickness along z direction; and L_x and L_y are the dimensions along x and y directions.

As explained in Sec. 2.3.1, we calculate the transition matrix element (TME) as $\mathcal{P}_{cv,i} = \langle \Psi_{c,\mathbf{k}} | \, \hat{\mathrm{e}} \cdot \mathbf{p}_i \, | \Psi_{v,\mathbf{k}} \rangle$, $i = x, y, z$. For the Hamiltonian matrix in this case, the expressions for the upspin and downspin TMEs along the x, y and z directions are given below [101].

$$\mathcal{P}_{cv,x\uparrow} = p_0 \sqrt{\frac{2}{m_0}} \sum_m \left(-\frac{i}{\sqrt{2}} a^3_{n_v,m} + \frac{i}{\sqrt{6}} a^5_{n_v,m} + \frac{i}{\sqrt{3}} a^8_{n_v,m} \right) a^{1*}_{n_c,m} \tag{2.20a}$$

$$\mathcal{P}_{cv,x\downarrow} = p_0 \sqrt{\frac{2}{m_0}} \sum_m \left(-\frac{i}{\sqrt{6}} a^4_{n_v,m} + \frac{i}{\sqrt{2}} a^6_{n_v,m} + \frac{i}{\sqrt{3}} a^7_{n_v,m} \right) a^{2*}_{n_c,m} \tag{2.20b}$$

$$\mathcal{P}_{cv,y\uparrow} = p_0 \sqrt{\frac{2}{m_0}} \sum_m \left(\frac{1}{\sqrt{2}} a^3_{n_v,m} + \frac{1}{\sqrt{6}} a^5_{n_v,m} + \frac{1}{\sqrt{3}} a^8_{n_v,m} \right) a^{1*}_{n_c,m} \tag{2.20c}$$

$$\mathcal{P}_{cv,y\downarrow} = p_0 \sqrt{\frac{2}{m_0}} \sum_m \left(\frac{1}{\sqrt{6}} a^4_{n_v,m} + \frac{1}{\sqrt{2}} a^6_{n_v,m} - \frac{1}{\sqrt{3}} a^7_{n_v,m} \right) a^{2*}_{n_c,m} \tag{2.20d}$$

$$\mathcal{P}_{cv,z\uparrow} = p_0 \sqrt{\frac{2}{m_0}} \sum_m \left(i\sqrt{\frac{2}{3}} a^4_{n_v,m} + \frac{i}{\sqrt{3}} a^7_{n_v,m} \right) a^{1*}_{n_c,m} \tag{2.20e}$$

$$\mathcal{P}_{cv,z\downarrow} = p_0 \sqrt{\frac{2}{m_0}} \sum_m \left(i\sqrt{\frac{2}{3}} a^5_{n_v,m} - \frac{i}{\sqrt{3}} a^8_{n_v,m} \right) a^{2*}_{n_c,m} \tag{2.20f}$$

and

$$|\mathcal{P}_{cv,i}|^2 = |\mathcal{P}_{cv,i\uparrow}|^2 + |\mathcal{P}_{cv,i\downarrow}|^2, i = x, y, z \tag{2.21}$$

2.3.3 16-band model: First Basis Type

The 8-band $\boldsymbol{k}\cdot\boldsymbol{p}$ models described in Sec. 2.3.1 and 2.3.2 are suited to study binary II-VI, III-V or group IV semiconductors such as InAs, GaAs, CdSe, CdS, Si, Ge, etc. But when we intend to study the effect of nitrogen and bismuth doping in the semiconductors, the 8-band Hamiltonian is not sufficient.

The 10-band $\boldsymbol{k}\cdot\boldsymbol{p}$ model used to study the nitrogen-doped QDs is based on the 8-band model extended by introducing the local nitrogen resonant state (additional 2 bands). Similarly, to investigate the bismuth-doped and nitrogen-doped QDs simultaneously, additional bands have to be added in the model to describe and study the effects of bismuth. Unlike the s-like state introduced by dilute nitride, the dilute bismide results in p-like states, which means that six states should be considered with the spin freedom including the SO coupling which is ignored in the O'Reilly 14-band model for dilute bismide-nitride semiconductors [56]. In view of the aforementioned consideration, we have constructed a 16-band model, to study quaternary dilute nitride/bismide III-V semiconductors. The 16-band Hamiltonian is represented in the Bloch function basis of $|S\rangle\uparrow$, $|S\rangle\downarrow$, $|1+1\rangle\uparrow$, $|1,0\rangle\uparrow$, $|1-1\rangle\uparrow$, $|1-1\rangle\downarrow$, $|1,0\rangle\downarrow$, $|1+1\rangle\downarrow$, $|S_N\rangle\uparrow$, $|S_N\rangle\downarrow$, $|1+1_{Bi}\rangle\uparrow$, $|1,0_{Bi}\rangle\uparrow$, $|1-1_{Bi}\rangle\uparrow$, $|1-1_{Bi}\rangle\downarrow$, $|1,0_{Bi}\rangle\downarrow$, $|1+1_{Bi}\rangle\downarrow$ as given by Eq. (2.22). Here $|1,\pm1\rangle\uparrow\downarrow = (|X\rangle \pm i|Y\rangle)/\sqrt{2}\uparrow\downarrow$, $|1,0\rangle\uparrow\downarrow = |Z\rangle\uparrow\downarrow$, $|1,\pm1_{Bi}\rangle\uparrow\downarrow = (|X_{Bi}\rangle \pm i|Y_{Bi}\rangle)/\sqrt{2}\uparrow\downarrow$ and $|1,0_{Bi}\rangle\uparrow\downarrow = |Z_{Bi}\rangle\uparrow\downarrow$.

$$H_{16} = \begin{pmatrix} H_{10\times10} & H_{10\times6} \\ H_{6\times10} & H_{6\times6} \end{pmatrix} + V_0, \tag{2.22}$$

where $H_{10\times10}$ is the 10-band model to describe the nitrogen-doped system, $H_{6\times6}$ is the 6-band model to describe the resonant bismuth states, $H_{10\times6}$ is the coupling between the valence band and Bismuth states, and the V_0 is the confinement potential of the system. As we use the $|1,0\rangle$, $|1-1\rangle$, $|1+1\rangle$ basis for the p-like states instead of $|HH\rangle$, $|LH\rangle$, $|SO\rangle$, the form of Hamiltonian is different form the O'Reilly's model and can be transformed into it under an unitary transformation. The details of the every element of $H_{10\times10}$ is given

below.

$$H_{10\times10} = \begin{pmatrix} E^C & 0 & \frac{i}{\sqrt{2}}P_-^* & iP_z & \frac{i}{\sqrt{2}}P_+^* & 0 & 0 & 0 & V_N & 0 \\ 0 & E^C & 0 & 0 & 0 & \frac{i}{\sqrt{2}}P_-^* & iP_z & \frac{i}{\sqrt{2}}P_+^* & 0 & V_N \\ -\frac{i}{\sqrt{2}}P_- & 0 & HH & S & R & 0 & 0 & 0 & 0 & 0 \\ -iP_z & 0 & S^* & Q-2\lambda & S & -\sqrt{2}\lambda & 0 & 0 & 0 & 0 \\ -\frac{i}{\sqrt{2}}P_+ & 0 & R^* & S^* & HH-\lambda & 0 & \sqrt{2}\lambda & 0 & 0 & 0 \\ 0 & -\frac{i}{\sqrt{2}}P_- & 0 & -\sqrt{2}\lambda & 0 & HH-\lambda & S & R & 0 & 0 \\ 0 & -iP_z & 0 & 0 & \sqrt{2}\lambda & S^* & Q-2\lambda & S & 0 & 0 \\ 0 & -\frac{i}{\sqrt{2}}P_+ & 0 & 0 & 0 & R^* & S^* & HH & 0 & 0 \\ V_N & 0 & 0 & 0 & 0 & 0 & 0 & 0 & E^N & 0 \\ 0 & V_N & 0 & 0 & 0 & 0 & 0 & 0 & 0 & E^N \end{pmatrix} \tag{2.23}$$

where

$$E^C = Eg + \frac{\hbar^2}{2m_0}\gamma_c(k_x^2 + k_y^2 + k_z^2) + \delta E^{CB} \tag{2.24a}$$

$$HH = -\frac{\hbar^2}{2m_0}\left[\frac{L^{'} + M^{'}}{2}(k_x^2 + k_y^2) + M^{'}k_z^2\right] + \delta E^{HH} \tag{2.24b}$$

$$Q = -\frac{\hbar^2}{2m_0}\left[M^{'}(k_x^2 + k_y^2) + L^{'}k_z^2\right] + \delta E^{Q} \tag{2.24c}$$

$$S = -\frac{\hbar^2}{2m_0}\left[\frac{1}{\sqrt{2}}N^{'}(k_x + ik_y)k_z\right] + \delta E_{Strain}^{S} \tag{2.24d}$$

$$R = -\frac{\hbar^2}{2m_0}\left[\frac{L^{'} - M^{'}}{2}(k_x^2 - k_y^2) + iN^{'}k_xk_y\right] + \delta E_{Strain}^{R} \tag{2.24e}$$

$$\delta E^{CB} = -\delta E_{VC}^{CB} + \delta E_{Strain}^{CB} \tag{2.24f}$$

$$\delta E^{HH} = \delta E^{HH}_{VC} + \delta E^{HH}_{Strain} \tag{2.24g}$$

$$\delta E^{Q} = \delta E^{Q}_{VC} + \delta E^{Q}_{Strain} \tag{2.24h}$$

$$P_{-} = p_0 \left(k_x^{'} - i k_y^{'} \right) \tag{2.24i}$$

$$P_{+} = p_0 \left(k_x^{'} + i k_y^{'} \right) \tag{2.24j}$$

$$P_z = p_0 k_z^{'} \tag{2.24k}$$

$$k_x^{'} = k_x - \epsilon_{xx} k_x - \epsilon_{xy} k_y - \epsilon_{xz} k_z \tag{2.24l}$$

$$k_y^{'} = k_y - \epsilon_{yz} k_y - \epsilon_{yy} k_y - \epsilon_{yz} k_z \tag{2.24m}$$

$$k_z^{'} = k_z - \epsilon_{xz} k_x - \epsilon_{yz} k_y - \epsilon_{zz} k_z \tag{2.24n}$$

$$p_0 = \hbar \sqrt{E_p / 2 m_0} \tag{2.24o}$$

$$V_N = \beta_N \sqrt{x} \tag{2.24p}$$

$$\gamma_c = \frac{m_0}{m_c} - \frac{E_p}{3} \left(\frac{2}{E_g} + \frac{1}{E_g + 3\lambda} \right) \tag{2.24q}$$

$$L^{'} = L - \frac{E_p}{E_g} \tag{2.24r}$$

$$M^{'} = M \tag{2.24s}$$

$$N^{'} = N - \frac{E_p}{E_g} \tag{2.24t}$$

$$\lambda = \Delta_{SO}/3 \tag{2.24u}$$

The δE_{VC} and δE_{Strain} are contributions from the VC and strain factors. The relevant terms will be subsequently explained.

The nitrogen/bismuth composition-dependent terms depending on α_N/α_{Bi}, κ_N/κ_{Bi}, γ_N/γ_{Bi} describe the VC contributions to the band edges. Other terms corresponding to the strain are added as the VC effect. They vary from the forms given by the 14-band O'Reilly model [56] since our basis are different from the Kane's. Here, we give the details about the VC and strain terms.

$$\delta E_{VC}^{CB} = \alpha_N x + \alpha_{Bi} y \tag{2.25a}$$

$$\delta E_{VC}^{HH} = \kappa_N x + \kappa_{Bi} y \tag{2.25b}$$

$$\delta E_{VC}^{Q} = \frac{1}{3}(2\kappa_N - \gamma_N)x + \frac{1}{3}(2\kappa_{Bi} - \gamma_{Bi})y \tag{2.25c}$$

$$\delta E_{Strain}^{CB} = a_c(\epsilon_{xx} + \epsilon_{yy} + \epsilon_{zz}) \tag{2.25d}$$

$$\delta E_{Strain}^{HH} = (a_v + \frac{b}{2})(\epsilon_{xx} + \epsilon_{yy}) + (a_v - b)\epsilon_{zz} \tag{2.25e}$$

$$\delta E_{Strain}^{Q} = (a_v - b)(\epsilon_{xx} + \epsilon_{yy}) + (a_v + 2b)\epsilon_{zz} \tag{2.25f}$$

$$\delta E_{Strain}^{S} = \sqrt{6}(d\epsilon_{xz} - i\epsilon_{yz}) \tag{2.25g}$$

$$\delta E^R_{Strain} = \frac{3}{2} b(\epsilon_{xx} - \epsilon_{yy}) - i2\sqrt{3} d\epsilon_{xy} \tag{2.25h}$$

The strain tensor can be calculated as follows

$$\epsilon_{xx} = \epsilon_{yy} = \frac{a_s - a_0}{a_0} \tag{2.26a}$$

$$\epsilon_{zz} = -\frac{2C_{12}}{C_{11}} \epsilon_{xx} \tag{2.26b}$$

where a_s is the substrate lattice constant and a_0 is the unstrained growth material lattice constant. C_{11} and C_{12} are the elastic stiffness constants of the material.

The coupling matrix $H_{10\times6}$ is

$$H_{10\times6} = \begin{pmatrix} 0 & 0 & 0 & 0 & 0 & 0 \\ 0 & 0 & 0 & 0 & 0 & 0 \\ V_{Bi} & 0 & 0 & 0 & 0 & 0 \\ 0 & V_{Bi} & 0 & 0 & 0 & 0 \\ 0 & 0 & V_{Bi} & 0 & 0 & 0 \\ 0 & 0 & 0 & V_{Bi} & 0 & 0 \\ 0 & 0 & 0 & 0 & V_{Bi} & 0 \\ 0 & 0 & 0 & 0 & 0 & V_{Bi} \\ 0 & 0 & 0 & 0 & 0 & 0 \\ 0 & 0 & 0 & 0 & 0 & 0 \end{pmatrix} \tag{2.27}$$

with

$$H_{6\times10} = H^{\dagger}_{10\times6} \tag{2.28}$$

where

$$V_{Bi} = \beta_{Bi}\sqrt{y}. \tag{2.29}$$

The last Bismuth resonant Hamiltonian, $H_{6\times6}$ is

$$H_{6\times6} = \begin{pmatrix} K & F & G & 0 & 0 & 0 \\ F^* & V_2 & F & T & 0 & 0 \\ G^* & F^* & V_3 & 0 & -T & 0 \\ 0 & T & 0 & V_3 & F & G \\ 0 & 0 & -T & F^* & V_2 & F \\ 0 & 0 & 0 & G^* & F^* & K \end{pmatrix} \tag{2.30}$$

where

$$K = E_{Bi}^{HH} + (a_{Bi} + \frac{b_{Bi}}{2})(\epsilon_{xx} + \epsilon_{yy}) + (a_{Bi} - b_{Bi})\epsilon_{zz} \tag{2.31a}$$

$$V_2 = \frac{1}{3}(2E_{Bi}^{LH} + E_{Bi}^{SO}) + (a_{Bi} - b_{Bi})(\epsilon_{xx} + \epsilon_{yy}) + (a_{Bi} + 2b_{Bi})\epsilon_{zz} \tag{2.31b}$$

$$V_3 = \frac{1}{3}(E_{Bi}^{LH} + 2E_{Bi}^{SO}) + (a_{Bi} + \frac{b_{Bi}}{2})(\epsilon_{xx} + \epsilon_{yy}) + (a_{Bi} - b_{Bi})\epsilon_{zz} \tag{2.31c}$$

$$T = \frac{\sqrt{2}}{3}(E_{Bi}^{SO} - E_{Bi}^{LH}) \tag{2.31d}$$

$$F = \sqrt{6}d_{Bi}\epsilon_{xz} - i\sqrt{6}d_{Bi}\epsilon_{yz} \tag{2.31e}$$

$$G = \frac{3}{2}b_{Bi}(\epsilon_{xx} - \epsilon_{yy}) - i2\sqrt{3}d_{Bi}\epsilon_{xy} \tag{2.31f}$$

This concludes the description of the Hamiltonian for the dilute nitride/bismide III-V QD system.

We assume that the QDs are periodically arranged in three dimensions and with the periodicities L_x, L_y, L_z. We have used the plane waves to expand the basis as follows

$$\Phi_m = \left\{\Phi_m^j\right\} \qquad (j = 1, 2, ..., 16) \tag{2.32a}$$

with

$$\Phi_m^j = \frac{1}{\sqrt{V}} \sum_{n_x,n_y,n_z} a^j_{m,n_x,n_y,n_z} \exp[i(k_{nx}x + k_{ny}y + k_{nz}z)] \tag{2.32b}$$

where $V = L_xL_yL_z$, $k_{nx} = \frac{2\pi n_x}{L_x}, k_{ny} = \frac{2\pi n_y}{L_x}, k_{nz} = \frac{2\pi n_z}{L_z}$ and n_x, n_y, n_z are the integer of plane wave numbers and j is the index of basis.

As explained in the Sec. 2.3.1, we calculate the transition matrix element (TME) as $\mathcal{P}_{cv,i} = \langle \Psi_{c,\mathbf{k}} | \, \hat{\mathrm{e}} \cdot \mathbf{p}_i \, | \Psi_{v,\mathbf{k}} \rangle$, $i = x, y, z$. For the 16-band Hamiltonian matrix described in this subsection, the expressions for the TMEs along the x, y and z directions are given below.

$$\begin{aligned}\mathcal{P}_{cv,x} = \frac{p_0}{\sqrt{2}} \sum_{n_x,n_y,n_z} \big[&(a^3_{v,n_x,n_y,n_z} + a^5_{v,n_x,n_y,n_z}) a^{1*}_{c,n_x,n_y,n_z} \\ &+ (a^6_{v,n_x,n_y,n_z} + a^8_{v,n_x,n_y,n_z}) a^{2*}_{c,n_x,n_y,n_z} \\ &+ (a^{3*}_{c,n_x,n_y,n_z} + a^{5*}_{c,n_x,n_y,n_z}) a^1_{v,n_x,n_y,n_z} \\ &+ (a^{6*}_{c,n_x,n_y,n_z} + a^{8*}_{c,n_x,n_y,n_z}) a^2_{v,n_x,n_y,n_z} \big]\end{aligned} \tag{2.33a}$$

$$\begin{aligned}\mathcal{P}_{cv,y} = \frac{ip_0}{\sqrt{2}} \sum_{n_x,n_y,n_z} \big[&(a^3_{v,n_x,n_y,n_z} - a^5_{v,n_x,n_y,n_z}) a^{1*}_{c,n_x,n_y,n_z} \\ &+ (a^6_{v,n_x,n_y,n_z} - a^8_{v,n_x,n_y,n_z}) a^{2*}_{c,n_x,n_y,n_z} \\ &+ (a^{3*}_{c,n_x,n_y,n_z} - a^{5*}_{c,n_x,n_y,n_z}) a^1_{v,n_x,n_y,n_z} \\ &+ (a^{6*}_{c,n_x,n_y,n_z} - a^{8*}_{c,n_x,n_y,n_z}) a^2_{v,n_x,n_y,n_z} \big]\end{aligned} \tag{2.33b}$$

$$\begin{aligned}\mathcal{P}_{cv,z} = p_0 \sum_{n_x,n_y,n_z} \big[&a^4_{v,n_x,n_y,n_z} a^{1*}_{c,n_x,n_y,n_z} \\ &+ a^7_{v,n_x,n_y,n_z} a^{5*}_{c,n_x,n_y,n_z} + a^{4*}_{c,n_x,n_y,n_z} a^1_{v,n_x,n_y,n_z} \\ &+ a^{7*}_{c,n_x,n_y,n_z} a^5_{v,n_x,n_y,n_z} \big]\end{aligned} \tag{2.33c}$$

where p_0 is the same as that in Sec. 2.3.1, and a_{c,n_x,n_y,n_z} and a_{v,n_x,n_y,n_z} are the plane wave expanding coefficient. The average of $\mathcal{P}_{cv,x}$ and $\mathcal{P}_{cv,y}$ contributes to the transverse electric (TE) mode emission, while $\mathcal{P}_{cv,z}$ contributes to the transverse magnetic (TM) mode emission.

2.3.4 16-band model: Second Basis Type

In Sec. 2.3.3 we explained the first 16-band $\boldsymbol{k}\cdot\boldsymbol{p}$ Hamiltonian. Here, we explain the mathematical framework of the second 16-band $\boldsymbol{k}\cdot\boldsymbol{p}$ Hamiltonian, also suited to study quaternary dilute nitride/bismide III-V semiconductors.

Broderick *et al.* had proposed a 12- and 14-band $\boldsymbol{k}\cdot\boldsymbol{p}$ Hamiltonian for dilute nitride/bismide III-V semiconductors [56]. Here, we propose a 16-band Hamiltonian including the so_{Bi} energy level ($E^0_{Bi,so}$), which was not accounted for in their model. The 16-band model is more accurate, especially for the higher excited states of hole, which can be closer to $E^0_{Bi,so}$, and thus the interaction between them cannot be ignored. We have extended the Kane's 8-band Hamiltonian and used the BAC and VBAC models to form a 16-band Hamiltonian. As explained in Sec. 2.3.3, the incorporation of N needs two additional bands to address the local N resonant s-like states, in addition to Kane's 8-bands. On the other hand, Bi introduces p-like states, for which six additional bands must be considered with the freedom of spin, including so coupling. Under the [001] orientation the 16-band Hamiltonian using the basis $|S_N\uparrow\rangle$, $|S_N\downarrow\rangle$, $|S\uparrow\rangle$, $|S\downarrow\rangle$, $-\frac{i}{\sqrt{2}}|(X+iY)\uparrow\rangle$, $-\frac{i}{\sqrt{6}}|[(X+iY)\downarrow -2Z\uparrow]\rangle$, $\frac{i}{\sqrt{6}}|[(X-iY)\uparrow +2Z\downarrow]\rangle$, $\frac{i}{\sqrt{2}}|(X-iY)\downarrow\rangle$, $\frac{i}{\sqrt{3}}|[(X+iY)\downarrow +Z\uparrow]\rangle$, $\frac{i}{\sqrt{3}}|[(X-iY)\uparrow -Z\downarrow]\rangle$, $-\frac{i}{\sqrt{2}}|(X_{Bi}+iY_{Bi})\uparrow\rangle$, $-\frac{i}{\sqrt{6}}|[(X_{Bi}+iY_{Bi})\downarrow -2Z_{Bi}\uparrow]\rangle$, $\frac{i}{\sqrt{6}}|[(X_{Bi}-iY_{Bi})\uparrow +2Z_{Bi}\downarrow]\rangle$, $\frac{i}{\sqrt{2}}|(X_{Bi}-iY_{Bi})\downarrow\rangle$, $\frac{i}{\sqrt{3}}|[(X_{Bi}+iY_{Bi})\downarrow +Z_{Bi}\uparrow]\rangle$, $\frac{i}{\sqrt{3}}|[(X_{Bi}-iY_{Bi})\uparrow -Z_{Bi}\downarrow]\rangle$ can be written in the following form.

$$H_{16\times16} = \begin{bmatrix} H_{2\times2} & H_{2\times8} & 0 \\ H_{8\times2} & H_{8\times8} & H_{8\times6} \\ 0 & H_{6\times8} & H_{6\times6} \end{bmatrix} \tag{2.34}$$

where $H_{8\times8}$ is the 8-band Hamiltonian given by [44]

$$H_{8\times8} = \begin{bmatrix} E^c & c.c. & c.c. & c.c. & c.c. & c.c. & c.c. & c.c. \\ 0 & E^c & c.c. & c.c. & c.c. & c.c. & c.c. & c.c. \\ \frac{1}{\sqrt{2}}P_- & 0 & P+Q & c.c. & c.c. & c.c. & c.c. & c.c. \\ -\sqrt{\frac{2}{3}}P_z & \frac{1}{\sqrt{6}}P_- & S^* & P-Q & c.c. & c.c. & c.c. & c.c. \\ -\frac{1}{\sqrt{6}}P_+ & -\sqrt{\frac{2}{3}}P_z & -R^* & 0 & P-Q & c.c. & c.c. & c.c. \\ 0 & -\frac{1}{\sqrt{2}}P_+ & 0 & -R^* & -S^* & P+Q & c.c. & c.c. \\ -\frac{1}{\sqrt{3}}P_z & -\frac{1}{\sqrt{3}}P_- & \frac{S^*}{\sqrt{2}} & -\sqrt{2}Q & -\sqrt{\frac{3}{2}}S & \sqrt{2}R & P-\Delta & c.c. \\ -\frac{1}{\sqrt{3}}P_+ & \frac{1}{\sqrt{3}}P_z & -\sqrt{2}R^* & -\sqrt{\frac{3}{2}}S^* & \sqrt{2}Q & \frac{S}{\sqrt{2}} & 0 & P-\Delta \end{bmatrix} \tag{2.35}$$

The Hamiltonian contains of both kinetic terms H_k and strain terms H_ε and can also be expressed as $H_{8\times8} = H_k + H_\varepsilon$. Each of the terms E^c, $P_\pm$, P_z, P, Q, R and S can be expressed as $(\cdot) = (\cdot)_k + (\cdot)_\varepsilon$, where $(\cdot)_k$ is the kinetic component and $(\cdot)_\varepsilon$ is the strain component. The kinetic components terms are given by

$$E_k^c = E_g + \frac{\hbar^2}{2m_0}\gamma_c\left(k_x^2 + k_y^2 + k_z^2\right) \tag{2.36a}$$

$$P_{\pm k} = p_0\left(k_x \pm k_y\right) \tag{2.36b}$$

$$P_{zk} = p_0 k_z \tag{2.36c}$$

$$P_k = -\frac{\hbar^2}{2m_0}\gamma_1\left(k_x^2 + k_y^2 + k_z^2\right) \tag{2.36d}$$

$$Q_k = -\frac{\hbar^2}{2m_0}\gamma_2\left(k_x^2 + k_y^2 - 2k_z^2\right) \tag{2.36e}$$

$$R_k = -\frac{\sqrt{3}\hbar^2}{2m_0}\left[-\gamma_2\left(k_x^2 - k_y^2\right) + i2\gamma_3 k_x k_y\right] \tag{2.36f}$$

$$S_k = \frac{\sqrt{3}\hbar^2}{m_0}\gamma_3\left(k_x - ik_y\right)k_z \tag{2.36g}$$

where terms such as Δ_{so}, E_g Luttinger parameters $(\gamma_1, \gamma_2, \gamma_3)$ etc. have the same meaning as explained in the previous subsections.

For strained material, the Bir-Pikus Hamiltonian must be taken into consideration. The strain component terms can be expressed as follows.

$$E_\varepsilon^c = a_c\left(\varepsilon_{xx} + \varepsilon_{yy}\right) \tag{2.37a}$$

$$P_{\pm\varepsilon} = -p_0\left[\varepsilon_{xy}\left(k_x \pm ik_y\right) + \varepsilon_{xz}k_z\right] \tag{2.37b}$$

$$P_{z\varepsilon} = -p_0\left(\varepsilon_{xz}k_x + \varepsilon_{yz}k_y\right) \tag{2.37c}$$

$$P_\varepsilon = a_v\left(\varepsilon_{xx} + \varepsilon_{yy} + \varepsilon_{zz}\right) \tag{2.37d}$$

$$Q_\varepsilon = \frac{b}{2}\left(\varepsilon_{xx} + \varepsilon_{yy} - \varepsilon_{zz}\right) \tag{2.37e}$$

$$R_\varepsilon = \frac{\sqrt{3}}{2}b\left(\varepsilon_{xx} - \varepsilon_{yy}\right) - id\varepsilon_{xy} \tag{2.37f}$$

$$S_\varepsilon = d\left(\varepsilon_{xz} - i\varepsilon_{yz}\right) \tag{2.37g}$$

Here, the strain tensor components, ε_{ij} are calculated as follows, using C_{11}, C_{12} and C_{44} that are the elastic stiffness constants of the material.

$$\varepsilon_{xx} = \varepsilon_{yy} = \varepsilon_{||} = \frac{a_s - a_0}{a_0} \tag{2.38a}$$

$$\varepsilon_{zz} = -\frac{2C_{12}}{C_{11}}\varepsilon_{xx} \tag{2.38b}$$

Each overall Hamiltonian term in $H_{8\times8}$ can be found by adding the kinetic $(\cdot)_k$ and strain $(\cdot)_\varepsilon$ counterparts enlisted above.

And γ_c is given as follows.

$$\gamma_c = \frac{1}{m_e^*} - \frac{E_p}{3}\left(\frac{2}{E_g} + \frac{1}{E_g + \Delta_{so}}\right) \tag{2.39}$$

The $H_{2\times2}$ is the s_{N}-like localized N impurity Hamiltonian and given by [44, 102]

$$H_{2\times2} = \begin{bmatrix} E_N^0 & 0 \\ 0 & E_N^0 \end{bmatrix} \tag{2.40}$$

In a strained III-V-N material, the nitrogen level parameter, E_N is with respect to the valence band maximum (VBM) with strain consideration, such that E_N weakly shifts with applied pressure [103]. However, for the unstrained VBM, the nitrogen level, E_N^0 is given by

$$E_N^0 = E_N + VBM^S \tag{2.41}$$

where VBM^S is the top of strained valence band at Γ-point ($k = 0$). This can be calculated by utilizing the strain induced 8-band H at $k = 0$ point [44].

Similar to N, in order to include the Bi band broadening effect, a modified $H_{6\times6}$ is proposed for the p-like localized Bi impurity Hamiltonian [45], given by

$$H_{6\times6} = \begin{bmatrix} E^0_{Bi} & 0 & 0 & 0 & 0 & 0 \\ 0 & E^0_{Bi} & 0 & 0 & 0 & 0 \\ 0 & 0 & E^0_{Bi} & 0 & 0 & 0 \\ 0 & 0 & 0 & E^0_{Bi} & 0 & 0 \\ 0 & 0 & 0 & 0 & E^0_{Bi,so} & 0 \\ 0 & 0 & 0 & 0 & 0 & E^0_{Bi,so} \end{bmatrix} \tag{2.42}$$

Similar to N, the Bi levels with respect to the unstrained VBM, E^0_{Bi} and $E^0_{Bi,so}$ are given by

$$E^0_{Bi} = E_{Bi} + VBM^S \tag{2.43a}$$

$$E^0_{Bi,so} = E_{Bi,so} + VBM^S \tag{2.43b}$$

The $H_{8\times2}$ Hamiltonian is for the interaction between the s_{N}-like localized N impurity state (with N composition x) and host material state and given by

$$H_{8\times2} = \sqrt{x}V_N \begin{bmatrix} 1 & 0 \\ 0 & 1 \\ 0 & 0 \\ 0 & 0 \\ 0 & 0 \\ 0 & 0 \\ 0 & 0 \\ 0 & 0 \end{bmatrix} \tag{2.44}$$

Similarly, the $H_{6\times8}$ Hamiltonian is for the interaction between the p-like localized Bi impurity state (with Bi composition y) and host material state and given by [45]

$$H_{6\times 8} = \sqrt{y}V_{Bi}\begin{bmatrix} 0 & 0 & 1 & 0 & 0 & 0 & 0 & 0 \\ 0 & 0 & 0 & 1 & 0 & 0 & 0 & 0 \\ 0 & 0 & 0 & 0 & 1 & 0 & 0 & 0 \\ 0 & 0 & 0 & 0 & 0 & 1 & 0 & 0 \\ 0 & 0 & 0 & 0 & 0 & 0 & 1 & 0 \\ 0 & 0 & 0 & 0 & 0 & 0 & 0 & 1 \end{bmatrix} \tag{2.45}$$

V_N and V_{Bi} are the coupling coefficient in the BAC model for N and Bi respectively. $H_{8\times 6}$ and $H_{2\times 8}$ are the transpose of the $H_{6\times 8}$ and $H_{8\times 2}$, respectively.

We can expand the sixteen dimensional hole and electron envelope wave function for the QWs as

$$\Phi_m = \left\{\Phi_m^j\right\} (j = 1, 2, ..., 16) \tag{2.46}$$

where

$$\Phi_m^j = \exp\left[i\left(k_x x + k_y y\right)\right] \sum_m a_{n,m}^j \frac{1}{\sqrt{L}} \exp\left[i\left(k_z + m\frac{2\pi}{L}\right)z\right] \tag{2.47}$$

The QW period is $L = l + d$, where the width of the well is l while the barrier width is d. k_i $(i = x, y, z)$ are the wavevectors, $a_{n,m}^j$ is the expansion coefficient while n is the energy subband index [101].

However for 0D QDs or 2D NPLs, we expand as follows.

$$\Phi_m^j = \frac{1}{\sqrt{L_x L_y}} \exp\left[i\left(k_x x + k_y y\right)\right] \sum_m a_{n,m}^j \frac{1}{\sqrt{L_z}} \exp\left[i\left(k_z + m\frac{2\pi}{L_z}\right)z\right] \tag{2.48}$$

where L_z is the NPL thickness or QD thickness along z direction; and L_x and L_y are the dimensions along x and y directions.

We calculate the transition matrix element (TME) as $\mathcal{P}_{cv,i} = \langle \Psi_{c,\mathbf{k}} | \hat{\mathrm{e}} \cdot \mathbf{p}_i | \Psi_{v,\mathbf{k}} \rangle$, $i = x, y, z$. For the 16-band Hamiltonian matrix described in this subsection, the expressions for the upspin and downspin TMEs along the x, y and z directions are given below [101].

$$\mathcal{P}_{cv,x\uparrow} = p_0\sqrt{\frac{2}{m_0}}\sum_m \left(-\frac{i}{\sqrt{2}}a^5_{n_v,m} + \frac{i}{\sqrt{6}}a^7_{n_v,m} + \frac{i}{\sqrt{3}}a^{10}_{n_v,m}\right) a^{3*}_{n_c,m} \tag{2.49a}$$

$$\mathcal{P}_{cv,x\downarrow} = p_0\sqrt{\frac{2}{m_0}}\sum_m \left(-\frac{i}{\sqrt{6}}a^6_{n_v,m} + \frac{i}{\sqrt{2}}a^8_{n_v,m} + \frac{i}{\sqrt{3}}a^9_{n_v,m}\right) a^{4*}_{n_c,m} \tag{2.49b}$$

$$\mathcal{P}_{cv,y\uparrow} = p_0\sqrt{\frac{2}{m_0}}\sum_m \left(\frac{1}{\sqrt{2}}a^5_{n_v,m} + \frac{1}{\sqrt{6}}a^7_{n_v,m} + \frac{1}{\sqrt{3}}a^{10}_{n_v,m}\right) a^{3*}_{n_c,m} \tag{2.49c}$$

$$\mathcal{P}_{cv,y\downarrow} = p_0\sqrt{\frac{2}{m_0}}\sum_m \left(\frac{1}{\sqrt{6}}a^6_{n_v,m} + \frac{1}{\sqrt{2}}a^8_{n_v,m} - \frac{1}{\sqrt{3}}a^9_{n_v,m}\right) a^{4*}_{n_c,m} \tag{2.49d}$$

$$\mathcal{P}_{cv,z\uparrow} = p_0\sqrt{\frac{2}{m_0}}\sum_m \left(i\sqrt{\frac{2}{3}}a^6_{n_v,m} + \frac{i}{\sqrt{3}}a^9_{n_v,m}\right) a^{3*}_{n_c,m} \tag{2.49e}$$

$$\mathcal{P}_{cv,z\downarrow} = p_0\sqrt{\frac{2}{m_0}}\sum_m \left(i\sqrt{\frac{2}{3}}a^7_{n_v,m} - \frac{i}{\sqrt{3}}a^{10}_{n_v,m}\right) a^{4*}_{n_c,m} \tag{2.49f}$$

and

$$|\mathcal{P}_{cv,i}|^2 = |\mathcal{P}_{cv,i\uparrow}|^2 + |\mathcal{P}_{cv,i\downarrow}|^2, i = x, y, z \tag{2.50}$$

2.4 Strain Effects on Bandstructure

Semiconductor nanostructure geometries often form heterostructures and thus their exists strain component in all directions due to lattice mismatch. A major difference in 3D confined QDs from 1D confined QWs is that, in the latter the strain can be considered to be uniform. For a quantum well growing along the z direction, the strain components are $\epsilon_{xx} = \epsilon_{yy} = \dfrac{a_{subs} - a_{well}}{a_{well}}$ where a_{subs} and a_{well} are the lattice constants of the substrate and the well materials respectively. In this thesis, for QWs, the strain is calculated in this fashion and used in Sec. 2.3.2 and 2.3.4, and subsequently used in their respective Hamiltonian matrices for the bandstructure calculation.

However, for non-uniform strain (such as in QDs), there are two approaches to calculate the strain: (*i*) Harmonic Continuum Elasticity (CE) and (*ii*) Atomistic Elasticity (AE) on which the Valence Force Field (VFF) model is based. In a comprehensive comparison between the two methods, Pryor *et al.* [104] suggest that the AE approach gives more accurate results compared to the CE model in case of larger strain. Thus, for QDs and NPLs we have considered employed the VFF model to calculate the stain used in the Hamiltonians in Sec. 2.3.1 and 2.3.3, unless otherwise stated.

According to the VFF model, every atom in the crystal lattice structure is assigned a position vector $\mathbf{r}$. The total strain energy is expressed as a function of atomic positions as

$$E_{strain} = \sum_{i(j)} \varepsilon_{2B}(\mathbf{r}_i - \mathbf{r}_j) + \sum_{i(j,k)} \varepsilon_{3B}(\hat{\theta}_{ijk}) \tag{2.51}$$

where ε_{2B} is the two-body interaction effect between atom$_i$ and atom$_j$ with position vectors $\mathbf{r}_i$ and $\mathbf{r}_j$ respectively. And, ε_{3B} is the three-body interaction effect between atom$_i$, atom$_j$ and atom$_k$ where $\hat{\theta}_{ijk}$ is the ideal bond angle between the three atoms (indexed i, j and k), with atom$_i$ at the vertex. Using the VFF method with Keating potential [105], one can expand Eq. 2.51 to get the following expression

$$\begin{aligned} E_{strain} = \frac{1}{2} \sum_{i(j)} \frac{3\alpha_{i-j}}{8d_{0,i-j}^2} \left(|\mathbf{r}_i - \mathbf{r}_j|^2 - d_{0,i-j}^2 \right)^2 \\ + \sum_{i(j,k)} \frac{3\beta_{j-i-k}}{8d_{0,i-j}d_{0,i-k}} \left(|\mathbf{r}_i - \mathbf{r}_j||\mathbf{r}_i - \mathbf{r}_k| - \cos\hat{\theta}_{ijk} \cdot d_{0,i-j}d_{0,i-k} \right)^2 \end{aligned} \tag{2.52}$$

where i, j and k index the atoms in the crystal lattice; $d_{0,i-j}$ denotes the ideal bond length

between atom$_i$ and atom$_j$ related to its lattice constant $a_{0,i-j}$ as $d_{0,i-j} = \left(\frac{\sqrt{3}}{4}\right) a_{0,i-j}$. $\hat{\theta}_{ijk}$ is already explained in the preceding paragraph. For zinc-blende structure, $\hat{\theta}_{ijk} = \frac{1}{3}$. α_{i-j} is the bond stretching force constant of the $i-j$ bond, and β_{j-i-k} is the bond bending force constant of the $j-i-k$ bond angle. These are inherent material parameters of any material (or material combination) and are closely related to the elastic constants of the bulk material [106].

Next, we obtain the final atomic configuration of the crystal lattice by repeated conjugate gradient minimization of E_{strain}. Each atom is allowed to vibrate and move along the direction of force acting on it. The force on atom$_i$ is given by $\boldsymbol{F}_i = -\nabla_i(E_{strain})$. This is continued until no more net-force in acting on the atoms and the system has attained stability. Now the energy-minimized final positions of each atom is compared to its initial strain-free location to obtain a 3D strain map (profile) of the QD crystal lattice system.

2.5 Optical Processes in Semiconductors

A semiconductor quantum nanostructure experiences spatial confinement of excitons resulting in energy band splitting. To quantify the probability of occupation of electron in the conduction and valence bands, we use the notion of quasi-Fermi distribution functions: f_c for conduction band and f_v for valence band. They are defined as [62]

$$f_c = \frac{1}{1 + e^{(E_{nc} - E_{fc})/k_B T}} \tag{2.53a}$$

and

$$f_v = \frac{1}{1 + e^{(E_{nv} - E_{fv})/k_B T}} \tag{2.53b}$$

Here f_c gives the probability of electron occupation in the conduction band and f_v gives the probability of electron occupation in the valence band.[1] E_{f_c} and E_{f_v} are the quasi-Fermi energy level for the conduction- and valence-band respectively, and $\Delta F = E_{f_c} - E_{f_v}$ is the quasi-Fermi energy separation, all of which depend on the injection carrier density. E is the energy of the conduction- or valence-band state in question. k_B is the Boltzmann's constant and T is the absolute temperature in Kelvin.

The quasi-Fermi distribution functions, f_c and f_v give the probability that the energy levels E_{nc} and E_{nv}, respectively, are *occupied by electrons*. Maximum optical gain is obtained when $f_c = 1$ (upper level fully *occupied by electrons*) and $f_v = 0$ (lower level totally void of electrons ie. fully *occupied by holes*). The opposite causes maximum absorption. The gain is proportional to the Fermi factor $(f_c - f_v)$ coming from $f_c(1 - f_v) - f_v(1 - f_c)$. The first term accounts for the stimulated emission and the second term for the band-to-band absorption [107]. Note that the Fermi factor diminishes to 0 as energy approaches towards the quasi-Fermi energy separation ΔF, beyond which absorption (negative gain) dominates. Thus the spectrum of interest for gain is limited to $E_g < \hbar\omega < \Delta F$. The Fermi factor is therefore a very important quantifiable measure to study the counteracting effects of emission and absorption to obtain optical gain.

[1] It is implied that $(1 - f_v)$ gives the probability of electron vacancy (i.e. hole occupancy) in the valence band.

2.5.1 Non-Excitonic Optical Processes

Optical gain is defined as the growth ratio of light intensity (photon density) per unit length of light propagation and generally expressed in inverse centimeters (1/cm). When a photon is incident of an semiconductor media, it could either get absorbed or it could generate gain. The absorption of a photon results in the creation of an electron - hole pair caused by the transition of an electron from a lower to a higher energy band. On the other hand, stimulated recombination of an existing electron - hole pair creating a second photon results in gain. This second photon exhibits the same phase and the same wavelength as the first photon, thus doubling the amplitude of the monochromatic wave. Further repetition of this process leads to strong light amplification. However, the absorption of photons by the generation of new electron - hole pairs is the competing process. And when more electrons are present at the higher energy level (CB) compared to the lower energy level (VB), stimulated emission prevails [107].

The optical gain is proportional to the probability that a given photon triggers an electron transition from a higher energy level c to a lower energy level v.

One approach to describe the non-excitonic optical processes in semiconductor nanostructures is to apply a 3D confinement treatment to the semiconductor nanostructure. This is suited for QDs of III-V semiconductors and dilute nitride/bismide alloys thereof, for which the exciton binding energy is relatively non-significant compared to the transition energy. On the basis of the density-matrix theory equation, we calculate the optical gain spectra of QDs using the following expression [108]

$$\mathscr{G}(\hbar\omega) = \frac{2\pi e^2}{c n_r \varepsilon_0 m_e^2 \Omega} \sum_{c,v} \frac{|\mathcal{P}_{cv}|^2 (f_c - f_v)}{\omega_{cv}} \times \mathscr{L}_{cv}(\hbar\omega - \hbar\omega_{cv}) \tag{2.54}$$

where n_r is the refractive index of the active NPL, e is the fundamental electronic charge, $\hbar\omega$ is the photon energy, ε_0 is the free-space dielectric constant, c is the speed of light in vacuum, m_0 is the electronic mass and $\hbar$ is the reduced plank's constant. f_c and f_v are the Fermi-Dirac distributions for the electrons and holes, as explained in Sec. 2.5. The term $|\mathcal{P}_{cv}|^2$ is the square of the optical transition matrix element (TME), which quantifies the strength of transition between the electron- and hole-subband. It has been described in fair depth in Sec. 2.3.

The gain spectra must however consider the transition energy broadening (dephasing) which is accounted by the Lorentzian lineshape, $\mathscr{L}_{cv}(\hbar\omega - \lambda)$ in Eq. 2.54, and given by

$$\mathscr{L}_{cv}(\hbar\omega - \lambda) = \frac{1}{\pi} \frac{\hbar/\tau_{in}}{(\hbar\omega - \lambda)^2 + (\hbar/\tau_{in})^2} \tag{2.55}$$

whose full width at half maximum (FWHM) is $2\hbar/\tau_{in}$ and scattering probability per unit time is $1/\tau_{in}$, where τ_{in} is the intraband relaxation time [62].

In the above discussion about the gain calculation, we had applied a 3D confinement treatment to the semiconductor nanostructure, suited for QDs. On the other hand, for quantum mechanical structures such as the QWs, we have to apply a 1D confinement treatment to the semiconductor nanostructure. For this case, the linear optical gain spectra is calculated based on the density-matrix theory using the following equations [101, 109]

$$\mathscr{G}\left(\hbar\omega\right) = \left[1 - \exp\left(\frac{\hbar\omega - \Delta F}{k_B T}\right)\right] \frac{\pi^2 c^2 \hbar}{n^2 \omega^2} \mathscr{R}_{sp}\left(\hbar\omega\right) \tag{2.56}$$

$$\begin{aligned} \mathscr{R}_{sp}\left(\hbar\omega\right) = \frac{ne^2\omega}{\pi m_0^2 \varepsilon_0 \hbar c^3} \sum_c \sum_v \int\int \frac{|\mathcal{P}_{cv}|^2}{4\pi^2 d} f_c f_v \\ \times \mathscr{L}_{cv}(\hbar\omega_{cv} - \hbar\omega) dk_x dk_y \end{aligned} \tag{2.57}$$

where $R_{sp}\left(\hbar\omega\right)$ is the spontaneous emission rate. f_c and f_v are the Fermi-Dirac distributions for the electrons and holes in the CB and VB respectively and $\Delta F = E_{f_c} - E_{f_v}$ is the quasi-Fermi energy level separation between the CB and VB which is dependent on the injection carrier density.

Furthermore, the stimulated emission rate $\mathscr{R}_{st}(\hbar\omega)$ is related to the spontaneous emission rate $\mathscr{R}_{sp}(\hbar\omega)$ as [62]

$$\mathscr{R}_{st}(\hbar\omega) = \left[1 - \exp\left(\frac{\hbar\omega - \Delta F}{k_B T}\right)\right] \cdot \mathscr{R}_{sp}(\hbar\omega) \tag{2.58}$$

2.5.2 Excitonic Optical Processes

The electron-hole (excitonic) interaction plays an important role in the calculation of the optical spectra of semiconductors. It not only affects the bound excitons in the energy-gap region, but also in the continuum [110]. A major part of this thesis focuses on the calculation of optical processes in CdSe and CdS NPLs. The thickness quantization energy in NPLs in much larger than the bulk exciton binding energy of 15 meV in CdSe and 26 meV in CdS [111], such that the NPL exciton binding energy is close to the 2D limit of a fourfold binding energy increase [112]. The binding energy gets enhanced by the lower dielectric constant of the NPL surrounding, and the reduced dielectric constant of the NPL for energies above the longitudinal optic (LO) phonon energy. The exciton oscillator strength increases with the exciton binding energy, and II-VI (CdSe, CdS, etc) NPLs exhibit giant oscillator strength transition (GOST) [7], so it is imperative to consider the excitonic effect in the calculation of optical processes for the NPLs studied in this thesis.

There are several approaches to calculate the excitonic optical processes in II-VI NPLs. First we describe a method to calculate the excitonic gain and spontaneous radiative rate wherein we apply a 3D confinement treatment to the semiconductor nanostructure. This approach is suited for QDs and NPLs treated like QDs. On the basis of the density-matrix theory equation, we calculate the optical gain spectra of NPLs considering excitonic effects as a sum of the contributions from excitonic bound states, $\mathscr{G}^{ex,b}$ and band-to-band continuum-states, $\mathscr{G}^{c}$. The excitonic bound state contributions is given by [113, 114]

$$\mathscr{G}^{ex,b}(\hbar\omega) = \frac{C_0}{d}\sum_{c,v}|\Psi_{1s}^{cv}(0)|^2|\mathcal{P}_{cv}|^2|I_{cv}|^2 \times (f_c - f_v)\,\mathscr{L}(\hbar\omega - \hbar\omega_{cv} - \hbar\omega_b) \tag{2.59a}$$

$$\Psi_{1s}(x) = \frac{4\beta}{a_B\sqrt{2\pi}}e^{-2x\beta/a_B} \tag{2.59b}$$

$$\hbar\omega_b = -4\beta^2 R_y \tag{2.59c}$$

And for the band-to-band continuum state contributions, we have [62, 114]

$$\mathscr{G}^c(\hbar\omega) = \frac{C_0}{V}\sum_{c,v}|\mathcal{P}_{cv}|^2(f_c - f_v)\times$$
$$S_{2D}(\hbar\omega - \hbar\omega_{cv})\,\mathscr{L}(\hbar\omega - \hbar\omega_{cv}) \tag{2.60a}$$

$$S_{2D}(\hbar\omega - \hbar\omega_{cv}) = \frac{2}{1+\exp\left(-2\pi\sqrt{R_y/(\hbar\omega - \hbar\omega_{cv})}\right)} \tag{2.60b}$$

where $C_0 = \dfrac{\pi e^2}{n_r c\varepsilon_0 m_0^2\omega}$, n_r is the refractive index of the active NPL, e is the fundamental electronic charge, $\hbar\omega$ is the photon energy, ε_0 is the free-space dielectric constant, c is the speed of light in vacuum, m_0 is the electronic mass and $\hbar$ is the reduced plank's constant. d is the NPL thickness, and V is the NPL volume in real space. The overlap integral between the electron and hole wavefunctions along the transverse direction is given by $I_{cv} = \left\langle \Psi^{E(c)}(z)\middle|\Psi^{H(v)}(z)\right\rangle$. The 1S exciton envelope function is given by $\Psi_{1s}(x)$ where x is the relative distance between the electron and hole along the transverse direction in the NPL. $\hbar\omega_b$ is the 1S exciton binding energy and β is a variational parameter, taken to be 1 for two-dimensional structures. $R_y = m_r e^4/32\pi^2\varepsilon_0^2\varepsilon_r^2\hbar^2$ and $a_B = 4\pi\varepsilon_0\varepsilon_r\hbar^2/m_r e^2$ are the excitonic Rydberg energy and excitonic Bohr radius respectively, where ε_r is the relative permittivity and m_r is the reduced mass of the electron-hole pair: $m_r^{-1} = m_e^{-1} + m_h^{-1}$. $S_{2D}(\hbar\omega - \hbar\omega_{cv})$ is the 2D Sommerfeld enhancement factor [62]. Subscripts c (for CB) and v (for VB) denotes the discrete energy states. f_c and f_v are the Fermi-Dirac distributions for the electrons and holes, as explained in Sec. 2.5. And $|\mathcal{P}_{cv}|^2$ is the square of the optical transition matrix element (TME), as described in Sec. 2.3. The term $\mathscr{L}_{cv}(\hbar\omega - \lambda)$ is the Lorentzian lineshape described by Eq. 2.55 in Sec. 2.5.1.

Similar to the gain calculation, the net spontaneous radiative rate can be estimated as a sum of the spontaneous radiative rate from the excitonic bound states, $\mathscr{R}_{sp}^{ex,b}$ and continuum-states, $\mathscr{R}_{sp}^{c}$. The excitonic bound state contribution is given by [113, 114]

$$\mathscr{R}_{sp}^{ex,b}(\hbar\omega) = \frac{e^2 n_r \hbar\omega}{\pi m_0^2 \varepsilon_0 c^3 \hbar^2 d} \sum_{c,v} |\Psi_{1s}^{cv}(0)|^2 |\mathcal{P}_{cv}|^2 \cdot |I_{cv}|^2 \times$$
$$f_c(1-f_v)\,\mathscr{L}(\hbar\omega - \hbar\omega_{cv} - \hbar\omega_b) \tag{2.61}$$

And for the band-to-band continuum state contributions, we have [62, 114]

$$\mathscr{R}_{sp}^{c}(\hbar\omega) = \frac{e^2 n_r \hbar\omega}{\pi m_0^2 \varepsilon_0 c^3 \hbar^2 V} \sum_{c,v} |\mathcal{P}_{cv}|^2 f_c(1-f_v) \times$$
$$S_{2D}(\hbar\omega - \hbar\omega_{cv})\,\mathscr{L}(\hbar\omega - \hbar\omega_{cv}) \tag{2.62}$$

The terms $S_{2D}(\hbar\omega - \hbar\omega_{cv})$, $\mathscr{L}(\hbar\omega - \hbar\omega_{cv})$, I_{cv}, R_y, a_B, etc are identical to those used in the excitonic gain equations.

In the above discussion about the excitonic gain and spontaneous radiative rate calculation, we had applied a 3D confinement treatment to the semiconductor nanostructure, which was suited for QDs and smaller NPLs treated like QDs. On the other hand, for quantum mechanical problems such as the QW or laterally large NPLs (behaving like typical QWs), we have the freedom to apply a 1D confinement treatment to the semiconductor nanostructure.

Now for this case, we calculate the optical absorption spectra of the active region of NPLs. The phenomenon of optical absorption can be simple understood by visualizing an incident photon facilitating the rise of an electron from a lower energy VB state to a higher energy CB state (vertical transition), essentially at constant momentum [115]. Here the presumption is that all such transitions have identical strength, but may have different vertical transition energies. Therefore, the optical absorption spectrum has a form that directly follows from the energy density-of-states (DOS), which for bulk is $\propto (E - E_g)^{1/2}$ and step like for quasi-2D structures, such as QWs and large NPLs. However, unlike bulk semiconductors, in quantum confined quasi-2D structures such as QWs and large NPLs the excitonic effects are very distinct even at room temperature (RT). It is possible to create

an exciton with an energy E_b^{ex} (exciton binding energy) less than that required to create a 'free' electron-hole pair, therefore we do observe optical absorption at photon energies just below the effective band-gap energy at an energy = $E_g^{\text{eff}} - E_b^{ex}$ [116].

Here, we calculate the optical absorption spectra of NPLs considering excitonic effects as a sum of the contributions from bound excitonic states absorption ($\alpha^{ex,b}$) and continuum band-to-band states absorption with Sommerfeld enhancement (α^c), given by Eq. 2.63b and 2.63a respectively.

$$\alpha^{ex,b}(\hbar\omega) = \frac{\pi e^2}{2\omega n_r m_0 \varepsilon_0 c} \sum_{n_c,n_v} \frac{|\mathcal{P}_{cv}|^2}{d} |I_{cv}|^2 \times |\varphi_{ns}(0)|^2 \frac{\tau_{ex}}{n_c n_v \hbar} \operatorname{sech}\left[\frac{\hbar\omega_{cv} - \hbar\omega_b - \hbar\omega}{n_c n_v \hbar/\tau_{ex}}\right] \tag{2.63a}$$

$$\alpha^{c}(\hbar\omega) = \frac{\pi e^2}{2\omega n_r m_0 \varepsilon_0 c} \sum_{n_c,n_v} \iint \frac{|\mathcal{P}_{cv}|^2}{4\pi^2 d} S_{2D}(\hbar\omega - \hbar\omega_{cv}) \times \frac{\tau}{n_c n_v \hbar} \operatorname{sech}\left[\frac{\hbar\omega_{cv} - \hbar\omega}{n_c n_v \hbar/\tau}\right] dk_x dk_y \tag{2.63b}$$

where

$$\hbar\omega_b = \frac{\hbar\omega_b^{3D}}{\left(n - \frac{1}{2}\right)^2} \tag{2.64a}$$

$$|\varphi_{ns}(0)|^2 = \frac{1}{\pi a_B \left(n - \frac{1}{2}\right)^2} \tag{2.64b}$$

The terms $S_{2D}(\hbar\omega - \hbar\omega_{cv})$, $\mathscr{L}(\hbar\omega - \hbar\omega_{cv})$, I_{cv}, R_y, a_B, etc are once gain identical to those used in the previous cases. $\hbar\omega_b$ is the absolute value of exciton binding energy, given by Eq. 2.64a, where $\hbar\omega_b^{3D}$ is the exciton binding energy for bulk material.

2.6 Temperature Effect on Bandgap

The band gap, E_g of most semiconductor vary in the order of 10^2 meV from around 10K to RT [11]. Due to such variations, the design of semiconductor optoelectronic devices require precise calibration. The variation of E_g is results in a change of emission color in LEDs or the low limit sensitivity of a photodetector. The band gap has a negative thermal coefficient (dE_g/dT) due to (i) the thermal dilatation of the lattice, with linear dependence at high temperature, and (ii) the temperature dependent electron-phonon interaction, proportional to T^2 at low temperature and linear in T at high temperatures. In this context, we have the Varshni relation [117] to explicate the behavior of E_g vs. T

$$E_g(T) = E_g(0) - \frac{\alpha T^2}{\beta + T} \tag{2.65}$$

where T is absolute temperature in Kelvin (K), and α and β are constants of a material. β is usually close to the Debye Temperature of the material. At high temperatures Equation 2.65 simplifies to

$$E_g(T) = E_g(0) - \alpha T \quad \text{and} \quad \frac{dE_g}{dT} = -\alpha \quad \text{if} \quad T \gg \beta \tag{2.66}$$

However, detailed systematic study of $E_g(T)$ for cubic II-VI semiconductors have shown that the Varshni relation doesn't give an accurate approximation [11]. Another semiempirical expression (Eq. 2.67) was suggested by O'Donnell *et al.* which takes into consideration the Bose-Einstein statistical factors for phonon emission and absorption.

$$E_g = E_g(0) - \frac{2S\langle\hbar\omega\rangle}{e^{\langle\hbar\omega\rangle/k_BT} - 1} \tag{2.67}$$

where S is a dimensionless electron-phonon coupling constant based on the vibronic model of Huang and Rhys. $\langle\hbar\omega\rangle$ is the average phonon energy. Equation 2.67 has the same functional dependence as Eq. 2.68 suggested by Cardona *et al.*

$$E_g = E_g(0) - \frac{2a_{ep}}{e^{\Theta/T} - 1} \tag{2.68}$$

where a_{ep} is the exciton-phonon coupling constant and Θ is the average phonon temperature, the average phonon energy being $k_B\Theta$.

Chapter 3

CdSe and CdS Nanoplatelets: Dimension Effect

3.1 Introduction

Optoelectronic properties of II-VI semiconductor NPLs are dictated by their electronic bandstructure and band mixing probabilities, which is strongly geometry dependent, as discussed in Sec. 1.2.1. Carriers have reduced freedom of movement in such low-dimensional structures, thus significantly modifying the density-of-states and wavefunction distributions [118]. The resulting discrete energy spectrum narrows down the optical transition energy between these states. This characteristic accompanied by increased carrier confinement results in the optical transition matrix enhancement, leading to improved performances in optoelectronic devices [119]. The most widely studied CdSe and CdS NPLs however have been reported to be characterized by their thickness alone [10, 25] claiming that they emit at discrete wavelengths depending on atomic-layer thickness. The lateral sizes often vary among these observations but are commonly neglected. This necessitates a study on the effect of vertical thickness and lateral size of NPLs in tandem for both CdSe and CdS. We have addressed this need by conducting a dimension effect study on CdSe and CdS NPLs in this chapter, wherein we have investigated the effect of lateral size and vertical thickness of CdSe and CdS nanoplatelets (NPLs) on their electronic structure and optical properties. The findings of our study enables us to obtain a relatively more continuously tunable emission spectrum rather than discrete emission wavelength dependent only on thickness. In Fig. 3.1, we show an illustration schematic and a 3D atom-by-atom

view of a typical NPL.

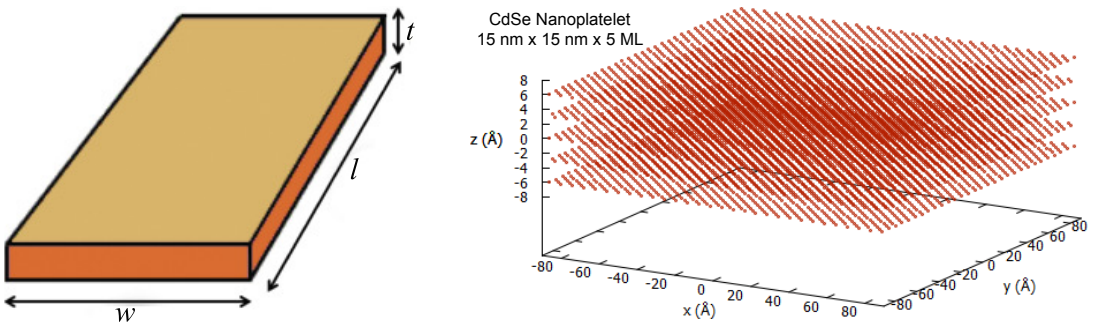

(a) (b)

Figure 3.1: (a: *left*) Schematic of NPL with lateral dimensions $l \times w$ and vertical thickness of t; and (b: *right*) 3D atom-by-atom view of a 15 nm × 15 nm × 5 ML CdSe NPL

3.2 Theoretical Framework

We have studied CdSe and CdS NPLs in the zincblende phase, assuming they are synthesized colloidally [8]. The 3D atom-by-atom model of a typical NPL is shown in Fig. 3.1 (b). In a colloidal solution, they are surrounded by a ligand dielectric medium, which helps to stabilize them and enhances their optical properties by passivating the surface electronic states. For each NPL geometry, we use an effective mass envelope function theory approach based on the 8-band $\boldsymbol{k}\cdot\boldsymbol{p}$ method using the first basis type described in Sec. 2.3.1, which simultaneously takes into account the nonparabolicity of the coupled conduction band (CB) and valence band (VB) including the orbit-splitting bands to solve its eigenenergy and obtain its electronic structure in the vicinity of the Γ-point of the Brillouin zone. The 8-band Hamiltonian is represented in the Bloch function basis as detailed in Eq. 2.8. The TMEs are calculated using Eq. 2.13.

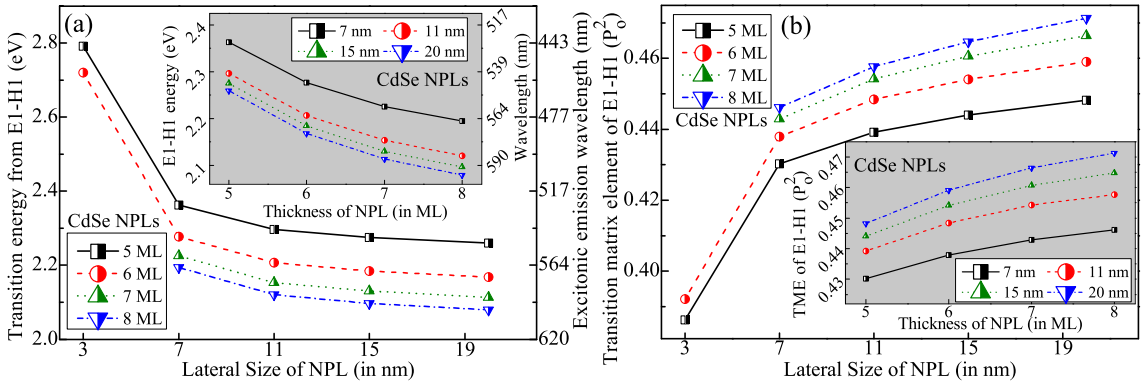

Figure 3.2: (a: *left*) E1–H1 excitonic transition energy (photon emission wavelength) vs. lateral size of NPL, and vs. thickness of NPL (*inset*); and (b: *right*) E1–H1 transition matrix element vs. lateral size of NPL, and vs. thickness of NPL (*inset*) for CdSe NPLs.

3.3 Results and Discussions

3.3.1 Electronic Bandstructure and Properties

The thickness and lateral sizes of both CdSe and CdS NPLs are varied to investigate their influence on the electronic bandstructure. Here we have considered only square NPLs i.e. $l = w$ for convenience of understanding and studied NPLs having thickness varying from 4 to 8 monolayers (MLs) and lateral size from 20 nm to as low as 3 nm. The thickness in ML can be converted to nm by computing ML $\times (a/2)$ where a is the lattice constant of the material in nm. For example: 5 ML CdSe NPL is 1.513 nm thick, while 5 ML CdS NPL is 1.458 nm thick [See data in Table A.1 on pg. 185].

Fig. 3.2 shows the excitonic transition energy (and emission wavelength) between bottom of conduction band (E1) to top of valence band (H1) i.e. E1–H1, and the transition matrix element values for the E1–H1 transitions for varying sizes and thicknesses of CdSe NPLs. The main plots show the variation as a function of the lateral size of NPLs while the insets show it as a function of the thickness. With an increase in both size and thickness there is a red shift in the transition energy (photon emission energy). This shift is gradual for laterally large NPLs, but we observe that for NPLs smaller than 7 nm (∼4 times the NPL thickness) the emission energy drastically increases. In reality, such small nanocrystals behave more like quantum dots (QDs) rather than NPLs.

The value of TME for E1–H1 transitions in CdSe NPLs, as shown in Fig. 3.2 (b) increases with an increase in the size and thickness of NPLs. This is because of the higher extent of electron and hole wavefunction overlap, as we shall subsequently see. We will show that

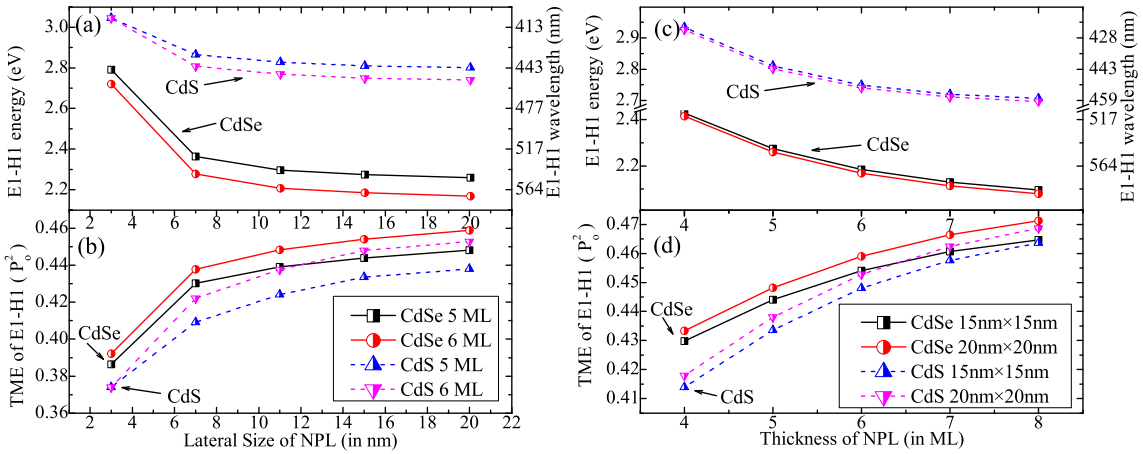

Figure 3.3: (a: *top left*) and (b: *bottom left*) E1–H1 transition energy/wavelength and TME for CdSe and CdS NPLs vs. lateral size; and (c: *top right*) and (d: *bottom right*) E1–H1 transition energy/wavelength and TME for CdSe and CdS NPLs vs. thickness. *Left* and *right* panel are a comparison between size and thickness effects.

the H1 (top most valence band level) corresponds to heavy hole (*hh*) in both CdSe and CdS which is *s*-like. Its overlap extent with E1 (also *s*-like) determines this TME value, which is expected to be higher for volumetrically larger NPLs.

Fig. 3.3 shows a comparison between how the E1–H1 emission energy and TME of CdSe and CdS NPLs of identical geometries are affected by their dimensions. CdSe has lower emission energy due to its smaller bandgap. Also, it is marginally more sensitive to size effect as its magnitude of red shift with increasing size is larger. CdSe also has a higher TME as its conductions electrons can strongly couple with the holes. This is because CdSe ($m_e^* = 0.13$) has a lower effective electron mass than CdS ($m_e^* = 0.25$) and thus a more concave dispersion curve relating from $m^* = \hbar^2 \left(\frac{\partial^2 E}{\partial k^2}\right)^{-1}$. CdSe can serve as a better active region material than CdS. CdS, on the other hand having a wider bandgap can be an efficient barrier to CdSe in nanoheterostructures.

Comparing Fig. 3.3 (a) with Fig. 3.3 (c), we have two important observations – (*i*) On doubling the lateral size from 10 nm to 20 nm the emission energy red shifts by ∼80–100 meV for CdS and CdSe NPLs of 5 ML and 6 ML. But on doubling the thickness from 4 ML to 8 ML the emission energy red shifts by ∼300–400 meV for CdS and CdSe NPLs of size 15 nm and 20 nm. While drawing this comparison we have ignored NPLs of size $<$ than 7 nm, because they are practically QDs. (*ii*) The difference in emission between 5 ML and 6 ML NPLs in Fig. 3.3 (a) is much greater than that between NPLs of size 15 nm and

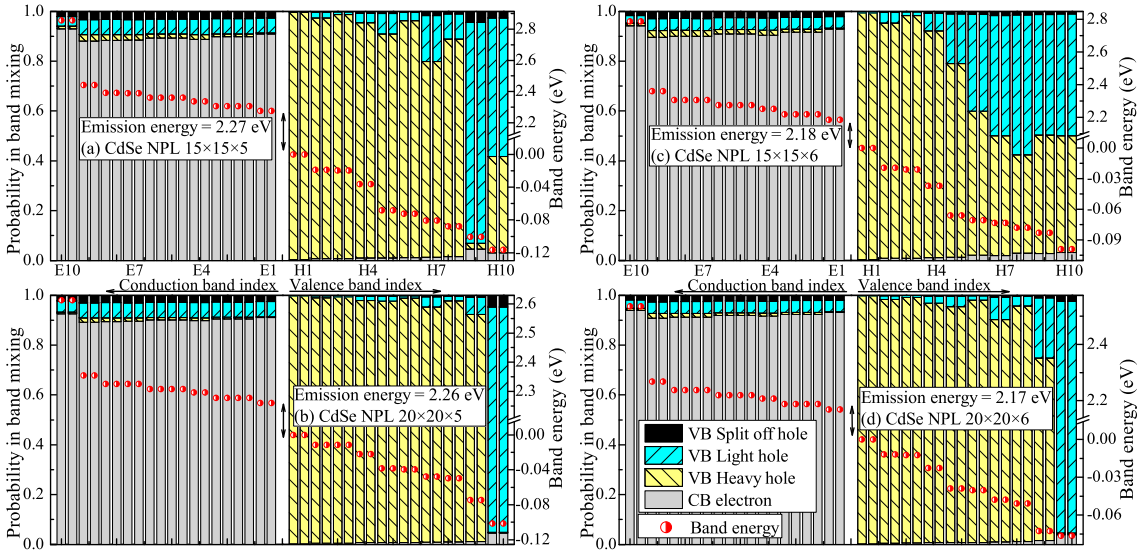

Figure 3.4: Electronic bandstructure and the probability in band mixing between conduction electrons and valence heavy holes, light holes and split off holes for CdSe NPLs of size (a) 15 nm × 15 nm × 5 ML (b) 20 nm × 20 nm × 5 ML (c) 15 nm × 15 nm × 6 ML (d) 20 nm × 20 nm × 6 ML. E1–H1 transition energies are indicated.

20 nm in Fig. 3.3 (c). From these two observations, we see NPLs emissions are considered to be primarily thickness dependent, as it is the most significant geometrical parameter in NPL design. The E1–H1 TME pattern in Fig. 3.3 (b) is consistent with Fig. 3.3 (d) as it increases with an increase in the volume. The *s*-like electron and hole wavefunction has a larger volumetric overlap with increasing size and thickness. However, a change in thickness affects the TME more than a change in the size, disregarding intentionally NPLs smaller than 7 nm. The increase in E1–H1 TME is ∼4–6 times larger on doubling the thickness from 4 ML to 8 ML as compared to doubling the size from 10 to 20 nm. This phenomenon can be understood by visualizing the *s*-like E1 and H1 wavefunctions that are like oblate ellipsoids [120] spread in all directions inside the NPL. Its semi-principal axes are determined by the NPL size and thickness. The wavefunction ellipsoid is spread largely in the x-y plane but restricted along the z direction. Thus the differential change on overlap integral for calculating TME would be larger on varying the thickness as compared to varying the lateral size.

Among all the NPL cases studied so far, Fig. 3.4 shows the electronic bandstructure and the probability in band mixing between conduction electrons and valence heavy holes, light holes and split off holes for CdSe NPLs of size (a) 15 nm × 15 nm × 5 ML (b) 20 nm

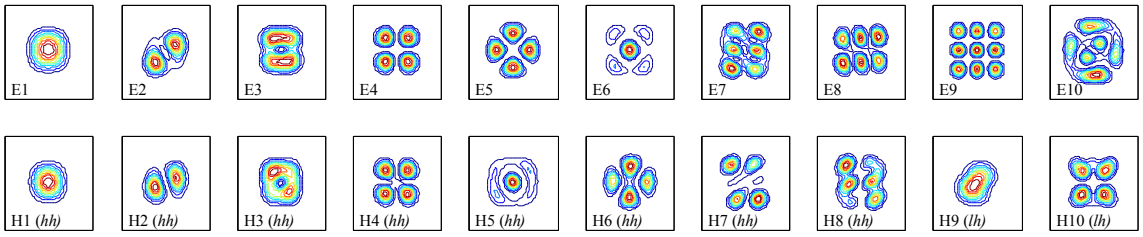

Figure 3.5: Spatial charge density distributions of the first 10 conduction (electron 'E') and valence (hole 'H') bands of CdSe NPL of size 15 nm × 15 nm × 5 ML at 300 K cut along the x-y plane at $z = 0$ [Refer Fig. 3.1 (b)]. *hh* stands for heavy hole, *lh* for light hole.

× 20 nm × 5 ML (c) 15 nm × 15 nm × 6 ML (d) 20 nm × 20 nm × 6 ML at 300 K. This choice is suitable to comparatively study the effect of thickness and size in tandem. We can observe that increasing the thickness from 5 ML to 6 ML red shifts the emission energy by 900 meV, while increasing the lateral size from 15 nm to 20 nm red shifts by only 100 meV. The effective heavy hole (*hh*) mass is much more that the effective electron mass for both CdSe and CdS [121], therefore the *hh* dispersion curve is much flatter than the conduction dispersion curve. Therefore the first 10 hole levels span only ∼10–12 meV, while the first 10 electron levels span ∼400–500 meV. The first few hole levels are *hh* dominant, while the *lh* contribution increases later. The band-mixing probabilities depend on the varying extent of coupling between the CB electrons and VB *hh*, *lh* and *so* holes, and it can be empirically determined for any NPL. But the observed band mixing probabilities for each level directly relates to the aggregate electron and hole wavefunction and associated charge densities.

The spatial charge densities of the first ten electron and hole states (square of the wavefunction i.e. probability of finding them) for the 15 nm × 15 nm × 5 ML CdSe NPL at 300 K cut along the x-y plane at $z = 0$ [refer Fig. 3.1 (b)] are shown in Fig. 3.5. This corresponds to the NPL of Fig. 3.4 (a). The E1 and H1 states are s-like, E2 and H2 are p-like, E3 and H3 are formed by s-p-mixing, E4 and H4 are d_{xy}-like. E5 and H6 are $d_{x^2-y^2}$-like, while E6 and H5 are d_{z^2}-like. *hh* has higher probability in the holes states H1 to H8 while H9 and H10 are *lh* dominated [see Fig. 3.4 (a)]. In the TE mode, E1–H1 (*hh*) transition has the highest strength (TME = 0.45), while the second highest transition strength is of the TM mode E1–H9 (*lh*) transition (TME = 0.44). Both H1 and H9 are s-like and have favorable spatial wavefunction overlap with E1. This is consistent with the notion that the primary peak of a typical CdSe NPL absorption spectra comes from *hh*, while the secondary peak from *lh* [25]. Spatial charge density distributions for other cases of Fig. 3.4 can also be obtained which will directly relate to their corresponding band mixing

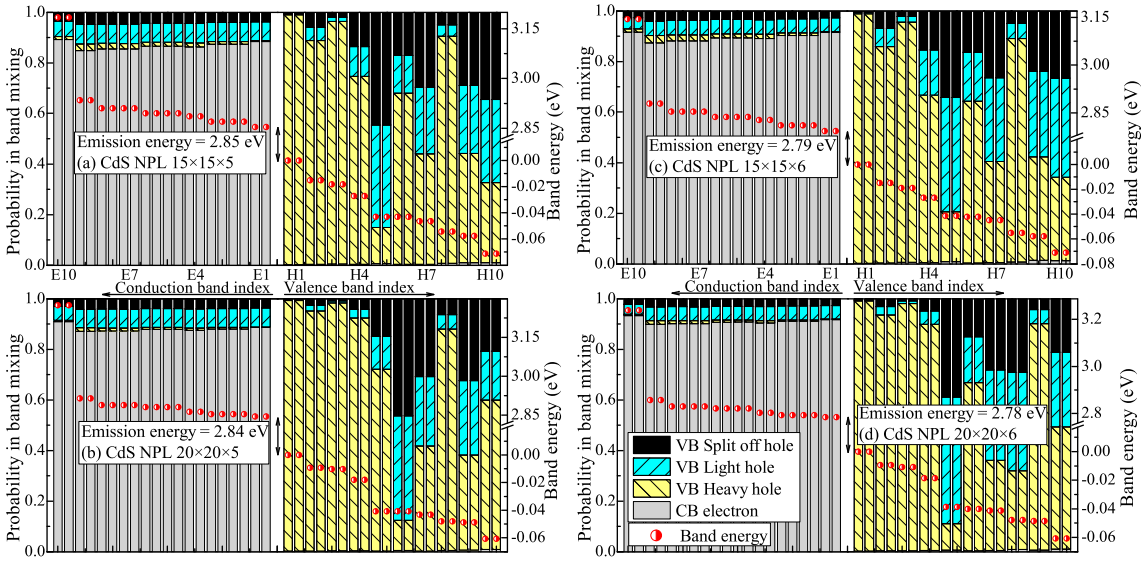

Figure 3.6: Electronic bandstructure and the probability in band mixing between conduction electrons and valence heavy holes, light holes and split off holes for CdS NPLs of size (a) 15 nm × 15 nm × 5 ML (b) 15 nm × 15 nm × 6 ML (c) 20 nm × 20 nm × 5 ML (d) 20 nm × 20 nm × 6 ML. E1–H1 transition energies are indicated.

probabilities.

Similar to the four cases of Fig. 3.4, we have shown the electronic bandstructure and the probability in band mixing for CdS NPLs in Fig. 3.6. Increasing the thickness from 5 ML to 6 ML red shifts the emission energy by 600 meV (as compared to 900 meV in CdSe, see Fig. 3.4), while increasing the lateral size from 15 nm to 20 nm red shifts by only 100 meV. Broadly, thickness has a greater impact in both cases, but more in CdSe than CdS. Comparing Fig. 3.4 and Fig. 3.6, we also see that the first 10 hole levels span ∼10–12 meV in CdSe, but only ∼6–8 meV in CdS. This is due to the heavier effective hole mass property of CdS compared to CdSe, making its dispersion curve even more flatter. The same follows for first 10 electron levels, which span ∼300–400 meV in CdS compared to ∼400–500 meV in CdSe. In the individual band mixing probabilities CdS has a much higher contribution from split-off holes because it's spin-orbit splitting energy is over six times smaller than that of CdSe [122, 123].

The charge densities of the first ten E and H states of the 15 nm × 15 nm × 5 ML CdS NPL of Fig. 3.6 (a) is shown in Fig. 3.7. E1 and H1 are *s*-like, E2 and H2 are *p*-like, E3 and H3 have *s*-*p*-mixing, E4 and H4 are d_{xy}-like, E5 and H8 are $d_{x^2-y^2}$-like. H5, H9 and H10 have varying ratios of *hh*, *lh* and *so* holes. The dominant contributors are 44% *so*

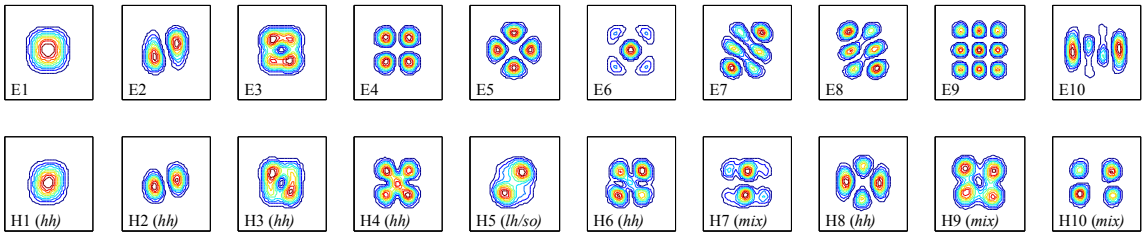

Figure 3.7: Spatial charge density distributions of the first 10 conduction (electron 'E') and valence (hole 'H') bands of CdS NPL of size 15 nm × 15 nm × 5 ML at 300 K cut along the x-y plane at $z = 0$. *hh* stands for heavy hole, *lh* for light hole and *so* for split-off hole.

(H5), 43 % *hh* (H9) and 34 % *so* (H10), but others are quite close, so we assign them as *mix*. The E1–H1 transition in TE mode is strongest (TME=0.43), followed by TM mode E1–H5 (lh/so) transition. The spatial charge density of E and H levels directly relate to their corresponding band mixing probabilities, and they have a fundamental structure. For zincblende semiconductors, the first few H levels are *hh* dominated followed by *lh* and *so* hole. The strongest TE transition comes from E1–H1 both of which are s-like and the second strongest from TM transition from E1–H(n)$_n$, which is near-s-like and n is case specific. Besides these, the detailed spatial charge densities and band mixing probabilities need to be empirically determined by calculation for a given NPL.

Section Highlights:

- Both thickness and lateral size have profound impact on the emission energy and TME. Although a differential change in the thickness has a larger impact, the effect of lateral size is also quite significant.
- Due to a larger m^*_{hh} compared to m^*_e in both CdSe and CdS, the *hh* dispersion curve is flatter and hole states are more densely packed in the energy spectrum.
- The spatial charge density relating to the probability in band mixing strongly depends on lateral size and thickness. Material properties determines the *hh*, *lh* and *so*-hole contributions and s-p-d mixing.

3.3.2 Optical Gain and Properties

Now we shall investigate the effect of lateral size and thickness on the optical properties of NPLs. For this we choose CdSe NPLs, which can be used to fabricate high quality red, yellow, green, blue laser amplifiers [23] and other photonic devices. Fig. 3.8 shows the optical gain spectrum of CdSe NPLs of varying size and thickness as a function of photon emission

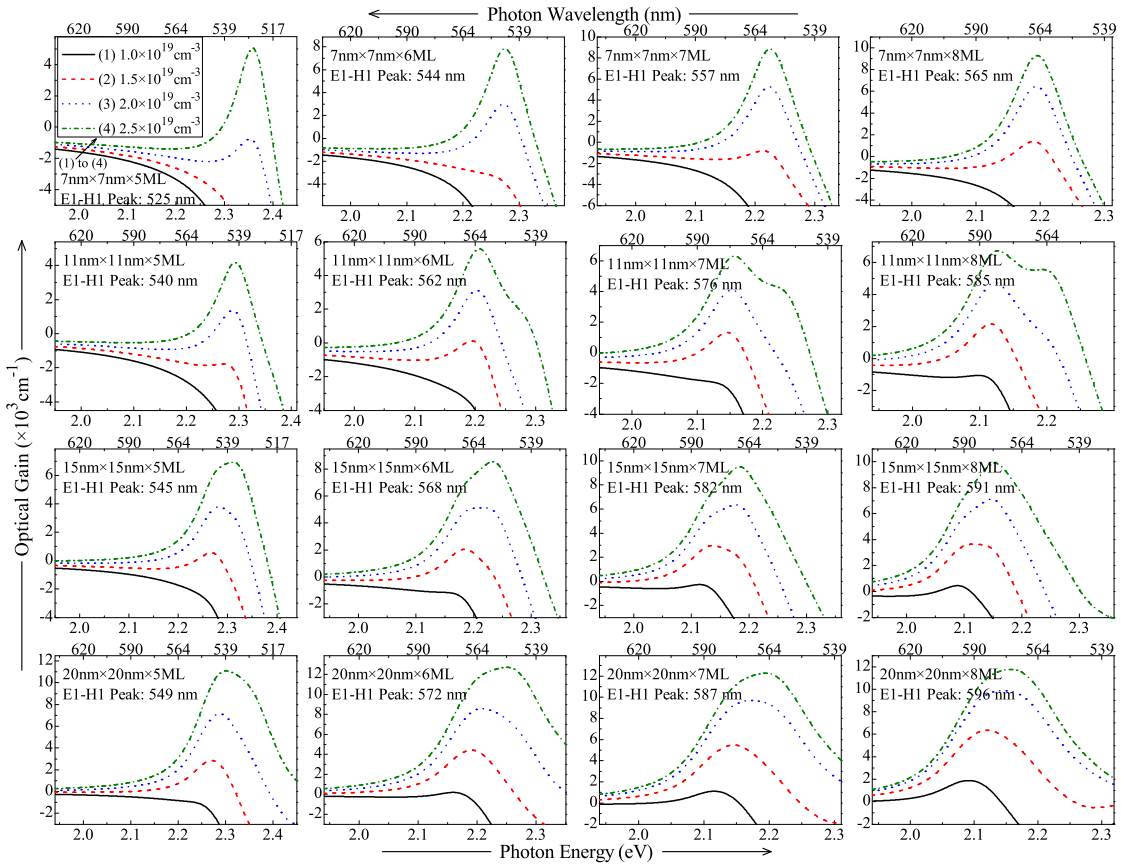

Figure 3.8: Optical Gain spectrum (cm^{-1}) of CdSe NPLs of varying lateral sizes (7, 11, 15, 20 nm) and thickness (5, 6, 7, 8 ML) for varying injection carrier density (1.0, 1.5, 2.0, 2.5 $\times$ 10^{19} cm^{-3}) at 300 K. Left to right is increasing thickness; while top to down is increasing size. Carrier densities and E1–H1 emission peak positions are indicated.

energy/wavelength. We have studied NPLs of sizes 7, 11, 15, 20 nm having thicknesses of 5 to 8 ML. Within each row the thickness increases from left to right, while the size is fixed. And within each column the size increases from top to down, while the thickness is fixed. This allows us to study the effect of both parameters simultaneously. For each NPL case we have the gain for varying carrier density ranging from 1 to 2.5 $\times 10^{19}$ cm^{-3}. A higher carrier density translates to a higher lasing threshold current density.

The optical gain spectrum depends on several factors such as the TME (depending on E and H wavefunction overlap), carrier density, Fermi factor, NPL dimensions, material, dephasing and scattering rate among others [see Eq. 2.54 in pg. 46]. Among the cases of Fig. 3.8, the dephasing rate does not change which is only material (CdSe) dependent. The

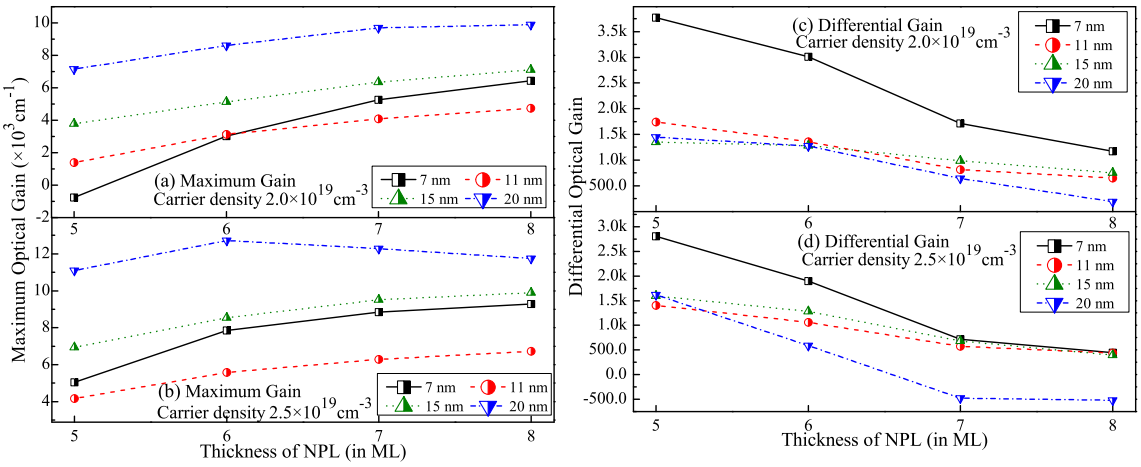

Figure 3.9: Maximum Optical Gain of CdSe NPLs at 300 K with carrier density (a: *Top Left*) 2×10^{19} cm^{-3} and (b: *Bottom Left*) 2.5×10^{19} cm^{-3}; and Differential Optical Gain of CdSe NPLs at 300 K with carrier density (c: *Top Left*) 2×10^{19} cm^{-3} and (d: *Bottom Right*) 2.5×10^{19} cm^{-3}. Dimensions of NPLs are indicated.

emission peak position is enlisted for each NPL case in the figure, which relates to the E1–H1 transition results in Fig. 3.2 (a). There is a red shift in the emission wavelength with an increase in both size and thickness. This is because as the volume increases, the quantum confinement reduces and the allowed energy levels come closer. Thus the E1–H1 transitions occur at lower energy. Among NPLs with same thickness but different lateral sizes, the red shift extent falls with an increase in the size. For example: $\Delta\lambda_{11\text{nm}-7\text{nm}}$ is in the range 15–20 nm, while $\Delta\lambda_{15\text{nm}-11\text{nm}}$ in 5–6 nm and $\Delta\lambda_{20\text{nm}-15\text{nm}}$ around 4–5 nm for the cases studied in Fig. 3.8. Similarly, among NPLs with same lateral size but varying thicknesses, the red shift extent falls with an increase in the thickness. In our case, $\Delta\lambda_{6\text{ML}-5\text{ML}}$ is in the range 19–23 nm, while $\Delta\lambda_{7\text{ML}-6\text{ML}}$ in 13–15 nm and $\Delta\lambda_{8\text{ML}-7\text{ML}}$ around 8–9 nm. This also goes to show that broadly the red shift is more prominent for increasing thickness compared to increasing size. The data obtained also shows that volumetrically smaller NPLs are more prone to undergo a peak shift compared to larger NPLs.

However, for any particular NPL case, there is slight blue shift in the emission peak with an increase in the carrier density. When more carriers are injected they start to occupy electronic states further away from the CB-bottom and VB-top and the gap between them increases. Excitonic recombinations occurring from such transitions have the emission energy larger than the E1–H1 gap, resulting in a blue shift (also known as band filling effect). We can observe that this effect is more prominent in volumetrically larger NPLs compared

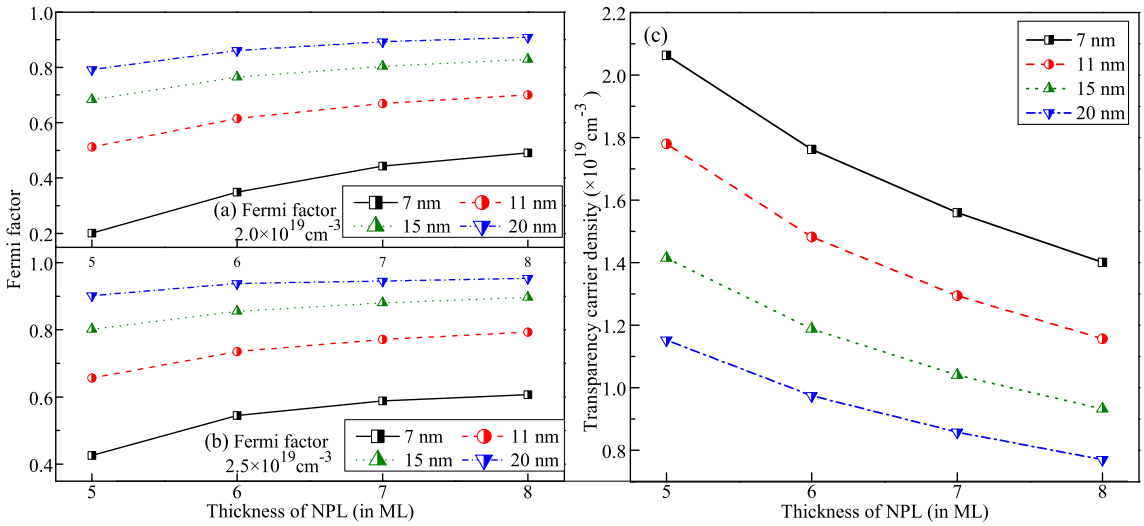

Figure 3.10: Fermi factor of CdSe NPLs at 300 K with carrier density (a: *Top Left*) 2×10^{19} cm^{-3} and (b: *Bottom Left*) 2.5×10^{19} cm^{-3}; and (c: *Right*) Transparency carrier density ($\times 10^{19}$ cm^{-3}) of CdSe NPLs at 300 K. Dimensions of NPLs are indicated.

to smaller. In larger NPLs, the allowed energy states due to quantum confinement are much closer. When more carriers are injected, there is a higher probability of *near*-E1–H1 transitions to occur. In smaller NPLs, the next higher transition after E1–H1 is much far away which also has a lower TME and therefore does not contribute much.

The maximum optical gain of CdSe NPLs studied in Fig. 3.8 are presented in Fig. 3.9 (a) and (b) for carrier densities 2 and 2.5 $\times$ 10^{19} cm^{-3}. This mainly depends on the TME, Fermi factor and volume of the NPL. The TMEs of the CdSe NPL cases studied were presented in Fig. 3.2 (b). It was found to be higher for larger and thicker NPLs due to higher absolute E and H wavefunction overlap. The other important parameter is the Fermi factor as shown in Figs. 3.10 (a) and (b) for the corresponding carrier densities. The Fermi factor also has a positive co-relation with size and thickness and increases with their increment. But the Fermi factor increases more rapidly for smaller NPLs compared to larger NPLs as it approaches towards unity. Broadly, it is higher for a higher carrier density. With an increase in the carrier density, the difference between the quasi-Fermi level separation and the effective bandgap increases more rapidly for volumetrically larger NPLs compared to smaller. Finally, from Eq. 2.54, the gain (thus maximum gain) is inversely proportional to the NPL volume in real space. Combining the effects of these three parameters, we obtained the results as shown in Fig. 3.9 (a) and (b). The 7 nm CdSe NPL is seen to have a higher maximum gain over the 11 nm NPL in some cases owing to its lower volume,

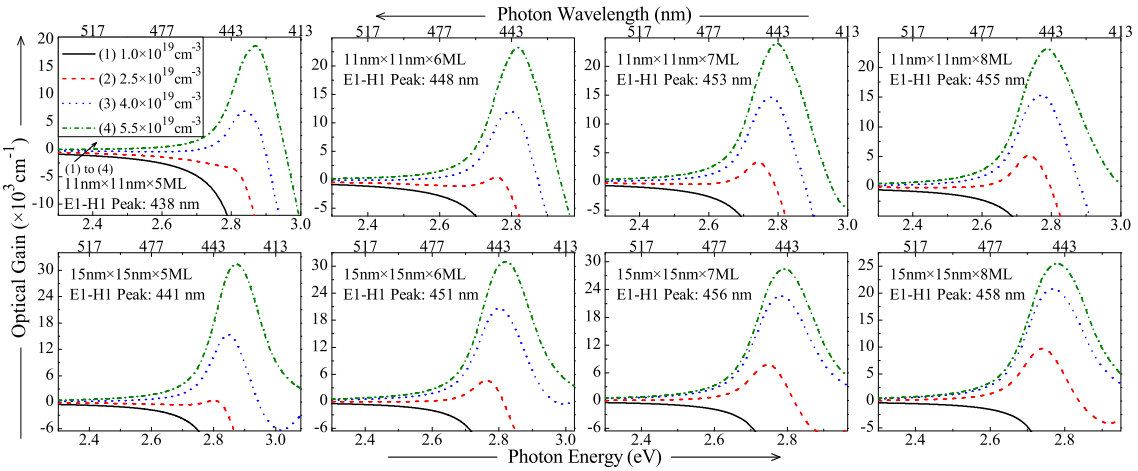

Figure 3.11: Optical Gain spectrum (cm^{-1}) of CdS NPLs of varying lateral sizes (11, 15 nm) and thickness (5, 6, 7, 8 ML) for varying injection carrier density (1.0, 2.5, 4.0, 5.5 $\times$ 10^{19} cm^{-3}) at 300 K. Left to right is increasing thickness; while top to down is increasing size. Carrier densities and E1–H1 emission peak positions are indicated.

which overcomes the counteractive effect of lower TME and Fermi factor. NPLs smaller than this practically have QD-like nanocrystal properties. In the case of 2.5 $\times$ 10^{19} cm^{-3}, the maximum gain of 20 nm CdSe NPL dips after 6 ML thickness. We can see that, by this stage the Fermi factor had almost reached saturation [Fig. 3.10 (b)]. For even larger NPLs, such high density leads to carrier occupation of levels not contributing much to the *near*-E1–H1 transitions. The reduction of the maximum gain can therefore be attributed to the aforementioned phenomenon. Another interesting aspect of optical properties of semiconductors is the differential gain, which is a measure of the effectiveness of a laser to transform injected carriers to photon emission. A higher differential gain corresponds to a narrower spectral emission width and a greater speed of modulation [124, 125]. The differential gain for the corresponding cases of Fig. 3.9 (a) and (b) are shown in Fig. 3.9 (c) and (d). It is smaller for higher density, which is expected as we approach saturation. It is also found to be decrease with increasing NPL thickness.

Finally, we study the transparency condition [126] for NPLs. It tells us which carrier density gives us zero gain – a density higher than that would yield a gain, while a lower density would result in absorption. NPLs with a smaller volume needs a higher density to attain the number of excitons required for transparency; while volumetrically larger NPLs can attain the transparency condition exciton count with a significantly lower density. This can be clearly understood from Fig. 3.10 (c). The photon wavelength for transparency is

same as the emission wavelength of the NPL at the onset of gain with a density just above the transparency density.

Similar studies on gain spectrum, maximum gain and Fermi factor were conducted for CdS NPLs. But in Fig. 3.11 we have shown only the gain spectrum of CdS NPLs with lateral size 11 and 15 nm, and thickness varying from 5 to 8 ML. Broad observations concerning the effect of size and thickness concur with those observed for CdSe. However comparing the optical performance of CdSe and CdS NPLs, we have found that for geometrically identical NPLs with the same carrier density, CdS NPLs have a lower gain spectrum, maximum gain and a lower Fermi factor. CdS needs higher carrier density than CdSe to obtain a near identical gain. The E1–H1 peak positions of the CdS NPL gain spectrum are marginally less affected by dimension change as can be understood by observing Fig. 3.8 and 3.11. For CdS NPLs, $\Delta\lambda_{6\mathrm{ML}-5\mathrm{ML}}$ is in the range 9–10 nm, while $\Delta\lambda_{7\mathrm{ML}-6\mathrm{ML}}$ in 4–5 nm and $\Delta\lambda_{8\mathrm{ML}-7\mathrm{ML}}$ around 2–3 nm, which is much lower than that of its CdSe counterpart. From Fig. 3.3, we have also seen that CdS has a lower TME. Also, the higher effective mass of CdS lowers its carrier mobility compared to CdSe. It also has a higher bandgap, thus geometrically identical CdS NPLs have lower emission wavelength than CdSe NPLs.

Section Highlights:

- Increment in thickness and size causes red shift in peak position. Although thickness has greater impact, but similar % variations incurs comparable extent of red shift. Thus, lateral size is an important parameter in the study of optical properties of NPLs.
- The gain is dependent on several parameters including Fermi factor and TME among others. NPL volume (i.e. both thickness and size) also plays an important role to determine the overall optical performance.
- The transparency carrier density requirement goes down with increasing thickness and size of NPL.

3.4 Summary and Conclusion

A comprehensive study of the electronic bandstructure, band mixing probability, charge densities, optical transitions and gain of quasi two-dimensional colloidal CdSe and CdS NPLs in the zincblende phase is performed – as a function of vertical thickness and lateral size.

Section Highlights in Sec. 3.3.1 and 3.3.2 emphasizes on some key results. Variations in size, thickness and material significantly affect the energy levels, optical gain, etc. There is a red shift in the gain peak position as we move from CdS to CdSe. For geometrically identical NPLs, CdSe has lower photon emission energy because of its lower bandgap. However, it has a higher TME due to its relatively lower effective electron mass. CdS has a much higher contribution from split-off holes because it's spin-orbit splitting energy is over six times smaller.

For any given NPL, an increase in carrier density leads to the band filling effect. The peak gain increases due to an increase in the Fermi factor. But for a fixed carrier density, the Fermi factor is higher for volumetrically larger NPLs. Incidentally, volumetrically larger NPLs need smaller injection carrier density to surpass absorption and transparency and produce gain. Thus the overall gain characteristics are determined by an sum effect of all these influencing factors.

On the whole, the choice of material and dimension of NPLs must be made while optimizing the performance for a desired application. The often neglected lateral size parameter of NPL was found to be of significant importance affecting the bandstructure and band mixing probabilities. It also contributes to the optical gain positions and magnitude. Therefore, it is recommended that both lateral size and thickness must be carefully considered for NPL device designs and applications for a precise estimation of the performance characteristics.

Chapter 4

CdSe Nanoplatelets: Temperature Effect

4.1 Introduction

Geometrical dimensions affecting the electronic bandstructure and other optical properties of NPLs was discussed in Chapter 3. But, with the recent developments and potential applications of NPLs in commercial optoelectronic devices [20, 26], it becomes imperative to study how-and-why the characteristics and performances of NPLs are influenced by temperature variations, particularly at elevated temperature – when both reversible and irreversible luminescence quenching processes come into play [27]. A change in operating temperature of NPLs greatly affects their electronic bandstructure and luminescence properties. Achtstein *et al.* [25] studied NPL characteristics at the cryogenic range, while there are several works studying QDs and other nanocrystals across varying temperature ranges [127–129]. But, a work addressing the study of NPL's optoelectronic properties at elevated temperatures above RT has not been reported thus far. To address this need, in this chapter, we study in tandem using theoretical modeling and experimental measurements, the underlying physical phenomena determining the optoelectronic characteristics of CdSe NPLs across varying temperature, above the room temperature (RT). As we shall discuss in the course of this chapter, we observed the photoluminescence (PL) spectra at various temperatures for their photon emission energy, PL linewidth and intensity by considering the exciton-phonon interaction with both acoustic and optical phonons using Bose-Einstein statistical factors. With rise in temperature we observed a fall in the

transition energy (emission redshift), matrix element, Fermi factor and quasi Fermi separation, with reduction in intraband state gaps and increased interband coupling. Also, there was a fall in the PL intensity, along with spectral broadening due to an intraband scattering effect. The predicted transition energy values and simulated PL spectra at varying temperatures exhibit appreciable consistency with experimental results. Our findings have important implications for application of NPLs in optoelectronic devices, such as NPL lasers and LEDs, operating much above room temperature.

4.2 Theoretical Framework

Similar to Chapter 3, we consider each NPL atom-by-atom in a 3D structure. We have studied the CdSe NPLs using an effective mass envelope function theory approach based on the 8-band $\boldsymbol{k}\cdot\boldsymbol{p}$ method using the first basis type described in Sec. 2.3.1, which simultaneously takes into account the nonparabolicity of the coupled conduction band (CB) and valence band (VB) including the orbit-splitting bands to solve its eigenenergy and obtain its electronic structure at the Γ-point. The 8-band Hamiltonian is represented in the Bloch function basis as detailed in Eq. 2.8. For the later part of the chapter we present a study on the effect of elevated temperature on the characteristics of colloidal CdSe NPLs. For the optical properties calculation we have used the formulations based on the density-matrix theory considering exciton-phonon interaction, as explained in Sec. 2.5.2.

The effect of temperature on the bandgap has already been discussed in Sec. 2.6 of Chapter 2. Now, in Sec. 4.3.2 of this chapter, in addition to the effect of temperature on bandgap, we will also study its effect on the emission linewidth and intensity. The mathematical models will be introduced in the concerned section.

4.3 Results and Discussions

4.3.1 Theoretical Results

Using our theoretical model, we have studied the optoelectronic characteristics of quasi two-dimensional colloidal CdSe NPLs of lateral dimensions 22 nm × 8 nm, and vertical thickness of 4 monolayer (ML), across temperature varying from room temperature (RT) to 90°C. We have modeled and studied NPLs of this particular dimension, based on experimental measurements as we shall describe in Sec. 4.3.2. Under this scheme, we have studied

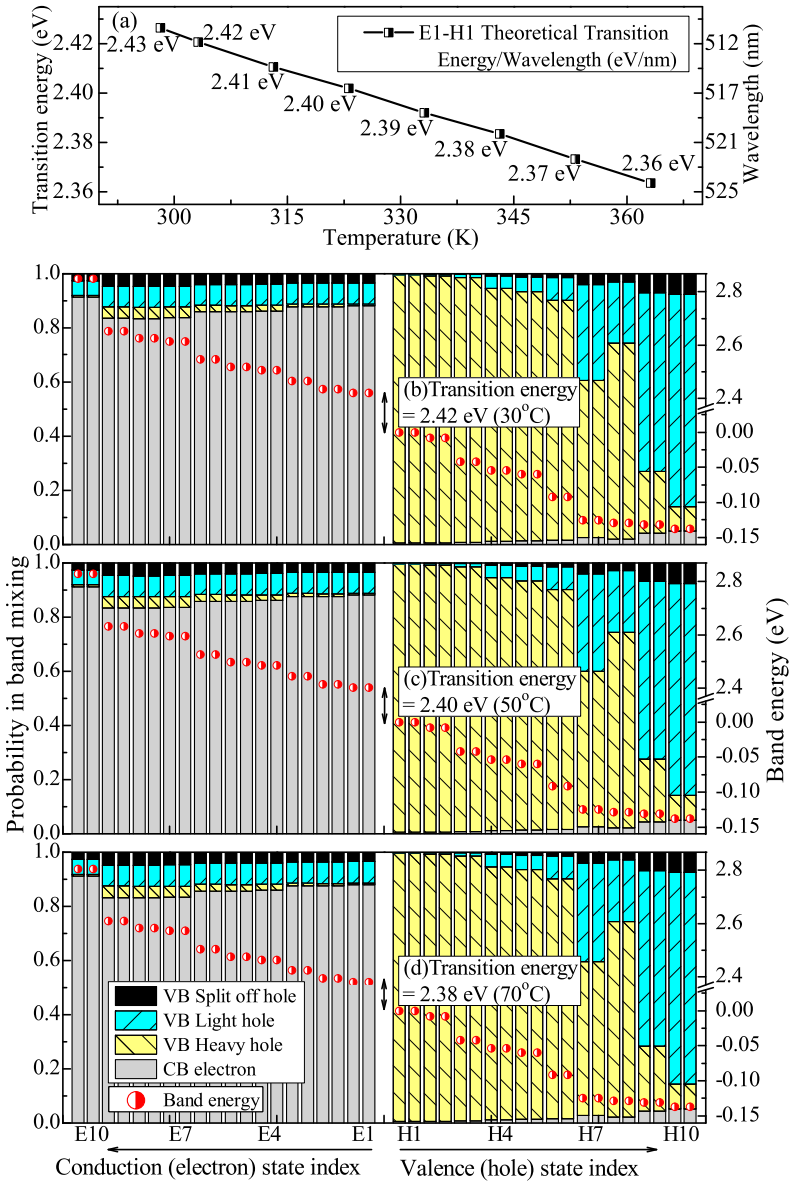

Figure 4.1: (a: *first*) Theoretical E1–H1 (bottom of conduction band to top of valence band) excitonic transition energy/wavelength as a function of temperature. Frames (b–d) show the electronic bandstructure and the probability in band mixing between conduction electrons and valence heavy-, light- and split off holes for 4 ML CdSe NPLs at (b: *second*) 30°C, (c: *third*) 50°C and (d: *fourth*) 70°C. E1–H1 transition energies are indicated. Legends show the band mixing probabilities.

how temperature affects their optoelectronic properties and predicted some temperature-dependent photoluminescence (PL) characteristics of CdSe NPLs. Fig. 4.1 (a) shows the

theoretically calculated excitonic transition energy (and photon emission wavelength) from the bottom of CB (E1) to the top of VB (H1) i.e. E1–H1, as a function of temperature. With an increase in temperature there is a red shift in the transition energy (photon emission energy). The reason is that the bandgap, E_g has a negative thermal coefficient (dE_g/dT) due to (i) lattice thermal dilatation and electron-phonon interaction $\propto T$ at high temperatures, and (ii) electron-phonon interaction $\propto T^2$ at low temperatures. In this context, we conventionally have the Varshni relation [117] to explicate the behavior of E_g. However, detailed systematic study for II-VI semiconductors have shown that sometimes the Varshni relation may not be very accurate [116]. Another semiempirical expression suggested by Cardona *et al.* [130] is more accurate as we shall subsequently see. Also, with an increase in temperature, the phonon concentration increases and causes increased scattering and non-radiative recombinations start occurring [131], which causes the E1–H1 TME to decrease.

Of the eight temperature cases studied in Fig. 4.1 (a), we present the electronic band-structure and the probability in band mixing between conduction electrons and valence heavy-, light- and split off-holes due to coupling for the 4 ML CdSe NPLs at 30, 50 and 70°C, in Fig. 4.1 (b-d). The E states represent the conduction electron states, while the H states represent the valence hole states. Each of the states is two fold degenerate, considering spin-up and spin-down alternatives. For the sake of discussion, let us consider the 4 ML CdSe NPL at 30°C of Fig. 4.1a as a case. The E1–H1 transition energy (2.42 eV) determines the PL peak emission energy.[1] The CB states mainly comprise of electrons with very low composition of *hh*, *lh* and split-off (*so*) hole, which comes from the coupling effects. The effective *hh* mass is much larger than the effective electron mass for CdSe [121], thus the *hh* dispersion curve is more flat than the conduction dispersion curve. Therefore, the first ten hole levels span only ∼140 meV, while the first ten electron levels span ∼425 meV. In the VB, the first few levels are *hh* dominated followed by increased influence of *lh* and *so*. Comparing the span of first ten electron and hole states and band-mixing probabilities of the three cases in Fig. 4.1 we have two significant observations: (i) an increase in temperature induces a faster reduction in the intra-CB state gaps compared to the intra-VB state gaps. For instance, a temperature rise of 20°C between adjacent frames of Fig. 4.1, the $\Delta_{\text{E1-E10}}$ is over five times larger than the $\Delta_{\text{H1-H10}}$. This is by virtue of the temperature-induced

[1] Later in Sec. 4.3.2 we will show that the experimental PL emission spectrum of 4 ML CdSe NPL at 30°C (Fig. 4.9), has its peak emission at 512 nm corresponding to the transition energy of 2.42 eV predicted by our model.

thermal lattice dilatation effects, given than the deformation potential of the CB is higher than that of the VB for CdSe; and (*ii*) an increase in temperature promotes *e*-*h* quantum state coupling – the conduction states start to have an increased contribution from holes and vice versa. Moreover, the intraband dynamics is also affected, such that the role of the dominant contributor diminishes with increasing temperature. For instance, the dominant contributors for H1 through H8 is *hh* while for H9 and H10 is *lh*, whose contribution falls as temperature rises. The contrast is however small to be reflected graphically. These band-mixing probabilities are affected by the varying degree coupling between the conduction electrons and valence *hh*, *lh* and *so* holes, which can be empirically determined. For each level, the band-mixing probabilities are dictated by their aggregate electron and hole wavefunctions and associated charge densities thereof.

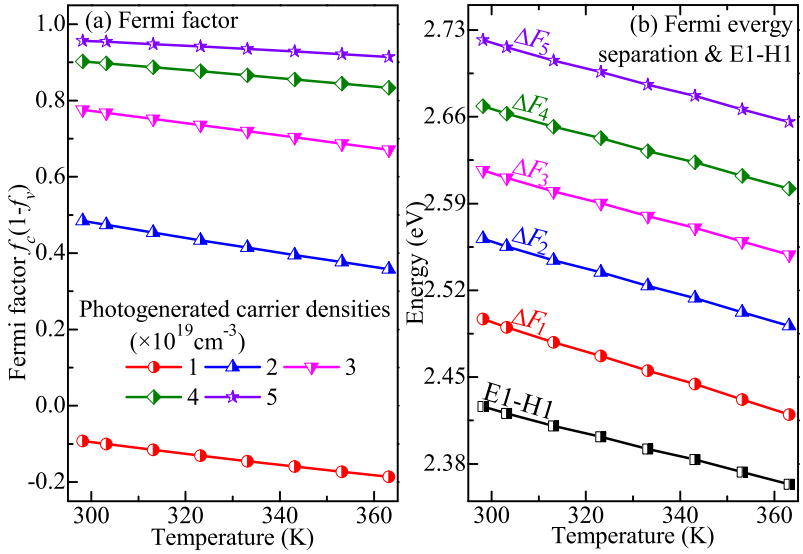

Figure 4.2: (a: *left*) Fermi factor $f_c(1-f_v)$ for E1–H1 transition, and (b: *right*) Fermi energy separation $\Delta F = E_{fc} - E_{fv}$ compared with the E1–H1 transition energy in 4 ML CdSe NPLs as a function of temperature for varying injection carrier concentration. Both, Fermi factor and ΔF have a negative temperature gradient.

The Fermi factor and energy levels are important determiners of the temperature-dependent optoelectronics characteristics. In Fig. 4.2 (a) we show the Fermi factor $f_c(1-f_v)$ at E1–H1 transition and in Fig. 4.2 (b) the Fermi energy separation $\Delta F = E_{fc} - E_{fv}$ in our 4 ML CdSe NPL as a function of temperature, for varying photogenerated carrier densities from 1 to 5×10^{19} cm^{-3}. The ΔF for each case is compared with the E1–H1 transition

energy, and ΔF>E1–H1 ensures the Bernard-Duraffourg inversion condition (population inversion) necessary for lasing [62]. With an increase in carrier density, both Fermi factor and Fermi energy separation increases. However, as we continue to increase the density, the extent of Fermi factor increment falls, at it approaches saturation. However, a rise in temperature has detrimental effects on both, Fermi factor and Fermi energy separation. With an increase in temperature, the fermions (electrons and holes) get thermally excited and therefore the probability of occupying higher CB and VB energy states is increased; so the f_c falls, while f_v rises. Consequently the Fermi factor decreases with temperature. Also, the quasi Fermi levels of the CB and VB (E_{fc} and E_{fv}) approach the band edges, and ΔF falls.

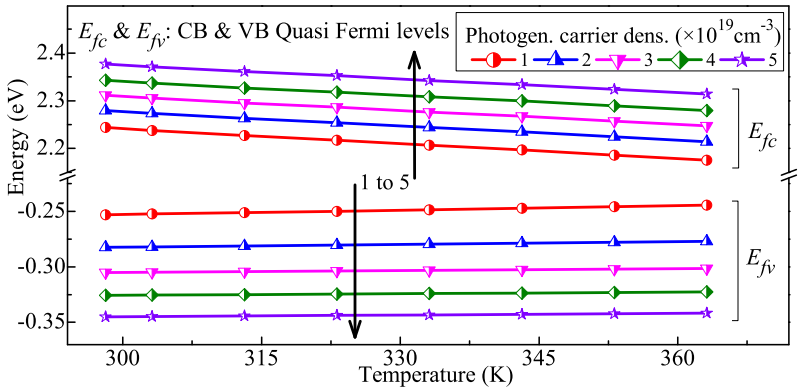

Figure 4.3: Quasi Fermi energy levels of the CB (E_{fc}) and VB (E_{fv}) as a function of temperature under varying photogenerated carrier densities. With increasing temperature, E_{fc} and E_{fv} approach each other and the Fermi energy separation decreases, as shown in Fig. 4.2 (b) and Fig. 4.4.

Fig. 4.3 shows the conduction band (CB) and valence band (VB) quasi Fermi energy levels, E_{fc} and E_{fv} respectively, as a function of temperature for varying photogenerated carrier densities from 1 to 5 $\times 10^{19}$ cm^{-3}. As the carrier density increases, the electrons and holes start to occupy higher CB and VB energy states, and thus their Fermi energy levels move farther away from the band edges. However, with increasing temperature, the both E_{fc} and E_{fv} approach the band edges. Thus, the quasi Fermi energy separation $\Delta F = E_{fc} - E_{fv}$ decreases with temperature.

Fig. 4.4 shows in contour form the variation of Fermi factor $f_c(1 - f_v)$ for the E1–H1 transition and the Fermi energy separation $\Delta F = E_{fc} - E_{fv}$ as a function of temperature and injection carrier concentration. With increasing carrier density both Fermi factor and

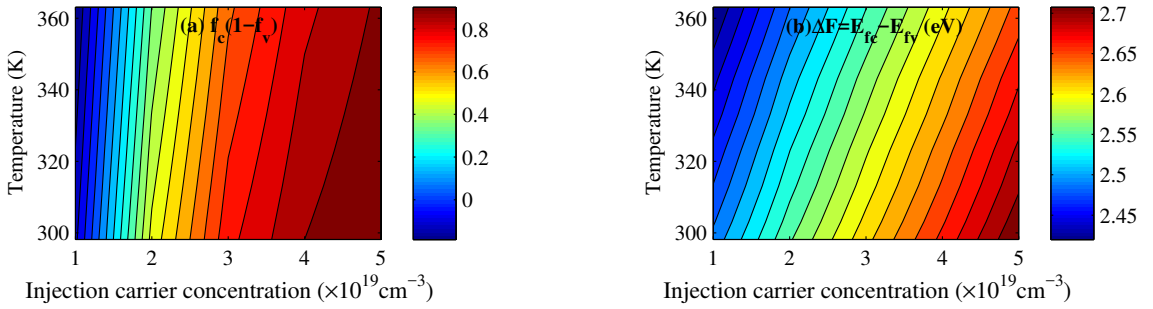

Figure 4.4: Contour plot of (a: *left*) Fermi factor $f_c(1-f_v)$ for the E1–H1 transition, and (b: *right*) Fermi energy separation $\Delta F = E_{fc} - E_{fv}$ (eV) as a function of temperature and injection carrier concentration in 4 ML CdSe NPLs.

ΔF increase. However, temperature has the opposite effect. For a fixed density, a rise in temperature causes the fermions (electrons and holes) to get thermally excited and therefore the probability of occupying higher CB and VB energy states is increased; so the f_c falls, while f_v rises. Consequently the Fermi factor decreases with temperature. Also, the quasi Fermi levels of the CB and VB (E_{fc} and E_{fv}) approach the band edges (Fig. 4.3), and therefore ΔF falls.

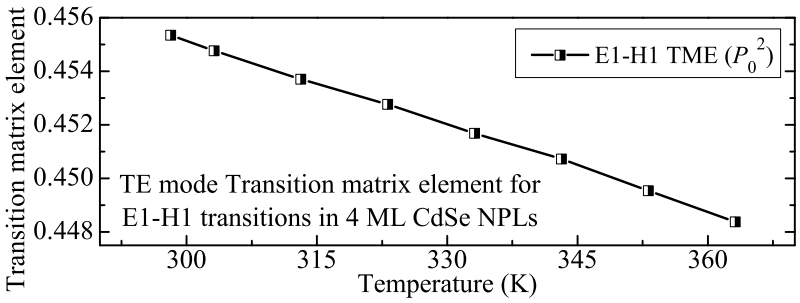

Figure 4.5: TE mode transition matrix element (TME) for the E1–H1 transitions as a function of temperature in 4 ML CdSe NPL. The other interband TMEs (both TE and TM mode) shall be discussed in Fig. 4.6 subsequently.

Another critical temperature-dependent optoelectronic factor is the transition matrix element (TME) which is shown in Fig. 4.5 for the E1–H1 transition in TE mode as a function of temperature. As the thermally excited fermions begin to occupy higher energy states the E1–H1 transition weakens. A physical equivalent of the TME is the oscillator strength $f_{cv} \propto \mu_{cv}^2$, where μ_{cv} is the transition dipole moment, and it can be calculated from the TME using $\mu_{cv} = e\hbar\mathcal{P}_{cv}/im_0E_{cv}$. It allows us to quantify the transition strength from state $|c\rangle$ to $|v\rangle$, which decreases with a rise in temperature.

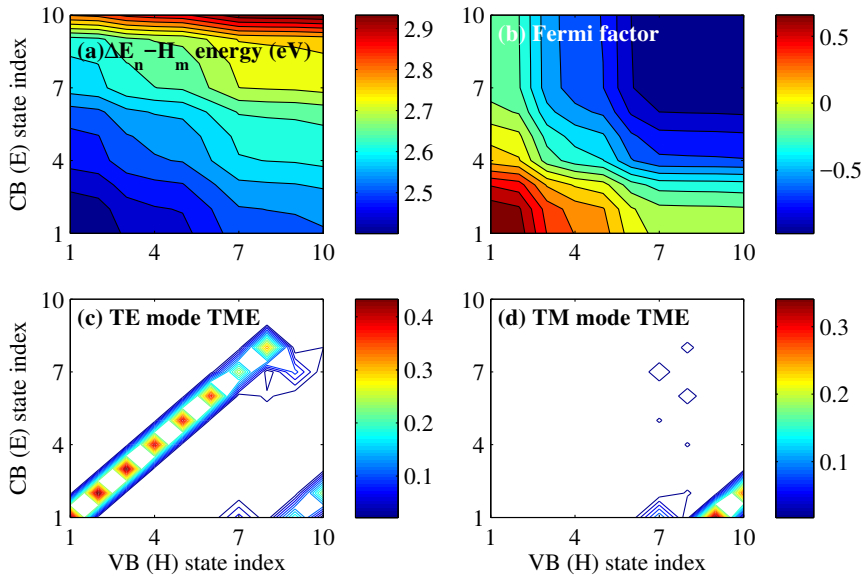

Figure 4.6: For 4 ML CdSe NPLs at 30°C (303.15 K), we have in contour form, the following: (a: *top left*) Transition energy between the first ten E and H states – the minimum (2.42 eV) occurs at ΔE1–H1, (b: *top right*) Fermi Factor for an injection carrier density of 3×10^{19} cm^{-3}, *max* = 0.768 at E1–H1 (c: *bottom left*) Transverse electric (TE) mode optical TME polarized in the *x*-*y* plane, where E1–H1 is the strongest (0.455), and (d: *bottom right*) Transverse magnetic (TM) mode optical TME polarized along the *z* direction, where E1–H9 is the strongest (0.358). All contours are plotted against the first ten CB (E) and VB (H) state indices, and values specified in colorbars.

To understand the ongoing transition dynamics, we have shown in Fig. 4.6 the (a) transition energy, (b) Fermi factor for carrier density 3×10^{19} cm^{-3}, (c) TE mode TME, and (d) TM mode TME for our 4 ML CdSe NPLs at 30°C, in contour form against the first ten CB and VB states. In Fig. 4.1 (b-d) we studied the electronic bandstructure showing the first ten CB and VB levels. Here, Fig. 4.6 (a) shows the varying E–H transition energies, while Fig. 4.6 (b) shows the corresponding Fermi factors for these transitions, the highest being the E1–H1 at 0.768. Only those with a positive value would contribute to the radiative recombination [see Eq. (2.61) and (2.62)]. Finally, Fig. 4.6 (c–d) shows the TE and TM mode TME values, giving an understanding of the allowed transitions with the highest possibilities. For the TE mode, the optical transition rule is followed, and the E1–H1 transition is the strongest with a TME value of 0.455. This the the heavy-hole dominated transition [see Fig. 4.1 (b)]. For the TM mode, however, the strongest is the E1–H9 transition, at 0.358, which is light-hole dominated. All of these correspond to 30°C, and as discussed earlier, with a rise in temperature, the transition energy, Fermi factor and the TME values decreases (See Fig. 4.1, Fig. 4.2 and Fig. 4.5).

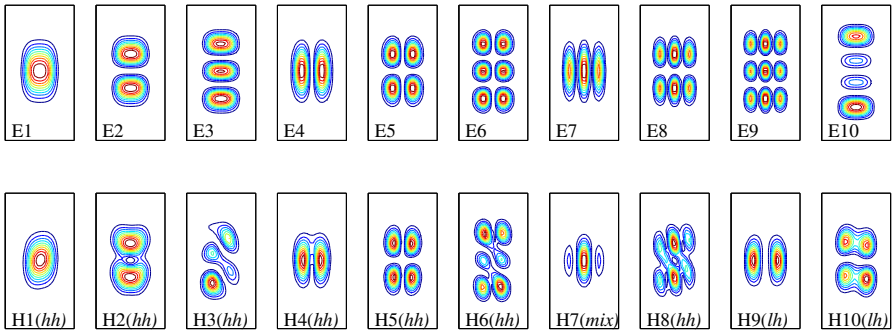

Figure 4.7: The spatial charge density of the first ten electron and hole states of 4 ML CdSe NPLs at 30°C (303.15 K) cut along the vertically central x-y plane ($z = 0$) of the NPL. Warmer (reddish) colors depict higher occupation probability over cooler ones (bluish). The rectangular boundary depicts our studied NPL (22 nm× 8 nm), but the dimensions are not to scale, for the sake of comprehensive visual representation.

Now we shall study the spatial manifestation of the electronic states. Fig. 4.7 shows the spatial charge densities of the first ten electron and hole states (square of the wavefunction $|\psi^2|$, i.e. probability of finding them), within the vertically central x-y plane of the 4 ML CdSe NPL at 30°C corresponding to Fig. 4.1b. The charge density description in terms of s and p orbitals in a quite general feature of III-V semiconductors. However in II-VI semiconductors the VB is influenced by chemically active d orbitals also. [132] The E1, H1 and H7 states are s-like. While H1 is dominated by *hh*, H7 has higher *lh* contribution. The E2 and H2 are p_y-like, while E4, H4 and H9 are p_x-like – H4 has greater *hh* influence while H9 has more of *lh*. The E3, E7 and H3 are formed by s-p-mixing. The E5 and H5 are d_{xy}-like, while the E6 and H6 again have some amount of mixing. It is observed that with changes in temperature the spatial charge densities have very inconsequential variations because it is a measure of the electron and hole probability density determined by the wavefunction localization, which is primarily affected by piezoelectric strain and external electric fields.

4.3.2 Experimental Results

We have synthesized 4 monolayer (ML) CdSe NPLs as they have been most widely investigated in literature [26, 31, 133–137] and found applications in LED color-conversion layers, lasers and luminescent solar concentrators. We have used colloidal synthesis techniques similar to those used in Refs. [137–140], as described in Appendix C.

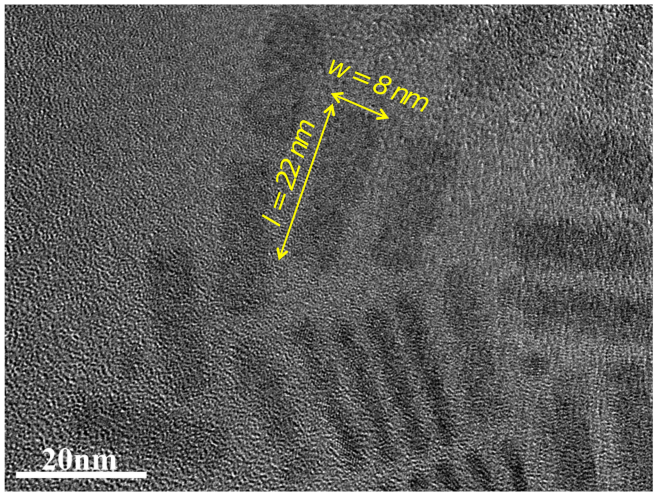

Figure 4.8: High-resolution transmission electron microscopy (TEM) image of 4 ML CdSe NPL ensemble population. Average lateral dimension is $l = 22$ nm and $w = 8$ nm (Scale: 20 nm)

Fig. 4.8 shows a high-resolution transmission electron microscopy (TEM) image of our synthesized NPL ensemble population. We can observe NPLs in two orientations: face view (laterally flat) and edge view (vertically stacked). We have done lateral dimension measurements over several NPL samples using ImageJ software. Their average length and width were measured to be 22 nm and 8 nm respectively. The theoretical results discussed in Sec. 4.3.1 correspond to the same dimensions of our synthesized NPLs.

By carefully inspecting the stacked (vertical) NPLs, it is observed that the thickness of NPLs is decreasing from top to bottom in Fig. 4.8. This is only possible when the stacked NPLs are tilted/folded and not perfectly vertical, which is a common phenomenon for NPLs, as also observed by several other groups [10,141]. This is confirmed by observing different thickness on the top (2.6 ± 0.1 nm) and bottom (1.73 ± 0.2 nm) part of the same NPLs using ImageJ software. Also, the ligands surrounding the NPLs have a contrast in the TEM image, so the NPL boundary is not strictly discernible. For this reason, thickness information obtained from TEM characterization is not entirely conclusive of the NPL thickness. Moreover, the resolution of our TEM machine is $\sim$0.22 nm which is comparable to the thickness of 1 ML (0.3 nm) of CdSe NPLs.

However, the optical properties of the CdSe NPLs with different thickness have very distinct features and are well established in the field of atomically flat NPLs. For 4 ML CdSe NPLs, the PL peak is observed at $\sim$512 nm and the absorption spectra have two distinct transition (light-hole at $\sim$480 nm and heavy-hole at $\sim$509 nm) [26, 31, 133–137].

The optical spectra results undoubtedly confirm that our CdSe NPLs are 4 ML (1.2 nm) thick. The quantized thickness of NPLs in ML can be converted to nm by computing ML $\times$ $(a/2)$ where a is the lattice constant of CdSe in nm. In our case the identification of the synthesized NPLs at 4 ML thick is in conjunction with the optical spectra properties, which is well accepted in the field of NPLs.

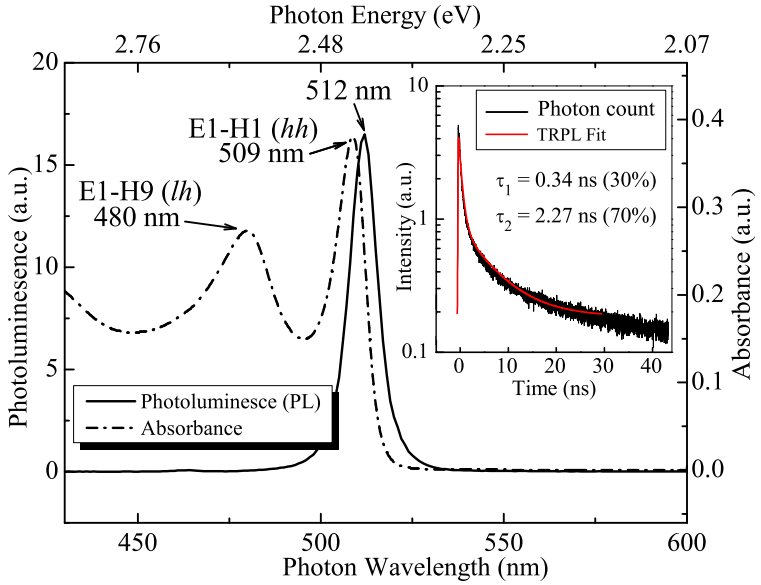

Figure 4.9: Experimental Photoluminescence (PL) and Absorption spectrum of 4 ML CdSe NPLs at 30°C (303.15 K). The PL excitation wavelength was 350 nm. Both PL and absorption were measured in solution form. PL peak is at 512 nm. Primary absorption peak, at 509 nm has a Stokes shift of 3 nm, while the secondary absorption peak is at 480 nm. Inset shows Time-Resolved PL (TRPL) spectrum and fit measured in thin-film form at 30°C. The fit and the system response is given in Appendix C.

Spectral characterization results in Fig. 4.9 show the experimental PL emission and absorption spectrum (both measured in solution form) for our 4 ML CdSe NPLs at 30°C. The PL was measured in a standard PL spectrometer with an excitation wavelength of 350 nm. We can observe the PL emission peak at 512 nm, which is in very good agreement with the E1–H1 transition energy prediction of 2.42 eV by our model, as shown in Fig. 4.1 (a–b). Similarly, with our E1–H1 predictions at other varying temperatures [Fig. 4.1 (a)] we can determine their expected PL emission wavelengths.

With a Stokes shift of 3 nm from the PL spectrum, the primary absorption peak occurs at 509 nm. This is due to the reorganization of the solvent in solution-processed NPLs plus dissipation and vibrational relaxation of the NPLs [142]. The primary absorption peak corresponds to the E1–H1 transition, where the H1 state is 2D-heavy holes (*hh*) dominated [as theoretically determined in Fig. 4.1 (b)]. A study of the TMEs make this clear. The transverse electric (TE) mode TME for the E1–H1 transition is maximum among all possible cases accounting to 0.455. The secondary absorption peak occurs at 480 nm. A study of the transverse magnetic (TM) mode TMEs of the transitions near the secondary absorption energy shows that this comes from E1-H9 transitions, for which the TME value is 0.358, which is weaker than the E1–H1 TME but is stronger than TMEs of other allowed transitions. The fraction of light holes (*lh*) involved in this transition is much higher (66 %) than their *hh* counterpart (22 %) [Fig. 4.1 (b)]. This conforms with the idea that *hh* contributes to the primary absorption peak of a typical CdSe NPL, while *lh* contributes to the secondary peak. [25] We have discussed about the TE and TM mode TME values for all possible transitions between E_{1-10} to H_{1-10} in Fig. 4.6 (c–d). Note that, the PL peak position at 512 nm, and the *hh* and *lh* absorption peaks at 509 nm and 480 nm respectively confirms that our synthesized NPL samples are indeed 4 ML (1.2 nm) thick [137, 143].

Time-Resolved PL (TRPL) spectrum and fit at 30°C (inset of Fig. 4.9) reveals a dual decay path mechanism following the model $I(t) = a_1 e^{-t/\tau_1} + a_2 e^{-t/\tau_2}$, with PL decay lifetimes of $\tau_1 = 0.34$ ns and $\tau_2 = 2.27$ ns with 30% and 70% contribution respectively, leading to an average lifetime of 2.15 ns calculated using $\tau_{\text{avg}} = \left(a_1\tau_1^2 + a_2\tau_2^2\right) / \left(a_1\tau_1 + a_2\tau_2\right)$, which is similar to previously reported τ_{avg} of CdSe NPLs at RT [10, 16]. The TRPL fit is shown again along with the system response in Appendix C. Previous radiative transition dynamics studies on CdSe NPLs have also observed a similar dual decay path mechanism where τ_1 is assigned as the radiative recombination decay time period relating to reversible PL losses, while τ_2 as the nonradiative recombination decay time period relating to the trap states which may cause irreversible losses in the PL intensity [25, 144], originating from the fast hole-trapping due to incomplete passivation of Cd atoms on the NPL surface [138].

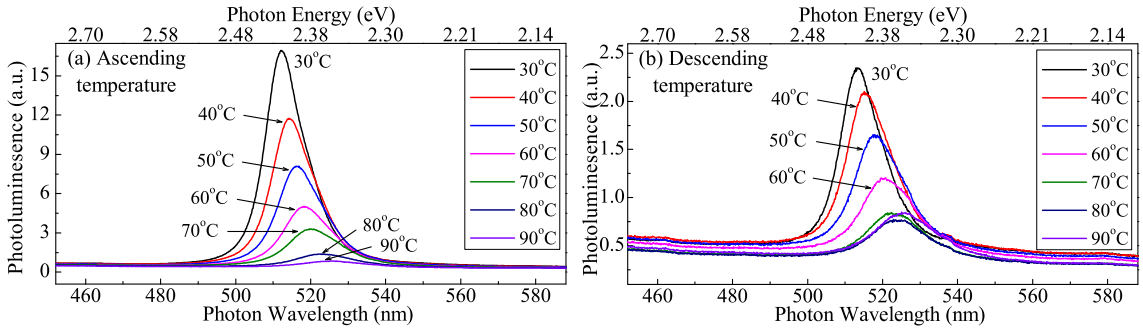

Figure 4.10: PL spectra of 4 ML CdSe NPLs measured in thin-film form while (a: *left*) ascending, and (b: *right*) descending temperature, respectively. Temperature of each PL spectrum is indicated. With an increase in temperature there is a redshift in the emission peak, broadening in the PL linewidth and reduction in PL intensity. Upon decreasing the temperature to RT, we observe substantial retractability in the peak position and linewidth, but not in the intensity. Fig. 4.11 shows the PL emission energy (peak position), linewidth and integrated intensity as a function of temperature.

Having observed the PL characteristics of NPLs at RT, in Fig. 4.9, now in Figs. 4.10 (a) and Fig. 4.10 (b) we show the effect of temperature on the experimentally measured PL spectra while ascending and descending temperature respectively. The measurements were done on NPLs in thin-film form using a laser excitation wavelength of 355 nm at 0.5 mW power. For every 10°C rise in temperature, there is a red-shift in the emission wavelength of ∼2 nm, and the PL intensity falls as the sample quality degrades. Also, the spectrum broadens due to intraband scattering effect.

Fig. 4.11 shows the photon emission energy, PL linewidth and PL integrated intensity as a function of ascending (black ⊡) and descending (red ×) temperature. For a particular temperature the emission energy and linewidth are almost identical in both. While cooling back to RT, the signal intensity increases, but is far from being retraced. The recovery is < 14 % [see logarithmic comparison in Fig. 4.11 (d)]. The effective photon emission energy (equivalent to the effective E1–H1 transition energy) has a negative thermal coefficient as already discussed in the context of Fig. 4.1a. For II-VI semiconductors, a semiempirical expression [Eq. (4.1)] suggested by Cardona *et al.* [130] takes into consideration the phonon emission and absorption using Bose-Einstein statistical factors.

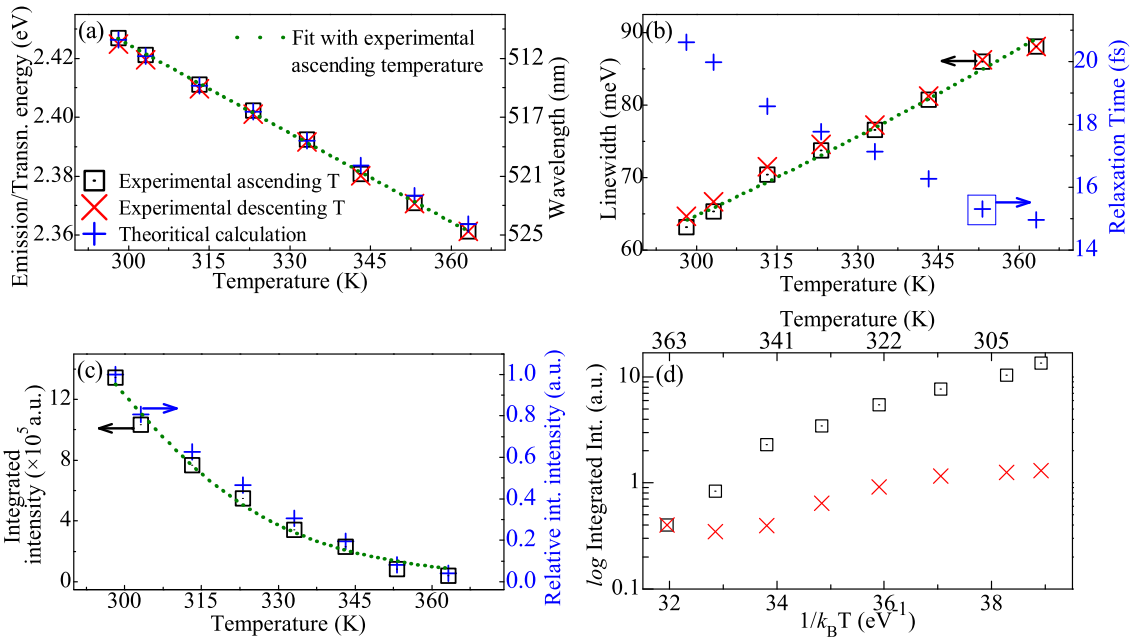

Figure 4.11: (a: *top left*) Experimental PL emission energy/wavelength while ascending and descending temperature compared with theoretically simulated E1–H1 transition energy values; (b: *top right*) Experimental PL linewidth while ascending and descending temperature and extracted intraband relaxation time τ_{in} used in theoretical model [Eq. (2.55)] from data of ascending temperature; (c: *bottom left*) Experimental PL intensity while ascending temperature compared with theoretically simulated relative PL integrated intensity; and (d: *bottom right*) Comparative Arrhenius plot for PL integrated intensity (log scale) while ascending and descending temperature. Consistent symbols have been used in all the frames: **black** ⊡ and **red** × for experimental data while ascending and descending temperature respectively, while **blue** + for theoretically predicted data or data used in theoretical model (comparison is discussed in Sec. 4.3.3). The **green** ··· dotted lines in frames (a), (b) and (c) show the fitted plots [using Eq. (4.1), (4.2) and (4.3)] with the data of ascending temperature.

$$E_{\text{exc}}(T) = E_{\text{exc}}(0) - a_{ep}(2n_B + 1) \tag{4.1}$$

Here a_{ep} is the exciton-phonon coupling constant and $n_B = 1/\left(e^{\Theta/T} - 1\right)$. Θ is the average phonon temperature, such that the average phonon energy is $k_B\Theta$. Both, acoustic and optical phonons contribute to the redshift incurred by increasing temperature. $E_{\text{exc}}(0)$ is the exciton energy at 0 K. T is the absolute temperature. Upon fitting the ascending temperature data of Fig. 4.11a with Eq. 4.1, we get $E_{\text{exc}}(0) = 2.727$ eV. This value is in good agreement with results of Achtstein *et al.*, [25] who reported 2.709 eV. This elevated

$E_{\text{exc}}(0)$ compared to bulk like ZB CdSe epilayers (1.739 eV) [145] is due to increased quantum confinement effects. Further, we obtain $a_{ep} = 18.2 \pm 2.8$ meV and $\Theta = 36 \pm 0.4$ K. Chia *et al.* [145] calculated $a_{ep} = 21$ meV for bulk like ZB CdSe epilayers. This shows that the increased confinement in the NPLs has reduced the average exciton-phonon coupling, also evident from the significant reduction in average phonon temperature of 305 K in bulk ZB CdSe. [121]

Moreover, the exciton-phonon interaction induced intraband scattering causes transition energy broadening. The temperature dependence of the linewidth of excitonic peaks is given by [62, 146]

$$\Gamma(T) = \Gamma_0 + \gamma_{AC} T + \frac{\Gamma_{LO}}{e^{(\hbar\omega_{LO}/k_B T)} - 1} \tag{4.2}$$

where Γ_0 is the inhomogeneous broadening due to intrinsic effects (eg. alloy disorder, impurities). γ_{AC} accounts for the exciton-acoustical phonon interaction. The last term comes from exciton-longitudinal optical (LO) phonon Fröhlich interaction. For practical purposes, the contribution of γ_{AC} compared to Γ_{LO} is negligible, hence sometimes it is considered zero. [25, 147] At cryogenic range, particularly < 50 K, the linewidth gradient drastically decreases. [25, 130] therefore extrapolating our data of $\geq$ RT to lower temperatures would underestimate Γ_0. We have used $\Gamma_0 = 32.5$ meV from ref. [25] following their linear fit at a low temperature range of 10-50 K. Further, based on the Raman spectra measurements of CdSe NPLs [25] and QDs [128], we have taken $\hbar\omega_{LO} = 25$ meV, to fit the other parameters of Eq. 4.2 using the ascending temperature data from Fig. 4.11b. We found $\Gamma_{LO} = 236.3 \pm 11.8$ meV and $\gamma_{AC} = 0.38 \pm 0.03$ meV, suggesting that the LO phonon contribution is much larger compared to that of the acoustic phonon, consistent with the calculations of Rudin *et al.* [146] Comparing with bulk-like CdSe epilayers ($\gamma_{AC} = 0.084$ meV) [145], NPLs have much higher γ_{AC} due to an increase in acoustic phonon coupling caused by reduced dimensionality of the system, which is theoretically consistent [148]. The interaction between excitons and LO phonons is dictated by the Fröhlich interaction, which is Coulombic in nature caused by the longitudinal electric field produced by LO phonons. Therefore, $\hbar\omega_{LO}$ and Γ_{LO} are related in the sense that a larger $\hbar\omega_{LO}$ induces a stronger Fröhlich interaction and a larger Γ_{LO}. Valerini *et al.* [149] have shown the presence of multiple temperature-dependent non-radiative processes in PL relaxation dynamics. At higher temperature, the contribution of LO phonons becomes predominant, eventually dominating the excitonic linewidth [147].

Furthermore, with increasing temperature, we also have a substantial reduction in the PL intensity as the excitons are trapped in the nonradiative centers, likely at NPL surfaces and dissociate into the continuum states. The integrated intensity of the PL spectra with varying temperature is given by [145, 150]

$$I(T) = I(0) / \left[1 + C \cdot e^{-E_a/k_B T}\right] \tag{4.3}$$

where $I(0)$ and $I(T)$ are the integrated PL intensities at 0 K and T K, respectively. The fitting constant C is related to the radiative and nonradiative lifetimes, E_a is the activation energy of the nonradiative channel. We fit the ascending temperature data of Fig. 4.11c with Eq. 4.3 to obtain $E_a = 494 \pm 6$ meV. Heating above RT induces both reversible and irreversible losses in the intensity, and the latter restricts it to trace back upon cooling [151] (Fig. 4.11d). Irreversible losses are generally caused by chemical processes like ligand loss or oxidative degradation damaging the NPL surface which disturbs the repopulation of mobile holes and electrons. [152] The extent to which the PL intensity is retraced in Fig. 4.10b is due to reversible losses, caused due to dynamic and static quenching [151]. Upon heating, dynamic quenching activates the thermally activated non-radiative recombination paths compared to radiative paths; while static quenching causes the ratio of dark to bright particles to increase inducing non-radiative decay. While actively heating up to 90°C took us a few minutes, every successive 10°C fall took increasingly longer time – 2, 4, 6, 11, 19 and 32 minutes till 30°C and even longer to RT. The Newton's cooling constant following $T(t) = T_a + \Delta T_0 e^{-kt}$ yeilds $k = 0.089$ min^{-1}. An attempt to fit the descending T integrated intensity with Eq. 4.3 yeilds a poor Chi-square fit, as expected, since the irreversible losses incurred over almost a span of 1 hr disturbs the liable excitonic properties. If the cooling is conducted in a vacuum environment (to avoid losses due to oxidation), it will result in an improved intensity recovery.

4.3.3 Comparison of Theoretical and Experimental Results

In Sec. 4.3.1 and 4.3.2, we have studied the temperature-dependent optoelectronic properties of CdSe NPLs from a theoretical and experimental point-of-view. Here we combine and compare our findings, and simulate the PL spectra for varying temperature, as shown in Fig. 4.12. A PL spectrum is characterized by three main parameters:

- *PL peak position*: We have theoretically calculated the temperature-dependent E1–H1 transition energy values [Fig. 4.1 (a)], using the 8-band $\boldsymbol{k}\cdot\boldsymbol{p}$ method described in Sec. 2.3.1 and material parameters from Table A.1 in Appendix A. The Hamiltonian matrix was solved by direct diagonalization to obtain the electronic structure and eigenenergy values, and E1–H1 transition energy (equivalent of the PL peak position). It match excellently with the experimental data of PL peak position, as shown in Fig. 4.11 (a).

- *PL linewidth*: The PL spectrum undergoes spectral broadening due to several empirical factors, such as local and extended structural defects, size dispersion, alloy disorders and impurities, which affects its linewidth [116]. Thus, different 4 ML CdSe NPL samples may have varying linewidths at the same temperature. We have used the experimental linewidth data of ascending temperature to extract the intraband relaxation time ($\tau_{in} = 2\hbar/\text{FWHM}$) used in our simulation as described in the calculation of spontaneous radiative rate from the excitonic bound states and continuum-states in Sec. 2.5.2. This helps to model the linewidth of the simulated PL spectra according to the Lorentzian broadening lineshape [Eq. (2.55)] for an accurate estimate. The extracted τ_{in} is shown in Fig. 4.11 (b).

- *PL intensity*: We have calculated the relative PL intensity, which shows an exponential fall with temperature, as verified experimentally. However, the experimental PL intensity (arbitrary units) is not the absolute total emission. It is therefore of interest to study and compare the relative intensities variation with temperature, which is influenced by several parameters such as Fermi factor, TME, etc. [see Eq. (2.61) and (2.62)]. Our theoretically predicted relative PL intensities have a very good comparison with the experimental intensities of ascending temperature, as shown in Fig. 4.11 (c).

We have published the raw data of theoretical and experimental (ascending and descending temperature) results [99], which is freely available in pubic domain[2]. Employing the above mentioned approach, we have studied the PL spectra of the 4 ML CdSe NPLs at varying temperature. Fig. 4.12 shows a comparison between the experimental and theoretically calculated PL spectra at 30°C, 50°C and 70°C. For a clear comparison of peak

[2]Interested readers may access the PL raw data from *Nanoscale*, 2017, **9**, 6595–6605.

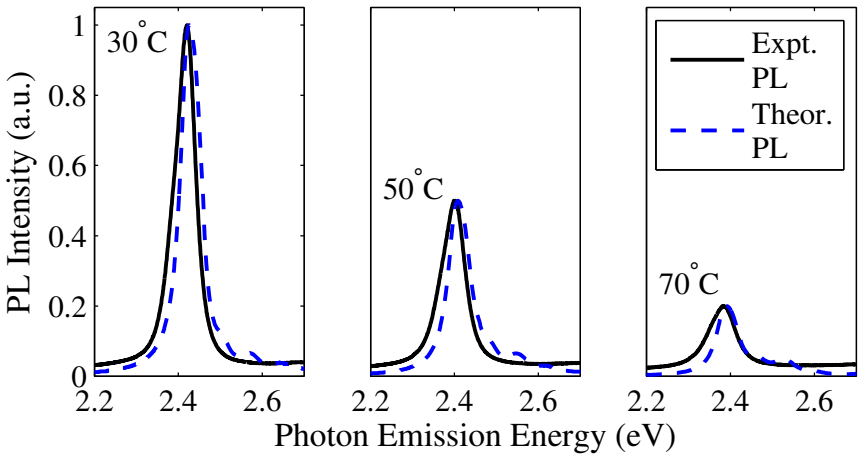

Figure 4.12: Comparison of experimental (solid black) vs. theoretical (dotted blue) PL spectra of 4 ML CdSe NPLs at 30, 50 and 70°C.

positions, linewidths and intensities, we have normalized both, the experimental and theoretical PL spectra with respect to the PL peak at RT. The experimental and theoretical PL spectra match appreciably, consistent with the results presented in Fig. 4.11.

In Appendix D, we have compared, extended and validated our calculations and measurements with existing low temperature results from literature. We have studied the temperature-dependent PL peak positions (E1–H1 transition energies), PL linewidth and relative PL intensity in tandem with results from seminal works of Achtstein *et al.* [25] and Erdem *et al.* [143] to validate our results.

4.4 Summary and Conclusion

In summary, we have comprehensively studied the electronic bandstructure, probability in band mixing, charge densities, optical transition matrix element, characteristic PL emission energy, linewidth and integrated intensity of CdSe NPLs – as a function of temperature, which is of critical importance particularly for commercial device applications at elevated temperature. Our theoretical investigations are based on a framework that relies on the effective-mass envelope function theory and density-matrix theory. From the quantum physics and optoelectronics point-of-view, the implications of rise in operation temperature of NPLs are many-fold, such as (*i*) reduction in effective band-edge transition energy, (*ii*) fall in optical transition matrix element strength, (*iii*) reduction in intraband state gaps, faster so in CB compared to VB, (*iv*) promotion of interband *e*-*h* coupling, (*v*) modification

in *hh-lh-so* band mixing probabilities, (*vi*) reduction in Fermi factor, (*vii*) shift of CB and VB quasi Fermi energy levels towards the band edges, and reduction in quasi Fermi separation, (*viii*) invariance in the charge density profile, (*ix*) redshift in peak photon emission energy in PL spectra, (*x*) widening of PL spectral linewidth owing to intraband scattering, (*xi*) exponential fall in PL integrated intensity, and (*xii*) phenomenological evidence of reversible and irreversible losses induced which affects the sample quality and dictates the PL traceability.

In conclusion, we have theoretically and experimentally studied the temperature-dependent optoelectronic characteristics of quasi-2D colloidal CdSe NPLs and established a model to predict and study the electronic bandstructure and PL spectra of NPLs at any arbitrary temperature, which can be effectively used by experimentalists to optimize device design iterations.

Chapter 5

Cd(S,Se) Nanoplatelets: Alloying Effect

5.1 Introduction

In Chapters 3 and 4, we discussed how the geometrical dimensions and temperature of NPLs affect their electronic bandstructure and other optical properties. But for any particular application, the dimensions and temperature are not the only parameters governing their optoelectronic characteristics – they also strongly dependent on the NPL material composition. The atomic-layer thickness of NPLs has traditionally been considered to be the primary determinant of their discrete emission wavelength [10, 25]. But this can be bypassed by alloying the NPL composition to obtain continuously tunable emission [28]. In this chapter, we study CdS_xSe_{1-x} NPLs in the zincblende (ZB) phase for varying alloy compositions in contrasting sizes, thicknesses and temperature on their electronic bandstructure, probability in band-mixing, electron and hole charge density, optical transition strengths and gain, Fermi factor and transparency properties. Variations in the composition of NPLs affect their energy levels, band-mixing probabilities, emission wavelengths, etc. We calculate the transition energies, optical transition matrix elements, Fermi factors to analyze and understand the exhibited behavior. The optical gain of NPLs is also strongly composition dependent with further dependence on the injection carrier density causing band-filling effect. They also affects the maximum and differential gain at varying composition, geometry and temperature.

5.2 Theoretical Framework

Similar to Chapters 3 and 4, we consider each NPL atom-by-atom in a 3D structure. We have studied the CdSe NPLs using an effective mass envelope function theory approach based on the 8-band $\boldsymbol{k}\cdot\boldsymbol{p}$ method using the first basis type described in Sec. 2.3.1, which simultaneously takes into account the nonparabolicity of the coupled conduction band (CB) and valence band (VB) including the orbit-splitting bands to solve its eigenenergy and obtain its electronic structure at the Γ-point. The 8-band Hamiltonian is represented in the Bloch function basis as detailed in Eq. (2.8).

5.3 Results and Discussions

5.3.1 Alloying effect on Cd(S,Se) NPLs

We have investigated the influence of varying the alloy composition of CdS_xSe_{1-x} NPLs on their electronic bandstructure and optical properties by varying x from 0 to 1, in steps of 0.2. For each of these compositions we have studied four variations of NPLs: (*i*) 12 nm × 12 nm × 5 ML at 300 K, (*ii*) 15 nm × 15 nm × 5 ML at 300 K, (*iii*) 15 nm × 15 nm × 5 ML at 350 K and (*iv*) 15 nm × 15 nm × 6 ML at 300 K. The choice of these four NPL variations is made with the intention of varying only one parameter at a time (size, thickness or temperature) while keeping the others constant, so as to understand the individual impact each of these has on the NPL's behavior. The excitonic transition energies (and emission wavelength) between bottom of conduction band (E1) to top of valence band (H1) i.e. E1-H1 for all our cases are shown in Fig. 5.1 (a).

CdS has a higher bandgap compared to CdSe, which is reflected in the plot, as we move from CdS to CdSe. The concavity is due to the influence of optical bowing coefficient of CdS_xSe_{1-x} = 0.28 eV [153]. Among the four NPL variations studied, the case (*iv*) 6 ML NPL has the largest volume, experiencing the minimum quantum confinement, thus has lowest transition energy for a given alloy composition. Likewise, the case (*i*) 12 nm–5 ML NPL has the highest transition energy owing to its minimum volume. Between the 15 nm–5 ML NPLs at 300 K and 350 K, i.e. cases (*ii*) and (*iii*), the one at higher temperature has a lower transition energy. This is because the bandgap has a negative gradient with temperature [See Sec. 2.6]. Comparing the NPLs with lateral size 12 nm (20% deviation from 15 nm) and thickness 6 ML (also 20% deviation from 5 ML), we see that thickness has a more profound impact on the transition energy compared to lateral size.

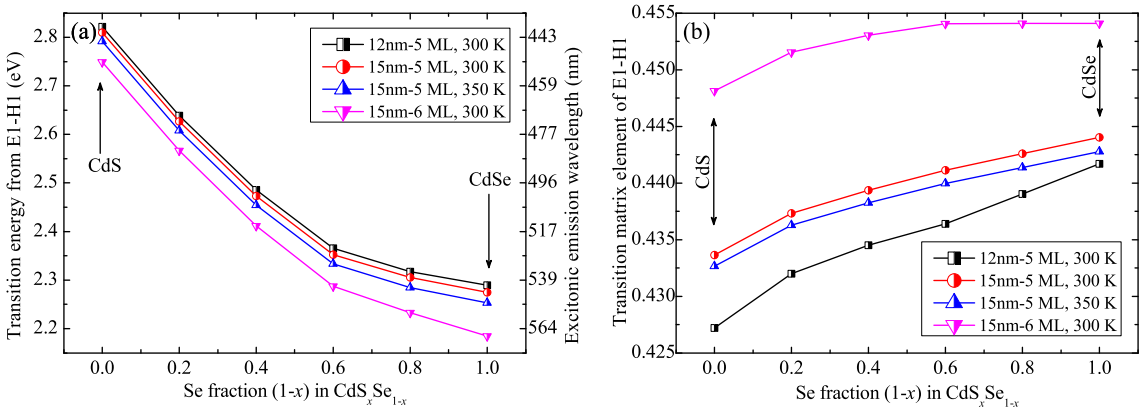

Figure 5.1: (a: *left*) Excitonic transition energy between bottom of conduction band (E1) to top of valence band (H1) i.e. E1-H1 considering bowing parameter effect of CdS_xSe_{1-x} = 0.28 eV [153], and (b: *right*) Transverse electric mode optical transition matrix element of E1-H1 vs. Se fraction $(1-x)$ in CdS_xSe_{1-x} NPLs of varying sizes, thicknesses and temperature as indicated in the legends.

For the same four NPL cases, Fig. 5.1 (b) shows the transition matrix element (TME) for the E1-H1 transitions, which quantifies the transition strength between hole- and electron-subband, depending on the couping extent between the system's initial and final state and possible number of paths to facilitate this transition (or density of the final states) [154]. For any given NPL geometry and temperature, the TME increases as we increase the fraction of Se composition in Cd(S,Se). This phenomenon can be attributed to the lower effective electron and hole masses (and more concave dispersion curves) in CdSe compared to CdS. Comparing the different geometries, the TME value increases with a rise in the size and thickness because of higher extent of electron and hole wavefunction overlap. However at 300 K, for a 20% variation in the thickness (5 to 6 ML) the change in the value of TME is $\sim$ 1.5 times (for CdSe) to 2.5 times (for CdS) compared to the change in the value of TME for a similar 20% variation in the size (15 nm to 12 nm). We can understand this phenomenon by visualizing the s-like E1 and H1 wavefunctions that are like oblate ellipsoids spread along all directions within the NPL. The NPL's dimensions determine their semi-principal axes, which are largely spread in the x-y plane and restricted along the z direction. Therefore, the differential change in the overlap integral for calculating TME would be higher when the thickness is varied compared to a lateral size variation. However, between the geometrically identical NPLs at 300 K and 350 K, the one with higher temperature has lower TME. This is because, with increasing temperature, the phonon concentration increases and results in increased scattering.

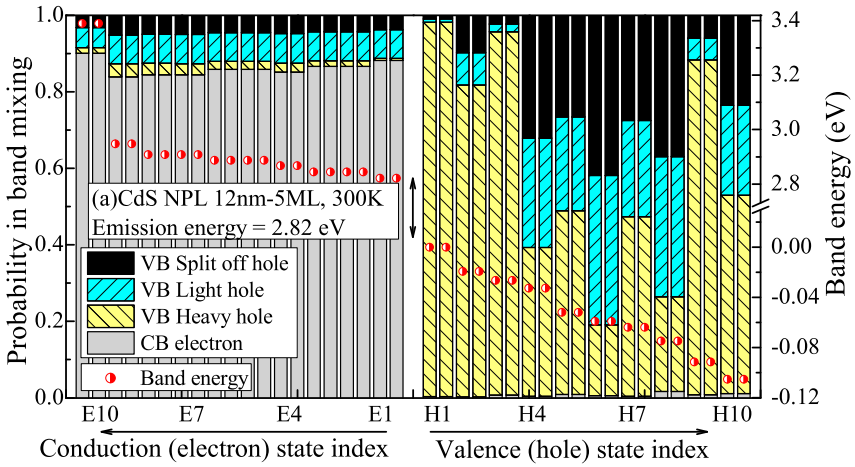

(a) 5 ML CdS NPL of size 12 nm × 12 nm at 300 K.

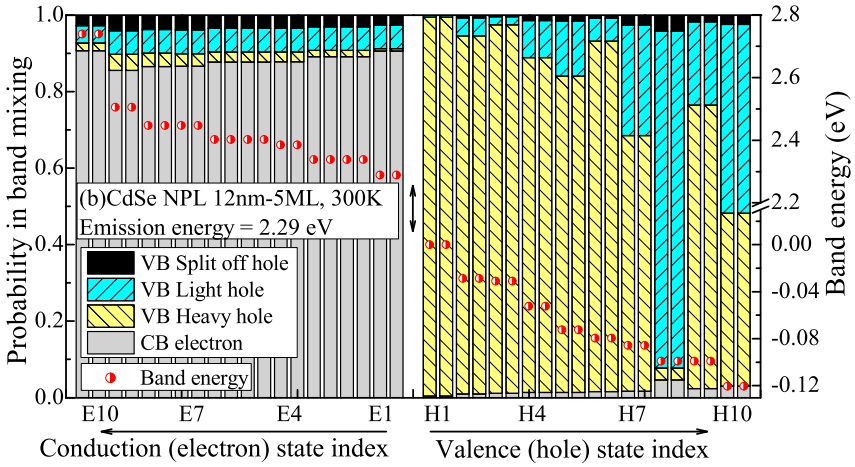

(b) 5 ML CdSe NPL of size 12 nm × 12 nm at 300 K.

Figure 5.2: Electronic bandstructure and the probability in band-mixing between conduction electrons and valence heavy holes, light holes and split off holes due to coupling effect for 5 ML (a: *top*) CdS and (b: *bottom*) CdSe NPLs of lateral size 12 nm at 300 K. Red dots indicate the band energy values, while the color bars show the probability.

Among the twenty-four cases portrayed in Fig. 5.1, we have shown the electronic bandstructure and the probability in band-mixing between the conduction electrons and valence heavy-, light- and split off-holes due to coupling effect for the 12 nm–5 ML NPLs at 300 K for CdS and CdSe in Fig. 5.2 (a) and (b) respectively. CdS NPLs have higher transition energy because of their higher bandgap. Comparing Fig. 5.2 (a) and (b), we see that the first ten valence hole states range about 105 meV in CdS, while about 120 meV in CdSe.

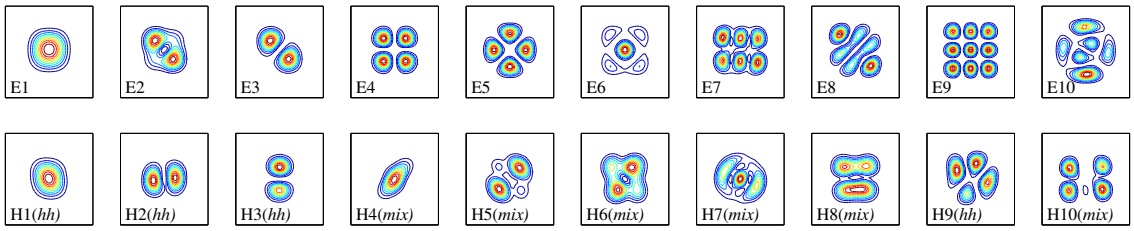

(a) Charge density of 5 ML CdS NPL of lateral size 12 nm at 300 K.

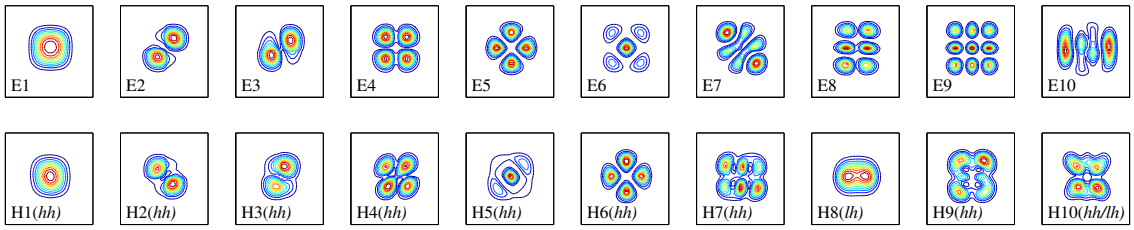

(b) Charge density of 5 ML CdSe NPL of lateral size 12 nm at 300 K.

Figure 5.3: Spatial charge density distributions of the first ten conduction (E) and valence (H) states of 5 ML (a: *top*) CdS and (b: *bottom*) CdSe NPLs of lateral size 12 nm at 300 K, along the x-y plane at $z = 0$. *hh* stands for heavy hole, *lh* for light hole and *so* for split-off hole, and *mix* for a combination of them.

This is owing to the heavier effective hole mass of CdS (0.981) compared to CdSe (0.62), which makes its dispersion curve flatter. A similar argument, that the effective electron mass of CdS (0.25) is higher than that of CdSe (0.12), results in the first nine states in CdS ranging about 125 meV compared to about 216 meV in CdSe. This follows from the lower concavity of the CdS dispersion curves relating from $m^* = \hbar^2 \left(\frac{\partial^2 E}{\partial k^2}\right)^{-1}$, which ensures that subsequent higher energy levels are more closely spaced. Also, since $m_h^* > m_e^*$, the H states are more closely packed than the E states. The intermediate NPLs of Cd(S,Se) alloy follow the trend. However, $\Delta_{\text{E9-E10}}$ in CdS is higher than CdSe since the next allowed states densities are at a higher quantized energy level in CdS. Also, the individual band-mixing probabilities in CdS has a much higher contribution from split-off holes because its spin-orbit splitting energy is over six times smaller than that of CdSe [122].

Fig. 5.3 shows the spatial charge densities of the first ten electron and hole states of the two NPL cases corresponding to Fig. 5.2. This is in the x-y plane at $z = 0$. For both CdS and CdSe, the first three E and H levels have similar patterns. The E1 and H1 states are s-like contributing highest to the TE TME, as we shall subsequently see. The E2, E3 and H2, H3 are p-like, while the E4 is d_{xy}-like, E5 is $d_{x^2-y^2}$-like and E6 is d_{z^2}-like.

In CdS, H1 to H3 have heavy hole (*hh*) dominance, after which there is increased contributions from light hole (*lh*) and split-off (so) hole. Except H9, H4 to H10 have varying ratios of almost one thirds for *hh*, *lh* and *so* holes. Among these the dominant types are 38% *hh* (H4), 47 % *hh* (H5), 41 % *so* (H6), 46 % *hh* (H7), 36 % *so* (H8) and 49 % *hh* (H10), while the others follow closely, therefore they are assigned as *mix*. The charge density spatial patters have varying *s*-*p*-*d*-mixing.

In CdSe, H1 to H7 and H9 are *hh* dominated while H8 (88 % *lh*) and H10 (49 % *lh*) have larger *lh* probability. The *so* contribution here is much lesser, as the *so* band is farther away from the *hh* and *lh* bands in CdSe compared to CdS, since the Δ_{so} of the former is over six times larger than that of the latter. Note that H4 in CdS and H8 in CdSe is the first non-*hh* dominant H states, and both have a *s*-like spatial pattern. Its overlap with E1 ensures a high TM mode TME. The higher order states again have have varying *s*-*p*-*d*-mixing. In CdS_xSe_{1-x} NPLs, as the Se fraction $(1-x)$ increases, the *so* contribution starts to diminish and *hh*-*lh* start to dominate. The spatial charge density distribution has a gradual shift from that in Fig. 5.3 (a) to 5.3 (b). Some, such as E1, H1 do not change significantly, others have much greater variation, like those in H4, H6, etc. Also, the TME values shift considerably as we shall further investigate.

To further understand the ongoing transition dynamics, we have shown in Fig. 5.4 and Fig. 5.5, the (a) transition energy, (b) fermi factor, (c) TE mode TME, and (d) TM mode TME for the two NPL cases (studied in Fig. 5.2 and Fig. 5.3) in contour form against the E and H state indices. A comparison of the transition energies (E_n–H_m) of the two cases, from frames (a) of Fig. 5.4 and Fig. 5.5 show that, the fall is much gradual until the E9 mark, as the E10 is at a higher quantized level for both, more so for CdS than CdSe. The $\Delta_{\text{E9-E10}}$ diminishes as the Se fraction in Cd(S,Se) increases. Discounting the E10 level, we can observe the effect of m_e^* and m_h^* – Cd(S,Se) NPLs with higher Se fraction have lower effective electron and hole masses and a more concave dispersion curve. Incremental E and H states get occupied at much higher (lower) levels in the conduction (valence) bands, and the resultant E_n–H_m has a steeper gradient. For instance, E1-H1 to E4-H4 and E4-H4 to E7-H7 is 149 meV and 95 meV in CdSe, while in CdS it is 78 meV and 72 meV, respectively. This is consistent with the discussion of inter-state spacing in context to Fig. 5.2. With increasing fraction of S in Cd(S,Se) NPLs, the states get more closely packed.

Frames (b) of Fig. 5.4 and Fig. 5.5 show the Fermi factor contour for an injection carrier density of 2.5×10^{19} cm^{-3} for CdS and CdSe respectively. While it is a strong function of the carrier density and NPL geometry, they are constant here and our attempt is to

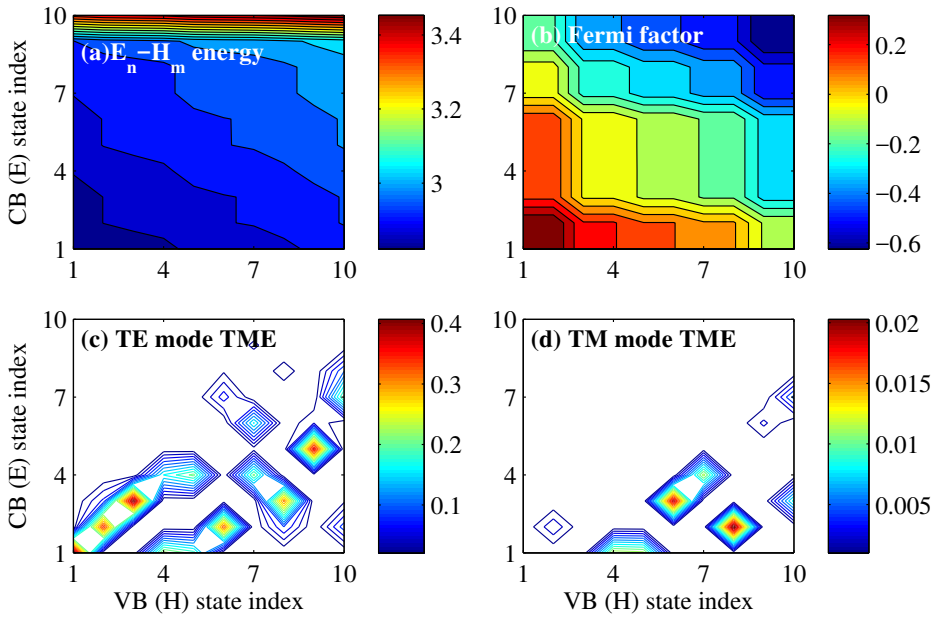

Figure 5.4: For 5 ML CdS NPLs of lateral size 12 nm, we have in a contour form, the following: (a: *top left*) Transition energy between the first ten E and H states – the minimum (2.82 eV) occurs at E1–H1 i.e. Γ-point, (b: *top right*) Fermi Factor for an injection carrier density of 2.5×10^{19} cm^{-3}, $max = 0.38$ (c: *bottom left*) Transverse electric (TE) mode optical TME polarized in the x-y plane, where E1-H1 is the strongest (0.427), and (d: *bottom right*) Transverse magnetic (TM) mode optical TME polarized along the z direction, where E1-H8 is the strongest (0.02). All contours are plotted against the first ten CB (E) and VB (H) state indices, and values specified in colorbars.

study the effect of alloying. The Fermi factor for the E1-H1 transition in CdS is 0.38, while in CdSe it is much higher at 0.69. Owing to the higher concavity of the CdSe dispersion curves, the E_{fc} and E_{fv} are further apart, which leads to a larger Fermi factor, as the Se fraction in the NPL increases. It is strongly correlated with the intensity of the optical gain, and transitions with negative values of Fermi factor would result in absorption. Therefore, the first few transitions with warmer colors contribute majorly to the optical gain.

Frames (c) of Fig. 5.4 and Fig. 5.5 show the TE mode TME transition strengths for CdS and CdSe respectively. The strongest is E1-H1 transition: 0.427 for CdS and 0.447 for CdSe. For CdS, the E1-H1 is followed by E_n-H_n (n=2,3). Other notable strong transitions are E5-H9, E3-H8 and E2-H6. For CdSe, the E1-H1 is followed by E_n-H_n (n=2,3,4), then E5-H6 and E6-H5. Other notable strong transitions are E1-H8, E7-H7 and E8-H9. This phenomenon can be understood by examining the extent of overlap between the wavefunctions involved that exhibit higher transition strengths.

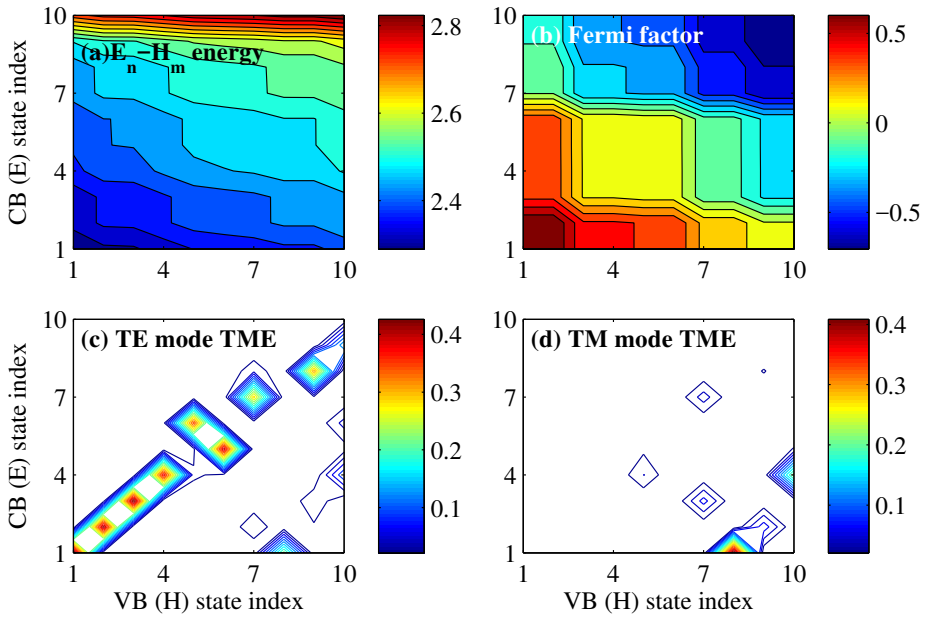

Figure 5.5: For 5 ML CdSe NPLs of lateral size 12 nm, we have in a contour form, the following: (a: *top left*) Transition energy between the first ten E and H states – the minimum (2.29 eV) occurs at E1–H1 i.e. Γ-point, (b: *top right*) Fermi Factor for an injection carrier density of 2.5×10^{19} cm^{-3}, $max = 0.69$ (c: *bottom left*) Transverse electric (TE) mode optical TME polarized in the x-y plane, where E1-H1 is the strongest (0.447), and (d: *bottom right*) Transverse magnetic (TM) mode optical TME polarized along the z direction, where E1-H8 is the strongest (0.429). All contours are plotted against the first ten CB (E) and VB (H) state indices, and values specified in colorbars.

Frames (d) of Fig. 5.4 and Fig. 5.5 show the TM mode TME transition strengths for CdS and CdSe respectively. It is generally weaker than TE modes in NPLs. In CdS, the notable ones are E1-H4, E1-H5, E3-H6 and E2-H8. Note that these H levels are *lh-so* rich, which contribute to the TM mode gain. Similarly, in CdSe, the notables ones are E1-H8 and E4-H10. Here, we observe that: (i) the H state having the strongest TM mode TME, i.e. H4 in CdS and H8 in CdSe is always paired with E1 and is s-like; and (ii) the H state having the strongest TM mode TME is the first H state with a major *lh* or *so* contribution. These are consistent behavior, as we have verified across varying NPL alloy compositions. However, the TM mode TME for CdS is much weaker compared to CdSe, and it increases as the Se fraction in Cd(S,Se) NPL increases.

5.3.2 Carrier density effects on Cd(S,Se) alloy NPLs

In Sec. 5.3.1, we examined the transition energy in CdS_xSe_{1-x} alloy NPLs and their corresponding TMEs and Fermi fermi factors. Here we study the optical gain of NPLs. We investigate the optical gain spectrum of 15 nm–5ML CdS_xSe_{1-x} NPLs at 300 K over varying injection carrier densities. Due to polarization of the gain, the x-y plane TE mode gain is much higher than the z direction TM mode gain.

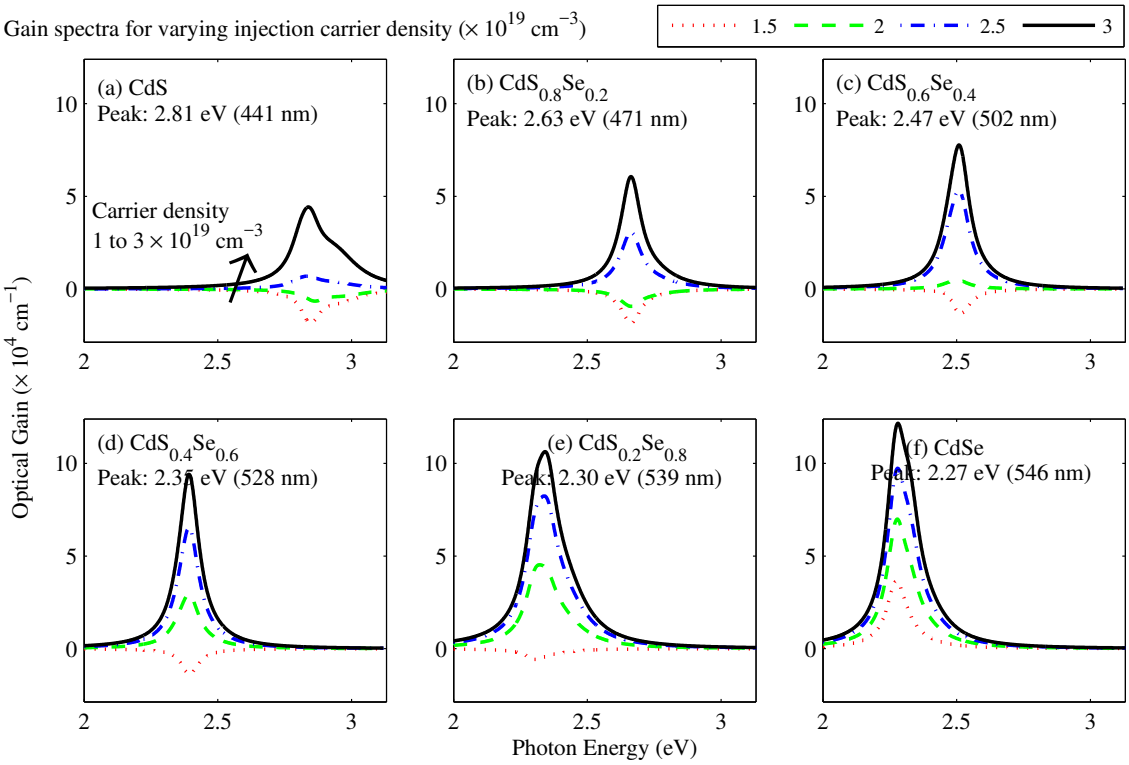

Figure 5.6: Optical gain spectra (cm^{-1}) of (a) CdS (b) $CdS_{0.8}Se_{0.2}$ (c) $CdS_{0.6}Se_{0.4}$ (d) $CdS_{0.4}Se_{0.6}$ (e) $CdS_{0.2}Se_{0.8}$ and (f) CdSe NPLs of lateral size 15 nm and 5 ML thickness at 300 K, for varying injection carrier density (1 to 3×10^{19} cm^{-3}). Note the shift in peak positions and gain intensities. Limits and scale of both axes are consistent to facilitate comparison.

Fig. 5.6 shows the TE gain spectrum of Cd(S,Se) alloy NPLs over 1 to 3×10^{19} cm^{-3} carrier density. With an increasing carrier density, the effective exciton pairs within the NPL rises and an increasingly larger number of carriers start occupying the higher energy levels, resulting in higher gain. A higher carrier density for gain-offset is equivalent to a higher lasing threshold current density. For a sufficiently low carrier density, we obtain

negative gain (absorption), while for some intermediate value, zero gain (transparency) will occur when the number of exciton recombinations and the number of photons generated are equal.

As we move from CdS to CdSe, the peak position experiences a redshift, mainly due to the bandgap decrement, shown by Fig. 5.1 (a), as the E1-H1 transition energy falls. However, for any particular Cd(S,Se) NPL, with increase in the carrier density, the peak position undergoes slight blueshift. As more carriers get injected, they start to occupy electronic states further away from the CB-bottom and VB-top. The difference between the highest occupied CV level and lowest occupied VB level increases, and excitonic recombinations resulting from such transitions have larger emission energy compared to the E1-H1 gap. Following the Pauli exclusion principle, the possible allowed transitions are between the higher occupied states. Thus for exciton recombination, the average band separation is higher for larger densities, resulting in the marginal blueshift. This phenomenon is sometimes termed as band-filling effect.

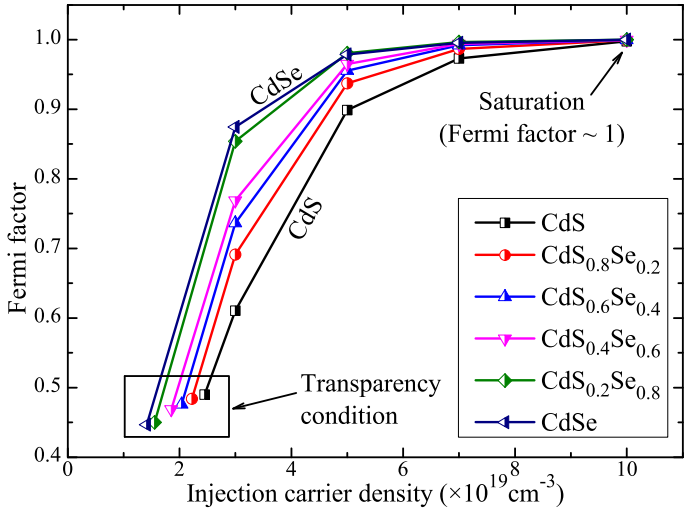

Figure 5.7: Fermi factor vs. injection carrier density for 15nm–5ML CdS_xSe_{1-x} NPLs at 300 K.

For a given carrier density, Cd(S,Se) NPLs with greater Se fraction have higher gain, as is evident from Fig. 5.6. This is due to the higher Fermi factor of CdSe NPLs compared to CdS. As we know, the gain is directly proportional to the Fermi factor. As shown in Fig. 5.7, for a given carrier density, Cd(S,Se) NPLs with greater Se fraction have higher Fermi factor, for similar geometrical and temperature parameters. CdSe, having a lower m_e^* and m_h^*, has

a higher concavity of the dispersion curves. Thus for the same carrier density, CdSe would have a greater extent of carrier occupation in both CB and VB. This implies that the CB and VB Fermi levels would be farther apart within the bands compared to CdS. Thus CdSe would have a larger quasi Fermi level separation, which by definition dictates the Fermi factor. For the same reason, CdSe has a lower transparency carrier density requirement compared to CdS. The transparency Fermi factor of CdS is however higher simply because more carriers need to be pumped to attain transparency. At a sufficiently high density all Cd(S,Se) NPLs attain saturation (Fermi factor ≈ 1).

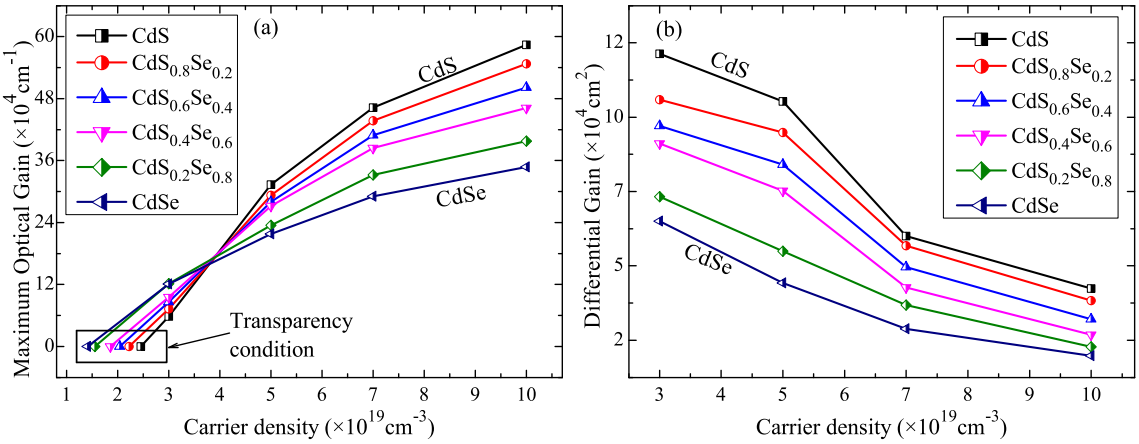

Figure 5.8: (a: *left*) Maximum optical gain (cm^{-1}) and (b: *right*) Differential gain (cm^2) vs. injection carrier density (cm^{-3}) for 15nm–5ML CdS_xSe_{1-x} NPLs at 300 K.

Next we study the effect of carrier density on the peak maximum gain of Cd(S,Se) NPLs, as shown in Fig. 5.8 (a). Transparency occurs at lower carrier density for Cd(S,Se) NPLs with higher Se fraction. Until a threshold density the maximum gain of CdSe NPLs is greater than that of CdS. But the maximum gain of CdS increases quickly, and after the threshold it exceeds that of CdSe. In the beginning, as carriers start to accumulate on the top (bottom) of valence (conduction) bands, their recombination energy is around the E1-H1 transition energy value. But, on further increasing the carrier density, more carriers begin to accumulate up (down) the conduction (valence) bands and the recombination energy of carriers in CdSe, with a steeper dispersion curve goes further away from the E1-H1 values which do not contribute to the peak maximum gain. On the contrary, for the relatively flatter CdS, the carrier recombination energy is still around the E1-H1 transition energy value, which contributes to the peak maximum gain.

The differential gain is yet another interesting aspect of optical properties of semiconductors. It is the measure of a laser's effectiveness to transform injected carriers to photons for emission, and affects the laser's resonant frequency. A greater differential gain corresponds to a narrower spectral emission width and a greater speed of modulation. [125] In Fig. 5.8 (b) we can see the differential gain of Cd(S,Se) NPLs with varying carrier density, which decreases with increasing density, more rapidly for Cd(S,Se) NPLs with higher S fraction. At higher carrier densities, Cd(S,Se) NPLs tend to attain saturation in gain.

5.3.3 Size and temperature effects on Cd(S,Se) alloy NPLs

In Sec. 5.3.2, we studied the impact that carrier density has on the gain spectrum of Cd(S,Se) alloy NPLs. In this section, we shall study the impact of contrasting size, thickness and temperature.

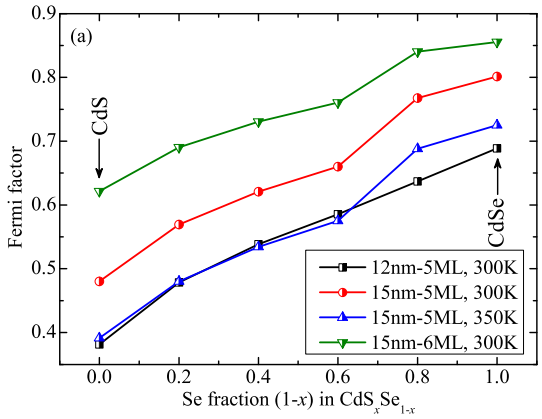

(a) Fermi factors at injection carrier density 2.5×10^{19} cm^{-3}

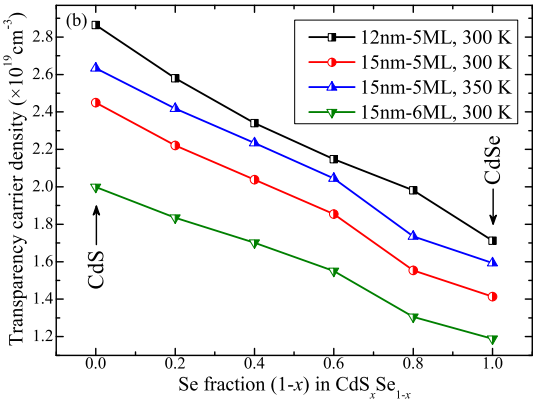

(b) Transparency carrier densities for CdS_xSe_{1-x} NPLs

Figure 5.9: (a: *left*) Fermi factor vs. Se fraction (1-x) in CdS_xSe_{1-x} NPLs with an injection carrier density of 2.5×10^{19} cm^{-3} at 300 K; and (b: *right*) Transparency carrier density (cm^{-3}) vs. Se fraction (1-x) in CdS_xSe_{1-x} NPLs. For both frames, the contrasting sizes, thicknesses and temperature are indicated in the legends.

We found that, for a fixed carrier density, the 6 ML NPL has a higher gain spectrum compared to 5 ML NPLs for all Cd(S,Se) compositions because it can accommodate more active excitons capable of radiative recombination and also has a higher TME and Fermi factor. However, it has a larger real space thickness and volume, which tends to reduce the gain [see Eq. (2.59) and (2.60)], but it is a weaker counteracting factor. Among the

other three 5 ML NPLs, the 12 nm NPL accommodates the least excitons and by the same argument exhibiting the lowest gain. The influence of NPL size is such that, thicker and larger NPLs have a higher Fermi factor than thinner and smaller NPLs [Fig. 5.9 (a)]. Among the two geometrically identical 15nm–5 ML NPLs, temperature differences come into the picture. With a rise in temperature, the bandgap (ergo the emission energy) decreases while the linewidth increases [see Sec. 2.6]. It is also noteworthy that warmer NPLs have a lower TME [Fig. 5.1 (b)] and lower Fermi factor [Fig. 5.9 (a)], owing to which their maximum peak gain is also lower for geometrically identical NPLs with the same carrier density. Also, lower temperature is favorable for a higher Fermi factor, for geometrically identical NPLs. However, the effect of composition is more imposing, as NPLs with a larger Se fraction have a higher Fermi factor.

Finally, we study the transparency condition for NPLs. [126] The transparency carrier densities of the four Cd(S,Se) alloy NPL cases are shown in Fig. 5.9 (b). A density higher than the transparency carrier density would yield a gain, while a lower density would result in absorption. Volumetrically smaller NPLs need a higher density to attain the requisite exciton count necessary for transparency; while for those with a larger volume, a significantly lower density can impel the transparency condition exciton count. Warmer NPLs have degraded optical performance over cooler ones as discussed. Therefore, for geometrically identical NPLs they have a higher density demand to attain transparency.

5.4 Summary and Conclusion

We have performed a comprehensive study of the electronic bandstructure, band-mixing probabilities, charge densities, optical gain Fermi factor and transparency properties of quasi two-dimensional CdS_xSe_{1-x} alloy NPLs in the ZB phase – over contrasting size, thickness and temperature.

Variations in the composition of Cd(S,Se) NPLs significantly affects its energy levels, band-mixing probabilities and optical gain. Those with a higher Se fraction have a lower E1-H1 transition energy. For NPLs of the same composition, volumetrically larger ones have lower transition energy due to lower confinement. Increasing the temperature has a similar effect due to the negative gradient of bandgap. NPLs with higher Se fraction, however, have a larger TME due to a lower effective electron and hole masses. For NPLs of the same material, decreasing its volume reduces the TME owing to the minimized overlap integral between the electron and hole wavefunctions. Increasing the temperature also has

a detrimental effect on the TME. Moving from CdS to CdSe, the emission peak position experiences a redshift due to effective bandgap reduction. For a given alloy composition, there is slight blueshift (and rise in intensity) with increasing carrier density due to band-filling effect. NPLs with higher Se fraction produce larger gain due to their higher Fermi factors and exhibit transparency at lower densities. The maximum gain of NPLs grows rapidly in the beginning but the differential gain saturates after a point. A study of the size and thickness effect shows that volumetrically larger NPLs can accommodate more recombination excitons resulting in higher gain compared to smaller NPLs. This follows from their higher Fermi factor. Also larger NPLs have a lower density demand to attain the exciton count to obtain transparency. Increasing the temperature of NPLs has a detrimental effect on the Fermi factor reducing its gain intensity. Also warmer NPLs need greater carrier density for transparency.

Chapter 6

CdSe Nanoplatelets: Polarized Excitonic Absorption

6.1 Introduction

Quasi-2D II-VI NPLs, as discussed through Chapter 3, 4 and 5 experience strong 1D vertical confinement, which induces a large exciton binding energy, while the increased exciton center-of-mass extension results in giant oscillator strength transition (GOST) in NPLs [25, 29]. This significantly enhances the NPL's absorption cross-section [29]. A study of the absorption cross-section of NPLs can be an important enabler in quantifying certain fundamental optoelectronic properties of NPLs. With the knowledge of the absorption cross-section, the number of excitons generated due to each photon absorbed by an NPL can be estimated; and the NPL fluorescence quantum yield can also be quantified [29]. The absorption cross-section results can also help to explain low amplified spontaneous emission threshold of NPLs [30], and determine the concentration of NPLs in solution/films [31].
The absorption spectra of NPLs have been well studied in literature and has a well recognized signature [8, 10] – a higher intensity electron/heavy-hole (HH) absorption peak with a small stokes shift from the emission spectra, and a blue-shifted lower intensity electron/light-hole (LH) absorption peak. However, recently Achtstein *et al.* discovered anomalous absorption spectral properties in ultrathin sub-nanometer (2 ML) CdSe NPLs characterized by increased intrinsic absorption and inverted HH and LH relative peak intensities [31]. They discounted its study in comparison with thicker NPLs due to fundamental

physical reasons.[1] In this chapter, we experimentally verify their observations and theoretically study the exciton dynamics in NPLs of varying thickness to understand how-and-why the electronic bandstructure and polarization dependent excitonic absorption of CdSe NPLs are affected by the thickness dependent quantum confinement. This is a first account of the theoretical treatment of the anomalous absorption spectral characteristics observed in sub-nanometer (2 ML) CdSe NPLs.

6.2 Theoretical Framework

To study the electronic bandstructure of CdSe NPLs, we have used an effective mass envelope function theory approach based on the Kane's 8-band $\boldsymbol{k}\cdot\boldsymbol{p}$ method using the second basis type to construct the Hamiltonian as described in Sec. 2.3.2. This is suitable for zinc-blende (ZB) strained semiconductor, containing both kinetic terms H_k (independent from k and with linear and quadratic dependence on k) and strain terms H_ε [44, 100], and is given by Eq. 2.14 as explained in Sec. 2.3.2. It takes into account the energy levels from conduction band (CB), heavy hole (HH), light hole (LH), and spin-orbit split-off-hole (SO) bands which can be seen in the main diagonal terms ($H_{cb}, H_{hh}, H_{lh}, H_{so}$). The off-diagonal terms account for the coupling effects. The energy eigenvalue problem is solved to obtain its eigenenergy and electronic bandstructure around the Γ-point. The TMEs are calculated using Eq. 2.20. In the later part of this chapter, we discuss about the excitonic absorption of CdSe NPLs, which is calculated as a sum of the contributions from bound excitonic states absorption and continuum band-to-band states absorption with Sommerfeld enhancement using Eq. 2.63 as described in Sec. 2.5.2.

6.3 Results and Discussions

6.3.1 Electronic Bandstructure Results

The optoelectronic characteristics of NPLs of any particular material is strongly dependent on the atomic-layer thickness, which is the primary determinant of their discrete emission/absorption wavelength. [10, 25] Here we study CdSe NPLs of varying thicknesses: 2,

[1] Owing to the ultra-strong transversal quantization in 2 ML CdSe NPLs, the exciton wavefunction extends significantly into the neighboring ligand region where the carriers experience a different dielectric environment and effective mass. This affects their electronic structure and exciton dynamics.

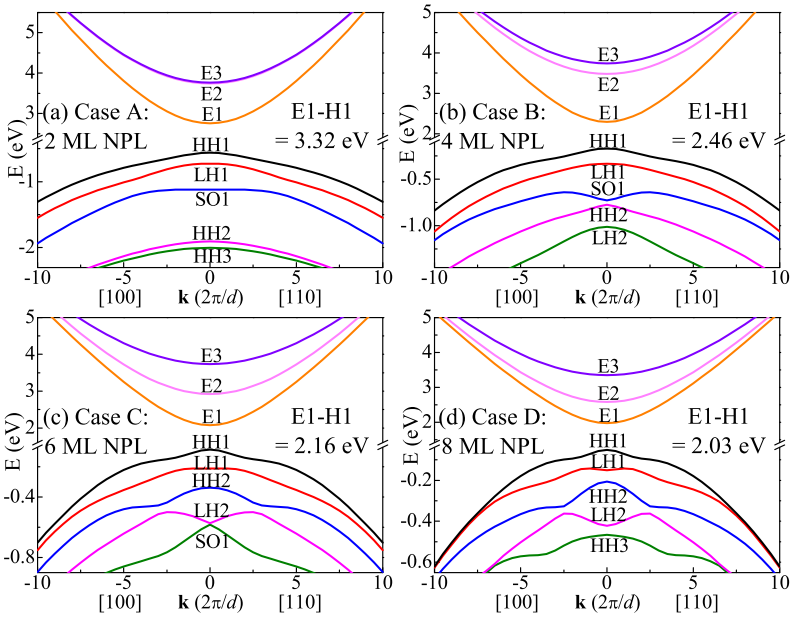

Figure 6.1: The energy dispersion curves of the first three electron and first five hole states in CdSe NPLs of thickness (a: *top left*) Case A: 2 ML; (b: *top right*) Case B: 4 ML; (c: *bottom left*) Case C: 6 ML; and (d: *bottom right*) Case D: 8 ML. **k** is wavevector along [100] and [110] directions. E stands for electron, HH for heavy hole, LH for light hole and SO for split-off hole levels, respectively. The sequence of hole-type in the valence band is tabulated in Table 6.1. The transition energy E1–HH1 for each case is mentioned.

4, 6 and 8 monolayer (ML).[2] The energy dispersion curves for the first 3 electrons and the first 5 holes subband states along the [100] and [110] wavevector direction for our four cases, viz. Case A to D (2 to 8 ML) CdSe NPLs are shown in Fig. 6.1. The NPL thickness of each case is mentioned in the figure. The electron states are labeled E1 to E3, while for the holes states we have specified the heavy-hole (HH), light-hole (LH) and split-off hole (SO) states distinctly. The H1 levels in all the cases are HH dominated, and the E1–H1 is the transition energy of the NPL i.e. the effective bandgap. In all the cases, the E and H subbands are isotropic due to the isotropy of the effective electron and hole mass. Fig. 6.2 shows the E1, H1 and E1–H1 transition energy values for all four cases. As the NPL thickness increases, the extent of vertical confinement reduces and therefore, the top of the valence band (VB) i.e. H1 and bottom of the conduction band (CB) i.e. E1 approach each other. Also, the intraband state-gaps between adjacent E states and adjacent H states

[2]The thickness of NPLs in ML can be converted to nm by computing ML $\times (a/2)$ where a is the lattice constant of the material in nm. For example, 4 ML CdSe NPL is 1.21 nm thick.

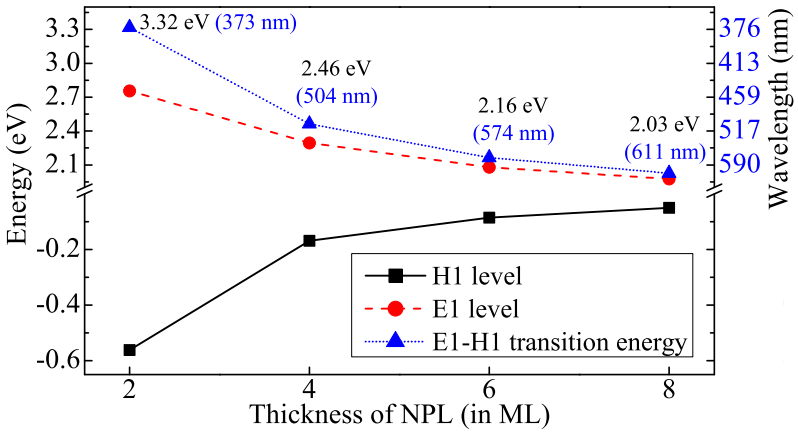

Figure 6.2: The E1 and H1 energy levels for 2, 4, 6 and 8 ML CdSe NPLs are shown. H1 is HH in all four cases. The E1–H1 transition energy value for each case is indicated with the corresponding excitonic wavelength.

reduces, as the NPL thickness increases. But the rate of intraband state-gaps reduction is faster in VB compared to CB. For instance, $\Delta_{\text{H1-H5}}$ reduces from 1441 meV in Case A (2 ML) to 415 meV in Case D (8 ML), while $\Delta_{\text{E1-E3}}$ is shifts only from 1374 meV to 1006 meV. This can be understood by comparing the CB and VB dispersion curves – the CB energy dispersion curve has a much higher concavity over the VB dispersion curve. This is because CdSe has a lower effective electron mass ($m_e^* = 0.12$) than effective hole mass ($m_h^* = 0.62$), which inversely affects the concavity, relating from $m^* = \hbar^2 \left(\frac{\partial^2 E}{\partial k^2}\right)^{-1}$.

An analysis of the coupling between E, HH, LH and SO [see Eq. 2.14] for the first 3 electron and the first 5 holes subband states yields the probability in band-mixing between them for each state, as shown in Fig. 6.3, using appropriate legends. The CB states are primarily dominated by E, with mild infusion of LH and SO as the NPL thickness increases, starting from E1 and subsequently moving on to E2 and E3. The extent of infusion, however, is larger for higher E states. For the VB states on the other hand, H1 is routinely HH dominated in all cases, consistent with the unstrained ZB bandstructure. The H2 state is LH dominated, and as the thickness increases, the extent of LH occupation increases, with minimal SO contribution. However, for higher VB states, SO contribution increases, more quickly in thinner NPLs compared to thicker. For example, the H3 state is SO dominated in Cases A and B (2 and 4 ML), while for Cases C and D (6 and 8 ML), only at H4/H5 we can see the SO effect. For each VB state, we have tabulated the major contributor in terms of band-mixing probability and listed them in Table 6.1.

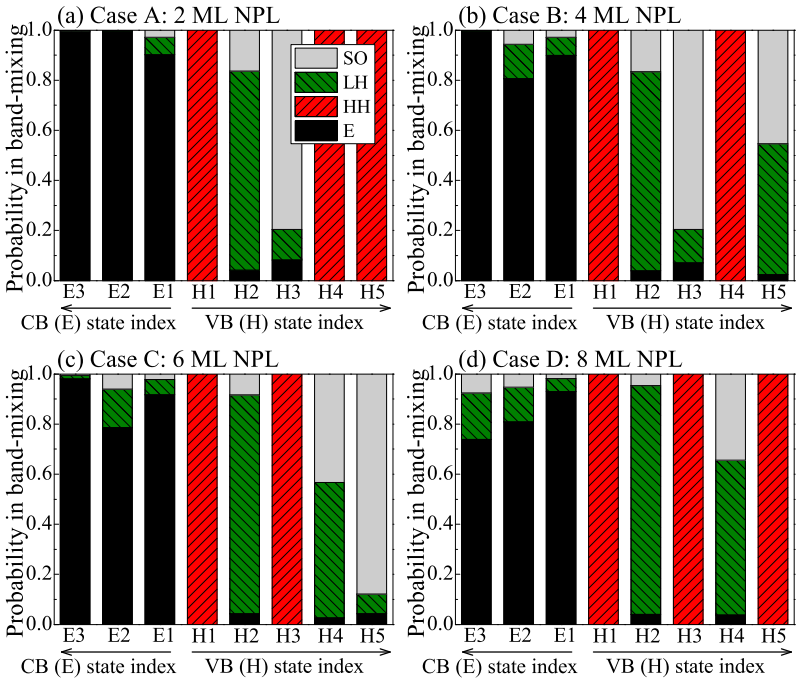

Figure 6.3: The probability in band-mixing between conduction electrons and valence heavy holes, light holes and split off holes due to coupling effect for the first three conduction band (E) and first five valence band (H) states in CdSe NPLs of thickness (a: *top left*) Case A: 2 ML; (b: *top right*) Case B: 4 ML; (c: *bottom left*) Case C: 6 ML; and (d: *bottom right*) Case D: 8 ML. E stands for electron, HH for heavy hole, LH for light hole, and SO for split-off hole levels, respectively. All CB states are dominated by E, H1 by HH, H2 by LH, and SO for higher H states.

Table 6.1: Predominant hole-type for the first 5 VB levels for 2, 4, 6 and 8 ML CdSe NPLs. Detailed band-mixing probability is shown in Fig. 6.3.

VB level	2 ML	4 ML	6 ML	8 ML
H1	Heavy	Heavy	Heavy	Heavy
H2	Light	Light	Light	Light
H3	Split-off	Split-off	Heavy	Heavy
H4	Heavy	Heavy	Light	Light
H5	Heavy	Light	Split-off	Heavy

Using this information, we have marked each VB energy dispersion curve with it's predominant hole-type in Fig. 6.1. We can study H3 to H5 in tandem for all 4 cases. H3, i.e. SO1 for 2 and 4 ML are similar, which moves to H5 for 6 ML, and predictably beyond H5 for 8 ML. H4 for 2 and 4 ML is HH2, which moves to H3 for 6 and 8 ML, and predictably should be H2 for even thicker NPLs. H4 has a well-balanced LH and SO contribution (LH

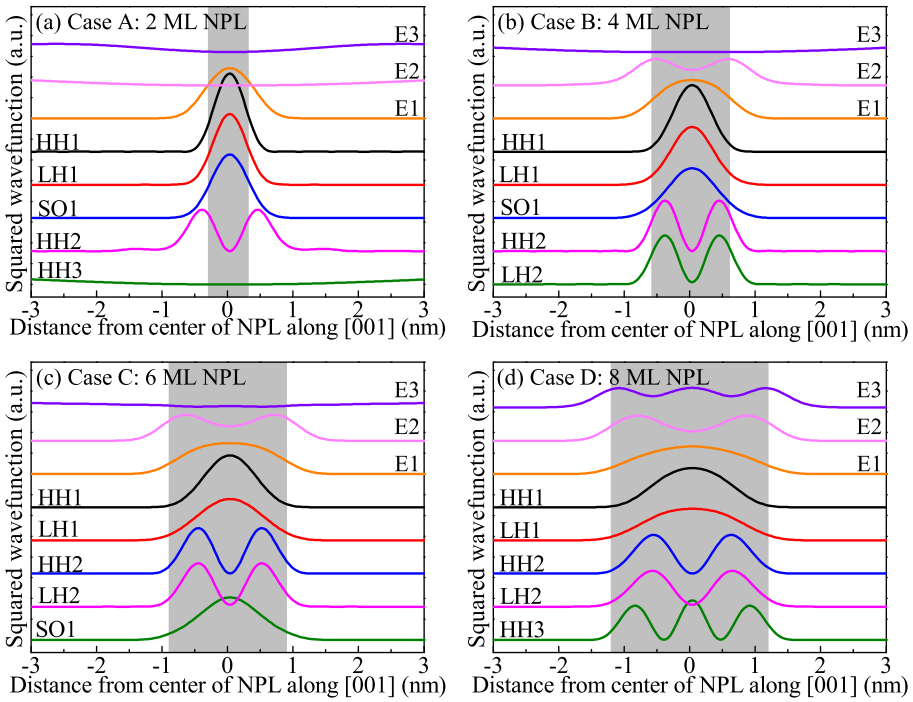

Figure 6.4: The squared wavefunctions at $\mathbf{k} = 0$ (Γ–point) for the first three electron and first five hole states in CdSe NPLs of thickness (a: *top left*) Case A: 2 ML; (b: *top right*) Case B: 4 ML; (c: *bottom left*) Case C: 6 ML; and (d: *bottom right*) Case D: 8 ML vs. distance from the center plane of the NPL along the [001] direction. The gray shaded region represents the NPL. The squared wavefunctions are shown with equal spacing for the sake of comprehensive visual representation, and are indicated as E standing for electron, HH for heavy hole, LH for light hole, and SO for split-off hole levels, respectively. The band-lineups for each case is shown in Fig. 6.5 with actual relative spacing between the E and H states energies.

is higher) for 8 and 6 ML, which has moved to H5 for 4 ML, and predictably beyond H5 for 2 ML. Additionally, we have observed that the lower the spin-orbit splitting energy, the higher is the extent of SO contributions in the VB states. For example, in CdS it is only 65 meV, compared to 420 meV in CdSe, which results in greater SO infusion.

It is now imperative to study the spatial manifestation of the electron and hole states. Fig. 6.4 shows the squared wavefunction of the first 3 electron and the first 5 hole energy levels at $\mathbf{k} = 0$ (Γ–point) point for Cases A to D (2 to 8 ML) CdSe NPLs. The predominant hole-types are mentioned. Considering NPLs as the colloidal equivalent of epitaxial quantum wells, we can see that as the NPL thickness increases, the E and H wavefunctions spreads out, as expected due to larger well (NPL) width. The gray shaded region in each frame of Fig. 6.4 represents the corresponding NPL, while the region beyond it

represents the organic ligand and solvent region. In all the cases, the wavefunctions of E1 has a reasonable overlap with that of H1 (HH1), which causes the E1–H1 fundamental transition [Fig. 6.2]. For transitions among higher E and H states, the optical selection rule is followed, which states that the only permitted transitions are those between states of the same quantum number in the VB and CB. [115] This is an implication of the fact that the optical absorption strength is proportional to the overlap integral of the conduction and valence envelope wavefunctions. Note that, in our calculation, we have used the CB and VB offset, $\Phi(z) = 2$ eV, therefore we can see the wavefunction leakage spreading beyond the NPL into the ligand/solvent region. This is a reasonable estimation, specially for thinner NPLs (e.g. 2 ML), where such phenomenon has been observed. [31] In Fig. 6.4, we have shown the squared wavefunctions with arbitrary units with equal spacing, for the sake of comprehensive visual representation. Each peak of the squared wavefunction is an antinode in the actual wavefunction, while each trough is a node. Every wavefunction Ψ_{n_c} or Ψ_{n_v}, corresponds to an energy level E_{n_c} and E_{n_v} at $\mathbf{k} = 0$, the value of which can be recovered from Fig. 6.1. Additionally, we have shown the band-lineup diagrams for each of our NPL cases in Fig. 6.5, which shows the absolute positions in terms of the energy difference of the E and H wavefunctions at the $\mathbf{k} = 0$ point. Here, we can clearly see the Type-I structure with the CdSe NPL in the middle region, and ligand/solvent in the outer region. As we move to higher CB or VB states, the wavefunction index n increases, and they begin to have more nodes i.e. locations where the probability of finding electrons/holes is zero. Band-lineup diagrams from Fig. 6.5, show us that as the NPL thickness decreases, the extent of confinement increases, and the quantized energy levels, E_{n_c} and E_{n_v} gets more spaced out in the energy spectrum. Certain higher CB and VB states have energies almost approaching the band offsets and therefore are not quantum confined any longer. Examples of this include E2, E3 and HH3 in 2 ML and E3 in 4 and 6 ML NPLs. Notice that the wavefunctions for these states are practically flat with no nodes or antinodes. The motivation of showing Fig. 6.4 and Fig. 6.5 separately is that, certain states, particularly H1 to H5 are confined within a very small intraband energy gap, making it difficult to study their wavefunction properties in the actual lineup diagram, which is otherwise necessary for an understanding of their energy positions compared to the CB and VB band offsets.

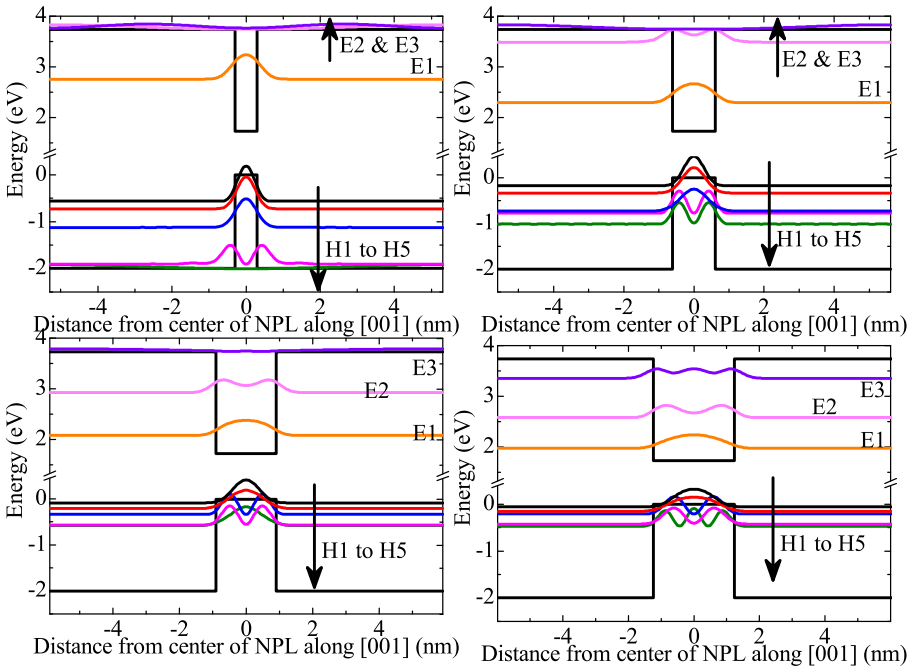

Figure 6.5: The band-lineup and squared wavefunctions with the absolute energy spacing at $\mathbf{k} = 0$ (Γ–point) for the first three electron and first five hole states in CdSe NPLs of thickness (a: *top left*) Case A: 2 ML; (b: *top right*) Case B: 4 ML; (c: *bottom left*) Case C: 6 ML; and (d: *bottom right*) Case D: 8 ML vs. distance from the center plane of the NPL along the [001] direction. The middle region of the Type-I structure with lower bandgap represents the NPL, and the outside regions represents the ligand/solvent. The confining potential used is 2 eV, and wavefunctions of states with energies close to it experience diminishing confinement effect (eg. E3 in 2, 4 and 6 ML; and H5 in 2 ML).

Now, we shall study the transition matrix element (TME), as discussed for Eq. 2.20 in Sec. 2.3.2 for both TE and TM modes. The four frames in Fig. 6.6 [(a) through (d)] show the TME values for our four NPL cases: 2, 4, 6 and 8 ML. And within each frame we have four sub-frames showing the TME values for transitions in the TE and TM modes from the first and second conduction states (E1 and E2) to the first five hole states. For each of the cases, the hole-type of the most prominent transitions are identified and indicated.

Firstly, for transitions from E1 in the TE mode, the E1–HH1 transitions are the strongest in all cases, followed by SO1 and LH1 in 4 and 6 ML, and LH1 in 8 ML. On the other hand, for transitions from E1 in the TM mode, the E1–LH1 transitions are the strongest. This is followed by SO1 in 4 and 6 ML. Also note that as the NPL thickness increases, the spread of the TME intensity in the **k**-space decreases [78]. Owing to the microscopic selection rules for the TM polarization mode associated with the unit cell wavefunctions,

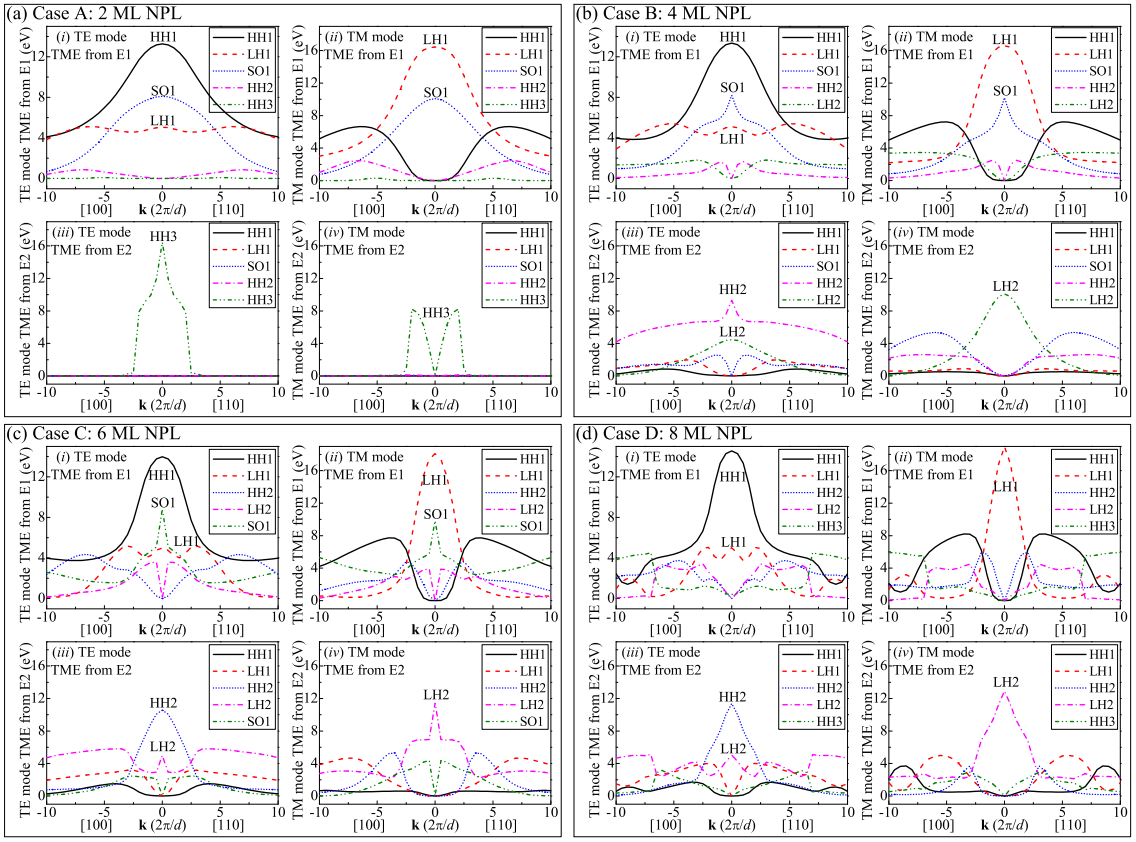

Figure 6.6: Optical transition matrix element (TME) values for transitions in CdSe NPLs of thickness (a: *top left*) Case A: 2 ML; (b: *top right*) Case B: 4 ML; (c: *bottom left*) Case C: 6 ML; and (d: *bottom right*) Case D: 8 ML. Within each frame, there are four sub-frames showing the transverse electric (TE) mode and transverse magnetic (TM) mode TMEs from the first and second conduction states (E1 and E2) to the first five hole states. They are (*i*: *top left*) TE mode TME from E1; (*ii*: *top right*) TM mode TME from E1; (*iii*: *bottom left*) TE mode TME from E2; and (*iv*: *bottom right*) TM mode TME from E2. The most prominent transition hole-types for each case is identified and indicated.

the HH to E transitions are forbidden, while only LH to E transitions are allowed. At thermal equilibrium, there are more HH than LH and hence the gain/absorption associated with HH (in TE polarization) is relatively larger.

Secondly, for transitions from E2 in the TE mode, the strongest ones in 4, 6 and 8 ML are the E2–H2 and E2–LH2. On the other hand, for those in the TM mode, the E2–LH2 transitions are the strongest. When the quantum confined energy of the state is within the confining potential, the optical selection rule ($\Delta n = 0$) is followed i.e transitions from E1 are only to (HH/LH/SO)1 and likewise for E2 to (HH/LH)2. But, as is the case for 2 ML

NPLs, the narrow NPL width induces greater quantum confinement and E and H states are much farther apart (see Fig. 6.5). The HH2 and HH3 states have almost overlapping energies that are comparable to the VB offset (2 eV). Therefore, we see the emergence of HH3 in the transitions from E2 for the 2 ML NPL case, where the selection rule ceases to hold as expected for finite wells.[3]

6.3.2 Optical Excitonic Absorption Results

In NPLs, the charge carriers are free to move along the x-y plane parallel to the NPL layers; hence, instead of having discrete E and H energy states like in quantum dots, they have 'subbands' starting at energy levels corresponding to the confined states. In addition to that, electrons in a given confined state can have extra kinetic energy for its in-plane momentum, rendering its total energy more than or equal to the confined-state energy for that subband. The DOS of quasi-2D NPLs is 'step-like' starting at the appropriate confinement energy, similar to that of quantum wells. Optical transitions must anyway conserve momentum, and therefore the optical absorption must still follow the DOS.

The TME values and DOS have important roles to play in determining the absorption spectra of NPLs, as we shall further examine. The four frames in Fig. 6.7 show the absorption spectra of our four NPL cases of 2, 4, 6 and 8 ML. The TE mode absorption is shown by red solid line, TM mode by blue dashed line and the weighted average by black dotted line. Each frame has two insets, showing its band-to-band absorption (α^c) component and excitonic bound state absorption ($\alpha^{ex,b}$) component, which contribute to the total optical absorption as discussed for Eq. 2.63 in Sec. 2.5.2.

For absorption near the band-edge, there are two kinds of holes that are relevant – HH and LH and they have distinctly different effective masses. This gives rise to two sets of hole subbands, with varying energy spacings. The HH subband are spaced close together owing to their heavier mass, and vice versa for LH. Consequently, there are two sets of 'steps' for the optical absorption. The HH to E set starts at a relatively lower energy than the LH to E set, and the former is spaced more closely than the latter. The dominant set for TE polarization mode is usually the HH set.

The absorption spectra of 2, 4 and 6 ML NPLs have three distinct peaks corresponding

[3] In finite wells the electron and hole wave functions with differing quantum numbers are not necessarily orthogonal to each other because of the differing decay constant in the barrier regions. This means that there are small departures from the selection rule of a infinite well. However these non-zero transitions are relatively weaker.

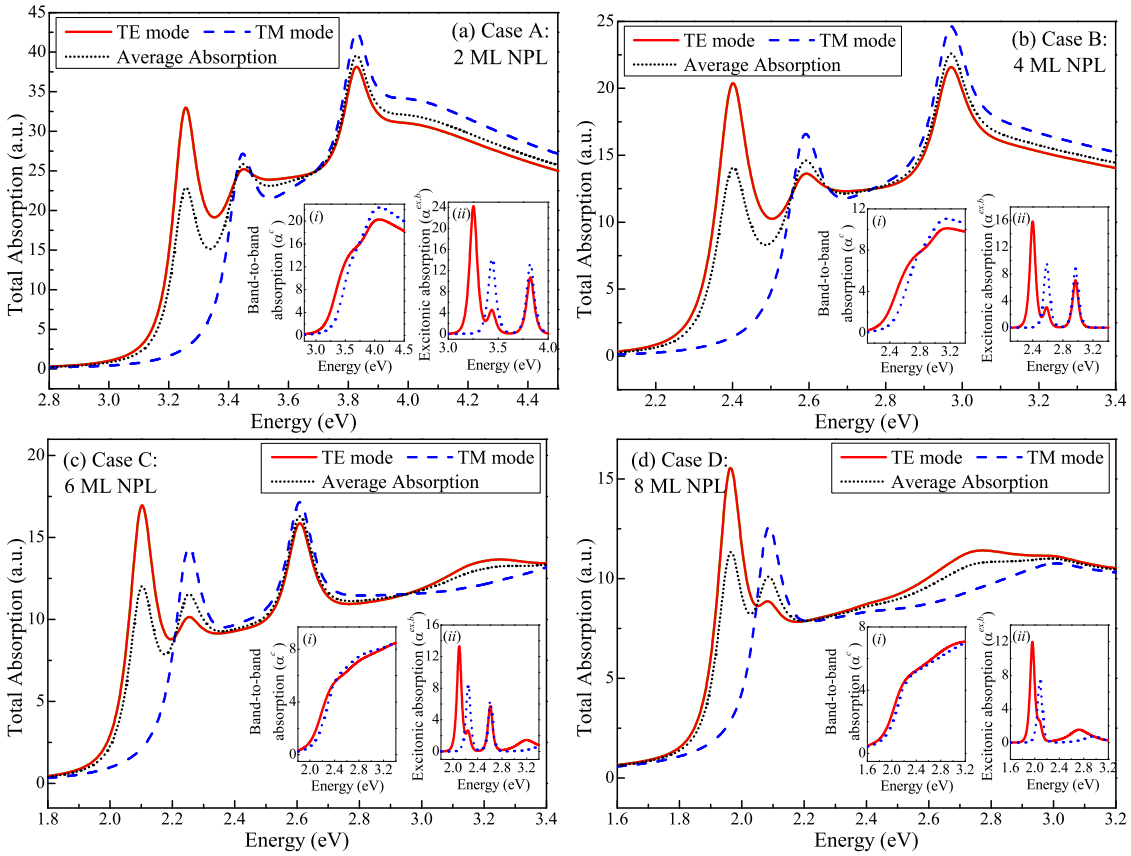

Figure 6.7: Total excitonic TE mode (red solid line), TM mode (blue dashed line) and weighted average absorption (black dotted line) in CdSe NPLs of thickness (a: *top left*) Case A: 2 ML; (b: *top right*) Case B: 4 ML; (c: *bottom left*) Case C: 6 ML; and (d: *bottom right*) Case D: 8 ML. Within each frame, the two insets are (inset: *i*) Band-to-band absorption, α^c, (inset: *ii*) Excitonic bound state absorption, $\alpha^{ex,b}$.

to HH, LH and SO hole having increasingly higher transition energies (peak positions) as tabulated in Table 6.2. A distinct SO peak is absent for 8 ML NPLs as there is no SO hole in the first five H levels, as also confirmed in Fig. 6.6. The HH, LH and SO peaks correspond to the E1–HH1, E1–LH1 and E1-SO1 transitions. Now, looking at the TME plots for these transitions, we see that in the TE mode, we have contributions from all three HH, LH and SO hole transitions; whereas in the TM mode, HH contribution is absent but LH and SO hole contribute. This observation is consistent with the optical selection rule discussed before. The weighted average absorption is determined by two-third contribution from the TE mode ($\mathcal{P}_{cv,x}$ and $\mathcal{P}_{cv,y}$) and one-third from the TM mode ($\mathcal{P}_{cv,z}$).

Table 6.2: Absorption peak positions for the heavy-hole, light-hole and split-off-hole transitions in 2, 4, 6 and 8 ML CdSe NPLs in Fig. 6.7.

Peak	2 ML	4 ML	6 ML	8 ML
Heavy-hole	3.26 eV	2.40 eV	2.10 eV	1.96 eV
Light-hole	3.45 eV	2.59 eV	2.25 eV	2.09 eV
Split-off-hole	3.83 eV	2.97 eV	2.61 eV	–

Table 6.3: Absorption peak intensities (a.u.) for the heavy-hole, light-hole and split-off-hole transitions in 2, 4, 6 and 8 ML CdSe NPLs in Fig. 6.7.

Peak	2 ML	4 ML	6 ML	8 ML
TE Heavy-hole	32.99	20.38	16.96	15.56
TE Light-hole	25.22	13.63	10.14	8.86
TE Split-off-hole	38.14	21.58	15.87	–
TM Light-hole	27.17	16.59	14.37	12.62
TM Split-off-hole	42.52	24.60	17.15	–

The intensity of absorption, as tabulated in Table 6.3 rises as the NPL thickness falls. This can be mathematically understood by following Eq. 2.63. The term d in the denominator is the NPL thickness to which the absorption is inversely proportional. Alternately, this can also be understood by studying the DOS of our four NPL cases, as shown in Fig. 6.8. Three distinct observations follow: (*i*) At any given energy, the CB DOS is higher for thinner NPLs, (*ii*) The inter subband energy spacings are higher for thinner NPLs, and (*iii*) In a given energy span, thicker NPLs have more frequent subband steps. The NPL absorption does indeed follow the DOS series of steps and is higher for thinner NPLs. Also for an NPL of given thickness, it increases with photon energy. But the sets of peaks in the spectra, which are in fact quite strong and particularly significant near the effective bandgap can not be explained or predicted by the 'non-excitonic' model. To understand this, the notion of excitons is necessary, where the electron and hole are in close proximity due to Coulombic attraction. The right treatment is to consider the creation of an electron-hole pair (exciton) instead of considering the vertical transition of an electron from a VB state to a CB state. This results in the excitonic bound state absorption ($\alpha^{ex,b}$) component as shown in the insets of the frames in Fig. 6.7. The photon absorption creating the excitons is what we see clearly as distinct $\alpha^{ex,b}$ peaks. The entire absorption spectrum of NPLs can in fact be properly described in terms of these excitonic states. Moreover, absorption above the effective bandgap energy creates unbound excitonic states, while absorption below the effective bandgap creates bound excitonic states [115]. The electron and hole are bound

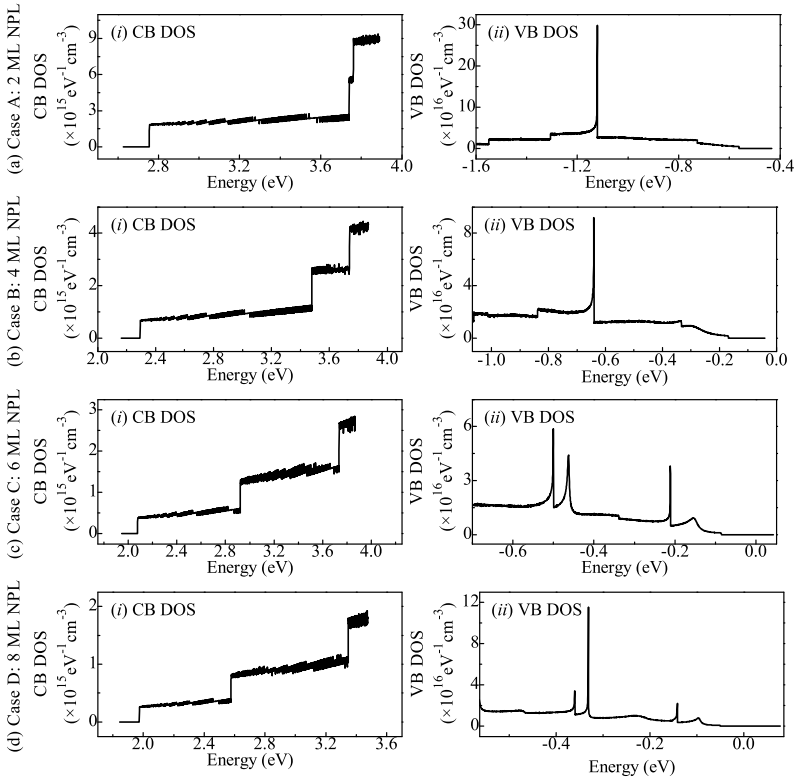

Figure 6.8: The density-of-states (DOS) of the CB and VB in CdSe NPLs of thickness (a: *top*) Case A: 2 ML; (b: *middle*) Case B: 4 ML; (c: *middle*) Case C: 6 ML; and (d: *bottom*) Case D: 8 ML.

very closely to each other in an exciton, thus the wavefunction in fact peaks at zero relative displacement. Hence the probability of finding them at the same place is very large, and thereby the resulting $\alpha^{ex,b}$ absorption peak intensity is relatively much stronger.

The other component is the band-to-band absorption (α^{c}). For many direct bandgap semiconductors, excitonic effects are distinct at low temperature. However, at RT, although they still significantly affect the linewidth and intensity of the absorption spectra, the peaks in the final spectra corresponding to the α^{c} absorption are difficult to resolve. This is because these states get rapidly ionized by collisions with optical phonons at RT. This broadens the associated linewidth to such an extent which is no longer distinctly resolvable.

Contributions from both $\alpha^{ex,b}$ and α^{c} result in the overall absorption spectra. It is noteworthy that the entire spectra is in fact excitonic, but absorption at the $\alpha^{ex,b}$ peaks creates excitons, while absorption at other energies do not, and are band-to-band. Incidentally, the two main peaks near the bandgap energy are the $\alpha^{ex,b}$ peaks associated with the HH1 to

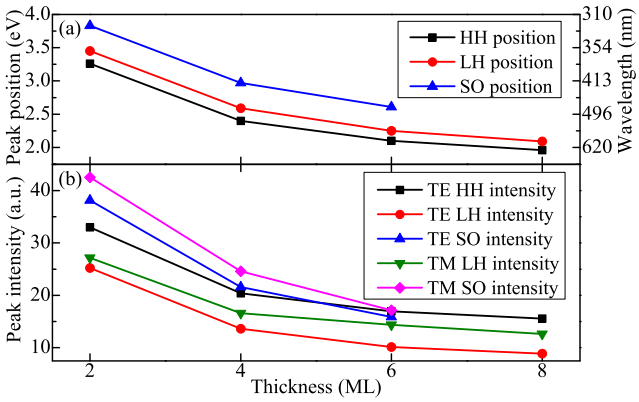

Figure 6.9: (a: *top*) Peak absorption position/wavelength for the HH, LH and SO peaks and (b: *bottom*) Peak intensity for the TE/TM mode HH and LH peaks and TE mode SO peak vs. the thickness of the CdSe NPLs.

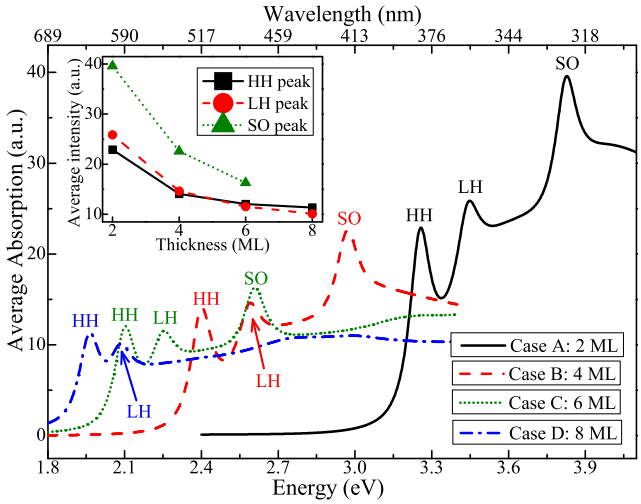

Figure 6.10: Comparison of the average absorption of the 2, 4, 6 and 8 ML CdSe NPLs. The HH, LH and SO peaks for all the cases are marked. The 8 ML NPL doesn't have a distinct SO peak. The *inset* shows a comparison of the average absorption intensity for HH, LH and SO peaks.

E1 transition and with the LH1 to E1 transition. Typically the HH1 to E1 transition has the stronger peak at lower photon energy, while the LH1 to E1 transition has the weaker peak at a higher photon energy [29, 115].

But in our study of sub-nm (2 ML) NPLs we see the emergence of anomalous absorption spectral properties characterized by increased average absorption intensity at the LH peak and inversion of HH and LH relative peak intensities. This has been experimentally verified in one of our recent works [155]. The individual HH, LH and SO peak positions and

intensities for all our NPL cases in TE and TM mode, from Table 6.2 and 6.3 are shown in Fig. 6.9, and their average absorption spectra juxtaposed in Fig. 6.10. Inset in Fig. 6.10 shows the relative average peak intensities between HH, LH and SO hole transitions, as we can see the HH and LH crossover wherein for 2 ML NPLs, the relative LH peak is stronger than the HH peak. The 2 ML NPLs are different from thicker NPLs in terms of the higher quantum confinement. This manifests into two important differences: (*i*) in the 3D space the electron and hole are even closely packed, so the creation of such an exciton results in an even higher absorption strength; and (*ii*) the large exciton binding energy due to the electron and hole being very closely packed results it to orbit faster, more so for the lighter LH excitons than heavier HH excitons. Consequently, the absorption for LH1 for E1 transition is larger than that for HH1 to E1 transitions in sub-nm 2 ML NPLs, resulting in the LH excitonic peaks getting stronger than the HH excitonic peaks. Now if we shine a laser beam on the NPL to generate a significant population of charge carriers, absorption occurring directly at the $\alpha^{ex,b}$ peaks will generate excitons (of the concerned hole type), whereas absorbing occurring at other higher photon energies will generate free band-to-band carriers.

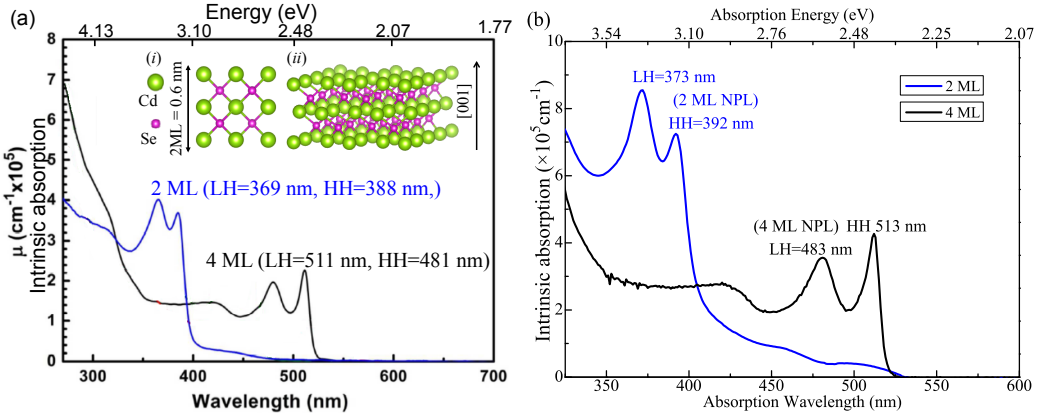

Figure 6.11: Comparison of experimental absorption spectra measured by (a: *left*) Achtstein *et al.* [31] [Reprinted (adapted) with permission from *J. Phys. Chem. C* **119** (34), 20156. Copyright (2015) American Chemical Society.], and (b: *right*) our group for 2 ML and 4 ML CdSe NPLs. For 2 ML NPLs, the as-measured LH peak is stronger than the HH peak in both cases, consistent with our theoretical findings. The LH and HH peak positions are marked for both cases, which can be compared to theoretically calculated values in Table 6.2. In frame (a), *insets* (*i*) and (*ii*) show the building block and schematic of a typical ($n = 2$) ML CdSe NPL, as an example, grown along the [001] direction, which has $n + 1$ layers of Cd and n layers of Se, and therefore sometimes it is referred to as n.5 ML NPL. [31]

Finally, we have experimentally verified our theoretical findings by measuring the absorption spectra of 2 ML and 4 ML CdSe NPLs. We have also compared our measurements with that of Achtstein *et al.* [31] for the sake of validation. Fig. 6.11 (a) shows the absorption spectra of 2 and 4 ML CdSe NPLs as reported by Achtstein *et al.* [reprinted (adapted) with permission from Ref. 31], while Fig. 6.11 (b) shows our measurements also for 2 and 4 ML CdSe NPLs. Insets in Fig. 6.11 (a) show the building block and schematic of a typical sub-nm ($n = 2$) ML CdSe NPL, as an example, grown along the [001] direction, which has $n + 1$ layers of Cd and n layers of Se, and therefore sometimes it is referred to as n.5 ML NPL. Indeed, as shown in frames (a) and (b) of Fig. 6.11, for 2 ML NPLs, the as-measured LH peak is stronger than the HH peak in both cases, consistent with our theoretical findings.

6.4 Summary and Conclusion

We have performed a comprehensive study of the electronic bandstructure (energy dispersion relation), probabilities of conduction and valence band-mixing due to coupling, charge densities (squared wavefunctions), relative band lineups and polarization dependent optical absorption spectra dependent on the transition matrix elements (TME) plus the density of states (DOS) for quasi two-dimensional CdSe NPLs of different thicknesses in the ZB phase. The electronic bandstructure was studied using the Kane's 8-band $\boldsymbol{k}\cdot\boldsymbol{p}$ model Hamiltonian for ZB semiconductor, containing both kinetic terms and strain terms. The optical absorption spectra was calculated considering excitonic effects as a sum of the contributions from continuum band-to-band states absorption with Sommerfeld enhancement and bound excitonic states absorption. The absorption spectra of NPLs has a well recognized trend with a higher intensity electron/heavy-hole (HH) absorption peak and a blue-shifted lower intensity electron/light-hole (LH) absorption peak. However, we have experimentally observed anomalous absorption spectral properties in ultrathin sub-nm (2 monolayer) CdSe NPLs characterized by increased intrinsic absorption and inverted HH and LH relative peak intensities. This was found to be consistent with our theoretical findings, wherein the emergence of such properties has been discussed in detail in light of the polarization dependent TMEs and the DOS, both of which fundamentally affect the absorption spectra, determined by the HH and LH excitons.

Chapter 7

Inverted CdS/CdSe Nanoplatelets: Quantum Ring

7.1 Introduction

VARIOUS optoelectronic characteristics of core-only NPLs – either CdSe, CdS or Cd(S,Se) alloys have so far been studied and discussed in Chapters 3, 4, 5 and 6. In this chapter, we will discuss about a core/crown topology forming a heterostructure, which essentially is two semiconductor materials grown conjointly [156]. Heterostructure quantum rings (QRs) are a very recently developed class of nanocrystals in which a traditionally used active material of lower bandgap is laterally grown around a traditionally used barrier material of higher bandgap. A typical example is the inverted Type-I CdS/CdSe core/crown colloidal QR [32,33]. This is a topological inversion of the popularly studied CdSe/CdS NPLs, which has a traditional Type-I structure of low band gap CdSe core, and high bandgap CdS crown [34]. QRs have extended emission window, which originates from the excitonic recombinations in the CdSe QR crown, as expected from the band alignment [32]. Owing to the non-trivial topology of semiconductor QRs, they exhibit interesting optoelectronic properties. They have high optical tunability and their emission characteristics can be spectrally tuned by varying the extent of lateral confinement. They exhibit high charge injection efficiency and enhanced absorption range [36]. QRs find application as phosphors for color conversion in white light LEDs, charge separator for solar cells and for light harvesting, LEDs, etc. To understand the physics of QRs for such applications, it is important to study how-and-why its optoelectronic properties can be tailored by varying the QR di-

mensions and ring size. In this chapter, we study the electronic structure along with strain profile and charge density, plus the optical gain characteristics for QRs of varying core and crown widths.

7.2 Theoretical Framework

We have studied inverted type-I core/crown CdS/CdSe QRs of 5 monolayer (ML) thickness in the zincblende (ZB) phase for varying core and crown sizes (i.e. ring widths), assuming that they are colloidally synthesized [32, 35, 36]. The dielectric ligand environment in the colloidal solution passivates the surface electronic states, where the QRs exist in a free-standing form. Fig. 7.1 (a) shows the 3D atom-by-atom view of a typical QR. It is an example showing 3 ML CdS core and CdSe crown forming a rectangular Type-I core/crown CdS/CdSe QR. Fig. 7.1 (b) shows the schematic of a typical QR of dimensions $a \times b \times t$. The width of the CdSe crown (ring) is d.

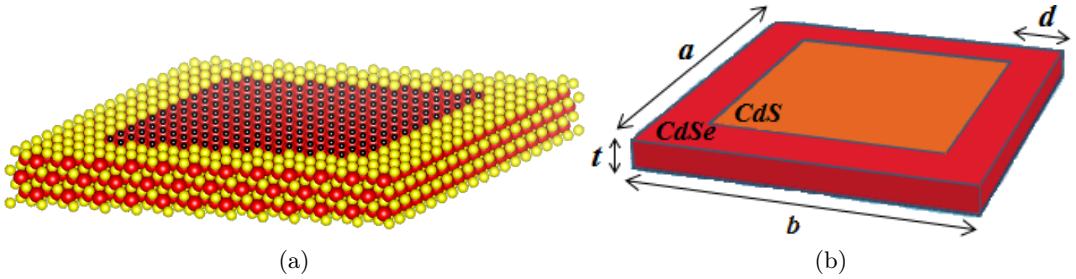

(a) (b)

Figure 7.1: (a: *left*) A 3D atom-by-atom view of a typical QR (*example*: 3 ML CdS/CdSe QR – of CdS core and CdSe crown). Red spheres are Cd atoms, yellow Se atoms and dark blue S atoms; and (b: *right*) Schematic of a typical inverted Type-I core/crown CdS/CdSe quantum ring of dimensions $a \times b \times t$ and crown width d.

For each inverted type-I core/crown CdS/CdSe QR case studied, we have used an effective mass envelope function theory approach based on the 8-band $\boldsymbol{k \cdot p}$ method using the first basis type described in Sec. 2.3.1, which simultaneously takes into account the nonparabolicity of the coupled conduction band (CB) and valence band (VB) including the orbit-splitting bands to solve its eigenenergy and obtain its electronic structure at the Γ-point. The 8-band Hamiltonian is represented in the Bloch function basis as detailed in Eq. 2.8. The excitonic optical gain spectra of the QRs are calculated using the methods described for Eqs. (2.59) and (2.60) in Sec. 2.5.2.

7.3 Results and Discussions

7.3.1 Strain Profile and Electronic Bandstructure

The lateral size, core width and crown (ring) width of the inverted type-I core/crown CdS/CdSe QRs are varied to investigate their influence on the strain profile, TMEs, charge densities and electronic bandstructure. Here we have considered only 5 ML thick square QRs i.e. $a = b$ for the convenience of study and understanding.

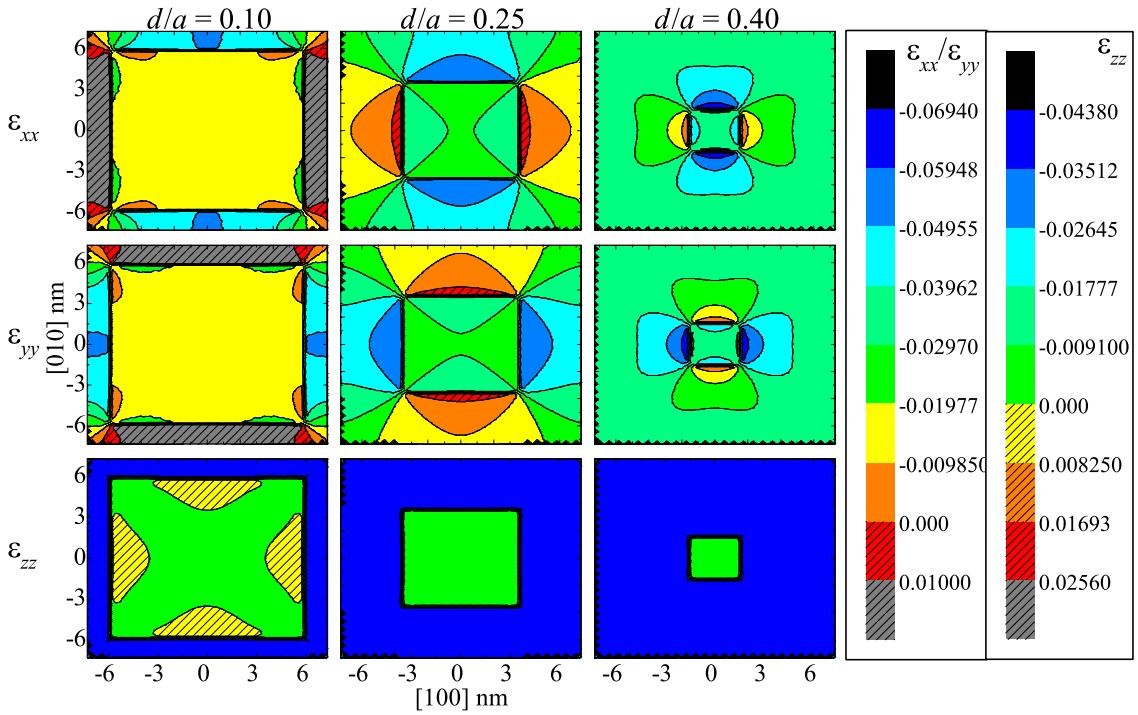

Figure 7.2: Strain profile distribution (ε_{xx}, ε_{yy}, ε_{zz}) in the (001) plane of the inverted type-I CdS/CdSe QRs of lateral size 15 nm, and thickness 5 ML, with varying crown width : QR width (d/a) of 0.10, 0.25 and 0.40. The (001) x-y plane is cut horizontally along the center ($z = 0$). Warmer colors (reddish) with shading represent tensile strain, while cooler colors (greenish/bluish) without shading represent compressive strain. Strain component and (d/a) ratios are indicated. Color chart shows strain values.

Fig. 7.2 shows the strain profile distribution (ε_{xx}, ε_{yy}, ε_{zz}) in the (001) plane of the CdS/CdSe QRs of lateral size 15 nm, and thickness 5 ML, with varying crown width : QR width (d/a) of 0.10, 0.25 and 0.40. The (001) x-y plane is cut horizontally along the center ($z = 0$). Each row shows a particular strain component: ε_{xx} in row 1, ε_{yy} in row 2 and ε_{zz}

in row 3; while each column stands for a particular (d/a) ratio: 0.10, 0.25 and 0.40. The strain components and the (d/a) ratios are indicated. Color chart shows strain values.

Warmer colors (reddish) with shading represent tensile strain, while cooler colors (greenish/bluish) without shading represent compressive strain. For both ε_{xx} and ε_{yy} there is compressive strain within the CdS core, which increases for thicker crowns (rings) as the (d/a) ratio rises. At the core/crown boundary there is an abrupt change in the strain profile. For ε_{xx}, as we move from the core to the crown, the strain type changes to tensile along the [100] direction, while along the [010] direction the extent of compressive strain increases. The magnitude of tensile (compressive) strain along the [100] ([010]) direction at the core/crown boundary also depends on the (d/a) ratio. It is higher for thinner crowns (rings) and falls as the crown (ring) width increases.

The ε_{xx} and ε_{yy} can be easily correlated as ε_{xx} along [010] is identical to ε_{yy} along [100]; and ε_{yy} in the [010] direction is identical to ε_{xx} in the [100] direction. Therefore, for ε_{yy}, as we move from the core to the crown, the strain type changes to tensile along the [010] direction, while along the [100] direction the extent of compressive strain increases. The dependency of the strain magnitude on the (d/a) ratio is similar to that of ε_{xx}.

For ε_{zz}, the strain pattern is predominantly compressive, and comparatively higher in the crown (ring) compared to the core. However for QRs with thinner crown (ring), there is marginal tensile strain within the core. The calculation of strain profile is important as it affects the Hamiltonian matrix [Eq. (2.8)] and thus the energy dispersion characteristics and electronic bandstructure.

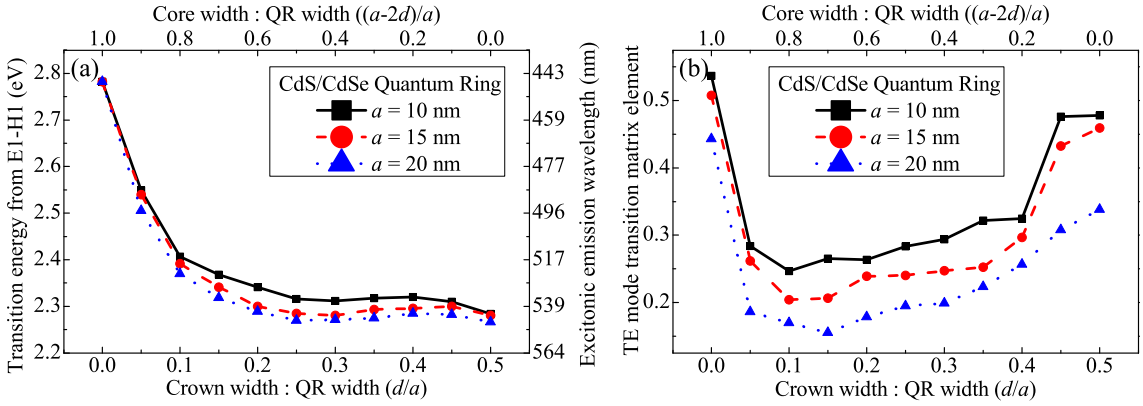

Figure 7.3: (a: *left*) E1–H1 excitonic transition energy (photon emission wavelength), and (b: *right*) Transverse electric (TE) mode transition matrix element (TME) vs. crown width : QR width (d/a).

Now, in Fig. 7.3 (a) we show the excitonic transition energy (and emission wavelength) between the bottom of the conduction band (E1) to the top of the valence band (H1) i.e. E1–H1 for varying QR lateral size (a) and crown width : QR width (d/a), for 5 ML thick QRs. For any QR having a given lateral size, as the (d/a) ratio rises from 0 to 0.5, the emission energy falls from 2.78 eV to 2.28 eV, since the QR transforms from pure CdS NPL ($d/a = 0$) to pure CdSe NPL ($d/a = 0.5$). A higher (d/a) ratio means that the QR has a higher fraction of CdSe over CdS – the former having a lower bandgap compared to the latter, and hence the pattern. However, the transition energy pattern is not truly monotonic, but has a concavity due to the influence of optical bowing coefficient of CdS_xSe_{1-x} = 0.28 eV, [153] which induces the minima to occur for an intermediate composition ergo an intermediate (d/a) ratio.

With an increase in the QR lateral size, there is a red-shift in the transition energy. However, when the QR transforms into pure CdS ($d/a = 0$) or pure CdSe ($d/a = 0.5$) NPL, the significance of lateral size (a) diminishes and the emission energy is almost identical for 10, 15 and 20 nm as expected, since the thickness for these three cases are the same, which is the primary determinant of the NPL emission energy. But for intermediate (d/a) ratios, as the QR crown grows, its influence comes into picture and the Δ(E1–H1) between $a = 10, 15, 20$ nm increases up to a point when the core is about half the QR width and decreases thereafter.

Fig. 7.3 (b) shows the TE mode transition matrix element (TME) of the E1–H1 transitions, for the QR cases studied in Fig. 7.3 (a). For QRs that have transformed into pure CdS NPL ($d/a = 0$) or pure CdSe NPL ($d/a = 0.5$), the TME values are higher as both the electron and hole wavefunction are localized within the single material without any leakage. However for CdS/CdSe QR heterostructures, the TMEs diminish and is dependent on the extent of overlap between electron- and hole-wavefunctions, that are mainly localized in the CdSe crown but also leaks into the CdS core. This can be seen from Fig. 7.4 which shows the spatial charge densities of the first ten electron and hole states for CdS/CdSe QRs of lateral size 15 nm, and thickness 5 ML, with varying crown width : QR width (d/a) of 0.10, 0.25 and 0.40. These are the three cases that were studied in Fig. 7.2 also. For a sufficiently low (d/a) ratio, such as 0.10 the extent of electron- and hole-wavefunctions overlap is limited, as can be seen from the E1 (1^{st} conduction electron level) and H1 (1^{st} valence hole level) charge density distribution in Fig. 7.4 (a) – this limits the TME. As the (d/a) ratio increases, the CdSe crown becomes larger and the spatial electron-hole wavefunctions overlap also increases [compare E1 and H1 of frame (a) with frame (b) and (c)

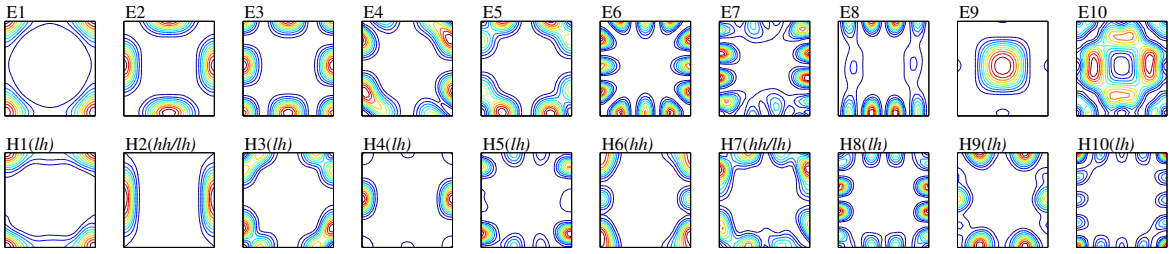

(a) For $d/a = 0.10$, charge density of CdS/CdS QR of lateral size 15 nm and thickness 5 ML.

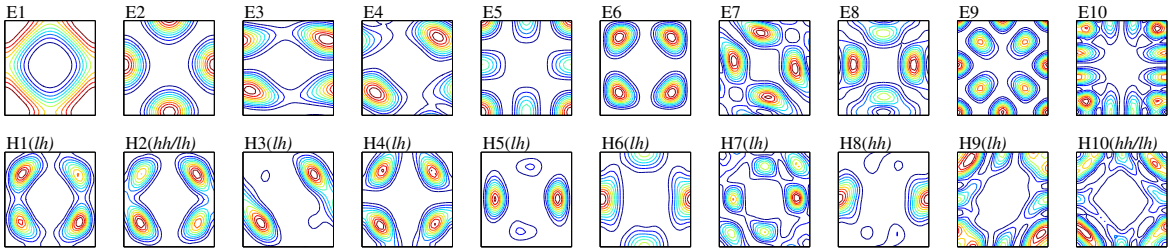

(b) For $d/a = 0.25$, charge density of CdS/CdS QR of lateral size 15 nm and thickness 5 ML.

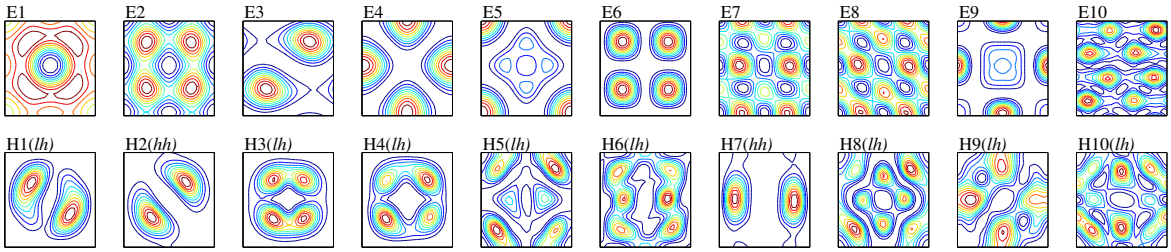

(c) For $d/a = 0.40$, charge density of CdS/CdS QR of lateral size 15 nm and thickness 5 ML.

Figure 7.4: Spatial charge density distributions of the first ten conduction (E) and valence (H) states of inverted type-I CdS/CdSe QR of lateral size 15 nm and thickness 5 ML, with varying crown width : QR width of (a: *top*) $d/a = 0.10$, (b: *middle*) $d/a = 0.25$ and (c: *bottom*) $d/a = 0.40$. Charge densities are shown in the (001) x-y plane cut horizontally along the center ($z = 0$). Hole-types (hh for heavy hole and lh for light hole) for every H state are mentioned from the band-mixing probabilities shown in Fig. 7.5.

in Fig. 7.4]. This results in the gradual increase in the TME with increasing (d/a). For a given (d/a), however, the TME is higher for QRs with lower lateral size as the electron- and hole-wavefunctions are more compactly packed enabling a greater overlap.

The spatial charge densities shown in Fig. 7.4 are in the x-y plane at $z = 0$. For most cases, the electron and hole wavefunctions are localized in the CdSe crown, more so for QRs with thinner crowns. As the crown (ring) width increases, the wavefunction distribution spreads and leaks into the CdS core gradually. The study of the first ten electron and hole state spatial charge densities is to be done in tandem with the electronic bandstructure and

the probability in band-mixing between the conduction electrons and valence heavy-, light- and split off-holes due to coupling effect, as shown in Fig. 7.5.

For the 15 nm CdS/CdSe QR with ($d/a = 0.10$), both E1 and H1 are s-like. E2 is p-like, while E3 has s-p-mixing. E4 and E5 have p-d-mixing, while E6 and E7 have minute amount of heavy-hole (hh) contributions, as inferred from Fig. 7.5. Most H states are light-hole (lh) dominated, with H2 (53% lh, 45% hh) and H7 (52% lh, 46% hh) having contributions from both hh and lh, while H6 is hh dominated.

The pattern of the first few E states of the 15 nm CdS/CdSe QR with ($d/a = 0.25$) is similar to that with ($d/a = 0.10$) – E1 being s-like, E2 p-like, E3 having s-p-mixing, and so on. Most of the H states are again lh dominated, with H2 (48% lh, 50% hh) and H10 (47% lh, 51% hh) having contributions from both hh and lh, while H8 is hh dominated, as can be inferred from Fig. 7.5.

Finally, for the 15 nm CdS/CdSe QR with ($d/a = 0.40$), the E1 state is s-like, while the E2 has s-p-mixing. Most of the H states are again lh dominated, with H2 (29% lh, 69% hh) and H7 (32% lh, 67% hh) being hh dominated, as can be inferred from Fig. 7.5. In most cases, the higher E and H states have complex s-p-d-mixing.

In Fig. 7.5, we show the electronic bandstructure and the band-mixing probabilities between the conduction electrons and valence hh, lh, and split-off (so) holes due to coupling effect for varying QR lateral width (a) and varying crown width : QR width (d/a) ratio. The QR lateral widths are varying row-wise between 10, 15 and 20 nm; while the (d/a) ratios are varying column-wise between 0.40, 0.25 and 0.10. The E1–H1 fundamental transition energy is indicated for each case, as the red dots indicate the band energies. The band-mixing probabilities are indicated using color shaded bars with legends.

The E1–H1 transition energy for each case is in accordance with the values plotted in Fig. 7.3 (a). For a fixed (d/a) ratio, as the size of the QR increases, the transition energy falls because of reduced quantum confinement experienced by the QR. From 10 to 15 nm, and 15 to 20 nm, the reduction is ∼200 meV, for all cases. However, for QRs having the same size, as the (d/a) ratio changes the transition energy pattern is as shown and discussed in Fig. 7.3 (a). At a broader scale, as the (d/a) rises, the transition energy decreases, since the fraction of CdSe in the QR system increase while the fraction of CdS decreases – and CdSe has a lower bandgap compared to CdS. However, at the three (d/a) values of 0.40, 0.25 and 0.10 we study, the characteristics has further intricacies. The transition energy pattern is not truly monotonic in the entire range, but has a concavity due to the influence of optical bowing coefficient of CdS_xSe_{1-x} = 0.28 eV, [153] [see Fig. 7.3 (a)], which induces

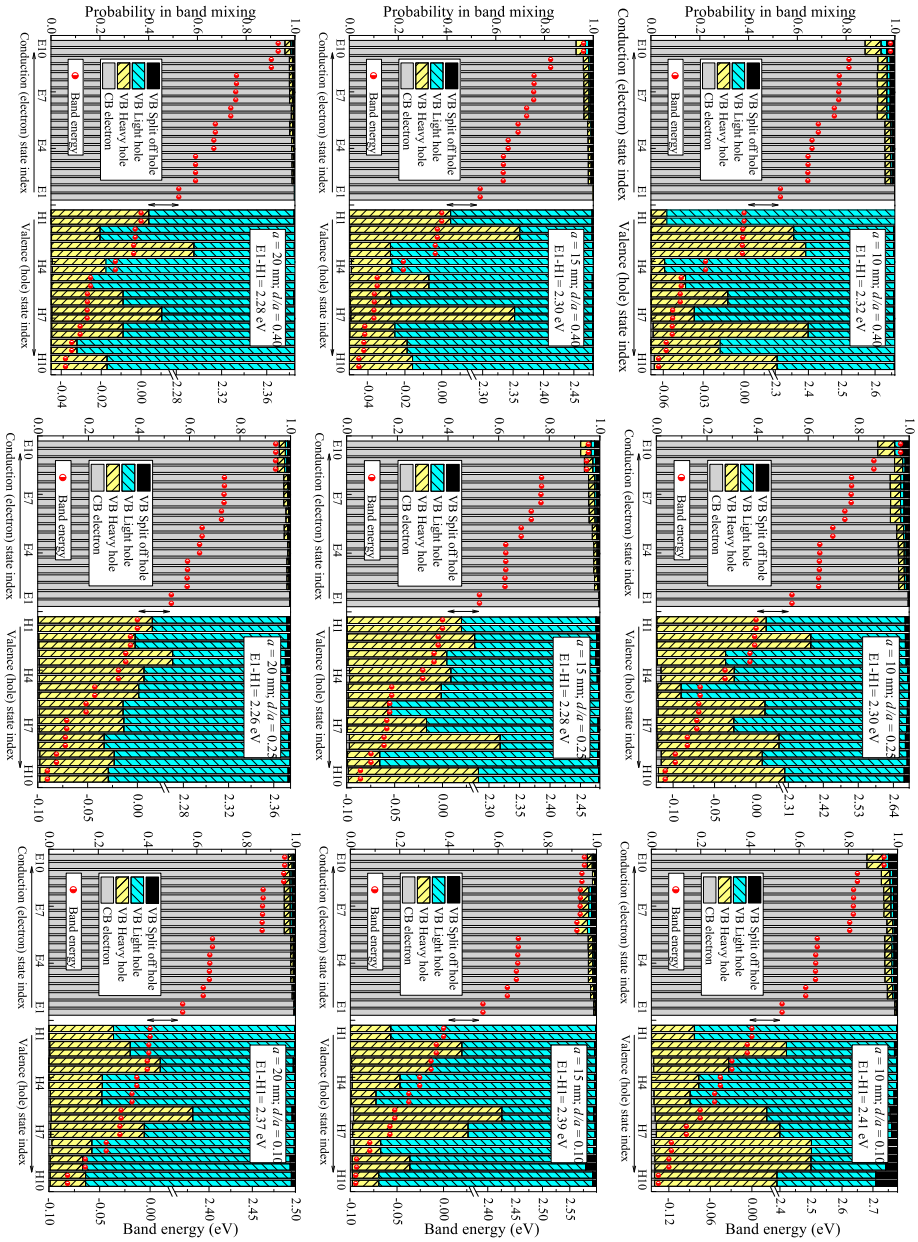

Figure 7.5: Electronic bandstructure and the probability in band-mixing between conduction electrons and valence heavy holes, light holes and split off holes due to coupling for 5 ML inverted type-I CdS/CdSe core/crown QRs of lateral size (a) = 10, 15 and 20 nm (varying row-wise); and crown width : QR width (d/a) = 0.40, 0.25 and 0.10 (varying column-wise). Red dots indicate the band energies, while the color bars show the band-mixing probability. Segments with double arrows represent E1-H1 energy gap.

the minima to occur for an intermediate intermediate (d/a) ratio. The fraction x relates to (d/a) as $x = [1 - 2\,(d/a)]^2$. We observe that among our three cases, for $(d/a) = 0.25$, we obtain the least transition energy. As the (d/a) falls to 0.10, the transition energy rises by ∼1100 meV, while as the (d/a) rises to 0.40, the transition energy rises by only ∼200 meV. This follows from the (d/a) dependent transition energy pattern where the differential transition energy variations are higher for lower values of (d/a).

Furthermore, we study the span of the first 10 E and H states from Fig. 7.5. For any given QR width, as the (d/a) ratio falls, the span of the first 10 E and H states i.e. ΔE_{1-10} and ΔH_{1-10} spreads out. For instance, considering $a = 10$ nm, ΔE_{1-10} increases from 329 to 334 to 340 meV; and ΔH_{1-10} increases from 63 to 109 to 135 meV, as we move from $(d/a) = 0.40$ to 0.25 to 0.10. This is owing to the higher effective hole mass of CdS (0.981) compared to CdSe (0.62); and higher effective electron mass of CdS (0.25) compared to CdSe (0.12), following from the dispersion curve concavity relation $m^* = \hbar^2 \left(\frac{\partial^2 E}{\partial k^2}\right)^{-1}$. As the (d/a) ratio falls, the QR is occupied with higher CdS fraction, which induces such an effect. This effect reduces for QRs of larger size.

In Fig. 7.5, we have also shown the band-mixing probabilities, that are empirically determined for any QR and depends on the varying extent of coupling between the CB electrons and VB *hh*, *lh* and *so* holes. The reported band-mixing probabilities for each state directly relates to the aggregate electron and hole wavefunction and associated charge densities. For most E states, the primary contributions are from electrons with minor *hh*/*lh*/*so* contributions. But for H states, there are comparable contributions form *hh* and *lh*. For each H state shown in Fig. 7.4, the single most major contributor as identified from Fig. 7.5 is mentioned, and for particular cases both *hh* and *lh* are mentioned for comparable contributions.

7.3.2 Optical Gain Properties

In Sec. 7.3.1 we examined the strain profiles, transition energy, transition matrix element (TME), charge densities and electronic bandstructure of inverted type-I CdS/CdSe core/crown QRs. In this section we will study the optical properties of the QRs. Fig. 7.6 shows the optical gain spectra of the CdS/CdSe core/crown QRs for varying QR lateral width (a) and varying crown width : QR width (d/a) ratio. The QR lateral widths are varying row-wise between 10, 15 and 20 nm; while the (d/a) ratios are varying column-wise between 0.40, 0.25 and 0.10. This allows us to study the effect of both QR size and crown width simultaneously. For each QR case we have the gain for varying carrier density ranging from 1 to 7×10^{19} cm^{-3}. A higher carrier density translates to a higher lasing threshold current density.

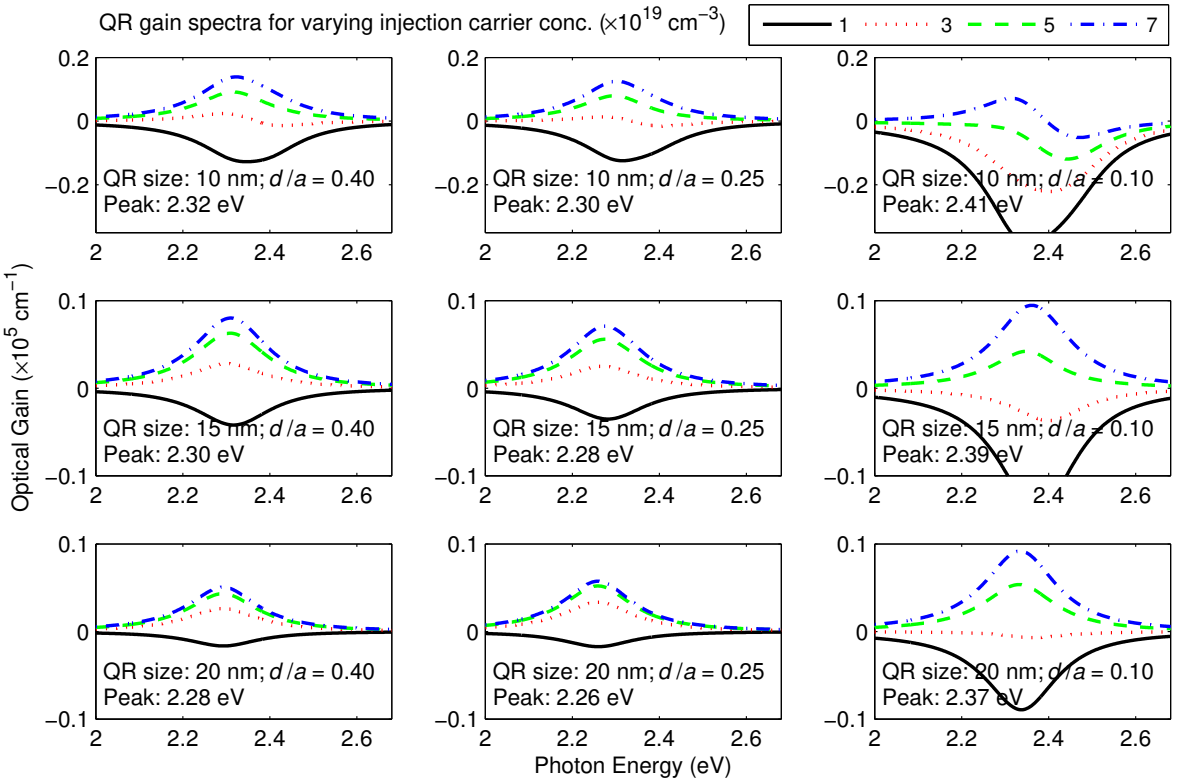

Figure 7.6: Optical gain spectra (cm^{-1}) of inverted type-I CdS/CdSe core/crown QRs of lateral size (a) = 10 nm, 15 nm and 20 nm (varying row-wise); and ring width : QR width (d/a) = 0.40, 0.25 and 0.10 (varying column-wise). For each case gain spectra for varying injection carrier concentrations of 1, 3, 5, 7 $\times10^{19}$ cm^{-3} is shown as indicated by the legends. Higher carrier concentrations impose a larger gain with a blue-shift in the peak due to band-filling effect.

The optical gain spectrum depends on several factors such as the TME (depending on E and H wavefunction overlap), carrier density, Fermi factor, QR dimensions and material, dephasing and scattering rate among others. Also, the optical gain strongly depends on the exciton binding energy. Based on the method discussed in Sec. 2.5.2, the emission peak position for each QR gain spectra is enlisted in Fig. 7.6, which relates to the E1–H1 transition results from Fig. 7.3 (a) or Fig. 7.5.

There is a red-shift in the emission wavelength with an increase in the QR size. This is because as the QR volume increases, the extent of quantum confinement reduces and the allowed energy levels come closer. Thus the E1–H1 transitions occur at lower energy. We see a reduction in peak gain energy by ∼200 meV as the QR width increases from 10 to 15 nm, and 15 to 20 nm, for all (d/a) cases. However, for QRs having the same size, the (d/a) ratio dependent peak gain energy characteristics is as discussed for Fig. 7.5. The optical bowing coefficient induced concavity in transition energy pattern results in the peak gain energy minima to occur for $(d/a) = 0.25$ and blue-shifted peaks for $(d/a) = 0.10$ and 0.40, more so for the former than the latter.

However, for any particular QR case, the optical gain increases with carrier density and there is a marginal blue-shift in the peak gain emission energy. With the injection of carriers, higher electronic states further away from the CB-bottom and VB-top start getting occupied and the subsequent transition typically occurs at a higher, blue-shifted E1–H1 energy value. This phenomenon is known as the band filling effect. This effect is more prominent in volumetrically larger QRs compared to smaller. The allowed energy states due to quantum confinement in larger QRs are much closer. So, there is a higher probability of *near*-E1–H1 transitions to occur as more carriers get injected. In smaller QRs, however, the next higher transition after E1–H1 is much further away, which does not contribute much.

Next we study the effect of carrier density on the peak maximum gain of CdS/CdSe QRs, as shown in Fig. 7.7. With an increase in the injection carrier density, the maximum gain increases since more carriers get injected, which results in increased radiative recombination. Considering the QR with width 15 nm as a case, we see that for $(d/a) = 0.40$ and 0.25, the maximum gain increment with injection carrier density has a similar gradient, while for $(d/a) = 0.10$, the rise in maximum gain is steeper, and has a comparative rapid increment. For a sufficiently high carrier density, it exceeds the maximum gain of the former cases. The crossover energy is observed to decrease with increasing QR size. For $a = 10$ nm, however, the maximum gains for $(d/a) = 0.10$ is not shown, since for our range of carrier densities (1

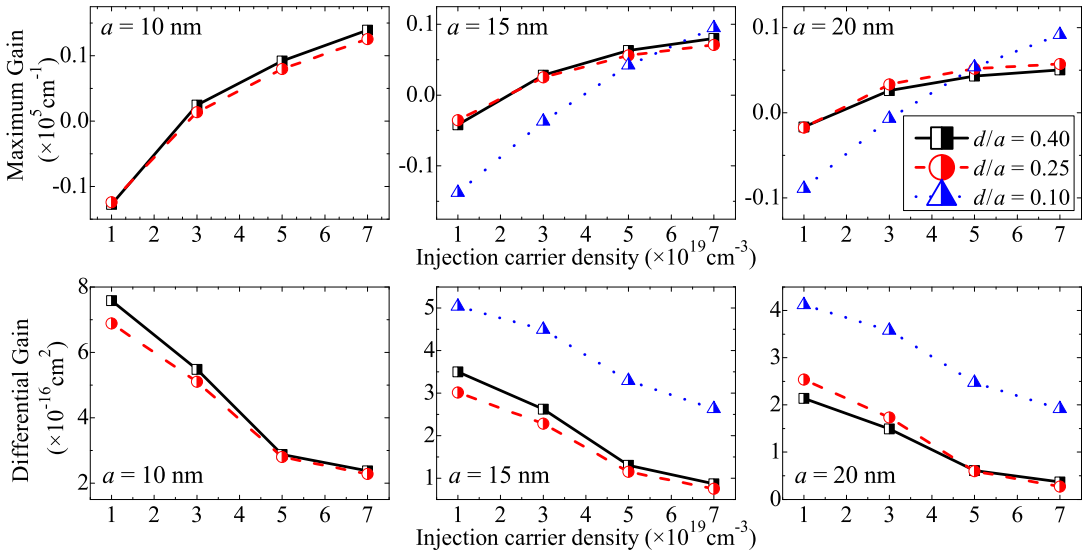

Figure 7.7: Maximum optical gain (*top row*) and differential optical gain (*bottom row*) of inverted type-I CdS/CdSe core/crown QRs as a function of varying carrier concentrations of 1 to 7 $\times$ 10^{19} cm^{-3}, varying crown width : QR width (d/a) of 0.40, 0.25 and 0.10 and varying QR sizes of 10, 15 and 20 nm. Dimensions of QRs and (d/a) ratios are indicated in each frame/in the legend.

to 7 $\times 10^{19}$ cm^{-3}), the gain spectra is still mainly in the absorption and transparency phase. Even for 7 $\times 10^{19}$ cm^{-3}, the gain spectra is not truly Lorentzian in shape, so its analysis for maximum gain has been excluded in Fig. 7.7. But for higher carrier densities is will approach Lorentzian gain spectra.

For a fixed injection carrier density, the maximum gain depends on the QR width and the (d/a) ratio. The QR width determines the QR volume. The QR thickness and QR volume inversely affect the optical gain [see Eq. (2.59) and (2.60)]. For a fixed (d/a) ratio of 0.40 and 0.25, we observed that the maximum gain falls with rise in QR size. The (d/a) = 0.10 case isn't considered once again since the gain spectra is not truly Lorentzian for a = 10 nm. Moreover, for QRs of the same size and same injection carrier density, the (d/a) ratio affects the maximum gain. As the (d/a) ratio increases, the maximum gain increases. This is because a higher (d/a) ratio implies a greater fraction of active CdSe crown in the QR, which has a higher TME [see Fig. 7.3 (b)] and higher Fermi factor.

The differential gain is yet another interesting aspect of optical properties of semiconductors. It is the measure of a laser's effectiveness to transform injected carriers to photons. A higher differential gain corresponds to a narrower spectral emission width and a greater modulation speed. [124,125] Also, a laser's resonant frequency is proportional to the square

root of the differential gain with respect to the density of carriers. [157] In Fig. 7.7 we can see how the differential gain of CdS/CdSe QRs vary with carrier density. The differential gain of QRs with $(d/a) = 0.10$ is observed to be higher than those with $(d/a) = 0.25$ or 0.40. But as the carrier density increases, the differential gain decreases for all (d/a) ratios in a similar fashion. At higher carrier densities, CdS/CdSe core/crown QRs tend to attain saturation in gain. In general, the differential gain is higher for laterally smaller QRs, and decreases as the QR width increases.

7.4 Summary and Conclusion

We have performed a comprehensive study of the strain profiles, transition energies, transition matrix elements (TMEs), spatial charge densities, electronic bandstructure, band-mixing probabilities, optical gain spectra, maximum and differential gains of type-I core/crown CdS/CdSe quantum rings (QRs) in the zincblende phase – over contrasting QR lateral size and crown width.

We observed compressive strain in the CdS core, which increases for thicker CdSe crowns. At the core/crown boundary the strain changes abruptly, the magnitude of which is higher for thinner crowns. Moreover, as the QR size increases the E1–H1 transition energy falls due to reduced quantum confinement. Also, with increasing crown width, we have a greater fraction of CdSe in the QR, and the E1–H1 transition energy falls, but non-monotonically due to the effect of bowing parameter. Furthermore, QRs transformed into pure NPLs have higher TMEs due to localized electron-hole wavefunction overlap in a single material. But for CdS/CdSe QRs, the TME increases with the CdSe crown width where most of the electron-hole wavefunctions are bound, as can be inferred from the spatial charge distributions. For QRs with thicker crowns, the wavefunctions have a greater spatial spread. In the electronic bandstructure, the energy span of the E and H states rises as the crown thickness falls, which is owing to the higher effective electron and hole mass of CdS over CdSe. In all the H states, the major contributing hole-type has been identified.

In the optical gain spectra, the peak emission position experiences a red-shift as the QR width increases owing to reduced confinement. For a given QR width, however, the peak emission position for varying crown widths are in accordance to the respective calculated transition energies. But, for a given QR case, with increasing carrier density, there is slight blue-shift due to band-filling effect, and a rise in the maximum gain and a reduction in the differential gain.

Chapter 8

GaNBiAs/GaAs Dilute Nitride-Bismide Quantum Dots

8.1 Introduction

DILUTE bismide alloys nanocrystals incorporated in GaAs host material have attracted much attention recently [37–42], as discussed for the literature review in Sec. 1.2.2. The increased interest results from its unique electronic bandstructure and potential application in optoelectronic devices in the infrared regime. Unlike dilute nitrogen alloys, for which the bandgap mainly decreases due to the coupling of nitrogen resonant state and conduction band (CB) [158], the bandgap of dilute bismide alloys is tuned by the coupling of the bismide resonant state and valence band (VB). The replacement of a small percentage of arsenic by bismuth in GaAs introduces the resonant energy levels. This resonant energy level couples with the host material's valence band and repulses each other. Therefore, in the presence of large repulsion interaction, the bandgap rapidly decreases and offers the possibility of long-wavelength operation of GaAs-based optical devices. Both bulk and GaBiAs quantum wells have attracted lot of interest recently. Some theoretical work [54, 55] has also been done since the 12-band $\boldsymbol{k}\cdot\boldsymbol{p}$ model [56–60] was proposed by O'Reilly based on the VBAC model. However, not much progress has been made on the study of GaBiAs QDs. In this chapter, the electronic bandstructure and optical gain of $GaN_xBi_yAs_{1-x-y}$/GaAs pyramidal quantum dots (QDs) are investigated using the 16-band $\boldsymbol{k}\cdot\boldsymbol{p}$ model, that has been extended from the 10-band $\boldsymbol{k}\cdot\boldsymbol{p}$ model for dilute nitrogen and the VBAC model.

8.2 Theoretical Framework

The 8-band $\boldsymbol{k}\cdot\boldsymbol{p}$ models used in Chapters 3 through 7 are suited to study binary II-VI or III-V semiconductors. But when we intend to study the effect of nitrogen and bismuth doping in the semiconductors, the 8-band Hamiltonian is not sufficient. The 8-band model is extended to construct the the 10-band $\boldsymbol{k}\cdot\boldsymbol{p}$ model used to study the nitrogen-doped QDs by introducing the local nitrogen resonant state (additional 2 bands). Similarly, to investigate the bismuth-doped and nitrogen-doped QDs simultaneously, additional bands have to be added in the model to describe and study the effects of bismuth. Unlike the s-like state introduced by dilute nitride, the dilute bismide results in p-like states, which means that six states should be considered with the spin freedom including the SO coupling which is ignored in the O'Reilly 14-band model for dilute bismide-nitride semiconductors [56]. In view of the aforementioned consideration, we have constructed a 16-band model, suited for studying GaNBiAs dilute nitride/bismide QDs. The 16-band Hamiltonian is represented in the Bloch function basis as described in Sec. 2.3.3 with all the Hamiltonian elements. The transition matrix elements are also calculated using Eq. (2.13) as discussed in Sec. 2.3.3. The optical gain spectra was calculated using methods described in Sec. 2.5.1.

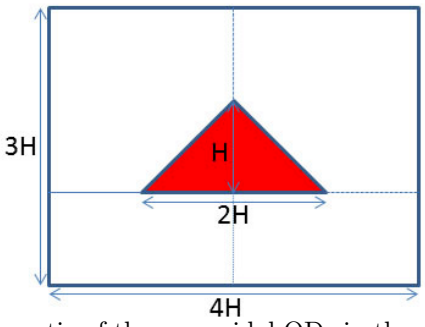

Figure 8.1: The geometry schematic of the pyramidal QDs in the side view. The height (H), width (2H) and dimensions of the system are an integer multiple of the lattice constant.

For $GaN_xBi_yAs_{1-x-y}$ /GaAs pyramidal QDs, the geometry schematic is shown in Fig. 8.1. The direction of pyramid growth is assumed to be along the positive z axis. The doped Nitrogen and Bismuth atoms are distributed in crystalline throughout the QD. A 3D view of a typical pyramidal QD with the wetting layer is shown in Fig. 8.2 (a), and Fig. 8.2 (b) shows its top view. All the calculations done and results reported in this chapter are for QDs of height 12H, except for the size effect section.

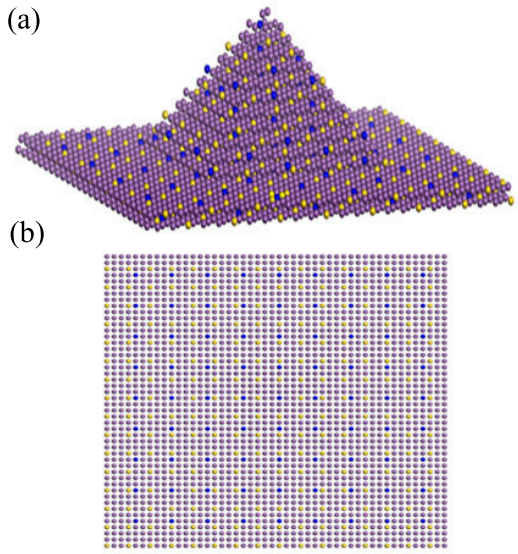

Figure 8.2: (a: *top*) 3D atom-by-atom view and (b: *bottom*) Top view of a typical pyramidal QDs structure. Here only anions are shown. The purple spheres represent the As atoms, blue spheres represent the N atoms and yellow spheres represent the Bi atoms. Impurity in the form of N and Bi are distributed uniformly.

8.3 Results and Discussion

We study the variation in the CB, VB and bandgap under different strain profile types: compressive, *near*-zero (an appropriate choice of N and Bi composition can help us minimize the strain close to but not exactly equal to zero) and tensile strain. We consider the first 6 conduction band labeled as CB1 to CB6 and the first 6 valence band as VB1 to VB6. Bands beyond this are too far to couple for practical purposes.

Taking the symmetry of x and y direction into consideration, we take the average of TMEs along the x and y directions as the transverse electric (TE) mode and TME along the z direction as transverse magnetic (TM) mode. Due to this symmetry of QD, the TE mode involves both the HH and LH states while the TM involves only LH state. Note that, the transition of optical gain is primarily due to the CB1–VB1 transition. The hole type (HH or LH) of VB1 determines the mode that gets excited. However, in reality, for our QD systems, the VB1 is mostly HH state for unstrained, compressive strain and relatively small tensile strain. Therefore we only show the results of TE mode in our optical transition calculation. All the calculations done and results reported in this chapter are for QDs of height 12H, except for the size effect section. Material parameters for GaAs and VC, BAC

and VBAC parameters for N and Bi effect are from Tables A.2 and A.3 in Appendix A.

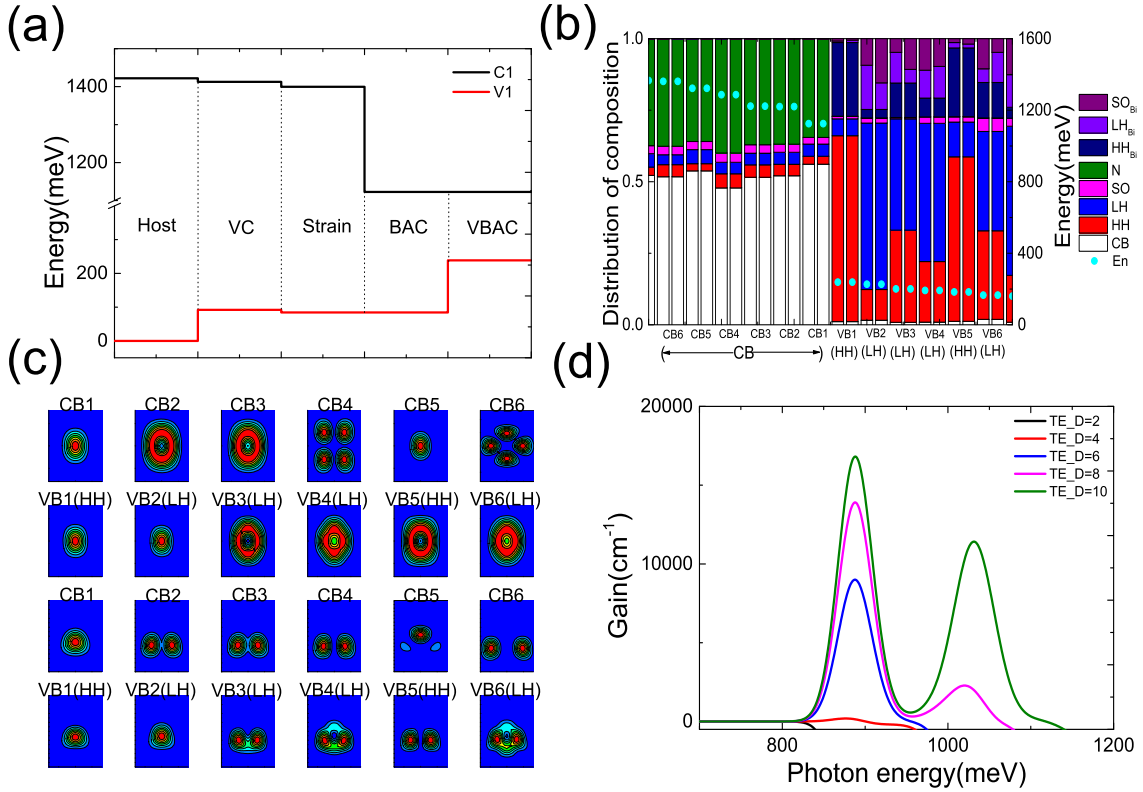

Figure 8.3: For $GaN_{0.064}Bi_{0.064}As_{0.872}$/GaAs QDs, $\epsilon_{xx} = +0.005$: (a) The schematic illustration of the VC, strain, BAC and VBAC. Here we show their independent influences. (b) The band mixing probabilities and the energy bandstructure profile. (c) The charge densities (square of the wavefunction) of the lowest 6 CBs and highest 6 VBs. The first two rows are in the x–y plane and the second two rows are in y–z plane. (d) The optical gain under four different carrier densities in the order of 10^{18}cm^{-3}.

Figs. 8.3, 8.4 and 8.5 shows three cases of $GaN_xBi_yAs_{1-x-y}$/GaAs pyramidal QDs undergoing positive, *near*-zero and negative strain (i.e tensile, near-zero and compressive strain). For each case, we have studied the four contributing factors to bandedge characteristics – VC, strain, BAC and VBAC. BAC is induced from doped Nitrogen and VBAC is induced from doped Bismuth. A stronger BAC lowers the CB1 level further, while a stronger VBAC elevates the VB1 level even further. Under the influence of BAC and VBAC, the bandgap decreases rapidly. The other two factors: VC and strain also change the bandedge characteristics. For VC, from the theoretical model, we have $\delta E_{VC}^{HH} = \kappa_N x + \kappa_{Bi} y$ and

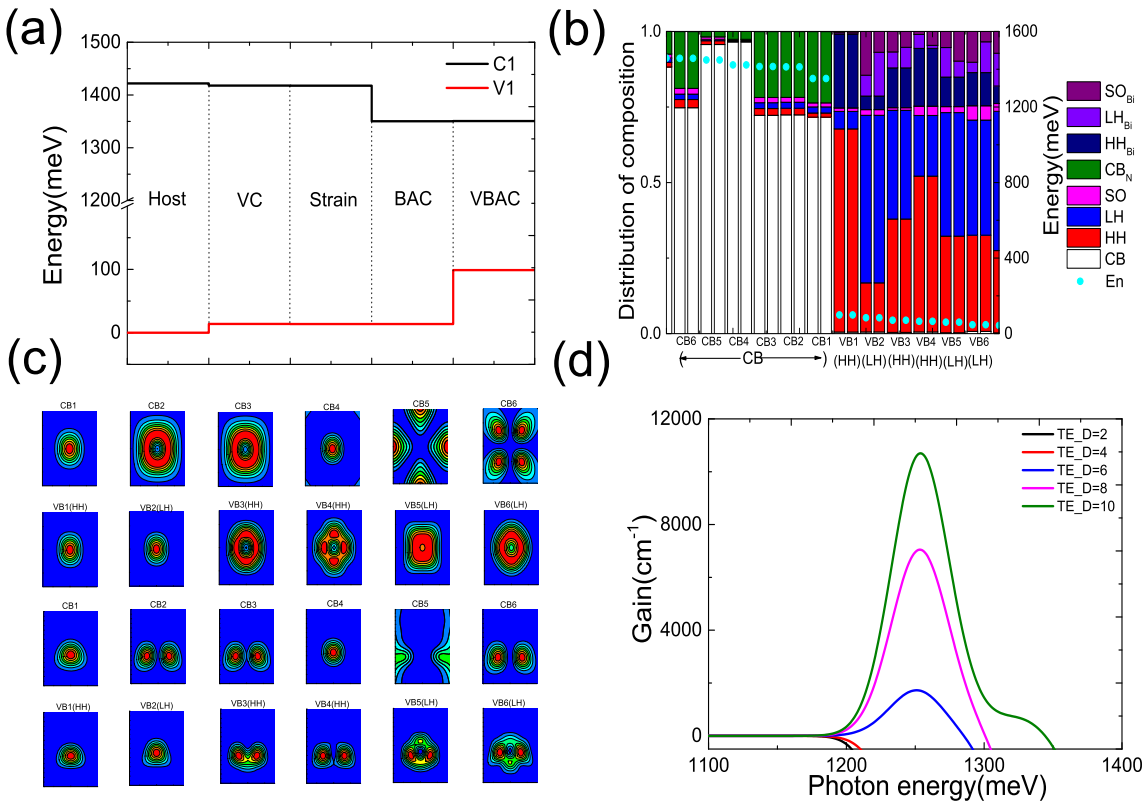

Figure 8.4: For $GaN_{0.016}Bi_{0.027}As_{0.957}/GaAs$ QDs, $\epsilon_{xx} \simeq 0.00$: the (a) bandstructure, (b) band-mixing probability, (c) charge density and (d) optical gain under different carrier densities, similar to Fig. 8.3. Here, the strain hardly affects the band structure of QD as the strain nearly equal to be zero. The C1 and V1 do not change when the strain is introduced. The component of the 12-bands and distribution of wave function are similar to Fig. 8.3. The peak of optical gain moves to right compared with Fig. 8.3 (d).

$-\delta E_{VC}^{CB} = -(\alpha_N x + \alpha_{Bi} y)$. Here we take VB1 band as HH-related term since HH is the dominant hole type in this band as we can see from the band mixing probability results. Obviously, $\delta E_{VC}^{HH} > 0$ as the parameters κ_N and κ_{Bi} are both positive. However, the sign of $-\delta E_{VC}^{CB} = -(\alpha_N x + \alpha_{Bi} y)$ is dependent on the choice of the N and Bi composition i.e. x and y. This is negative for all our three cases studied here. Therefore, the CB1 will be lowered while VB1 will be elevated induced by VC effect. This can explain the variation in the CB1 and VB1 induced by VC in frames (a) of Figs. 8.3, 8.4 and 8.5. Likewise, the variation induced by strain can also be explained in a similar way. The sign of the ϵ_{xx} directly determines the mobility of the CB1 and VB1. As the model says, $\delta E_{strain}^{CB} = a_c(\epsilon_{xx} + \epsilon_{yy} + \epsilon_{zz})$ and $\delta E_{strain}^{HH} = a_v(\epsilon_{xx} + \epsilon_{yy} + \epsilon_{zz})$ (without the b related terms as its magnitude is too

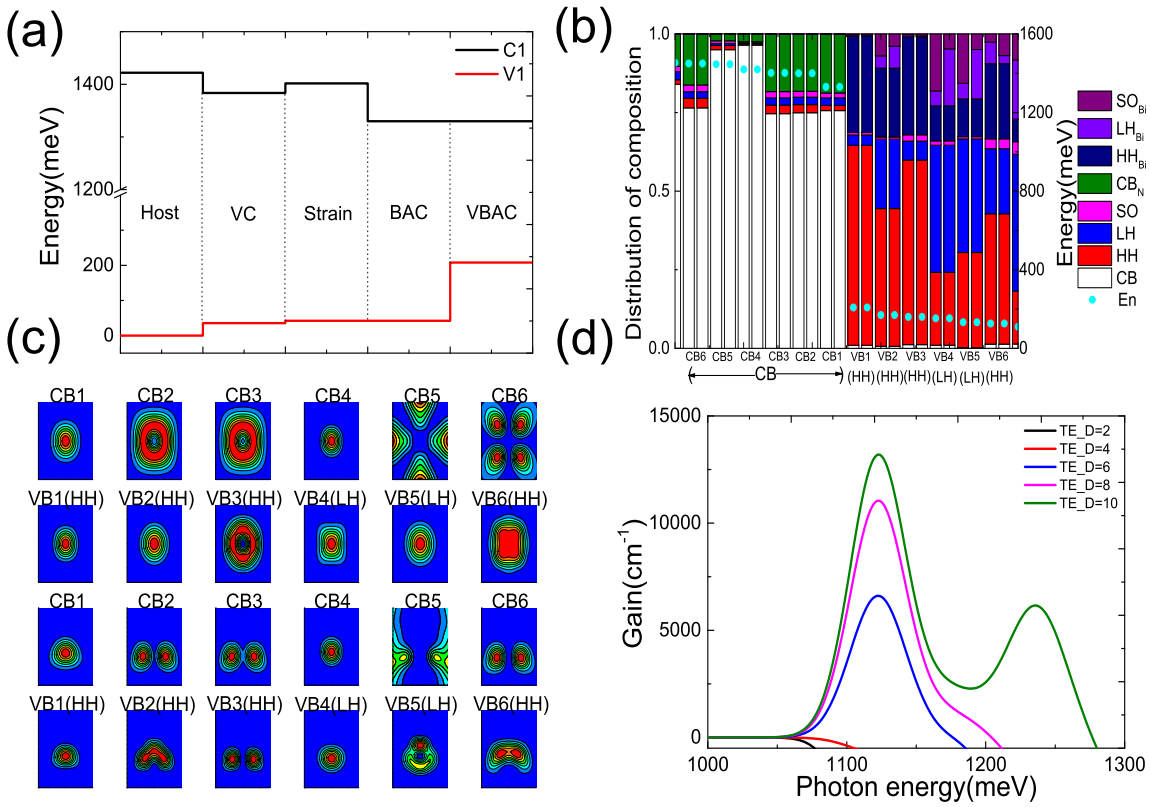

Figure 8.5: For $GaN_{0.013}Bi_{0.064}As_{0.923}/GaAs$ QDs, $\epsilon_{xx} = -0.005$: the (a) bandstructure, (b) band-mixing probability, (c) charge density and (d) optical gain under different carrier densities, similar to Figs. 8.3 and 8.4. Here, the compressive strain increases the band gap. The distribution of wave functions has some differences compared to Figs. 8.3 and 8.4. The peak of optical gain also moves.

small compared with the a_v related terms). Thus, δE^{CB}_{strain} will be positive (negative) while δE^{HH}_{strain} will be of opposite sign when the $\epsilon_{xx} < 0$ ($\epsilon_{xx} > 0$) when $a_c < 0$ and $a_v > 0$.

Frames (b) of Figs. 8.3, 8.4 and 8.5 show the band mixing probabilities and energy band-structure profile for different strain types occurring from different N and Bi compositions. The conduction band are mainly made of CB state and N state with minimal composition of HH, LH and SO which come from the coupling between CB and these bands. For different valence bands, the fraction of HH and LH contributions are different. The VBAC couples with the HH (LH) as HH_{Bi} (LH_{Bi}). As a result, the composition of HH_{Bi} is greater than (less than) LH_{Bi} where the composition of HH is greater than (less than) the LH.

Frames (c) of Figs. 8.3, 8.4 and 8.5 show the contour plot of the charge density (square of the absolute wave function $|\psi|^2$) for the CB1-CB6 and VB1-VB6 bands in QD whose

height is H = 12a, where a is the lattice constant of the host material. The first two rows in each case represents the charge densities in the x–y plane and the second two rows in the y–z plane. The CB1 is s-like, CB2 and CB3 are both p-like for the three cases although the strain is different. The s-p splitting is defined as $\Delta_{sp} = E_{CB2} - E_{CB1}$. In our cases, the related Δ_{sp} are 95 meV, 62 meV and 69 meV for Fig. 8.3, 8.4 and 8.5 respectively. The two p-like states are in fact degenerate due to the C_{4v} symmetry instead of C_{2v} in our $\boldsymbol{k}\cdot\boldsymbol{p}$ model. The next three bands are different for the different sign of the ϵ_{xx}. The CB4 is s-like while the CB5 and CB6 are d-like when the sign of the ϵ_{xx} is positive. For negative ϵ_{xx}, the CB4 and CB6 are d-like while the CB5 is p-like. For the valence band in QD with 3D confinement, the band mixing is so strong that they cannot be classified into a single explicit band according to their nodal structure like CB. In our system, not only the host's HH, LH and SO bands, but the Bismuth-related HH, LH and SO mix together as is evident from frame (b) of Fig. 8.3, 8.4 and 8.5. However, we can classify the bands according to the highest contributing hole type among HH, LH and SO. For example, in VB1, the fraction of HH is highest, thus we regard this as an HH band. For the first 6 VBs, HH and LH dominate primarily for all the compositions. Thus far, we have seen the influence of strain on the CB and VB. Here, through the wavefunction, more insight can be revealed. Since the strain is isotropic in our model, the splitting due to the strain arises first in CB4. The sign of ϵ_{xx} has a profound influence on the wavefunction characteristics.

Frames (d) of Figs. 8.3, 8.4 and 8.5 show the optical gain spectra for the TE mode for different carrier densities in the order of 10^{18}cm^{-3}. For a sufficiently high carrier density, we obtain a secondary peak in addition to the primary peak. The position of the peak is determined directly by the effective bandgap (CB1-VB1). Therefore, strain has an influence on the optical gain as it can alter the peak position by altering the effective bandgap. The peak broadening due to inhomogeneous effects is considered in our model.

So far, we have investigated the electronic bandstructure, wavefunction and optical gain spectrum for three typical samples of QDs with different kinds of strain. Now we offer a more general picture of the variation of CB1, VB1, bandgap and strain (ϵ_{xx}) with different combinations of N and Bi compositions as shown in Fig. 8.6. It displays the variation in CB1 and VB1 for varying compositions, which is mainly affected by the differences in BAC and VBAC. Further, yet another interesting aspect attracts our attention. When we fix the Nitrogen composition, the CB1 remains close to the origin level with little change, while the VB1 increases nearly linearly. On the other hand, when we fix the composition of Bismuth at low density and vary the composition of Nitrogen, both the CB1 and VB1 changes. It is

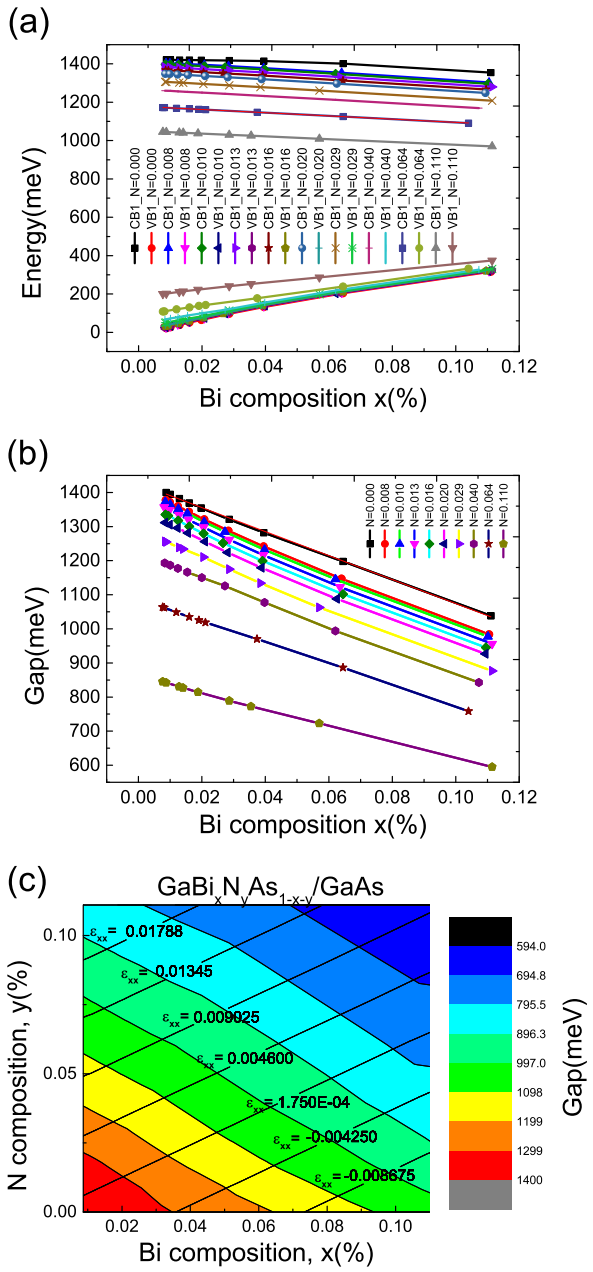

Figure 8.6: (a) and (b) The variation in CB1, VB1 and bandgap with the composition of doped N and Bi. (c) The contour of the bandgap and strain with the composition of doped Nitrogen and Bismuth. As the N and Bi are doped uniformly, the composition of the two impurities are discrete. Therefore, the isopotential lines of the strain and bandgap are not continuous.

of considerable interest to reason why the variation of CB1 is less in the at first case and the VB1 is relatively large in second case. The explanation is in the view of VC and strain for the above scheme. The variations induced by VC are $\delta E_{VC}^{CB} = -\alpha x$ and $\delta E_{VC}^{HH} = \kappa x$; and that induced by strain are $\delta E_{strain}^{CB} = a_c(\epsilon_{xx} + \epsilon_{yy} + \epsilon_{zz})$ and $\delta E_{strain}^{HH} = a_v(\epsilon_{xx} + \epsilon_{yy} + \epsilon_{zz})$. From Table A.3 in page 187 we know that the sign of α for Nitrogen is negative while for Bismuth is positive and the sign of a_c is negative while a_v is positive. Larger Bismuth composition means decreasing the δE_{VC}^{CB} and increasing the δE_{strain}^{CB} for a fixed Nitrogen composition. These two effects partially cancel the contribution to the CB1, resulting in little variation in CB1. Likewise, greater Nitrogen composition means increasing δE_{VC}^{HH} and δE_{strain}^{HH}. These two effects together lift the VB1 even higher when we fix the Bismuth composition and vary the Nitrogen. Fig. 8.6 (b) illustrates this variation in the bandgap. A linear decrement of the bandgap occurs at a rate of $\sim$ 36 meV for 1% variation. Compared with the bulk materials [56], the bandgap decrement rate of the in QDs is lesser than that of bulk materials. This can be understood in the view of quantum confinement, as we shall see in the case of size scaling. Here we do not show the variation of SO as a strong mixing in QDs among HH LH and SO. Although we have redefined the band considering their major contributors among HH and LH, but still we cannot point where the SO starts. This is different from the bulk states. The effective bandgap of $GaN_xBi_yAs_{1-x-y}$/GaAs pyramidal QDs can be tuned by varying the composition of N and Bi, such that the emission wavelength spans the range of 1.3 μm–1.55 μm, suitable for device applications in fiber technology. Fig. 8.6 (c) shows the contour of the bandgap and ϵ_{xx} varying with N and Bi composition. This picture gives a more clear way to decrease the band gap along the zero strain line. This is essential in real experimental systems.

The size of the QD is another important design parameter while considering its optical gain characteristics. Due to 3D confinement, the quantum effect is more obvious with the size decrease in QDs. Comparing the results of the rate of the bandgap decrement (81 meV for 0.1% variation) in the $GaBi_yAs_{1-y}$ system in our case, the quantum confinement that slows down the decrement rate. This means that for sufficiently large QDs the decrement rate will tend to that in bulk material. This phenomenon can be proved from the shift of the peaks. Fig. 8.7 confirms these predictions. In Fig. 8.7, we set three different sizes of QD as H = $12a$, $16a$ and $20a$ where a is the lattice constant of the host material, GaAs in our case. The carrier density is fixed at $6{\times}10^{18}$ cm^{-3} for all the four cases of Fig. 8.7, with varying N and Bi compositions. Besides the red shift, another interesting phenomenon about the number of the peak is noteworthy. For the H = $12a$ there is only 1 peak while

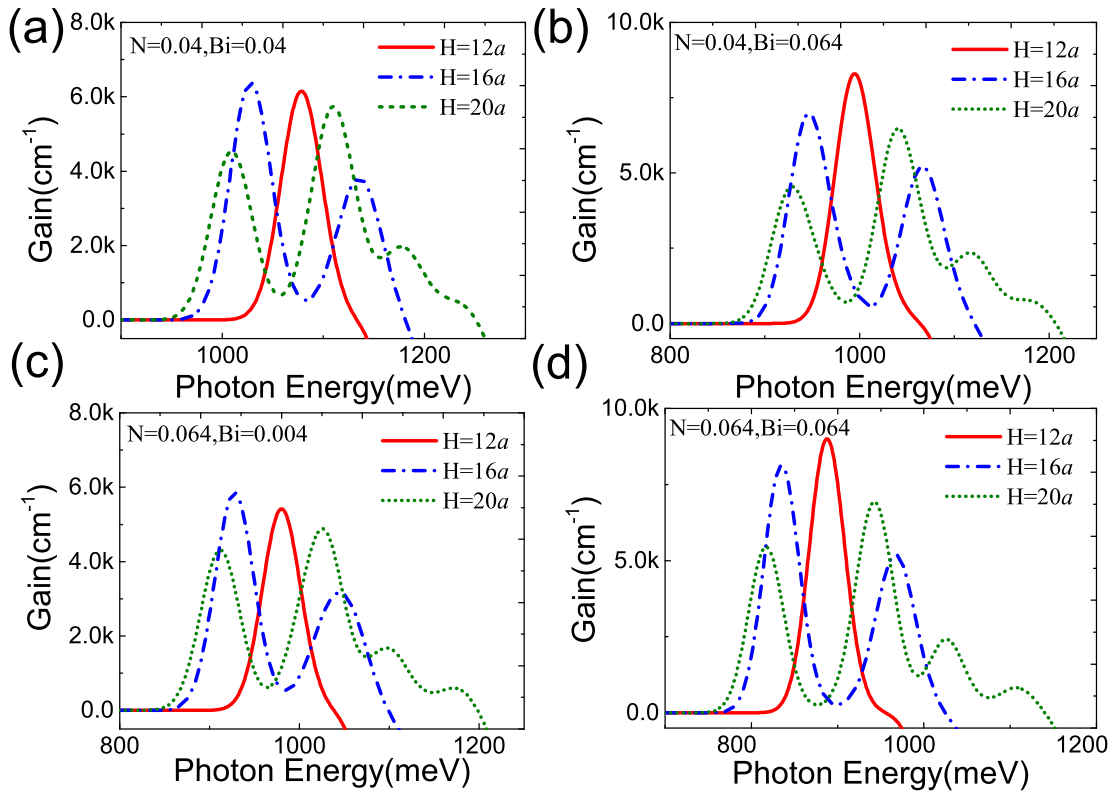

Figure 8.7: The optical gain spectra for different size of QDs (H = 12a, 16a and 20a where a is the lattice constant of the host material). For each case the carrier density is fixed at 6×10^{18} cm^{-3}. Four different N and Bi composition compositions are shown here in frames (a) through (d). The shift of the first peak is obvious as the band gap decreases as the QD size increases.

for the H = 16a there are 2 peaks, and even 4 peaks for H = 20a. Large size of the QDs means smaller subband gap which is easier to be excited. Different peaks describe different transition between levels of CB and VB. Thus we need to determine where the transitions take place. This can be done with the help of the location of polarized matrix element. Taking Fig. 8.7 (d) as an example with considering the H = 16a and 20a, the second peak comes from the transition between CB3 and VB5.

8.4 Summary and Conclusion

The electronic bandstructure and optical gain of $GaN_xBi_yAs_{1-x-y}$/GaAs pyramidal quantum dots (QDs) are investigated using the 16-band $\boldsymbol{k}\cdot\boldsymbol{p}$ model with constant strain. The optical gain is calculated taking both homogeneous and inhomogeneous broadenings into

consideration. The effective bandgap falls as we increase the composition of Nitrogen (N) and Bismuth (Bi) and with an appropriate choice of composition we can tune the emission wavelength to span within 1.3 μm–1.55 μm, for device application in fiber technology. The extent of this red shift is higher in QDs compared to bulk material due to quantum confinement. Other factors affecting the emission characteristics include virtual crystal (VC), strain profile, band anticrossing (BAC) and valence band anticrossing (VBAC). The strain profile has a profound impact on the electronic structure, specially the valence band of QDs, which can be determined using the composition distribution of wavefunctions. All these factors eventually affect the optical gain spectrum. With an increase in QD size, we observe a red shift in the emission energy and emergence of secondary peaks owing to transitions of greater energy compared to the fundamental transition.

Chapter 9

GaNBiAs/GaAs Dilute Nitride-Bismide Quantum Wells

9.1 Introduction

We studied GaNBiAs/GaAs QDs in Chapter 8, but dilute nitride bismide GaNBiAs QWs are also a potential semiconductor candidate for near- and mid-infrared applications, particularly in 1.55 μm optical communication systems, as discussed for the literature review in Sec. 1.2.2. Incorporating dilute amounts of bismuth (Bi) into GaAs reduces the effective bandgap rapidly, while significantly increasing the spin-orbit-splitting energy. Additional incorporation of dilute amounts of nitrogen (N) helps to attain lattice matching with GaAs, while providing a route for flexible bandgap tuning. From the experimentalist's point-of-view, GaBiAs QW are well studied [37–42]. Most of them use molecular beam epitaxy followed by related optical characterization of the bandedge [52, 53]. In this chapter, we study various cases of lattice matched GaNBiAs QWs grown on GaAs barrier, aiming for applications in the 1.55 μm GaAs-based laser for fiber optical communication systems. A recent work [61] by the O'Reilly group has reported GaBiAs/GaAs QWs, while our work focuses on GaNBiAs QWs, which has better electron confinement due to repulsion between N and the host material's band edge. The larger CB and VB offsets of GaNBiAs/GaAs benefit the QW laser performance, such as rendering a larger characteristic temperature. Nasr *et al.* [159] have worked on GaNBiAs QWs, but limit their investigation only up to optical absorption. However, here we study the optical gain essential for device design and performance, plus report the modeling and optimization of lattice matched GaNBiAs

QW lasers. Gladysiewicz *et al.* [160] have reported GaInAsBi QWs, but haven't studied GaNBiAs.

9.2 Theoretical Framework

As stated in Chapter 8, the 8-band $\boldsymbol{k}\cdot\boldsymbol{p}$ models used through Chapters 3 to 7 are suited to study binary II-VI or III-V semiconductors. But when we intend to study the effect of nitrogen and bismuth doping in the semiconductors, the 8-band Hamiltonian is not sufficient. Broderick *et al.* had proposed a 12- and 14-band $\boldsymbol{k}\cdot\boldsymbol{p}$ Hamiltonian for GaNBiAs [56]. Here, we propose a 16-band Hamiltonian including the so_{Bi} energy level ($E^0_{Bi,so}$), which was not accounted for in their model. The 16-band model is more accurate, especially for the higher excited states of hole, which can be closer to $E^0_{Bi,so}$, and thus the interaction between them cannot be ignored. We have extended the Kane's 8-band Hamiltonian and used the BAC and VBAC models to form a 16-band Hamiltonian. In addition to Kane's 8-bands, the incorporation of N needs two additional bands to address the local N resonant s-like states. On the other hand, Bi introduces p-like states, for which six additional bands must be considered with the freedom of spin, including so coupling. The 16-band Hamiltonian used to study the $GaN_xBi_yAs_{1-x-y}$ QW for this Chapter is described in Sec. 2.3.4 with all the Hamiltonian elements. The transition matrix elements are also calculated using Eq. (2.49) as discussed in Sec. 2.3.4. The optical gain spectra was calculated using methods described in Sec. 2.5.1. Material parameters for GaAs, BAC and VBAC parameters for N and Bi effect are from Tables A.2 and A.3 in Appendix A.

9.3 Results and Discussions

The bandgap (E_g) for $GaN_xBi_yAs_{1-x-y}$ semiconductor alloy pseudomorphically grown on GaAs depends on the compositions of N (x) and Bi (y) replacing the As from GaAs. Both GaN and GaBi have lower bandgap compared to GaAs, and combined addition of N and Bi reduces the E_g of GaNBiAs alloy as shown in the Fig. 9.1 contour (This result is at 300 K). The lattice constant of GaN is smaller than GaAs, while that of GaBi is larger. Therefore a sufficiently large N fraction induces a tensile strain ($\varepsilon_{xx} > 0$), while a sufficiently large Bi fraction induces a compressive strain ($\varepsilon_{xx} < 0$). In this work, we focus on lattice matched GaNBiAs/GaAs QW structures, for which it is essential to maintain a ratio of N : Bi = 0.58 for zero strain, as shown by the red line, which is the line of lattice matching.

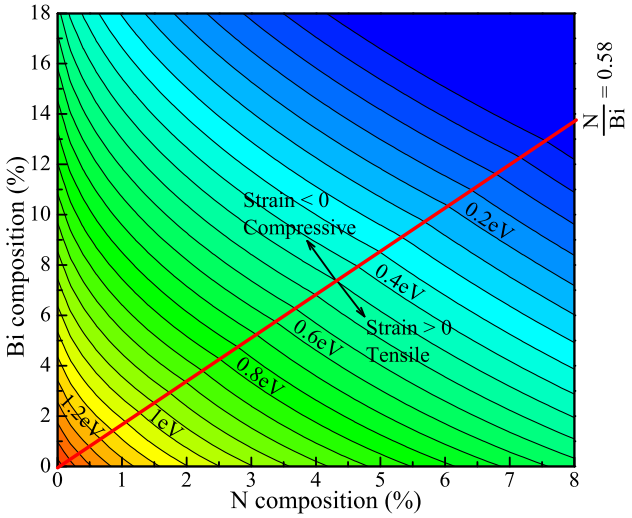

Figure 9.1: Variations in the bandgap (E_g) of GaNBiAs pseudomorphically grown on GaAs at 300 K vs. N and Bi composition (%). The red line is the line of lattice matching (N : Bi = 0.58).

From the viewpoint of device physics, strain in the QW material may be beneficial, for example, compressive strain reduces the hole effective mass to improve laser performance. But, from the viewpoint of material growth, strain has the potentially deleterious effects on the performance of laser [161]. Furthermore, the critical thickness of the strained quantum well limits thicker material growth. So, lately there has been many works reporting strain compensated structure to minimize the strain to achieve the high-performance lasers [162, 163]. Here, adhering to the condition of lattice matching, we have studied the photon emission energy of GaNBiAs/GaAs QWs for varying well widths as shown in Fig. 9.2.

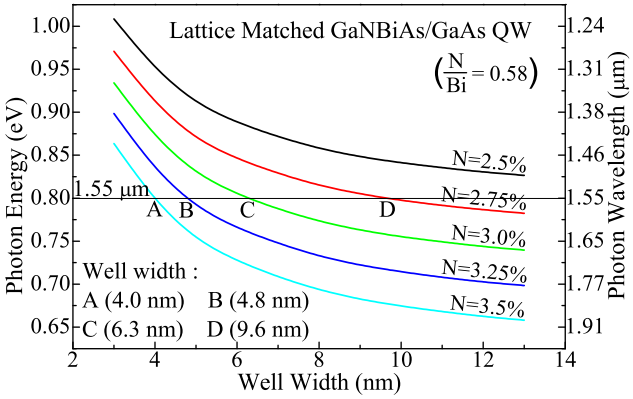

Figure 9.2: Photon emission energy/wavelength vs. well width of lattice matched GaNBiAs QWs with varying N and Bi concentration. Cases A to D are labeled.

Focusing on the 1.55 μm emission wavelength optical fiber telecom communication applications, we have chosen 4 cases labeled A to D, with varying well widths of 4, 4.8, 6.3 and 9.6 nm respectively. These cases correspond to varying N compositions of 3.5, 3.25, 3 and 2.75 % and corresponding Bi compositions for lattice matching with GaAs. The well width increases from Case A to D, and therefore the extent of quantum confinement decreases. Ideally this should lead to a fall in the photon emission energy. But since the composition of N and Bi also reduces simultaneously, this effect is compensated for. A lower fraction of N and Bi is less capable of reducing the effective bandgap of GaNBiAs. Therefore, these two contrasting phenomenon suitably counterbalance and all the four cases exhibit emission around the 0.8 eV (1.55 μm) mark targeted towards telecom devices, as shown.

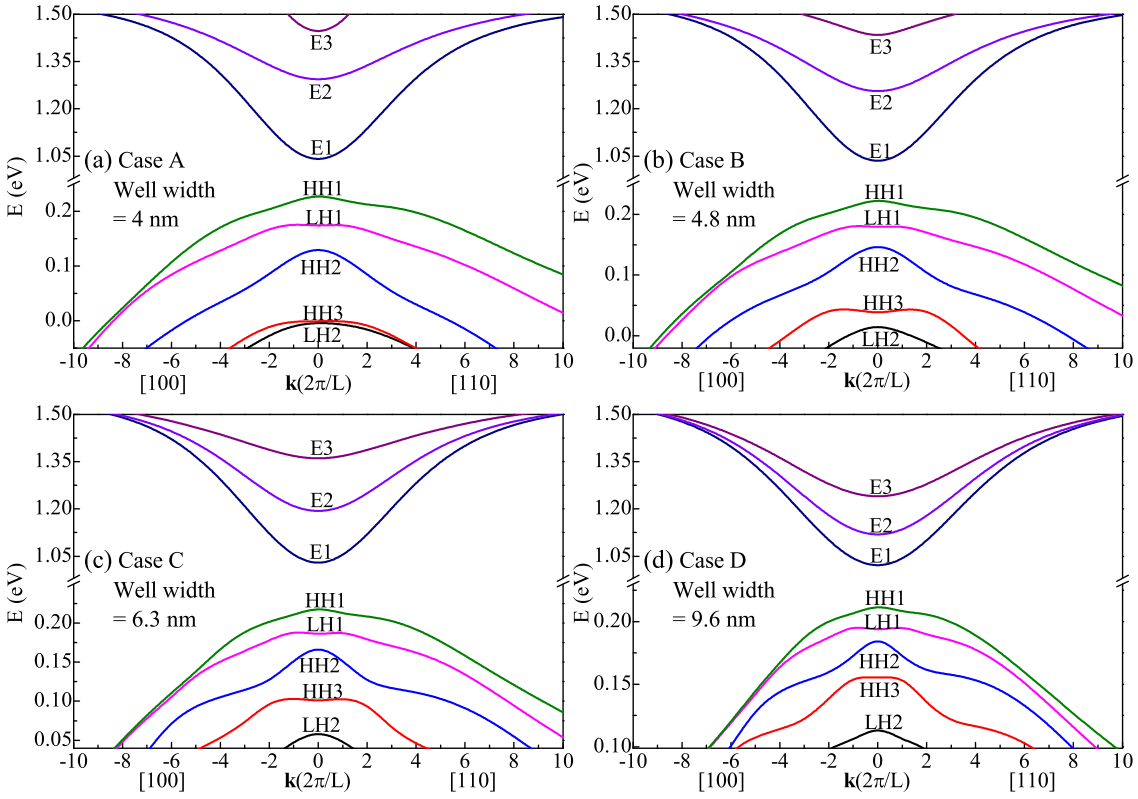

Figure 9.3: First 3 electron and first 5 hole energy dispersion curves of lattice matched GaNBiAs QWs of (a: *Top Left*) Case A (well width = 4 nm); (b: *Top Right*) Case B (well width = 4.8 nm); (c: *Bottom Left*) Case C (well width = 6.3 nm); (d: *Bottom Right*) Case D (well width = 9.6 nm). **k** is wavevector along [100] and [110] directions. E stands for electron, HH for heavy hole levels and LH for light hole levels. The photon emission energy for all cases are $\sim$ 0.8 eV (1.55 μm).

The energy dispersion curves for the first 3 electron and the first 5 holes subband states along the [100] and [110] wavevector direction for Case A to D GaNBiAs/GaAs QWs are shown in Fig 9.3. The well width of each case is mentioned in the figure. The electron states are labeled E1 to E3, while for the holes states we have specified heavy hole (HH) and light hole (LH) states distinctly. We can see that the energy dispersion curves clearly depends on the well width and the (N,Bi) composition. As the well width increases from Case A to D, the (N,Bi) compositions falls, and the two counteracting effects balance to ensure the 1.55 μm emission. We see that the conduction subband energy dispersion curves are isotropic-like due to the isotropy of electron effective mass. On the other hand, the valence subband energy dispersion curves are more affected by varying well width and composition. There is anisotropy effect in all cases, and they are more spread along the [110] wavevector direction compared to [100] direction. Also, from Case A to D, their **k** span decreases. But in all four cases, the hole type sequence is same: HH1, LH1, HH2, HH3, LH2. We also notice that as the well width increases from Case A to D, the gap between adjacent E states and adjacent H states reduces. On the whole, $\Delta_{\text{E1-E3}}$ reduces from 403 meV in Case A to 222 meV in Case D. Similarly $\Delta_{\text{HH1-LH2}}$ reduces from 234 meV in Case A to 96 meV in Case D. This can be attributed to the loosening confinement effect. For instance in Case D, due to these effects, E1 and E2 have come very close, and so have HH1 and LH1. This affects the optical performance as we shall subsequently examine.

The TE mode optical gain spectra of GaNBiAs QWs of Case A to D are shown in Fig. 9.4. The injection carrier density was varied from 2 to 8 $\times 10^{18}$ cm^{-3}. The temperature considered is 300 K. The intraband relaxation time τ was taken to be 0.1 ps. For any particular GaNBiAs QW case, there is a marginal blue shift in the emission peak position as the injection carrier density increases. With more and more carriers being injected they begin to occupy electronic states further away from the bottom of the conduction band and top of the valence band. Now, the excited state recombinations that incur from such transitions will have their emission energy larger than the E1-HH1 separation, thus resulting in a blue shift. This effect is also generally known as band filling effect in QWs. Comparing Case A to D, we can observe that the band filling effect is more profound in thicker QWs compared to thinner QWs. In thicker QWs, the quantum confinement effect is weaker and therefore the permissible energy levels are much closely packed. With the injection of more and more carriers, there is a higher probability of them occupying the next nearest electronic state and contributing to the emission. Comparing the gain curves, we see that the spectral width increases from Case A to D. There are several factors dictating

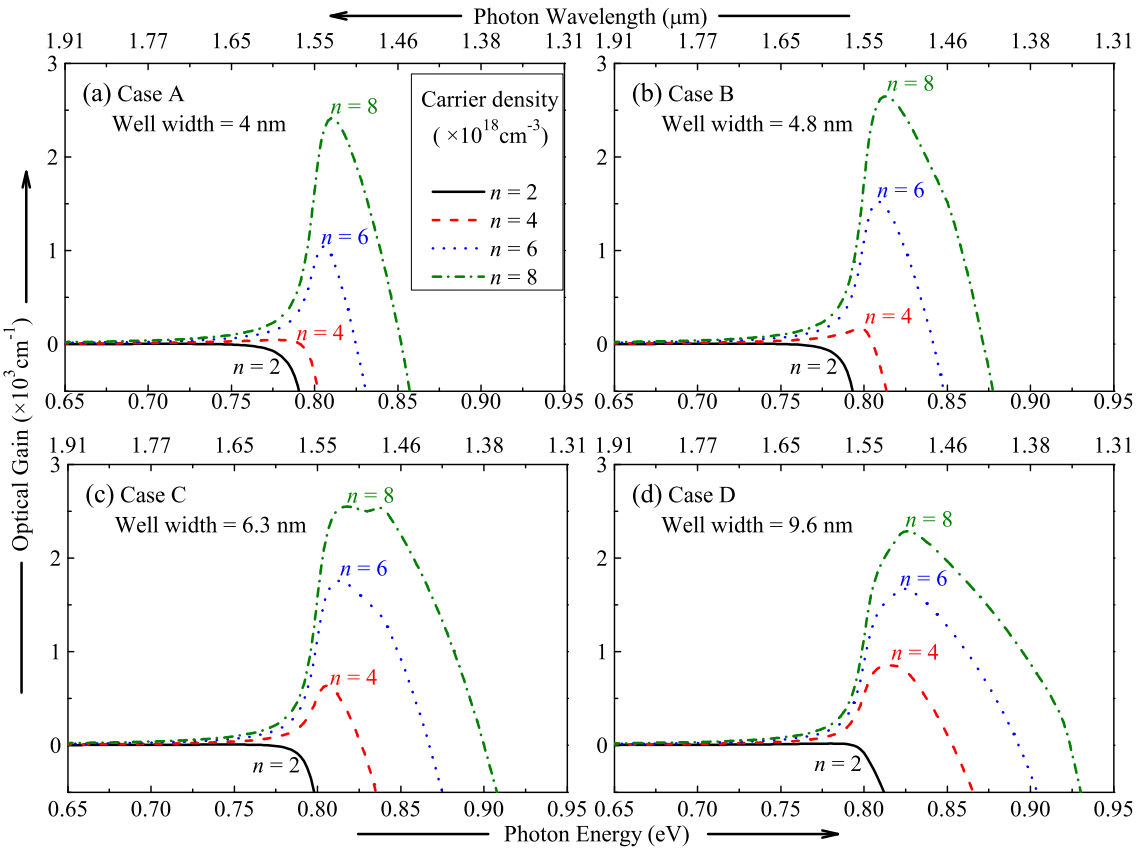

Figure 9.4: TE mode optical gain spectra of lattice matched GaNBiAs QWs at 300 K for (a: *Top Left*) Case A (well width = 4 nm); (b: *Top Right*) Case B (well width = 4.8 nm); (c: *Bottom Left*) Case C (well width = 6.3 nm); and (d: *Bottom Right*) Case D (well width = 9.6 nm), for varying injection carrier density (n) = 2, 4, 6 and 8 $\times 10^{18}$ cm^{-3}. The peak emission position of all cases are $\sim$ 0.8 eV (1.55 μm).

this trend, the primary being band filling effect as just discussed. Additionally, as seen for Fig. 9.3, the adjacent E and adjacent H states come closer. Under such circumstances if we increase the injection carrier density, there is a high probability that electrons exceed E1 and start to occupy E2 and so on. Similarly holes can exceed HH1 and occupy LH1, HH2, etc. Considering, Case D for instance, it has a fairly large gain spectral width – because it results from electron-hole recombinations not only from E1-HH1, but also E1-LH1, E2-HH2, etc. However, smaller gain spectral width is better for stable single mode operation.

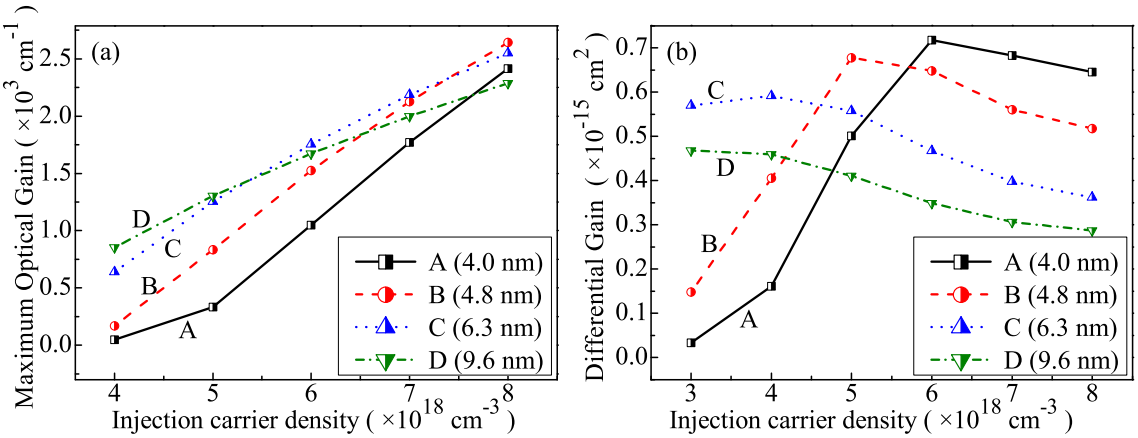

Figure 9.5: (a: *Left*) Maximum Optical Gain and (b: *Right*) Differential Gain of lattice matched GaNBiAs QWs at 300 K for Case A (well width = 4 nm), Case B (well width = 4.8 nm), Case C (well width = 6.3 nm) and Case D (well width = 9.6 nm) vs. varying injection carrier density. Each case is labeled.

The maximum optical gain of the 4 GaNBiAs QW cases studied in Fig. 9.4 are presented in Fig. 9.5 (a), with some additional data points. We have ignored 2×10^{18} cm^{-3} because at such low density, there is no positive gain. There are several factors affecting the maximum gain, such as TME, quasi-Fermi levels, temperature and thickness of the QW among others [see factors in Eq. (2.56) and (2.57)]. Usually thicker QWs have higher TMEs due to the higher absolute overlap of the electron and hole wavefunction. Also, the difference between the quasi-Fermi level separation (ΔF) and photon energy (E) is important and for positive (maximum) gain, ΔF must be larger than the fundamental transition energy E1-HH1. Finally, from Eq. (2.56) and (2.57), we can also see that the gain (thus maximum gain) is inversely proportional to the well width (l). Therefore, combining the effects of these and other parameters involved, we get the final result as shown in Fig. 9.5 (a). The overall observation is that as the injection carrier density increases, so does the maximum optical gain. This is because a higher carrier density results in more and more electronic states getting filled and greater number of recombinations occur around the *near*-E1-HH1 energy gap. Now comparing the 4 QW cases, we found that their transparency carrier density [126] is around the 1.9–3.3$\times10^{18}$ cm^{-3} mark. This is the carrier density that gives us neither gain nor absorption around the emission peak position (we get zero gain). But on closer inspection we found that, thinner GaNBiAs QWs have higher transparency carrier density requirement compared to thicker QWs. It was found to be 3.3, 2.5, 2.1 and 1.9$\times10^{18}$ cm^{-3} for QW Cases A to D respectively, by interpolation method. Just after the onset of gain, say

at 4×10^{18} cm^{-3}, the maximum gain pattern is Case D>C>B>A, in accordance with their thicknesses. But with further increase in carrier density, the maximum gain is affected by other factors such as band filling effect and reduced confinement. The overall effect on the 4 QW cases can be seen in Fig. 9.5 (a). While Case C and D QWs have steadily increasing maximum gain, Case C exceeds D at 8×10^{18} cm^{-3} density, as D approaches saturation. We shall further discuss this effect in the detailed context of Fig. 9.5 (b), which shows the differential gain of the 4 GaNBiAs QW cases being studied. A higher differential gain translates to greater modulation speed and narrower width of emission spectra [124, 125]. Thus differential gain is a performance index of how effectively injected carriers produce photon emissions. The thinner QWs (Case A and B) have a steadily increasing differential gain initially, before dipping at sufficiently high densities. On the other hand, the thicker QWs (Case C and D) have a relatively more stable differential gain, but they decrease with increasing carrier densities. Among these, Case D has a lower differential gain and also it is monotonically decreasing from density 2 to 8 $\times10^{18}$ cm^{-3}. Case C has a higher and more stable differential gain across varying carrier densities.

Now we are in a situation to compare the 4 GaNBiAs QW cases studied, on the basis of their optical gain spectral width [Fig. 9.4], transparency carrier density, maximum optical gain [Fig. 9.5 (a)] and differential gain [Fig. 9.5 (b)]. The gain spectral width increases from Case A to D. While Cases A, B and C have a steady form function, for Case D it get very wide with increasing carrier density. This is because at such large thickness, the confinement effect drops and the gap between adjacent E and H states shrinks. Other excited electron-hole transition routes open broadening the spectra. This has an adverse effect on the optical performance, as smaller gain spectral width is better for stable single mode operation. When it comes to the maximum optical gain, Cases C and D have steady increment. Also at sufficiently high carrier density, the Case C maximum gain exceeds that of Case D. The maximum gain of Case B also increases rapidly, but it is much less at lower densities. Moreover, the transparency carrier density of Case C and D are relatively lower than that for A and B. Finally, the study of differential gain shows us that Case C has the best suitable characteristics to deliver high and steady optical performance over a wide range of injection carrier density. The other cases exhibit diminishing differential gain at either low density or high density. These observations are symbolically summarized in Table 9.1.

Table 9.1: Comparative analysis of the 4 GaNBiAs QW cases studied

GaNBiAs QW Case	N : Bi : As ratio	Gain spectral width	Maximum gain	Transparency density	Differential gain
Case A (4.0 nm)	3.50 : 6.03 : 90.47	✓	✗	✗	✗
Case B (4.8 nm)	3.25 : 5.60 : 91.15	✓	✗	✗	✗
Case C (6.3 nm)	3.00 : 5.17 : 91.83	✓	✓	✓	✓
Case D (9.6 nm)	2.75 : 4.74 : 92.51	✗	✓	✓	✗

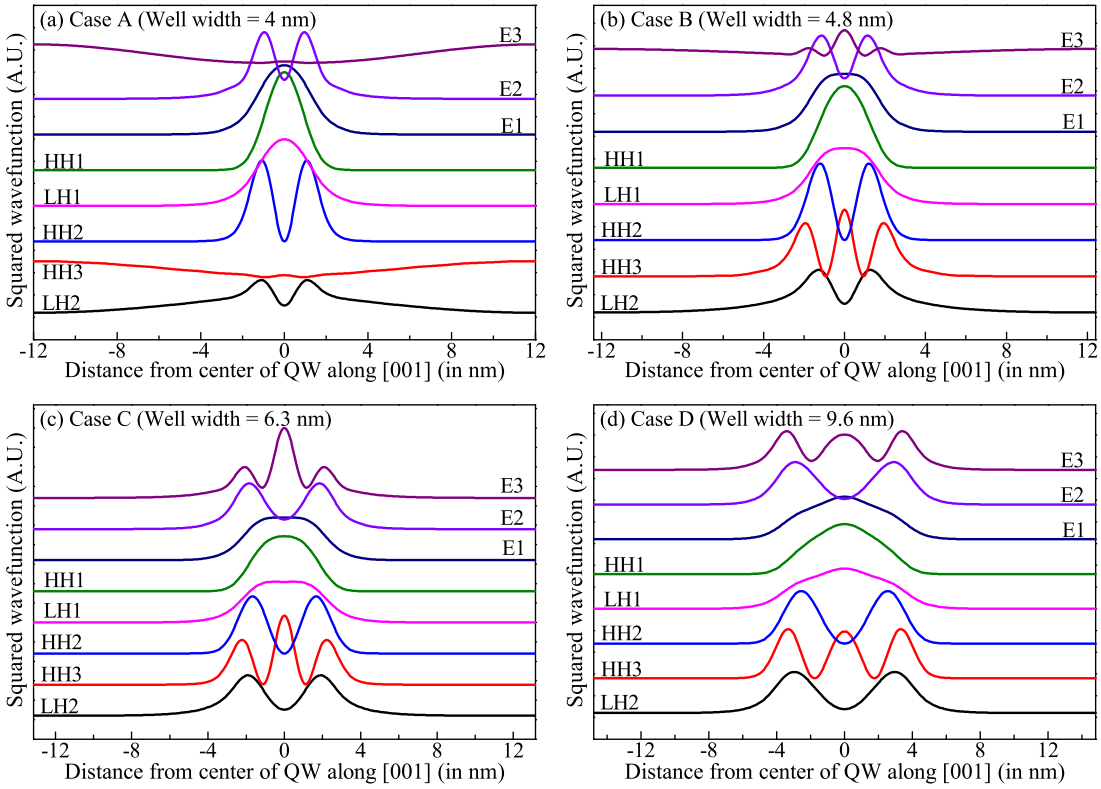

Figure 9.6: First 3 electron and first 5 hole squared wavefunctions at $\mathbf{k} = 0$ point for GaNBiAs QWs of (a: *Top Left*) Case A (well width = 4 nm); (b: *Top Right*) Case B (well width = 4.8 nm); (c: *Bottom Left*) Case C (well width = 6.3 nm) and (d: *Bottom Right*) Case D (well width = 9.6 nm) vs. distance from the center plane of QW along the [001] direction. E stands for electron, HH for heavy hole levels and LH for light hole levels.

Fig. 9.6 shows the squared wavefunction of the first 3 electron and the first 5 hole energy levels at $\mathbf{k} = 0$ point for Case A to D GaNBiAs/GaAs QWs. We can see that as the thickness increases, the E and H wavefunctions spreads out, as expected due to larger well width. In all the cases, the wavefunctions of E1 has a reasonable overlap with that of HH1, which causes the E1-HH1 fundamental transition. Transitions among higher E and H states follow the optical transition rule and depend on the extent of probability of wavefunction overlap.

On the whole, as summarized in Table 9.1, we find that for our intended 1.55 μm (0.8 eV) GaAs-based fiber optic laser diode applications, the 6.3 nm thick $GaN_3Bi_{5.17}As_{91.83}$ lattice matched quantum well (Case C), gives the best optical performance. This is in comparison with the other three cases. Further fine tuning may lead us to better design parameters. GaNBiAs/GaAs QWs are excellent candidates for 1.55 μm optical applications. But it is important to carefully consider the design parameters which determine the final optical performances.

Having concluded our findings above, we would now like to highlight couple of important research aspects relating to dilute-N-Bi QW lasers. Firstly, it is well known that for bulk material, the conduction-heavy hole-split off hole-heavy hole (CHSH) Auger recombination is significant. However, there exists contradictory viewpoints in the QW domain. For example, Hausser *et al.* have experimentally shown that the Auger recombination in QWs is about 3 times smaller than that in bulk [164]. Other works have reported a reduction in Auger recombination by two orders of magnitude in QWs compared to bulk [165]. These works show that the Auger recombination in QWs is of very minor significance, owing to which we have chosen to simplify our calculations. However, there are some counter arguments in existing literature which state that Auger recombination is a significant problem for long wavelength QW semiconductor lasers [157, 166]. In this context, more conclusive work is elicited to obtain a comprehensive understanding of the Auger effects in GaNBiAs QWs. In order to fully understand the nonradiative recombination, we would also like to trigger the investigation of the other two types of Auger recombination in GaNBiAs QWs: conduction-heavy hole-conduction-conduction (CHCC) and conduction-heavy hole-light hole-heavy hole (CHLH). We know that the CHSH Auger recombination can be suppressed by controlling the Bi composition (ensuring that the spin-orbit splitting energy exceeds the effective bandgap [43]), and more readily so in the presence of N. But this does not continue to hold in case of CHCC or CHLH Auger recombination, for which there is no significant evidence in literature. Secondly, the major challenge with GaNBiAs QW laser

is that, it is difficult to grow high quality material even with advanced molecular beam epitaxy or metal organic chemical vapor deposition. Incorporating both N and Bi requires different growth optimizations. One issue is that adding N into GaAs degrades the material quality [167]. On the other hand, Bi as surfactant may increase the efficiency of N incorporation in GaNAs by up to 60% [168]. However, too high a Bi % can also be detrimental to the material quality. The Volz group has demonstrated GaBiAs QW lasers [169] with 2.2% Bi having a threshold current density of 1.56 kA/cm^2.

9.4 Summary and Conclusion

We have studied the electronic bandstructure and optical properties of lattice matched GaNBiAs/GaAs quaternary alloy quantum well (QW) based on the 16-band $\boldsymbol{k}\cdot\boldsymbol{p}$ model. The different QW cases studied have their thicknesses and N : Bi : As composition tuned in such a way to have their emission peak at 1.55 μm, aiming towards optical communication systems. We have obtained insights on how the well thickness and (N,Bi) compositions affects the energy dispersion curves and closeness of electron and hole energy levels. An increase in the injection carrier density increases the maximum gain and also the gain spectral width. In our study we see that while thinner wells have decreasing differential gain at lower density, thicker wells show the same at higher density. It is, thus, of significant importance to determine the critical well thickness for a steady optical performance. Among our cases studied, we have identified the 6.3 nm thick $GaN_3Bi_{5.17}As_{91.83}$ lattice matched QW to exhibit optimized optical performance for our intended 1.55 μm (0.8 eV) optoelectronic device/system applications. Therefore, it is recommended that the design parameters such as material composition and well width must be carefully considered from the device application point-of-view for an accurate optimization of the optoelectronic performance characteristics.

Chapter 10

InNBiAs/InP Dilute Nitride-Bismide Quantum Dots

10.1 Introduction

DILUTE bismide alloys and dilute nitride alloys have garnered increasing research interest over the past few years [170–172], as it promises increased engineering flexibility in the design of advanced compound semiconductor heterostructure devices. Increased control over key device parameters such as lattice constant, bandgap and band offsets opens the door to improved performance for a wide range of electronic and optoelectronic devices.

In Chapters 8 and 9 we studied about GaNBiAs QDs and QWs, but the concepts of dilute nitride/bismide III-V semiconductors encompass a wider range of III-V materials such as InAs, InSb, etc. Bulk InAs has a much lower room temperature bandgap of 0.354 eV compared to 1.424 eV of bulk GaAs [62], which implies that InAs based devices would have comparatively longer operating wavelengths. Dilute N and Bi doping in InAs would open new avenues of bandstructure engineering such as supressed Auger recombination, in a similar fashion to that discussed for GaNBiAs in the preceding chapters. InNBiAs in particular is a promising candidate for mid-infrared emission device applications. In view of this, this chapter is dedicated to the study of the electronic bandstructure and optical gain of InNBiAs/InP pyramidal QDs investigated using a 16-band $\boldsymbol{k}\cdot\boldsymbol{p}$ model, with an objective of achieving emission wavelength in the range of 2–5 μm suitable for mid-infrared device applications.

10.2 Theoretical model

As discussed in Chapter 8, in order to study the effect of nitrogen and bismuth doping in the semiconductors, we employ a 16-band $\boldsymbol{k}\cdot\boldsymbol{p}$ Hamiltonian model. The 8-band Hamiltonian, generally used for binary II-VI or III-V semiconductors is not suitable anymore. The 8-band model is usually extended to construct the the 10-band $\boldsymbol{k}\cdot\boldsymbol{p}$ model used to study the nitrogen-doped QDs by introducing the local nitrogen resonant state (additional 2 bands). Similarly, to investigate the bismuth-doped and nitrogen-doped QDs simultaneously, additional bands have to be added in the model to describe and study the effects of bismuth. Unlike the s-like state introduced by dilute nitride, the dilute bismide results in p-like states, which means that six states should be considered with the spin freedom including the SO coupling which is ignored in the O'Reilly 14-band model for dilute bismide-nitride semiconductors [56]. In view of the aforementioned consideration, we have constructed a 16-band model, suited for studying InNBiAs/InP dilute nitride/bismide QDs. The 16-band Hamiltonian is represented in the Bloch function basis as described in Sec. 2.3.3. As we use the $|10\rangle$, $|1-1\rangle$, $|11\rangle$ basis for the p-like states instead of $|HH\rangle$, $|LH\rangle$, $|SO\rangle$, the form of Hamiltonian is different form the O'Reilly's model and can be transformed into it under an unitary transformation. The details of the every element of the Hamiltonian is described in Sec. 2.3.3. The transition matrix elements quantifying the strength of transition between the electron- and hole-subbands are calculated using Eq. (2.13) as discussed in Sec. 2.3.3. The optical gain spectra was calculated using methods described in Sec. 2.5.1.

10.3 Results and Discussion

In this work, the electronic bandstructure and optical gain of InNBiAs/InP pyramidal quantum dots are investigated using the 16-band $\boldsymbol{k}\cdot\boldsymbol{p}$ model with constant strain. The geometry schematic of $\mathrm{InN}_x\mathrm{Bi}_y\mathrm{As}_{1-x-y}$/InP QD is shown in Fig. 10.1 with the direction of pyramid growth along the positive z axis. The doped nitrogen and bismuth atoms are distributed uniformly in crystal throughout the QD. The details of the structure is similar to that explained in Chapter 8. Here the H represents the height of the QD which takes the lattice constant (a) as the unit length. In this work we will study the InNBiAs QDs of different heights (H). The interaction between the doped atoms is not taken into consideration.

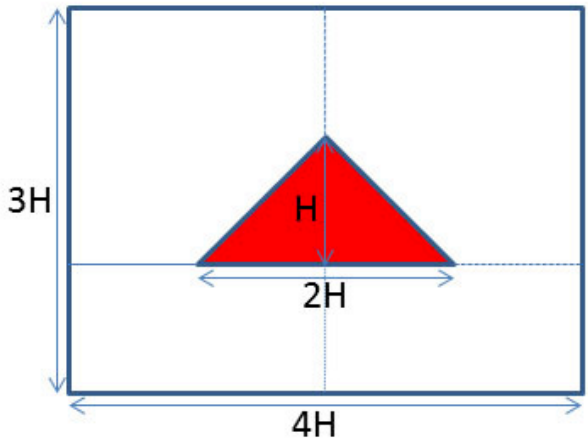

Figure 10.1: The geometry schematic of the pyramidal QDs in the side view. The height (H), width (2H) and dimensions of the system are an integer multiple of the lattice constant.

First we investigate the energy level and band-mixing probability (or distribution of composition) of a typical InNBiAs/InP QD, as shown in Fig. 10.2 for QD of height = $12a$ and concentration of N and Bi = 2.86%.

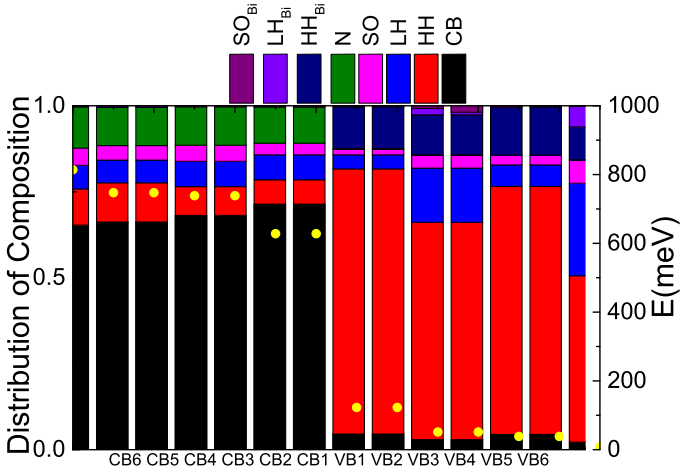

Figure 10.2: Electronic bandstructure and probability in band-mixing between electron, heavy-hole, light-hole, split-off-hole and N and Bi holes. The yellow dots in the bar represents the energy level of QD. The concentration of nitrogen and bismuth are 2.86% each and the height of QD is H=$12a$.

The CB# represents the conduction band index, while the VB# represents the valence band index. The distribution of compositions are shown in different colors as marked in the legend. We can see that the majority of CB is electron state and the majority of VB is heavy hole state. VB3 and VB4 have increased LH contribution compared to VB1 and VB2. The distribution of compositions for Bismuth resonant states and nitrogen resonant states are also shown. The coupling of the resonant states of N with the CB states (BAC) introduces the resonant N state contributions in the CB states shown in olive green. Similarly the coupling of the resonant states of Bi with the VB states (VBAC) introduces the resonant Bi state contributions in the VB states shown in navy blue, violet and indigo. The yellow dots in the bar represents the CB and VB energy levels of the QD.

Another important factor for QD is the QD size i.e the height. Fig. 10.3 shows the effect of size on the CB1 level, VB1 level and effective bandgap of the QD as a function of the Bi% composition in the QD. The bandedge of the CB (CB1) goes down, while the bandedge for the VB (VB1) goes up with increasing Bi concentration for three different heights of QD (H = $12a$, $16a$ and $20a$, as shown) when the nitrogen concentration is fixed at 1.6%. The gradient of CB1, VB1 and E_g is similar for all QD heights. However, as the size increases, the CB1 decreases while the VB1 increases (note: ΔCB1$>$ ΔVB1). Effectively the E_g = CB1 $-$ VB1 decreases. For a similar analysis keeping the Bi concentration fixed and varying the N composition instead, we would observe a similar trend for E_g.

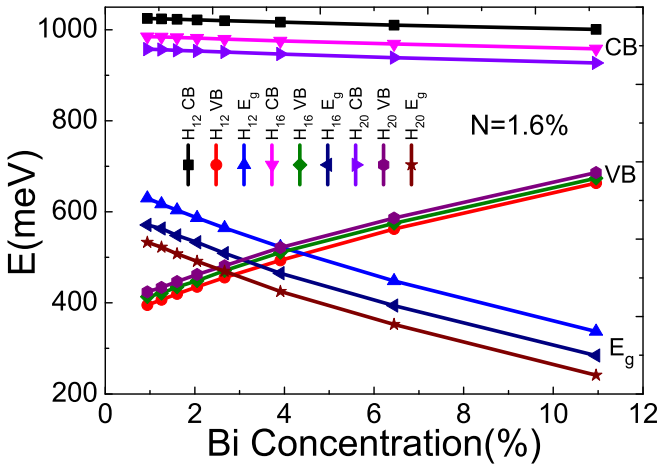

Figure 10.3: The variation in CB1, VB1 and bandgap E_g for InNBiAs/InP QDs of H = $12a$, $16a$ and $20a$ for varying composition of doped Bi and fixed N composition = 1.6%. We see that the range of the bandgap (emission energy) varies from ∼250 to ∼650 meV, making the InNBiAs/InP QDs suitable for mid-infrared (2–5 μm) applications.

In Fig. 10.3 we see that the range of the bandgap (emission energy) varies from ∼250 to ∼650 meV, making the InNBiAs/InP QDs suitable for mid-infrared (2–5 μm) applications.

Now we shall study the variation of the bandgap and strain with varying nitrogen and bismuth concentration in the InNBiAs/InP QD system. The results are shown in Fig. 10.4. As seen in Fig. 10.3, the initial idea to utilize the BAC and VBAC to realize the 2–5 μm emission is achievable. A suitable composition from the bandgap range of 250 to 650 meV could be chosen from Fig. 10.4.

In Fig. 10.4, both nitrogen and bismuth composition are varied from 0 to 10 %. The color contour shown the bandgap variation as indicated on the legend on the right, while the isopotential lines shown the ε_{xx} strain component. Incorporation of nitrogen and bismuth both reduce the bandgap. This can be seen by keeping one fixed and increases the composition of the other. But while Bi induces compressive strain, N helps to achieve lattice matching for suitable material growth by inducing an opposite tensile strain [78]. The dilute-N-Bi quantum structures are expected to have better electron and hole quantum confinement. Such fundamental properties of their electronic structure render these materials much suited for telecommunication laser applications compared to conventional III-V materials.

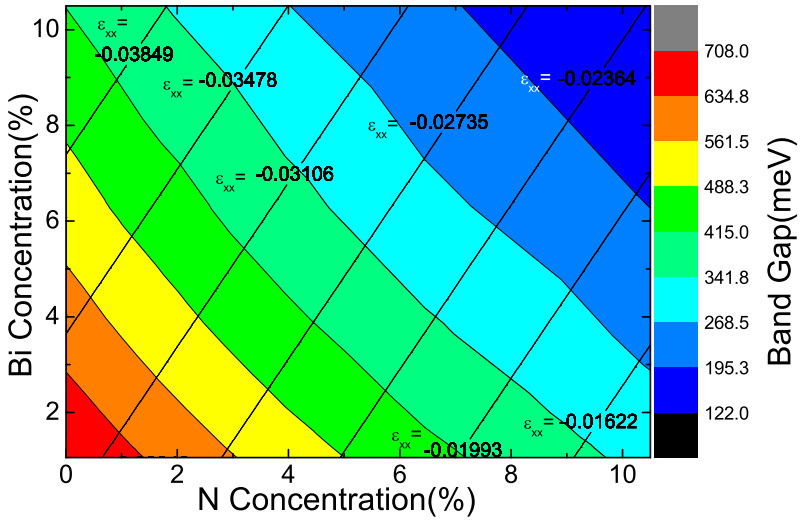

Figure 10.4: Variations in the bandgap (E_g) of $InN_xBi_yAs_{1-x-y}$/InP QDs at 300 K vs. N and Bi composition (%) as shown in the legend. The strain component ε_{xx} is mentioned using isopotential lines.

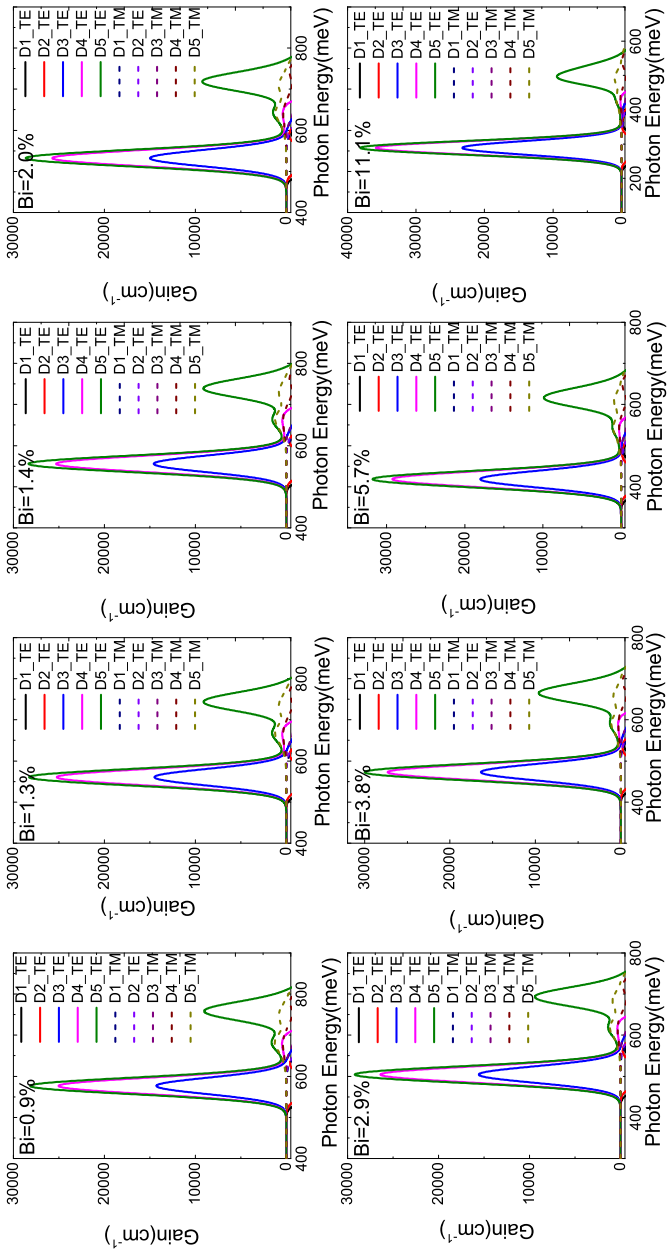

Figure 10.5: TE and TM mode optical gain for InNBiAs/InP QDs for varying injection carrier density from 1 to 5 $\times 10^{18}$ cm^{-3}. The Bi composition is varied from 0.9% to 11.1%, while the N composition is fixed at 2.9%. The height of QD is H = 12a.

Finally we study one of the most important factor for lasers i.e. the optical gain spectra in Fig. 10.5. Fixing the nitrogen concentration, we show the TE and TM mode optical gain spectra for InNBiAs/InP QDs for varying injection carrier density from 1 to 5 $\times 10^{18}$ cm^{-3}. The Bi composition is varied from 0.9% to 11.1%, while the N composition is fixed at 2.9%. The height of QD is H = $12a$. We tune the carrier densities and investigate the variation of gain as shown. As the carrier density increases the maximum gain increases. This is because for a larger injection carrier density, more number of charge carriers per unit volume are available for radiative recombination.

However, the magnitude of transverse magnetic (TM) mode optical gain is relatively smaller compared to the magnitude of transverse electric (TE) mode optical gain. As the Bi composition increases from 0.9% to 11.1%, the position of the first peak experiences a red-shift.

10.4 Summary and Conclusion

We have investigated the electronic bandstructure and optical gain of InNBiAs/InP QD. Utilizing the BAC and VBAC effects, we can achieve the goal that the emission wavelength of laser be in the range 2–5 μm while meeting the strain requirements for lattice matching for suitable material growth. We observe that, with an appropriate choice of N and Bi doping composition, we can tune the emission wavelength in the range of 2–5 μm suitable for mid-infrared device applications, such as guided missile technology, spectroscopy of trace gases and more recent medical applications such as less-invasive, high-precision, laser surgery. One of the important characteristics of the III-V semiconductor based mid-infrared laser structures is that it possesses strong differences in band gap energy and band discontinuity allowing the formation of deep confining QW in the laser's active region, which cannot be obtained by using group IV based semiconductors. With the advancement of epitaxy growth techniques, it is possible to fabricate high quality III-V based quantum confined structures for mid-IR lasers; and InNBiAs QDs as studied in this chapter can be a potential candidate for the same.

Chapter 11

InNBiSb/InSb Dilute Nitride-Bismide Quantum Wells

11.1 Introduction

DOPING of dilute nitride and bismide in III-V semiconductors is known to reduce the bandgap, as already discussed in Chapters 8, 9 and 10. Also, they induce opposite kinds of strain to attain a near-lattice-matching conducive for lattice growth. But particularly for InSb, as discussed in Sec. 1.2.2, with the simultaneous incorporation of nitrogen and bismuth we can see new emerging properties such as Quantum spin Hall (QSH) effect, which enables topological phase transitions to be realized in $InN_xBi_ySb_{1-x-y}$/InSb semiconductor QWs. QSH effect, a fundamentally new quantum state of matter and topological phase transitions are characteristics of a kind of electronic material, popularly referred to as topological insulators (TIs). TIs are similar to ordinary insulator in terms of their bulk bandgap, but have gapless conducting edge-states that are topologically protected. These edge-states are facilitated by the time-reversal symmetry and they are robust against non-magnetic impurity scattering. Recently, the quest for new materials exhibiting non-trivial topological state of matter has been of great research interest, as TIs find applications in new electronics and spintronics and quantum-computing devices. In this chapter, we propose and demonstrate as a proof-of-concept that QSH effect and topological phase transitions can be realized in $InN_xBi_ySb_{1-x-y}$/InSb semiconductor QWs.

Phase diagram for bandgap shows that as we increase the QW thickness, at a critical thickness, the electronic bandstructure switches from a normal to an inverted type.

In the course of this chapter, we shall confirm that such transition are topological phase transitions between a traditional insulator and a topological insulator exhibiting QSH effect – by demonstrating the topologically protected edge-states using the bandstructure, edge-localized distribution of the wavefunctions and edge-state spin-momentum locking phenomenon, presence of non-zero conductance in spite of the Fermi energy lying in the bandgap window, crossover points of Landau levels in the zero-mode indicating topological band inversion in the absence of any magnetic field and presence of large Rashba Spin-Splitting, which is essential for spin-manipulation in topological insulators.

11.2 Theoretical Framework

Band theory of solids is an excellent framework to study and understand TIs, wherein we use a crystal's momentum $\mathbf{k}$ to classify its electronic states by exploiting the translational symmetry of the crystal within a periodic Brillouin zone [64]. The energy bands that collectively determine the electronic bandstructure can be obtained by solving for the eigenvalues of the Hamiltonian H defining the quantum mechanical system [133]. Previously, both Bernevig *et al.* [67] and König *et al.* [68] have used the 8-band $\boldsymbol{k}\cdot\boldsymbol{p}$ model and 4-band effective Hamiltonian to study HgTe/CdTe QW TIs. But in this work we propose a 16-band $\boldsymbol{k}\cdot\boldsymbol{p}$ model due to the presence of N and Bi in our system. In addition to to Kane's 8-bands, we need two additional bands to incorporate the local N resonant s-like states. Moreover, we also need six additional bands to incorporate the local Bi resonant p-like states with freedom of spin, including spin-orbital coupling [78]. According to the methodology introduced in refs. [78, 86, 173, 174], the 16-band Hamiltonian for $InN_xBi_ySb_{1-x-y}$ is represented in the Bloch function basis as described in Sec. 2.3.4 with all the Hamiltonian elements. All material parameters related to InSb used in this work can be found in Table A.2, while other parameters corresponding to N and Bi impurities can be found in Table A.3 in Appendix A.

11.2.1 Effective Hamiltonian derivation

In order to investigate the topological transitions in edge states of TIs, we need to construct an effective Hamiltonian like the one introduced by Bernevig *et al.* [67]. The projection of the conventional Hamiltonian from the $\boldsymbol{k}\cdot\boldsymbol{p}$ theory given by Eq. (2.34) into the low energy

subspace can be done in two steps [175]. First, we divide the Hamiltonian into two parts:

$$H = H(0,0,-i\frac{\partial}{\partial z}) + H^{'}(k_x, k_y, -i\frac{\partial}{\partial z}) \tag{11.1}$$

where $H(0,0,-i\frac{\partial}{\partial z})$ is the non-perturbative Hamiltonian and $H^{'}(k_x, k_y, -i\frac{\partial}{\partial z})$ is the perturbative Hamiltonian. After numerically diagonalizing $H(0,0,-i\frac{\partial}{\partial z})$, we obtain the eigenenergies E_m and eigenstates ψ_m where m is the band index. In order to perform the degenerate perturbation calculation, we need to cast the eigenstates of $H(0,0,-i\frac{\partial}{\partial z})$ into two classes. The first one, denoted as A class, includes the low energy subspace that we are interested in. The second class, denoted as B class, includes the states that need to be taken into consideration in the subsequent perturbative iteration.

Now, we calculate the effective Hamiltonian according to Lowding perturbation method, given as [175]

$$H^{eff}_{mm'} = E_m\delta_{mm'} + H'_{mm'} + \frac{1}{2}\sum_l H'_{ml}H'_{lm'}(\frac{1}{E_m - E_l} + \frac{1}{E_{m'} - E_l}) \tag{11.2}$$

where $m, m' \in A$ class and $l \in B$ class. Hence this calls for an appropriate choice of A class and B class to construct the effective Hamiltonian which can accurately describe the $InN_xBi_ySb_{1-x-y}$ QW bandstructure.

11.2.2 Two-terminal conductance

Based on the effective Hamiltonian, we can calculate the two-terminal conductance of a finite rectangular sample to confirm the existence of topologically protected edge states. At absolute zero temperature, the two-terminal conductance can be expressed by Green's function as [176]

$$G = \frac{e^2}{h}\mathrm{Tr}\left[\Gamma_S G^r \Gamma_D G^a\right] \tag{11.3}$$

where $G^{r/a}$ is the retarded/advanced Green's function, and $\Gamma_{S(D)} = i\left(\sum^r_{S(D)} - \sum^a_{S(D)}\right)$ with $\sum^{r/a}_{S(D)}$ being the retarded/advanced self-energies due to the source (drain) lead, respectively.

11.3 Results and Discussions

11.3.1 Band Inversion Phenomenon in InNBiSb/InSb QWs

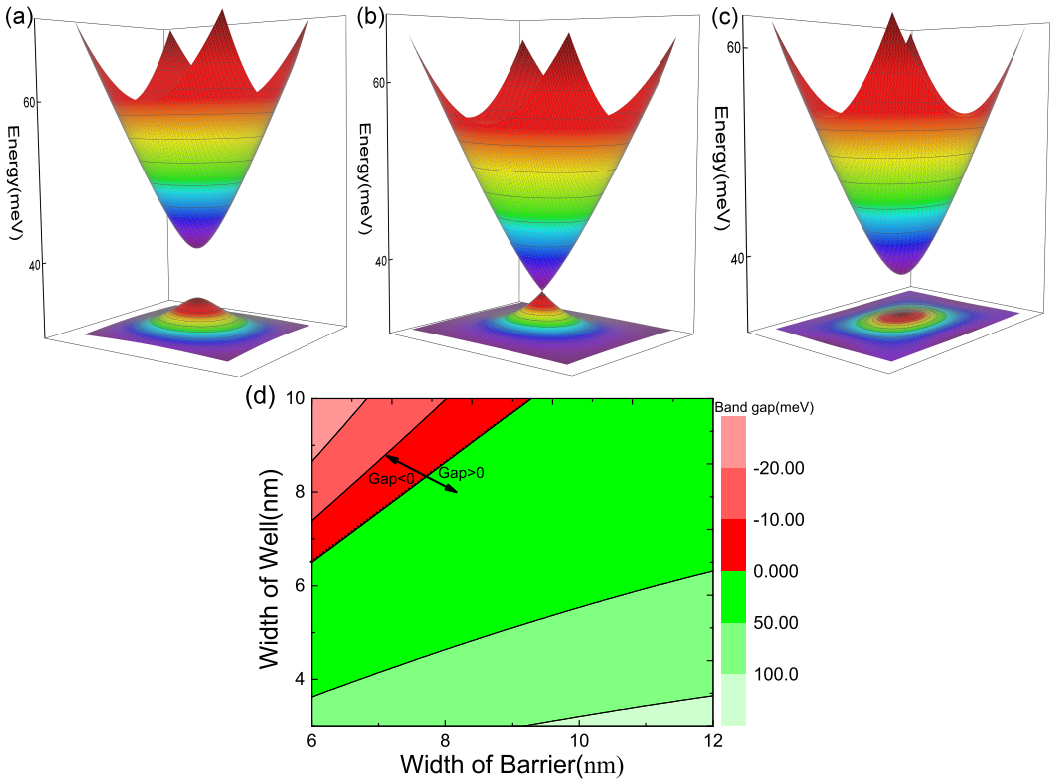

Figure 11.1: The electronic bandstructure around the Γ–point of the $InN_xBi_ySb_{1-x-y}$/InSb QW for well-width of (a) 7 nm, (b) 7.7 nm, and (c) 8.2 nm, respectively. The barrier width was fixed at 7.0 nm for all three cases. N and Bi concentration of well region is fixed at 2.4% and 3.2% respectively, leading to about 0.48% tensile strain. We find that QWs below a critical thickness (7.7 nm in our case) have 'normal' electronic structure, while those above the critical thickness have an inverted electronic structure. (d) A phase diagram for the topological phase transitions showing the variation in bandgap as a function of the width of well and barrier. The whole region is divided into two different phases: the positive bandgap corresponds to the trivial phase and negative bandgap corresponds to the non-trivial phase, respectively.

We have studied $InN_xBi_ySb_{1-x-y}$/InSb QWs of varying well thickness and barrier thickness having varying compositions of N and Bi. It was found that topological phase transition can be realized in $InN_xBi_ySb_{1-x-y}$ by suitably increasing the width of the QW.[1] We have considered $InN_xBi_ySb_{1-x-y}$ of well widths 7 nm, 7.7 nm and 8.2 nm and fixed InSb barrier of width 7.0 nm. The well region had concentrations of N and Bi set to 2.4% and 3.2% respectively, leading to about 0.48% tensile strain. Fig. 11.1 (a–c) shows the electronic bandstructures of these three cases around the Γ–point demonstrating band-inversion with increasing QW widths. For the narrowest QW of the three (7 nm), the first CB subband (CB1) is at a higher energy than the first VB subband (VB1) as shown in Fig. 11.1 (a). When the well-width is increased, the CB1 and VB1 tend to approach each other. We found that for a critical well-width of 7.7 nm, gapless state can be achieved where the CB1 and VB1 energies coincide, as shown in Fig. 11.1 (b).[1] However, for well-width larger than the critical width, the CB1 and VB1 states crossover and band-inversion is achieved. For instance, QW of 8.2 nm well-width has an inverted bandstructure as shown in Fig. 11.1 (c).

Now, we compute the energy bandgaps for $InN_xBi_ySb_{1-x-y}$/InSb QWs having varying well-width (6 nm to 10 nm) and barrier width (6 nm to 12 nm). Fig. 11.1 (d) shows the bandgap as a function of the width and barrier of the QW. This can serve as a phase diagram for the topological phase transitions, with the positive bandgap corresponding to the trivial phase and negative bandgap corresponding to the non-trivial phase, respectively.

11.3.2 The effective Hamiltonian of InNBiSb/InSb QWs

The band-inversion characteristic of $InN_xBi_ySb_{1-x-y}$/InSb QWs studied in Fig. 11.1 is a necessary but not sufficient condition to establish the existence of QSH effect and topologically protected surface states. But, in order to confirm that the phase exhibiting band-inversion is indeed a topological phase, we will demonstrate the existence of edge states from a quasi-one-dimensional ribbon geometry. To investigate the edge states, we have constructed an effective Hamiltonian according to the theoretical description of Eq. (11.2). Our 6-band effective Hamiltonian can be expressed as

[1] Konig *et al.* [68] experimentally demonstrated TIs for the first time in HgTe QWs. They found that QWs below a critical thickness had 'normal' electronic structure, while those above the critical thickness had an inverted electronic structure. The former showed zero edge state conductance, while the latter exhibited an edge channel transport conductance as expected in a QSH insulator, which was independent of the QW thickness, indicative of the fact that they were edge-states driven.

$$H^{eff} = \begin{pmatrix} H(\mathbf{k}) & 0 \\ 0 & H^*(-\mathbf{k}) \end{pmatrix} \tag{11.4}$$

where $H(\mathbf{k}) = \varepsilon(\mathbf{k})\mathbf{I}_{3\times 3} + h(\mathbf{k})$.

$$\varepsilon(\mathbf{k}) = C - Dk_{||}^2 \tag{11.5}$$

$$h(\mathbf{k}) = \begin{pmatrix} M - Bk_{||}^2 & A_2k_- & A_1k_+ \\ A_2k_+ & -\left(M - Bk_{||}^2\right) & Nk_+^2 \\ A_1k_- & Nk_-^2 & \left(E - Fk_{||}^2\right) \end{pmatrix} \tag{11.6}$$

$$\tag{11.7}$$

where $k_{||}$ denotes the in-plane momentum, and $k_\pm = k_x \pm ik_y$. The A_1, A_2, B, C, D, E, F and N are expansion parameters that depend on the heterostructure. M is the Dirac mass parameter. The new parameters E, F and N account for the additional VB2 subband in our calculation. These parameters were calculated to be: $A_1 = -0.4395$ eVnm, $A_2 = -0.2911$ eVnm^2, $B = -0.5841e$ Vnm^2, $C = 0.0347$ eV, $D = -0.4116$ eVnm^2, $E = -0.0145$ eV, $F = 0.5114$ eVnm^2, $N = 0.1070$ eVnm^2, $M = -0.0031$ eV. The Dirac mass parameter M can be continuously tuned from a positive value $M > 0$ for thin QWs with thickness less than the critical thickness (7.7 nm in our case), to a negative value $M < 0$ for thick QWs with thickness less than the critical thickness. For our $InN_xBi_ySb_{1-x-y}$/InSb QW case of 8.2 nm, we have $M < 0$, which is consistent with that of the CdTe/HgTe QW TI [67, 68].

Unlike the 4-band model of HgTe/CdTe QW case [67], ours is a 6-band model. There are two main reasons for this difference. Firstly, the states most involved in the electronic structure determination are the first conduction subband (CB1) and first valence subband (VB1). The major components contributing to them are light-hole (LH) for CB1 and electron (E) for VB1, as shown in Fig. 11.2. But for the HgTe/CdTe QW case, the major components of CB1 and VB1 were heavy-hole (HH) and E, respectively. In our case, it is the tensile strain introduced by impurities that push the LH band higher than the HH band. Secondly, the gap between the VB1 subband and VB2 subband is too small, which

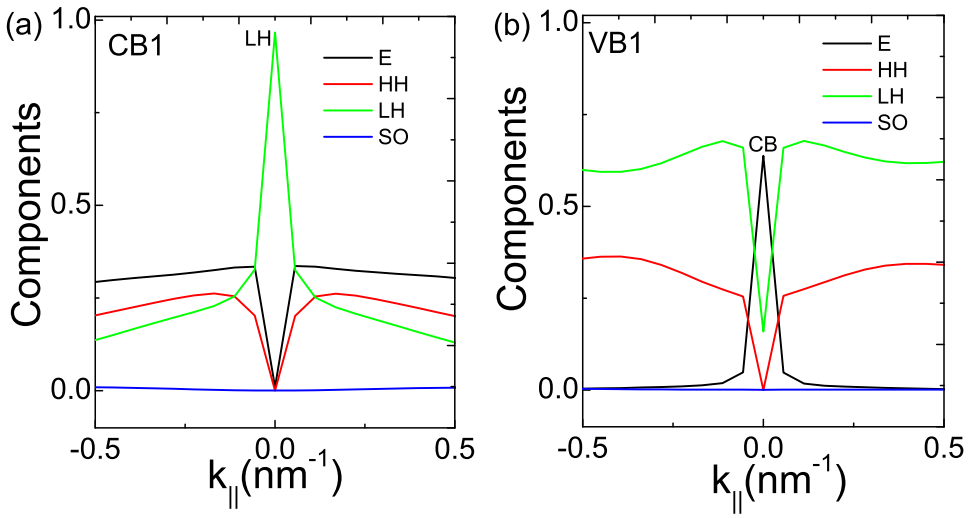

Figure 11.2: The electron (E), heavy-hole (HH), light-hole (LH) and split-off hole (SO) band components of the (a) first conduction subband (CB1) and (b) first valence subband (VB1) are shown. Around the Γ point ($k_{||} = 0.0$ nm^{-1}), the majority of the CB1 is LH dominated while the majority of VB1 is E dominated. This is a direct confirmation of band-inversion. Unlike the HgTe/CdTe QW case, here the inverted bands are E and LH dominated, which is a result of the induced tensile strain.

leads to strong coupling between the VB1 and VB2 states. Therefore, the projected low energy subspace, A class, needs to include CB1, VB1 and VB2 with the spin degeneracy leading to a 6-band effective Hamiltonian. Another noteworthy point is that the N-related terms $Nk_{\pm}^2$ in Eq. (11.4), takes into account the coupling between HH and E bands.

Now, using our effective 6-band Hamiltonian we will study the QW case of Fig. 11.1 (c), which demonstrated band-inversion and had a well with 2.4% N and 3.2% Bi impurity doping, a well-width of 8.2 nm and barrier width of 7.0 nm. Fig. 11.3 (a) shows the bandstructure of this QW case calculated from the effective Hamiltonian of Eq. 11.4 (shown in color lines), which is in good agreement with the bandstructure calculated by full 16-band $\boldsymbol{k}\cdot\boldsymbol{p}$ envelope functions of Eq. (2.34) (shown in black lines) near the Fermi energy level. This verifies the validity of our effective Hamiltonian of Eq. (11.4).

11.3.3 Edge states and spin-momentum locking phenomenon

Using our newly derived effective Hamiltonian, we have calculated the band structure of a ribbon geometry, as shown in Fig. 11.3 (b). The red curves show topological edge states which connect the CB and VB. For this ribbon structure, Fig. 11.3 (c) illustrates that the

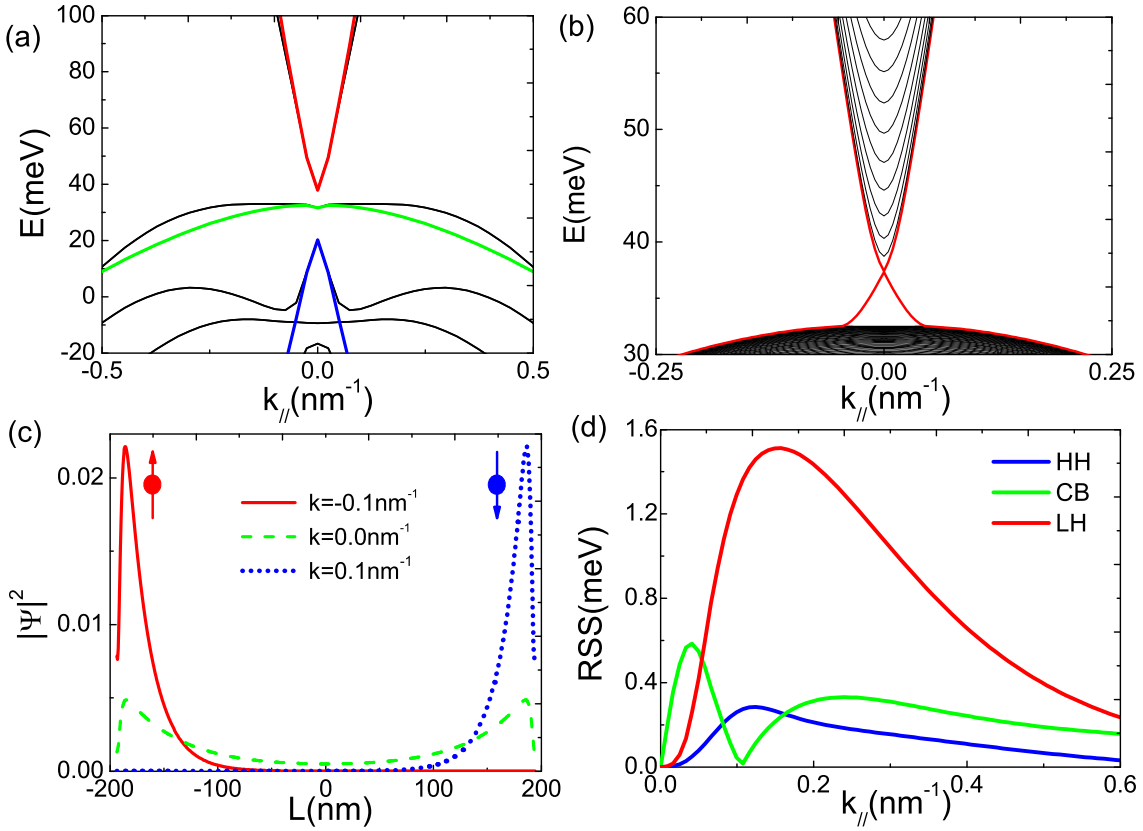

Figure 11.3: (a) Comparison of the electronic bandstructure of $InN_xBi_ySb_{1-x-y}$/InSb QW of Fig. 11.1 (c) calculated by the 16-band $\boldsymbol{k}\cdot\boldsymbol{p}$ model with envelope functions (shown by black curves) and the 6-band effective Hamiltonian (shown by red, green and blue curves corresponding to LH, CB, HH respectively). The differences between the 16-band model and 6-band effective model around the Γ–point is minuscule. This confirms the rationality of using our 6-band effective Hamiltonian. (b) The electronic bandstructure of the ribbon geometry based on our 6-band effective Hamiltonian. The red curves connecting the CB and VB demonstrate the existence of topological edge states. (c) The wavefunctions have localized distribution at the ribbon edges and have edge-state spin-momentum locking, which justifies the existence of topological edge states. (d) When our QW system in subjected to external electric field ($F = 0.5$ mV/nm), there is Rashba Spin-Splitting of CB, LH and HH, as shown. The magnitude of RSS even exceeds 1 mev for LH. Such huge splitting is an enabling feature for several spintronics application.

associated wavefunctions at the ribbon edges for $k_{||} = -0.1, 0.0$ and 0.1 nm^{-1}. Notice that for $k_{||} = -0.1$ and 0.1 nm^{-1}, the wavefunctions are localized at the edges and are spin-momentum locked. This is a typical QSH effect phenomenon demonstrated by 2D TIs [67]. This is the first proof that confirms the TI properties.

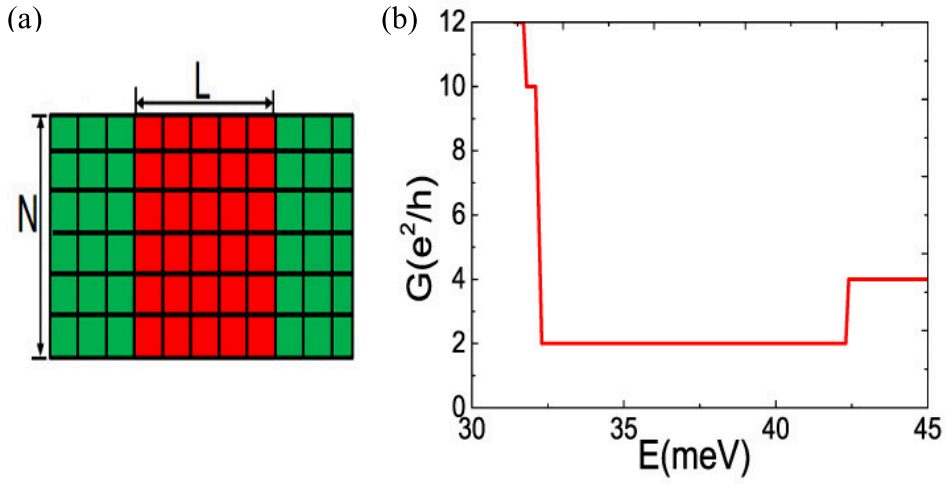

Figure 11.4: The two-terminal conductance of rectangular superlattice sample of $L \times N$. (a) The sample of the two-terminal sample. Note that the red region represents central region or sample, and the green regions represent the external infinite leads. (b)The non-zeros conductance indicates the presence of topological edge states.

Another important term Rashba spin splitting (RSS)[2] is associated with the splitting of CB or VB when the system is subjected to an external electric field. The RSS of our QW system of Fig. 11.1 (c) is shown in Fig. 11.3 (d), where the external electric-field is $F = 0.5$ mV/nm. The nonlinear RSS behavior agrees well with the previous results [81]. The magnitude of RSS was found to be in the order of 1–2 meV. Such remarkable Rashba spin-orbit coupling offers possibilities of generation, manipulation and detection of spin currents [177, 178].

11.3.4 The transport properties of edge states

Furthermore, the transport properties of a 2-terminal rectangular superlattice sample of dimensions $L \times N$ are investigated. The two-terminal conductance, G of a finite sample as a function of Fermi energy is shown in Fig. 11.4. Even when the Fermi energy lies in the bandgap window, the conductance, G is not zero, but has a finite value (here it is $2e^2/h$). It exhibits an edge channel transport conductance as expected in a QSH insulator, which is independent of the QW thickness, indicative of the fact that they are edge-states driven. The second proof in the view of the transport properties demonstrates the edge state of TI.

[2]RSS stands for Rashba Spin-Splitting, which is a momentum-dependent splitting of spin bands in semiconductor heterostructures.

11.3.5 The effect of magnetic field

The third proof to confirm the TI properties comes from the magnetic field effects consideration. Now we shall investigate the influence of a perpendicular magnetic field $\mathbf{B} = B\hat{z}$ (without the loss of generality. we assume $B > 0$). When the two-dimensional electron gas is subjected to a perpendicular magnetic field, the wavevector get modified as $\mathbf{k} = -i\nabla + e\mathbf{A}$, where $\mathbf{A}$ is the vector potential such that $\mathbf{B} = \nabla \times \mathbf{A}$. The Zeeman energy induced by the magnetic field here is ignored. Here, we choose the Landau gauge $A = (-By, 0, 0)$. The Laudau levels (LLs) can be found by defining the two ladder operators $a = -\left(\frac{y}{l_B} + l_B\partial_y - l_B k_x\right)/\sqrt{2}$, and $a^\dagger = -\left(\frac{y}{l_B} - l_B\partial_y - l_B k_x\right)/\sqrt{2}$, where the magnetic length $l_B = \sqrt{\hbar/eB}$. Now, we assume the following trial solution

$$\psi_n(x,y) = \frac{1}{\sqrt{L_x}} e^{ik_x x} \begin{pmatrix} C_{n_1}|n\rangle \\ C_{n2}|n+1\rangle \\ C_{n_3}|n-1\rangle \\ C_{n_4}|n\rangle \\ C_{n_5}|n-1\rangle \\ C_{n_6}|n+1\rangle \end{pmatrix} \qquad n \geq 1 \tag{11.8}$$

$$\psi_n(x,y) = \frac{1}{\sqrt{L_x}} e^{ik_x x} \begin{pmatrix} C_{n_1}|0\rangle \\ C_{n2}|1\rangle \\ 0 \\ C_{n_4}|0\rangle \\ 0 \\ C_{n_6}|1\rangle \end{pmatrix} \qquad n = 0 \tag{11.9}$$

where $|n\rangle = \frac{1}{\sqrt{n!2^n l_B\sqrt{\pi}}} \exp\left[-\frac{(y-y_0)^2}{2l_B^2}\right] H_n\left(\frac{y-y_0}{l_B}\right)$ and H_n are Hermite polynomials. As Buhmann *et al.* [179] have stated, that there will be a crossing point between zero-mode LLs for topological phase while there will be no crossing point for normal phase; this can be used to verify the topological phase transition. Fig. 11.5 gives the LLs structure. The crossing point between the two LLs labeled by red curves indicates the existence of topological band inversion at zero magnetic field [179] as the case of the CdTe/HgTe QW [68].

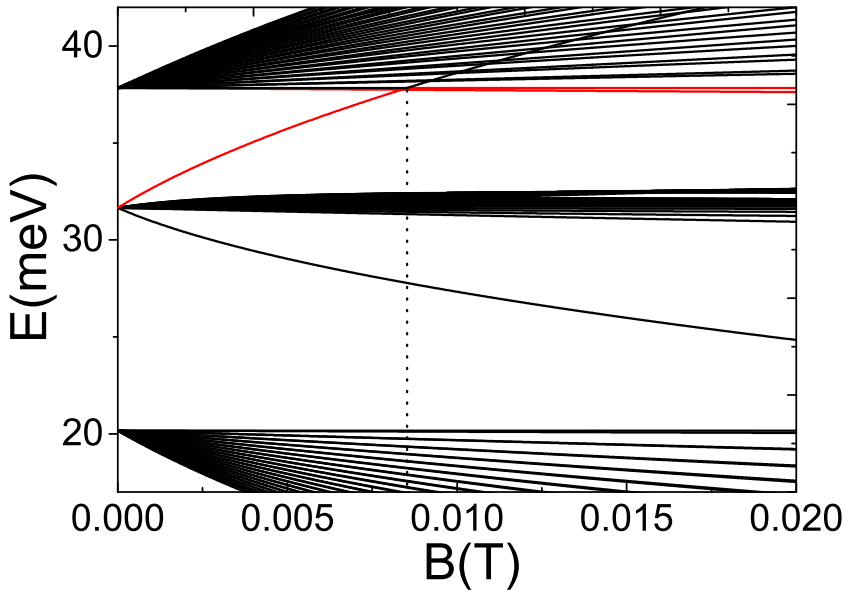

Figure 11.5: The Laudau levels (LLs) fan figure calculated according to our effective 6-band model. The crossing point between the two red curves indicates the topological transition [179].

11.3.6 Topological phase transition with varying impurity concentrations

Having studied the band inversion in $InN_xBi_ySb_{1-x-y}$ QWs of fixed N and Bi composition, we would like to study the effect of the impurity doping concentration on its properties. The possibility of the use of $InN_xBi_ySb_{1-x-y}$ QWs as TIs opens up avenues for designing TIs with effective bandgap and strain tuning by varying the doping concentrations of N and Bi. For the same, we have studied a range of QWs with fixed well-width of 7.0 nm and barrier width of 7.0 nm and varying N composition (0% to 4%) and varying Bi composition (0% to 8%). Fig. 11.6 shows the topological phase diagram for the topological phase transitions showing the variation in bandgap as a function of N and Bi concentration. The whole region is divided into two different phases: the positive bandgap corresponds to the trivial phase and negative bandgap corresponds to the non-trivial phase, respectively. A prominent feature is that the boundary separating the positive and negative bandgap regions is a broken line. This is different from Fig. 11.1 (d) in which the boundary is a straight line. We explain the reason here. Changing the well-width and barrier-width keeps the strain invariant while different concentrations of N and Bi impurities leads to varying degrees of tensile or compressive strain. The type of the strain directly determines the highest valence subbands (VB1). Tensile strain corresponds to $|LH\uparrow\downarrow\rangle$, while compressive strain

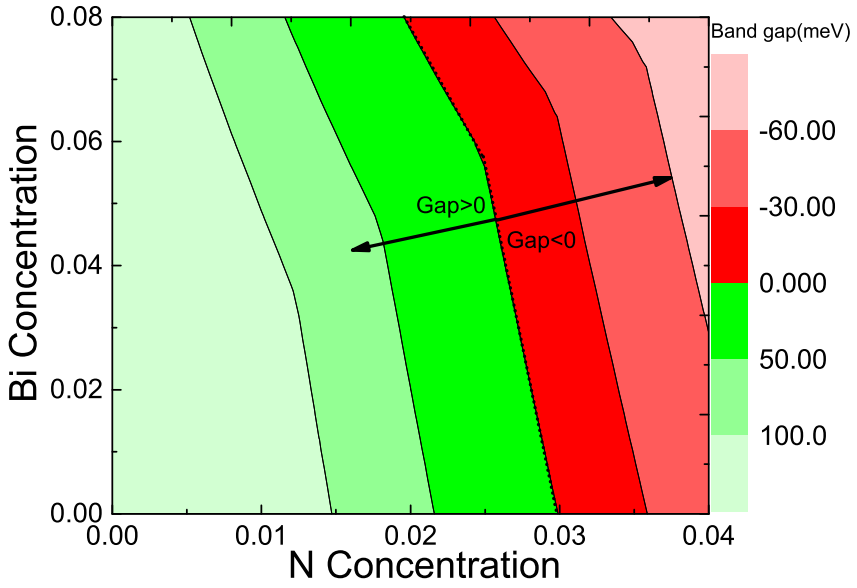

Figure 11.6: A phase diagram for the topological phase transitions showing the variation in bandgap as a function of N and Bi concentration. Similar to Fig. 11.1 (d), the region is divided into two different phases: the positive bandgap corresponds to the trivial phase and negative bandgap corresponds to the non-trivial phase, respectively. Here, the well-width and barrier-width is fixed at 8.2 nm and 7.0 nm, respectively. The magnitude of negative band gap can exceed the 60 meV mark. This is essential for practical implementation of TIs.

corresponds to $|HH\uparrow\downarrow\rangle$ subbannds as the highest valence subbands. Therefore, the kind of the phase boundary in Fig. 11.6 corresponds to the differences arising from these two strain cases.

11.4 Summary and Conclusion

We have proposed a practical scheme to realize quantum Hall spin (QSH) effect and topological phase transitions in $InN_xBi_ySb_{1-x-y}$/InSb QW. The well-width, barrier-width and concentrations of N and Bi impurity doping can be used to effectively attain band-inversion as we have comprehensively demonstrated. The coupling between the impurity resonant states is critical and has a profound effect on the narrowing down of the bandgap until band-inversion occurs.

In summary, we have confirmed the (*i*) band-inversion in $InN_xBi_ySb_{1-x-y}$ QWs above a certain critical thickness [Fig. 11.1 and Fig. 11.2], (*ii*) topologically protected edge-states using bandstructure analysis [Fig. 11.3 (b)], (*iii*) edge-localized distribution of the wave-

functions and edge-state spin-momentum locking phenomenon [Fig. 11.3 (c)], (*iv*) presence of non-zero Hall conductance in spite of the Fermi energy lying in the bandgap window [Fig. 11.4], (*v*) crossover points in Landau levels for which $n = 0$ indicating topological band inversion in the absence of any magnetic field, and (*vi*) presence of a large Rashba Spin-Splitting [in the order of 1–2 eV in the presence of an external electric field of 0.5 mV/nm], which is essential for spin-manipulation in topological insulators. We have also provided the phase diagrams of topological states for our $InN_xBi_ySb_{1-x-y}$ QW structures with varying well/barrier-widths and varying N abd Bi doping concentrations, which is helpful for experimental realizations.

In conclusion, with all of the aforementioned characteristics in view, we are in a position to confirm the existence of QSH effect and topological phase transitions in $InN_xBi_ySb_{1-x-y}$/InSb quantum wells as a proof-of-concept.

Chapter 12

Thesis Summary and Conclusions

12.1 Thesis Summary

Semiconductors have been a major player in forwarding science and technology throughout the 20^{th} century and continues to be at the core of several ubiquitous applications such as computers, cellular phones, televisions, data storage, display technologies, broadband Internet, mobile telephony and satellite communication today. It will play an even critical role in revolutionizing modern society in the decades to come. Quantum confined semiconductor nanostructures such as quantum dots, quantum wells, quantum rings and the coming-of-age nanoplatelets have been the key enablers in this evolution.

Among the wide range of available and newly studied semiconductor quantum nanostructures, firstly (*i*) NPLs and QRs of II-VI materials and alloys thereof, and secondly (*ii*) QDs and QWs of III-V dilute nitride/bismide alloy materials are two families of nanostructures that have emerged as very promising candidates for novel semiconductor device and optoelectronic applications. In this thesis, we report studies on the aforementioned two families of semiconductor quantum nanostructures.

In Chapter 1 we discuss the history, background and motivation of the work done and reported in this thesis and follow it with a review of the relevant literature. In Chapter 2 we lay down the mathematical framework of the optoelectronic theory of semiconductors to study the various optoelectronic properties of semiconductor quantum nanostructures studied in the rest of the thesis, broadly under two parts as described below.

The first part of the thesis, spanning Chapters 3, 4, 5, 6 and 7 focuses on the study of II-VI (CdSe and CdS) NPLs and optoelectronic properties thereof under varying physical

conditions such as geometrical dimensions, temperature, material composition, topology and optical polarization.

Furthermore, the second part of the thesis, spanning Chapters 8, 9, 10 and 11 focuses on the study of quaternary dilute nitride/bismide III-V (InNBiAs, InNBiSb and GaNBiAs) QDs and QWs for their optoelectronic properties and application.

12.2 Thesis Conclusions

We begin by discussing the history, background and motivation of semiconductors and semiconductors quantum nanostructures in **Chapter 1**, leading to the premise of the work done and reported in this thesis. Thereafter, we provide an in-depth review of the relevant literature giving a general account of the current state-of-the-art practices concerning the various aspects covered in this thesis. In **Chapter 2**, we give a mathematical account of the various optoelectronic processes in semiconductors. We introduce, under fair mathematical rigor, the $\boldsymbol{k}\cdot\boldsymbol{p}$ perturbation theory and multi-band variants thereof to calculate the bandstructure of semiconductors. This is followed by a mathematical treatment of the photon generation process in semiconductors and the influence excitonic interactions has on them. Material parameters used in our calculation and results reported are enlisted comprehensively in **Appendix A**. The core machinery of our modeling and simulation study of semiconductor quantum nanostructures uses an effective-mass envelope function theory based on the 8-band and 16-band $\boldsymbol{k}\cdot\boldsymbol{p}$ models. The optical properties calculations are based on the density-matrix equation and takes into consideration the excitonic effects with intraband scattering and temperature effects. During the course of the work done for this thesis, the source code for the various multi-band $\boldsymbol{k}\cdot\boldsymbol{p}$ models were developed in-house, and packaged into a software platform called *KdotPsoft*, an end-to-end modeling and simulation software platform for semiconductor quantum nanostructures with a friendly graphical user interface. **Appendix B** explains further about *KdotPsoft*, its internal modules, connectivities, dependencies and working flow.

For every nanostructure (NPL, QD or QW) studied, we have performed a comprehensive inspection on a range of optoelectronic characteristics such as the strain tensor profiles, excitonic transition energies, optical transition matrix elements, Fermi factors, spatial change densities, electron-hole wavefunctions, electronic bandstructure/band lineups, band-mixing probabilities, photoluminescence emission spectra, optical gain/absorption spectra, maximum and differential gains and transparency properties.

Here, we enlist in a structured fashion the Chapter-wise (and related Appendices) research findings and conclusions reported in this thesis. Chapters 3, 4, 5, 6 and 7 focus on the study of II-VI (CdSe and CdS) NPLs and optoelectronic properties thereof under varying physical conditions such as geometrical dimensions, temperature, material composition, topology and optical polarization. Chapters 8, 9, 10 and 11 focuses on the study of quaternary dilute nitride/bismide III-V (InNBiAs, InNBiSb and GaNBiAs) QDs and QWs for their optoelectronic properties and application. And this is Chapter 12 which summarizes and concluded the thesis.

- **Chapter 3: CdSe and CdS Nanoplatelets: Dimension Effect**
  We studied the electronic bandstructure, band mixing probability, charge densities, optical transitions and gain of quasi two-dimensional colloidal CdSe and CdS NPLs in the zincblende phase – as a function of vertical thickness and lateral size. Variations in size, thickness and material significantly affect the energy levels, optical gain, etc. There is a red shift in the gain peak position as we move from CdS to CdSe. For geometrically identical NPLs, CdSe has lower photon emission energy because of its lower bandgap. However, it has a higher TME due to its relatively lower effective electron mass. CdS has a much higher contribution from split-off holes because it's spin-orbit splitting energy is over six times smaller. For any given NPL, an increase in carrier density leads to the band filling effect. The peak gain increases due to an increase in the Fermi factor. But for a fixed carrier density, the Fermi factor is higher for volumetrically larger NPLs. Incidentally, volumetrically larger NPLs need smaller injection carrier density to surpass absorption and transparency and produce gain. Thus the overall gain characteristics are determined by an sum effect of all these influencing factors.

  On the whole, the often neglected lateral size parameter of NPL was found to be of significant importance affecting the bandstructure and band mixing probabilities. It also contributes to the optical gain positions and magnitude. Therefore, it is recommended that both lateral size and thickness must be carefully considered for NPL device designs and applications for a precise estimation of the performance characteristics.

- **Chapter 4: CdSe Nanoplatelets: Temperature Effect**
  After studying the effect of NPL dimensions, we studied the electronic bandstructure, probability in band mixing, charge densities, optical transition matrix element, characteristic PL emission energy, linewidth and integrated intensity of CdSe NPLs – as a function of temperature, which is of critical importance particularly for commercial device applications at elevated temperature. From the quantum physics and optoelectronics point-of-view, the implications of rise in operation temperature of NPLs are many-fold, such as (*i*) reduction in effective band-edge transition energy, (*ii*) fall in optical transition matrix element strength, (*iii*) reduction in intraband state gaps, faster so in CB compared to VB, (*iv*) promotion of interband *e-h* coupling, (*v*) modification in *hh-lh-so* band mixing probabilities, (*vi*) reduction in Fermi factor, (*vii*) shift of CB and VB quasi Fermi energy levels towards the band edges, and reduction in quasi Fermi separation, (*viii*) invariance in the charge density profile, (*ix*) redshift in peak photon emission energy in PL spectra, (*x*) widening of PL spectral linewidth owing to intraband scattering, (*xi*) exponential fall in PL integrated intensity, and (*xii*) phenomenological evidence of reversible and irreversible losses induced which affects the sample quality and dictates the PL traceability.

  We also theoretically and experimentally studied the temperature-dependent optoelectronic characteristics of quasi-2D colloidal CdSe NPLs and established a model to predict and study the electronic bandstructure and PL spectra of NPLs at any arbitrary temperature, which can be effectively used by experimentalists to optimize device design iterations.

  - **Appendix C: Nanoplatelets Synthesis and Characterization**
    Here we describe the NPL synthesis techniques, purification and film preparation methods and TEM/optical characterization processes.
  - **Appendix D: Low Temperature NPL Photoluminescence Characterization**
    Here we study in tandem and validate our theoretical calculations and experimental PL measurements of 4 ML CdSe NPLs with existing low-temperature results in literature.

- **Chapter 5: Cd(S,Se) Nanoplatelets: Alloying Effect**
  After studying the effect of NPL dimensions and temperature, we studied the elec-

tronic bandstructure, band-mixing probabilities, charge densities, optical gain Fermi factor and transparency properties of quasi two-dimensional CdS_xSe_{1-x} alloy NPLs in the ZB phase – over contrasting size, thickness and temperature.

Variations in the composition of Cd(S,Se) NPLs significantly affects its energy levels, band-mixing probabilities and optical gain. Those with a higher Se fraction have a lower E1-H1 transition energy. For NPLs of the same composition, volumetrically larger ones have lower transition energy due to lower confinement. Increasing the temperature has a similar effect due to the negative gradient of bandgap. NPLs with higher Se fraction, however, have a larger TME due to a lower effective electron and hole masses. For NPLs of the same material, decreasing its volume reduces the TME owing to the minimized overlap integral between the electron and hole wavefunctions. Increasing the temperature also has a detrimental effect on the TME. Moving from CdS to CdSe, the emission peak position experiences a redshift due to effective bandgap reduction. For a given alloy composition, there is slight blueshift (and rise in intensity) with increasing carrier density due to band-filling effect. NPLs with higher Se fraction produce larger gain due to their higher Fermi factors and exhibit transparency at lower densities. The maximum gain of NPLs grows rapidly in the beginning but the differential gain saturates after a point. A study of the size and thickness effect shows that volumetrically larger NPLs can accommodate more recombination excitons resulting in higher gain compared to smaller NPLs. This follows from their higher Fermi factor. Also larger NPLs have a lower density demand to attain the exciton count to obtain transparency. Increasing the temperature of NPLs has a detrimental effect on the Fermi factor reducing its gain intensity. Also warmer NPLs need greater carrier density for transparency.

- **Chapter 6: CdSe Nanoplatelets: Polarized Excitonic Absorption**
  As concluded from the preceding chapters, NPLs experience strong 1D vertical confinement, which induces a large exciton binding energy, while the increased exciton center-of-mass extension results in giant oscillator strength transition (GOST) in NPLs. This significantly enhances the absorption cross-section of NPLs.

  Based on this, we studied the electronic bandstructure (energy dispersion relation), probabilities of conduction and valence band-mixing due to coupling, charge densities (squared wavefunctions), relative band lineups and polarization dependent optical absorption spectra dependent on the transition matrix elements (TME) plus the den-

sity of states (DOS) for quasi two-dimensional CdSe NPLs of different thicknesses in the ZB phase. The absorption spectra of NPLs has a well recognized trend with a higher intensity electron/heavy-hole (HH) absorption peak and a blue-shifted lower intensity electron/light-hole (LH) absorption peak. However, we have experimentally observed anomalous absorption spectral properties in ultrathin sub-nm (2 monolayer) CdSe NPLs characterized by increased intrinsic absorption and inverted HH and LH relative peak intensities. This was found to be consistent with our theoretical findings, wherein the emergence of such properties has been attributed to the polarization dependent TMEs and the density of states, both of which have fundamental affects on the absorption spectra, determined by the HH and LH excitons. Other thickness dependent absorption characteristics of NPLs were also identified.

  - **Appendix E: Anomalous Spectral Characteristics of sub-nm CdSe NPLs**

    The relative strength of the HH and LH/SO absorption largely depends on the lateral size of the ultrathin sub-nm 2ML CdSe NPLs governed by its TE and TM polarized TMEs. The narrow band-edge absorption suggests that the samples are monodisperse. Therefore, the high QY broad PL emission is the result of a multitude of surface-related trap emitting states. The significantly higher intrinsic absorption, high quantum yield and large Stokes shift make these ultrathin colloidal CdSe NPLs an ideal candidate for optoelectronic applications. With concerted efforts to effectively use TOA as a solvent, the QY can be improved, and then using them as phosphors integrated as high quality color conversion layers with blue LEDs pleasant and healthy white-light can be produced.

- **Chapter 7: Inverted CdS/CdSe Nanoplatelets: Quantum Ring**

  After studying core-only NPLs in preceding chapters, we studied the strain profiles, transition energies, transition matrix elements (TMEs), spatial charge densities, electronic bandstructure, band-mixing probabilities, optical gain spectra, maximum and differential gains of the inverted topology type-I core/crown CdS/CdSe quantum rings (QRs) in the zincblende phase – over contrasting QR lateral size and crown width.

  We observed compressive strain in the CdS core, which increases for thicker CdSe crowns. At the core/crown boundary the strain changes abruptly, the magnitude of which is higher for thinner crowns. Moreover, as the QR size increases the E1–H1

transition energy falls due to reduced quantum confinement. Also, with increasing crown width, we have a greater fraction of CdSe in the QR, and the E1–H1 transition energy falls, but non-monotonically due to the effect of bowing parameter. Furthermore, QRs transformed into pure NPLs have higher TMEs due to localized electron-hole wavefunction overlap in a single material. But for CdS/CdSe QRs, the TME increases with the CdSe crown width where most of the electron-hole wavefunctions are bound, as can be inferred from the spatial charge distributions. For QRs with thicker crowns, the wavefunctions have a greater spatial spread. The energy span of the E and H states rises as the crown thickness falls, which is owing to the higher effective electron and hole mass of CdS over CdSe. In all the H states, the major contributing hole-type has been identified. The gain peak emission position experiences a red-shift as the QR width increases owing to reduced confinement. For a given QR width, however, the peak emission position for varying crown widths are in accordance to the respective calculated transition energies. But, for a given QR case, with increasing carrier density, there is slight blue-shift due to band-filling effect, and a rise in the maximum gain and a reduction in the differential gain.

– **Appendix F: Inverted Type-I CdS/CdSe Core/Crown Quantum Ring**
We have colloidally synthesized 3 monolayer (ML) thick CdS/CdSe QR samples using seed-mediated method. We measured the PL and absorption spectra of CdS/CdSe QRs for two contrasting cases having a (*i*) thin, and a (*ii*) thick CdSe crown. As the crown thickness increases, there is lesser extent of lateral confinement, and thus a red-shift in the PL peak position. Also the linewidth of the emission spectra narrows down as more CdSe is deposited in the crown. This is owing to the randomly dispersed CdSe islands of varying sizes formed around the CdS NPLs at the initial phase of the CdSe crown growth resulting in a normal distribution of energy levels. For a sufficiently thick CdSe crown, the electronic structure and optical properties of CdS/CdSe QR is identical to CdSe NPLs alone, characterized by narrower linewidths. We have also studied the spatial charge density distributions of first electron and hole states in the 3 ML CdS/CdSe QRs theoretically.

This concludes the first part of the thesis on the study of NPLs and QRs of II-VI materials and alloys thereof.

- **Chapter 8: GaNBiAs/GaAs Dilute Nitride-Bismide Quantum Dots**
  We studied the electronic bandstructure and optical gain of $GaN_xBi_yAs_{1-x-y}$/GaAs pyramidal quantum dots (QDs). The effective bandgap falls as we increase the composition of Nitrogen (N) and Bismuth (Bi) and with an appropriate choice of composition we can tune the emission wavelength to span within 1.3 μm–1.55 μm, for device application in fiber technology. The extent of this red shift is higher in QDs compared to bulk material due to quantum confinement. Other factors affecting the emission characteristics include virtual crystal (VC), strain profile, band anticrossing (BAC) and valence band anticrossing (VBAC). The strain profile has a profound impact on the electronic structure, specially the valence band of QDs, which can be determined using the composition distribution of wavefunctions. All these factors eventually affect the optical gain spectrum. With an increase in QD size, we observe a red shift in the emission energy and emergence of secondary peaks owing to transitions of greater energy compared to the fundamental transition.

- **Chapter 9: GaNBiAs/GaAs Dilute Nitride-Bismide Quantum Wells**
  After studying GaNBiAs/GaAs QDs, we studied the electronic bandstructure and optical properties of lattice matched GaNBiAs/GaAs quaternary alloy quantum well (QW). The different QW cases studied have their thicknesses and N : Bi : As composition tuned in such a way to have their emission peak at 1.55 μm, aiming towards optical communication systems. We have obtained insights on how the well thickness and (N,Bi) compositions affects the energy dispersion curves and closeness of electron and hole energy levels. An increase in the injection carrier density increases the maximum gain and also the gain spectral width. In our study we see that while thinner wells have decreasing differential gain at lower density, thicker wells show the same at higher density. It is, thus, of significant importance to determine the critical well thickness for a steady optical performance. Among our cases studied, we have identified the 6.3 nm thick $GaN_3Bi_{5.17}As_{91.83}$ lattice matched QW to exhibit optimized optical performance for our intended 1.55 μm (0.8 eV) optoelectronic device/system applications. Therefore, it is recommended that the design parameters such as material composition and well width must be carefully considered from the device application point-of-view for an accurate optimization of the optoelectronic performance characteristics.

- **Chapter 10: InNBiAs/InP Dilute Nitride-Bismide Quantum Dots**
  After studying dilute nitride bismide doped GaAs, we have investigated the electronic bandstructure and optical gain of InNBiAs/InP QD. Utilizing the BAC and VBAC effects, we can achieve an emission wavelength of laser in the range 2–5 μm while meeting the strain requirements for lattice matching for suitable material growth. We observe that, with an appropriate choice of N and Bi doping composition, we can tune the emission wavelength in the range of 2–5 μm suitable for mid-infrared device applications, such as guided missile technology, spectroscopy of trace gases and more recent medical applications such as less-invasive, high-precision, laser surgery. One of the important characteristics of the III-V semiconductor based mid-infrared laser structures is that it possesses strong differences in band gap energy and band discontinuity allowing the formation of deep confining QW in the laser's active region, which cannot be obtained by using group IV based semiconductors. With the advancement of epitaxy growth techniques, it is possible to fabricate high quality III-V based quantum confined structures for mid-IR lasers; and InNBiAs QDs can be a potential candidate for this.

- **Chapter 11: InNBiSb/InSb Dilute Nitride-Bismide Quantum Wells**
  We proposed a practical scheme to realize quantum Hall spin (QSH) effect and topological phase transitions in $InN_xBi_ySb_{1-x-y}$/InSb QW. The well-width, barrier-width and concentrations of N and Bi impurity doping can be used to effectively attain band-inversion as we have comprehensively demonstrated. The coupling between the impurity resonant states is critical and has a profound effect on the narrowing down of the bandgap until band-inversion occurs.

  In our study we confirmed the following: (*i*) band-inversion in $InN_xBi_ySb_{1-x-y}$ QWs above a certain critical thickness, (*ii*) topologically protected edge-states using bandstructure analysis, (*iii*) edge-localized distribution of the wavefunctions and edge-state spin-momentum locking phenomenon, (*iv*) presence of non-zero Hall conductance in spite of the Fermi energy lying in the bandgap window, (*v*) crossover points in Landau levels for which $n = 0$ indicating topological band inversion in the absence of any magnetic field, and (*vi*) presence of a large Rashba Spin-Splitting ($\sim$1–2 eV in the presence of an external electric field of 0.5 mV/nm), which is essential for spin-manipulation in topological insulators. We also provided the phase diagrams of topological states for our $InN_xBi_ySb_{1-x-y}$ QW structures with varying well/barrier-widths and varying N

abd Bi doping concentrations, which is helpful for experimental realizations.

With all of the aforementioned characteristics in view, we are in a position to confirm the existence of QSH effect and topological phase transitions in $InN_xBi_ySb_{1-x-y}$/InSb quantum wells as a proof-of-concept.

12.3 Future Research Scope

True to the title of this thesis, '*Semiconductor Quantum Nanostructures for Optoelectronic Applications*', its focus and contributions were directed towards, but limited to, two major families of quantum nanostructures, using several variants of the multi-band $\boldsymbol{k}\cdot\boldsymbol{p}$ models. They were (*i*) NPLs and QRs of II-VI semiconductors and alloys thereof, and (*ii*) QDs and QWs of dilute nitride/bismide III-V semiconductors. However, scientific research on quantum nanostructures is immensely wide as they have many potential applications in medicine/health-care, physics, optics, electronics, energy, computation, etc [180]. Here we identify three such possible areas having promising future research scope, with the potential to not only unravel new physical phenomena and theory but also provide us with an understanding for efficient optoelectronic device design and applications.

- *Study of novel quantum nanostructure systems: Dot-in-rod & Graded core-shell QD:* In this thesis, we have focused on studying quasi-2D NPLs, pyramidal QDs, and QWs. However, there are several other promising novel nanostructures, which have gained increasing research interest recently. One of them in the quantum dot in quantum rod (also know as dot-in-rod) structure. A promising area of future research could be to study in-depth the optoelectronic properties and physics governing the dot-in-rod structures. Recently, Zahra *et al.* [181] have reported theoretical investigations on the energy transfer between a CdSe/CdS quantum-dot/quantum-rod core/shell structure and a weakly doped graphene layer, separated by a dielectric spacer. In another study, Wen *et al.* [182] have investigated CdSe/CdS dot-in-rod nanocrystals for the temperature dependence of their spectral properties such as the bandgap, bandwidth and fluorescence intensity. Dot-in-rod nanocrystals have the potential of finding next-generation cutting edge applications making them a promising area for future research exploration —

  I. Pisanello *et al.* [183] have proposed colloidal CdSe/CdS dot-in-rods as nonclassical sources for quantum information technology. Such nanoemitters show spe-

cific properties such as strongly polarized emission of on-demand single photons at room temperature, dipolelike behavior and mono-exponential recombination rates, making us envision their suitability as sources of single photons with well defined quantum states in quantum cryptography based devices.

II. Albers *et al.* [184] have demonstrated the use of dual-emitting dot-in-rods as nanothermometers with enhanced response and sensitivity in living cells. Temperature is a key parameter in physiological processes, and probes able to detect small changes in local temperature are necessary for accurate and quantitative physical descriptions of cellular events. Thermoresponsive dual emission is conferred by a Förster resonant energy transfer process between CdSe–CdS dot-in-rods as donors and cyanine dyes as acceptors, which are conjugated to the dot-in-rods using an amphiphilic polymer coating. They delivered the nanothermometers to live cells, which showed an unexpected enhancement in their temperature response and sensitivity, highlighting the need to calibrate these and similar probes within the cell.

Another promising family of nanocrystals are the graded core-shell QDs. These are QDs which have a core of one material and a shell of another wherein the alloy composition is made to vary gradually from one material to another (core to shell) instead of an abrupt change of semiconductor material in heterostructure boundaries. Engineering the compositional gradient of core/shell semiconductor nanocrystals in such a fashion improves their optical properties [185]. In a study by Bae *et al.* [186], they have shown that controlled alloying of graded core-shell interface in CdSe/CdS QDs can aid to suppress Auger Recombination. It also effectively reduces non-radiative processes and surface trapping, suppresses re-absorption and assists in tuning the Stokes shift [187]. Alloying also enables switching between Type-I and quasi-Type-II configurations and synthesis of highly luminescent and photo-stable, graded core-shell QDs. The resultant graded QDs can have high quantum yields and superior robustness toward environmental influences and quenching agents. High PL quantum yields are correlated to a narrow distribution of single-particle lifetimes and suppressed fluorescence intermittency [188]. In yet another study, Yarema *et al.* [185] have demonstrated an approach to quantify grading in nanocrystal structures. Graded core-shell QDs can therefore be a focus area for future research with potential applications in QD-based display technology.

- *Study of optoelectronic properties under the influence of external electromagnetic field:*

  In this thesis, we have studied various nanostructures, albeit without the influence of any external electromagnetic field. But the effect of external electromagnetic field on their optoelectronic properties is significant. The quantum-confined Stark effect describes the effect of an external electric field upon the light absorption spectrum or emission spectrum of quantum nanostructures. The electric field dependence of the single-dot spectrum is characterized by a highly polarizable excited state, in the presence of randomly oriented local electric fields with temporal variations. These local fields result in spontaneous spectral diffusion and contribute to ensemble inhomogeneous broadening. The Stark shift effects in QDs can be leveraged for their potential applications in electro-optic modulation devices [189].

  In a recent study, Rowland *et al.* [190] reason that, the intrinsic properties of QDs and the growing ability to interface them controllably with living cells has far-reaching potential applications in probing cellular processes such as membrane action potential. The electric field typical of those found in neuronal membranes results in suppression of the QD photoluminescence (PL) and, the QD PL can be used to track the action potential profile of a firing neuron with millisecond time resolution. They also show that this effect to be connected with electric-field-driven QD ionization and consequent QD PL quenching, in contradiction with the conventional understanding that suppression of the QD PL is attributable to the quantum confined Stark effect.

  In view of the aforementioned, an in-depth study of the optoelectronic properties of quantum nanocrystals under the influence of external electromagnetic field is warranted, and this can be a promising field of research in future studies.

- *Extending the $\boldsymbol{k}\cdot\boldsymbol{p}$ model for studying optoelectronic properties of perovskite materials:* In this thesis, we have used variants of the 8-band and 16-band $\boldsymbol{k}\cdot\boldsymbol{p}$ models to study II-VI and doped III-V semiconductor nanostructures. However the $\boldsymbol{k}\cdot\boldsymbol{p}$ framework can be extended to study the very promising perovskite materials [191]. In the past half-a-decade, solution-processed organometallic perovskite materials ($^{\mathrm{XII}}\mathrm{A}^{2+}{}^{\mathrm{VI}}\mathrm{B}^{4+}\mathrm{X}^{2-}{}_3$) based solar cells have emerged as a promising candidate for thin-film photovoltaic technology. The world record power-conversion efficiency of perovskite solar cells have improved from ∼4% in 2009 to ∼18% in 2014 [192]. As of today, perovskite material devices have started finding optoelectronic applications in domains similar to conventional semiconductors. However, in this new family of materials, the spin-orbit

coupling is significant and reflects in the conduction band. They are also characterized by distinctive features such as the critical wavevector being located at one of the edges of the reference Brillouin zone and the band gap being direct [193, 194].

In future works, we can study their electronic bandstructure using multiband $\boldsymbol{k}\cdot\boldsymbol{p}$ models [195]. The excitonic effects play a crucial role in ensuring device efficiencies. For instance, in 3D halide-based hybrid perovskites, the strong reduction of the exciton binding energy at room temperature is essential for the operation of photovoltaic devices [193, 196]. Related 2D Ruddlesden-Popper phases, composed of perovskites layers sandwiched between two layers of large organic cations, have recently demonstrated improved photostability under standard illumination as well as humidity resistance, affording high conversion efficiencies. The intrinsic quantum and dielectric carrier confinements are afforded by the organic inner barriers, which leads to a stable Wannier exciton at room temperature [197, 198], making perovskites a compelling domain for future research exploration using certain multi-band $\boldsymbol{k}\cdot\boldsymbol{p}$ model variants.

12.4 Closing Remarks

Firstly, the findings reported in this thesis in whole and as summarized and concluded here, in **Chapter 12** have important implications for the application of II-VI NPLs and QRs; and dilute nitride/bismide III-V QDs and QWs in optoelectronic devices, such as LEDs, lasers, solar cells etc. They serve as an enabler for designing experiments and predicting optoelectronic characteristics in tandem with measurements and fabrication and can be used to tune reiterations parameters to reduce time and cost of device production.

Secondly, as a by-product of the work done for this thesis, we introduce our in-house software simulation platform called *KdotPsoft*. The source code for the various multi-band $\boldsymbol{k}\cdot\boldsymbol{p}$ models were developed using Fortran and Python. Finally, they were packaged under the name *KdotPsoft*, an end-to-end modeling and simulation software for semiconductor quantum nanostructures with a friendly graphical user interface. After further developments and beta-testing, *KdotPsoft* holds the potential of being rolled out as a commercial software package suitable for both academia and industry and the research community at large.

Closing note: This thesis ends here, with the hope and belief that it forwards the understanding and methodologies used in modeling and simulation of semiconductor quantum nanostructures; contributes to future optoelectronics research; and assists the research community is some useful way.

Appendix A

Semiconductor Material Parameters

Calculations done for the range of results reported in this thesis rely on a set of material parameters specific to every semiconductor material. The parameters for the various materials studied in this thesis are enlisted in the Tables in this appendix, with references to the original source(s).

Table A.1 enlists the material parameters of CdSe and CdS.

Table A.2 enlists the material parameters of GaAs, InAs and InSb.

Table A.3 enlists the of VC, BAC and VBAC parameters of dilute nitride bismide III-VI semiconductors.

Other specific parameters used in this thesis are enlisted within the relevant chapter, wherever relevant.

Table A.1: Material Parameters of CdSe and CdS

Parameter	Symbol (Unit)	CdSe	CdS
Lattice Constant [121]	a (Å)	6.052	5.832
Effective Electron Mass [121]	m_e^* (m_0)	0.12	0.25
Effective Hole Mass [146]	m_h^* (m_0)	0.62	0.981
Kane Matrix Element [10]	E_p (eV)	16.5	21.0
Bulk Bandgap [121, 199]	E_g (eV)	1.732	2.5
Spin-orbit Splitting Energy [122, 123]	Δ_{so} (meV)	420	65
Refractive Index [199, 200]	n_r	2.5	2.529
Bohr radius [201, 202]	a_B (nm)	5.6(5.3)	5.8
Luttinger Parameters [203]	γ_1	3.265	2.721
	γ_2	1.162	0.841
	γ_3	1.443	1.152
Deformation Potentials [133]	a_c (eV)	-2.83	-2.78
	a_v (eV)	1.15	1.61
	b (eV)	-1.05	1.09
	d (eV)	-3.10	-3.50
VFF Parameters [204]	$\alpha_{\text{Cd-X}}$	35.22	39.63
(X = Se, S)	$\beta_{\text{Cd-X-Cd}}/\beta_{\text{X-Cd-X}}$	3.14	3.68
Varshni Parameters [116]	$E_g(0)$ (eV)	1.834	2.558
	α (meV/K)	0.424	0.386
	β (K)	118	103
Cardona Parameters [205]	$E_g(0)$ (eV)	1.866	
	a_{ep} (meV)	36	–
	Θ (K)	179	
Scattering Parameters [146, 206]	Γ_0 (meV)	30.4	30
	γ_{AC} (μeV/K)	21	20
	Γ_{LO} (meV)	29.9	63.6
	$\hbar\omega_{LO}$ (meV)	26.1	36.8

Table A.2: Material Parameters of GaAs, InAs and InSb

Parameter	Symbol (Unit)	GaAs	InAs	InSb
Lattice Constant [62, 207, 208]	a (Å)	5.65325	6.0584	6.4790
Bulk Bandgap [62, 96, 208]	E_g (eV)	1.422	0.354	0.237
Kane Matrix Element [62, 207, 208]	E_p (eV)	25.5	22.2	21.2
Spin-orbit Splitting Energy [62, 207, 208]	Δ_{so} (meV)	341	380	810
Effective Electron Mass [62, 208]	m_e^* (m_0)	0.067	0.023	0.014
Effective Hole Mass [62]	m_h^* (m_0)	0.50	0.40	
Luttinger Parameters [62, 208]	γ_1	6.8	20.4	37.1
	γ_2	1.9	8.3	16.5
	γ_3	2.73	9.1	17.7
Deformation Potentials [62, 96, 208–210]	a_c (eV)	-7.17	-5.08	-6.17
and Elastic Constants	a_v (eV)	1.16	1.00	0.36
	b (eV)	-1.7	-6.08	-2.1
	d (eV)	-4.55	-1.8	-4.6
	C_{11} (10^{11} dyne/cm^2)	11.879	8.329	6.5335
	C_{12} (10^{11} dyne/cm^2)	5.376	4.526	2.8226
	C_{44} (10^{11} dyne/cm^2)	5.94	3.96	2.6388

Table A.3: Parameters of VC, BAC and VBAC used in calculation of dilute nitride bismide band-structure of III-VI semiconductors.

Parameter/Symbol (Unit)	GaAs	GaSb	GaP	InAs	InSb	InP
a (Å)	5.65325	6.0959	5.4505	6.0583	6.4794	5.8697
Eg(eV)	1.420	0.812	2.886	0.417	0.235	1.4236
Δ_{so}(eV)	0.341	0.76	0.08	0.39	0.81	0.108
m_e^*	0.067	0.039	0.13	0.026	0.0135	0.0795
γ_1	6.98	13.4	4.05	20.0	34.8	5.08
γ_2	2.06	4.7	0.49	8.5	15.5	1.60
γ_3	2.93	6.0	2.93	9.2	16.5	2.10
E_p (eV)	28.8	27.0	31.4	21.5	23.3	20.7
a_c (eV)	-7.17	-7.5	-8.2	-5.08	-6.94	-6.0
a_v (eV)	1.16	0.8	1.7	1.00	0.36	0.6
b (eV)	-2.0	-2.0	-1.6	-1.8	-2.0	-2.0
d (eV)	-4.8	-4.7	-4.6	-3.6	-4.7	-5.0
C_{11}	1221	884.2	1405	832.9	684.7	1011
C_{12}	566	402.6	620.3	452.6	373.5	561
C_{14}	600	432.2	703.3	395.9	311.1	456
VBO (eV)	-0.80	-0.03	-1.27	-0.59	0	-0.94
E_N (eV)	1.706	0.89	2.18	1.44	0.65	1.79
V_N (eV)	2.00	2.83	3.05	2.0	3.0	3.0
E_{Bi} (eV)	-0.183	-1.17	0.1	-0.4	-1.0	-0.23
$E_{Bi,so}$ (eV)	-1.9	-2.67	-1.4	-1.9	-2.5	-1.73
V_{Bi} (eV)	1.13	1.01	2.1	1.26	1.33	1.9
α_N (eV)	1.51	0.12	0.957	0.267	0.675	0.294
β_N (eV)	1.36	2.61	1.37	1.79	2.38	1.44
γ_N (eV)	1.53	1.87	1.31	1.40	1.576	1.34
κ_N (eV)	1.36					
α_{Bi} (eV)	-2.82	-2.78	-3.00	-1.03	-1.44	-1.75
β_{Bi} (eV)	1.01	0.38	1.62	0.94	0.35	1.29
γ_{Bi} (eV)	-0.55	-1.06	-0.5	-0.87	-1.04	-0.80
κ_{Bi} (eV)	1.01					

Appendix B

KdotPsoft: Modelling and Simulation of Semiconductor Physics

B.1 Introduction

I hereby introduce our in-house software simulation platform called *KdotPsoft*, to model and simulate semiconductor quantum nanostructure systems. During the course of the work done leading to this thesis, the source code for the various multi-band $\boldsymbol{k}\cdot\boldsymbol{p}$ models described in Chapter 2 were developed using Fortran and Python. Finally, they were packaged under the name *KdotPsoft*, an end-to-end modeling and simulation software platform for semiconductor quantum nanostructures with a friendly graphical user interface. After further developments and beta-testing, *KdotPsoft* holds the potential of being rolled out as a commercial software package or independent suitable for both academia and industry and the research community at large.

It is suitable to design and study multiple QW (MQW) based quantum cascaded lasers (QCL), vertical-cavity surface-emitting laser (VCSEL), etc in conjunction with experiment and fabrication. For fundamental physics and device physics applications, *KdotPsoft* is an ideal platform to model, simulate and study semiconductor quantum nanostructure. It is based on the 8-band and 16-band $\boldsymbol{k}\cdot\boldsymbol{p}$ perturbation theory model described in Chapter 2, and it supports all conventional group IV, III-V and II-VI semiconductor materials, and also can works for dilute nitride and bismide doped III-V semiconductors. It can be used to study the energy dispersion curves, optical gain spectra and electron-hole wavefunctions, band lineups, energy dispersion relation, density of states (DOS), polarization-dependent

transition matrix element strengths, optical gain/absorption spectra, spontaneous emission rate, radiative current density, electric field effects on the optoelectronic properties etc.

B.2 KdotPsoft Platform

Semiconductor quantum nanostructures, such as 0D quantum dots (QDs), 1D nanorods and 2D nanoplatelets (NPLs), quantum rings (QRs) and quantum wells (QWs) exhibit unique quantum mechanical and optoelectronic properties due to spatial confinement of excitons in one or more dimensions ($\sim 10^{-9}$ m). They have received increasing research interest in recent years owing to their intriguing fundamental properties that can be leveraged for potential applications in optoelectronic and display devices as cost-effective and quantum-efficient luminophores. They have been successfully used to implement and design light-emitting diodes (LEDs), lasers, photodetectors, solar cells, biomedical imagers, etc. This is owing to their morphological bandgap tunability, fast fluorescence lifetime and unique optical characteristics supporting tunable pure-color or wide spectral emission.

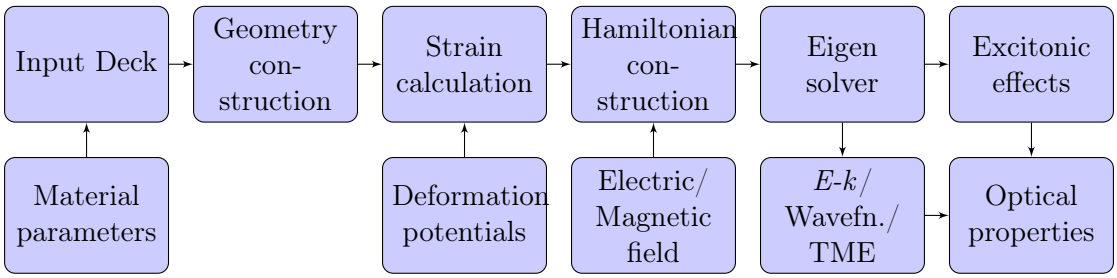

Figure B.1: Flowchart showing the modules, connectivities, dependencies and working flow of the *KdotPsoft* platform. More info: kdotpsoft.com

Our newly introduced platform, *KdotPsoft* can be used to model and to simulate such semiconductor nanostructure systems. Fig. B.1 shows the flowchart summarizing the working flow of the *KdotPsoft* software. We have developed a friendly graphical user interface (GUI) platform with built-in semiconductor material parameters. The input deck helps the user to design the nanostructure geometry from a choice of semiconductor materials and possible alloying. These material parameters could be manually altered by experienced users. After the nanostructure geometry construction, the strain is calculated using material deformation potentials. We use the $\boldsymbol{k}\cdot\boldsymbol{p}$ model Hamiltonian, which is affected by the strain calculated in the previous step. In the $\boldsymbol{k}\cdot\boldsymbol{p}$ Hamiltonian construction, we can include

optional electric field/magnetic field terms if the user requires to study those effects. Then the Eigen-solver is used to calculate the Eigen-energy values of the nanostructure system. Additionally outputs include, density of states, the energy-wavevector dispersion curves, energy bandstructure, electron-and-hole wavefunctions, band-lineup diagrams, polarization-dependent optical transition matrix, etc. The effect of excitonic recombination can also be considered for materials in which the excitonic binding energy is considerable. Finally, *KdotPsoft* can also calculate the optical gain/absorption spectra, spontaneous emission rate, radiative current density, etc.

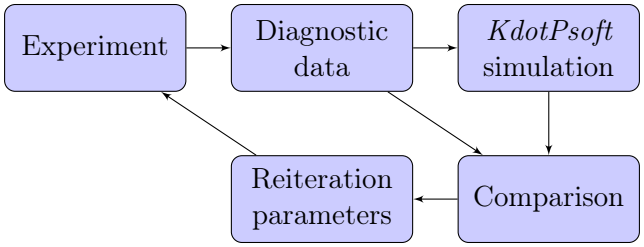

Figure B.2: The setup of *KdotPsoft* platform working in tandem with experiments and measurements.

Fig. B.2 shows the setup of *KdotPsoft* software platform that can be used in both academia and industry, and the research community at large to design experiments and predict optoelectronic characteristics in experiments and fabrication of QCL, VCSEL, etc. It can serve as a comparison tool between experimentally observed measurements and theoretically predicted results [155], and functions in a closed loop circuit as shown. It can be used to tune reiterations parameters for experiment and fabrication to reduce time and cost of production.

B.3 Summary and Conclusion

KdotPsoft is an ideal platform to model, simulate and study semiconductor quantum nanostructure systems for fundamental physics and device physics applications. It can study multiple QW (MQW) based structures such as quantum cascaded lasers (QCL), vertical-cavity surface-emitting laser (VCSEL), etc. *KdotPsoft* is based on the 8-band and 16-band $\boldsymbol{k}\cdot\boldsymbol{p}$ perturbation theory model and it supports all conventional semiconductor materials, and also can works for dilute nitride and bismide doped semiconductors. It can be used to study

the energy dispersion curves, optical gain spectra and electron-hole wavefunctions, the band lineups, energy dispersion relation, DOS, polarization-dependent transition matrix element strengths, optical gain/absorption spectra, spontaneous emission rate, radiative current density, electric field effects on the semiconductor quantum nanostructure.

Appendix C

Nanoplatelets Synthesis and Characterization

C.1 Synthesis Techniques

Colloidal CdSe nanoplatelets (NPLs) of 4 monolayer (ML) thickness were synthesized using synthesis protocol similar to those used in Refs. [137–140]. The following chemicals were used: Cadmium acetate dihydrate $Cd(OAc)_2{\cdot}2H_2O$, oleic acid, technical grade 1-octadecene, cadmium nitrate, cadmium nitrate, *n*-hexane, powder form selenium and myristic acid sodium salt. These were procured from Sigma Aldrich. The first step is to synthesize Cadmium $(myristate)_2$, by dissolving 1.23 g of Cadmium nitrate in methanol (40 mL). This was followed by dissolving sodium myristate (3.13 g) in methanol (250 mL) for 60 min with continuous stirring. When the two solutions were mixed, a white precipitate is formed after full dissolution. This precipitate was washed with methanol and dried under vacuum for about 24 h. 12 mg (0.15 mmol) of selenium (Se) and 170 mg (0.3 nmol) of $Cd(myristate)_2$ were introduced in a three-neck flask along with 15 mL of octadecene (ODE) and degassed under vacuum. Under argon (Ar) flow, the mixture was heated up, until 240°C, and left there for 10 mins. When the color of the solution becomes yellowish, at $\sim$ 195°C, 80 mg (0.30 mmol) of $Cd(OAc)_2{\cdot}2H_2O$ was introduced. 5 mL of *n*-hexane and 0.5 mL of oleic acid was added at the end of the synthesis, and the solution was allowed to cool down to RT. A centrifuge was used to precipitate the NPLs before storing them in hexane. This synthesis also produces some 5 ML NPLs and spherical nanocrystals with distinctly different emission wavelength. The 4 ML NPLs were separated from the rest

using selective precipitation.

C.2 Purification and Film Preparation

The synthesized NPLs were centrifuged for 5 min at 4500 rpm, followed by removal of the supernatant solution. Nitrogen was used to dry the precipitate, before dissolving it in hexane to centrifuge for 10 min at 4500 rpm. The supernatant solution was made turbid by addition of ethanol, followed by centrifuging again for 10 min at 4500 rpm. Finally, using a 0.20 μm filter, the dissolved precipitate in hexane was filtered. Later, piranha solution was used for 30 min to clean quartz substrates of size 1.5 $\times$ 1.5 cm followed by DI-water. It was dried at 80°C for 30 min in an oven and the filtered solutions was spin-coated for 1 min at 2000 rpm to prepare solid thin-films of NPLs.

C.3 TEM Characterization

High-resolution transmission electron microscopy (TEM) images of NPL samples were taken on a JEOL JEM-2010 HR TEM operating at 200 kV, which has a resolution of $\sim$0.22 nm. The TEM images have been analyzed using ImageJ software.

C.4 Optical Characterization

The steady state photoluminescence (PL) spectra measurements were done using a cooled iDus CCD system. The time resolved PL (TRPL) measurements were done with a Becker & Hickl DCS 120 confocal scanning FLIM system with an excitation laser of 375 nm. The system has temporal resolution of 200 ps.

Fig. C.1 shows the time-resolved photoluminescence (TRPL) emission spectrum for our 4 ML CdSe NPLs at 30°C, as shown in Fig. 4.9 (in Chapter 4). The blue line shows the instrument response function.

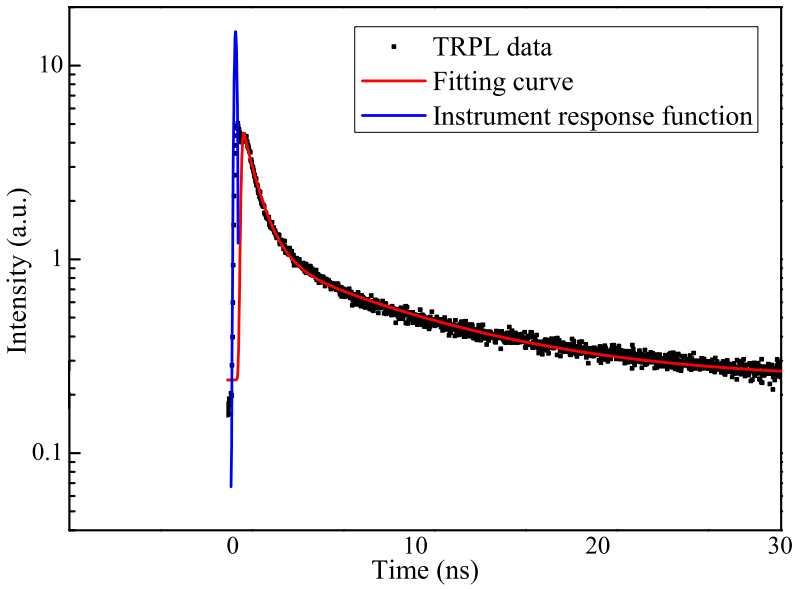

Figure C.1: Time resolved Photoluminescence (TRPL) emission spectrum for 4 ML CdSe NPLs at 30°C (black dots), dual exponential decay fitting curve (red curve), and the instrument response function (blue line). This has been discussed in detail in Fig. 4.9 (in Chapter 4).

Appendix D

Low Temperature NPL Photoluminescence Characterization

HERE we study in tandem and validate our theoretical calculations and experimental photoluminescence (PL) measurements of 4 ML CdSe NPLs studied in Chapter 4, with existing low-temperature results in literature. Fig. D.1 shows the comparison of our calculated E1–H1 transition energy values (which matches with our experimental PL emission energy, Fig. 4.11 in Chapter 4, pg. 80) with existing results from Achtstein *et al.* [25]. The red dot-line on the left frame is their experimental data for actual 4 ML CdSe NPLs at low temperature. The red plot in the right frame is our E1–H1 values from 303–363 K. The PL emission of 512±3 nm (∼2.42 nm) is from 4 ML NPLs, and the comparison with our results can be seen in the Fig. D.1, showing the continuity in the PL emission energy.

Also, as shown in Fig. D.2, we have compared and extended our PL spectra at higher temperature (>RT), with PL spectra at lower temperature (<RT) as measured by Erdem *et al.* [143]. We have adjusted the x-axis range (2.3–2.55 eV) and y-axis range (0–2000) to ensure a correct superimposition of the results. The solid lines show the results of Erdem *et al.*, while the dotted lines show our result. There is a smooth continuity in the PL emission peak positions, PL linewidths and PL relative intensities. From Fig. D.1 and D.2, we believe that measurements and calculations done at lower temperature range would yield similar results for us.

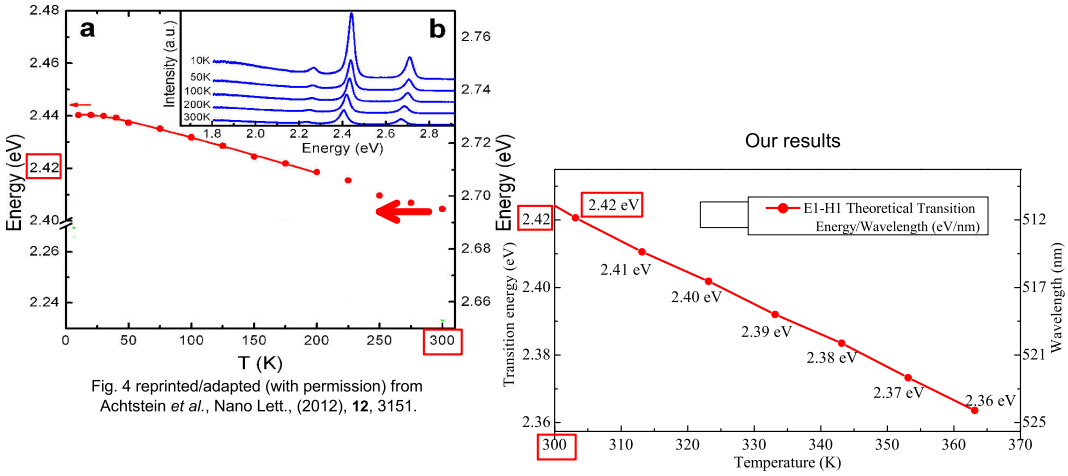

Figure D.1: Comparison and extension of PL emission energy (by Achtstein *et al.*, [Reprinted (adapted) with permission from *Nano Lett.* **12** (6), 3151. Copyright (2012) American Chemical Society.] in the *left* frame) with our E1-H1 transition energy results in the *right* frame.

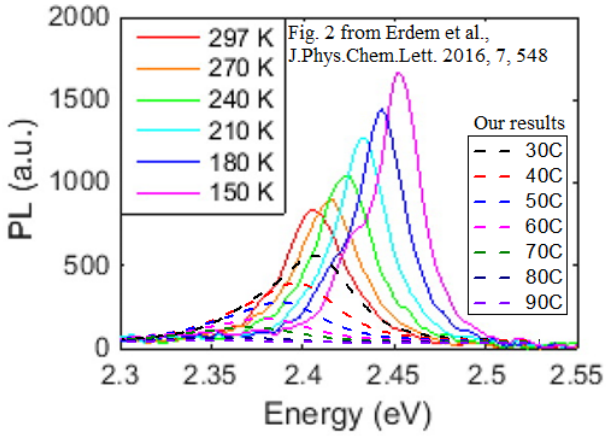

Figure D.2: Comparison and extension of PL spectra (as measured by Erdem *et al.*, [Reprinted (adapted) with permission from *J. Phys. Chem. Lett.* **7** (3), 548. Copyright (2016) American Chemical Society.] in low temperature range shown by solid lines) with our PL spectra measurements at elevated temperature shown by dotted lines. There is a smooth continuity in the emission peak positions and the linewidths.

Appendix E

Anomalous Spectral Characteristics of sub-nm CdSe NPLs

E.1 Introduction

Quasi-2D atomically-flat colloidal CdSe nanoplatelets (NPLs) have emerged as a new class of novel nanostructures recently [211], with application in high efficiency display devices, LEDs and lasers. The surface effects in ultrathin CdSe NPLs become important as their thickness reduces to sub-nanometer level. Here we study the anomalous photoluminescence (PL) and absorption spectra ultrathin sub-nanometer CdSe nanoplatelets (NPLs) of thickness 2 monolayer (ML) i.e. 0.6 nm. They exhibit high quantum yield broad photoluminescence emission and polarization-characterized lateral size dependent anomalous heavy hole and light/split-off hole absorption intensities. Fig. E.1 shows the building block and schematic of a typical CdSe NPL – this particular example shows a 2 ML CdSe NPL case.

E.2 Experimental and Theoretical Results

Colloidal CdSe NPLs are known to have narrow PL linewidths [10], but for 2 ML CdSe NPLs, we observed broad PL emission [Fig. E.2 (a)] covering the visible range suitable for white-light emission, with quantum yield (QY) over 85% in solution and 70% in solid film.

Such highly efficient broad emission originates from the deep surface trap states as probed by continuous-wave and time-resolved PL (TRPL) techniques. The average carrier

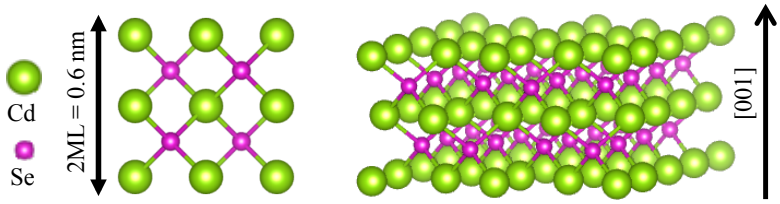

Figure E.1: Building block and schematic of a typical CdSe NPL. Example shows the case of 2 ML CdSe NPL.

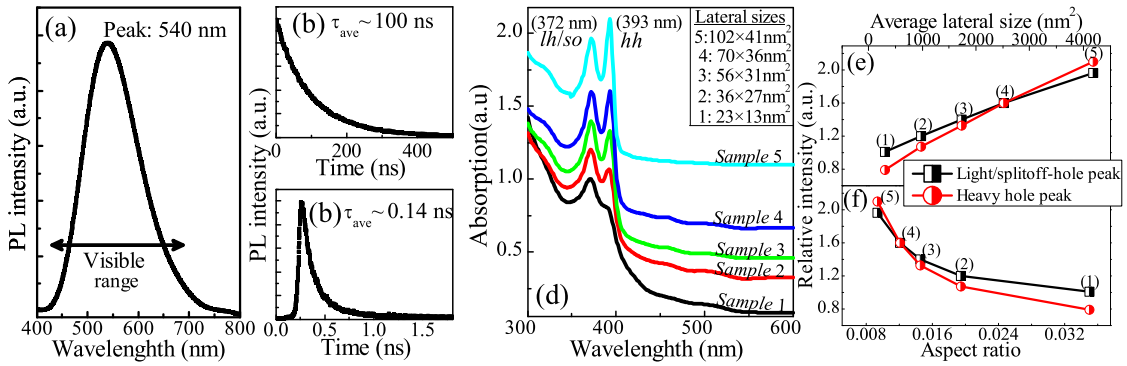

Figure E.2: (a) Photoluminescence spectrum, (b) Time-Resolved Photoluminescence spectrum measured at 550 nm, (c) Time-Resolved Photoluminescence spectrum measured at 400 nm, (d) Absorption spectra comparison of 2 ML NPLs with varying lateral sizes; and Relative absorption peak intensity of heavy hole (∼393 nm) and light/split-off hole (∼372 nm) vs. (e) Average NPL lateral area, and (f) NPL aspect ratio $= \frac{\text{NPL thickness}}{\sqrt{\text{NPL lateral area}}}$.

lifetime (ave) for the pure trap states is 100 ns, while that of the band edge is much shorter, 0.14 ns [Fig. E.2 (b-c)] due to carrier trapping. Owing to its low aspect ratio, the number of the trap sites in these ultrathin NPLs is much higher, as a major fraction of the atoms are at the surface. We significantly modified the emission kinetics in 2 ML NPLs by using trioctylamine (TOA) as a solvent instead of octadecene (ODE), which enhances the deep trap states QY. Also, absorption measurements show the anomalous dependence of excitonic transition strength on the lateral size of NPLs [Fig. E.2 (d)], which can be controlled by adjusting the growth time after the injection of the Se precursor (TOP-Se) as shown in the TEM images of Fig. E.3. The relative strength of the heavy hole (hh∼393 nm) and light/split-off hole (lh/so∼372 nm) absorption largely depends on the lateral size of the 2 ML CdSe NPLs [Fig. E.2 (e-f)], but the spectral position of the peaks

stays same throughout. Above a certain lateral size (*ex*: *Sample* 4), the typical absorption characteristic of thicker NPLs is regained where *hh* peaks are of higher intensity than *lh*/*so*. To the best of our knowledge, such dependence of excitonic transitions on the lateral size of NPLs has not been reported earlier. Additionally, the 2 ML NPLs were observed to exhibit significantly higher intrinsic absorption compared to thicker NPLs (4 and 5 ML) at their *lh*/*so* absorption peak signifying the presence of giant oscillator strength (GOST) [31]. f

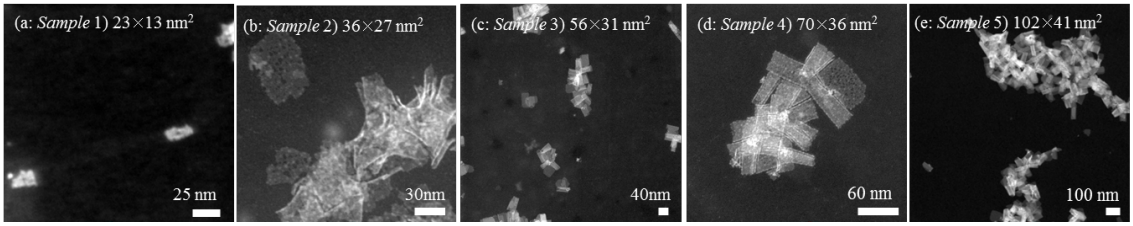

Figure E.3: High-resolution Transmission Electron Microscopy (TEM) images of 2 ML thick CdSe NPLs with average lateral sizes (a: *Sample* 1) 23×13 nm^2, (b: *Sample* 2) 36×27 nm^2, (c: *Sample* 3) 56×31 nm^2, (d: *Sample* 4) 70×36 nm^2, and (e: *Sample* 5) 102×41 nm^2. Scales are indicated.

To investigate the origins of such lateral size dependent anomalous characteristics, we studied the five samples of our 2 ML CdSe NPLs using an effective mass envelope function theory approach based on the Kane's 8-band $\boldsymbol{k}\cdot\boldsymbol{p}$ method using the first basis type to construct the Hamiltonian as described in Sec. 2.3.1. The 8-band Hamiltonian simultaneously accounting for the nonparabolicity of the coupled conduction- and valence-band including the orbit-splitting bands was solved, to obtain their electronic bandstructure (*ex*: Fig. E.5 for *Sample* 1). The complete absorption spectrum can be calculated as the sum of the bound-state and continuum-state contributions [62], which is strongly dependent on the optical transition matrix elements (TMEs) given by Eq. (2.13) in Sec. 2.3.1.

Numerical results for *Sample* 1 [Fig. E.4] show that the TM mode E1-H9 transition TME (= 0.69) is stronger than the TE mode E1-H1 transition TME (= 0.43). From Fig. E.5, we see the former has greater *lh*/*so* dominance and occurs at 3.27 eV, while the latter has greater *hh* dominance and occurs at 3.1 eV, which is comparable consistent with our experimental observation [Fig. E.2 (d)]. Both H1 and H9 states have *s*-like spatial charge density pattern [Fig. E.6], overlapping excellently with the E1 state to produce strong excitonic transition, more so for TM E1-H9 than TE E1-H1, as numerically confirmed. Numerical simulations for laterally larger NPLs show rise in both TE and TM mode TME, but the rise in TE mode TME is relatively faster as expected, and exceeds the TM mode TME beyond a certain lateral size – where the typical absorption characteristics become

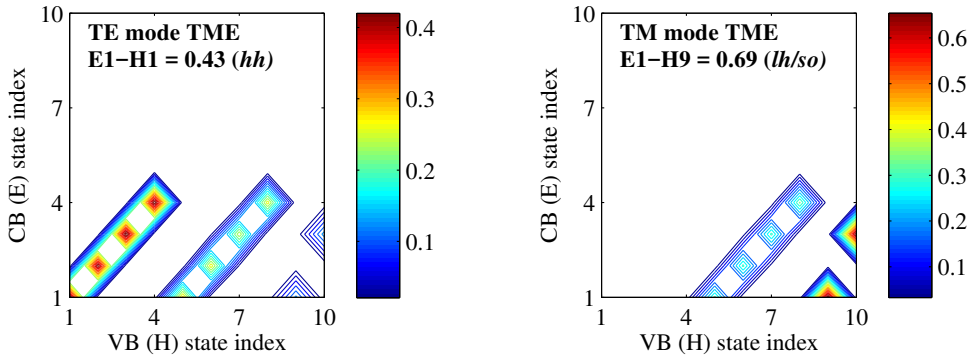

Figure E.4: For *Sample* 1: TE and TM polarized optical transition matrix elements (TME) contour.

similar to that of thicker NPLs and the *hh* peak becomes larger than the *lh*/*so* peak.

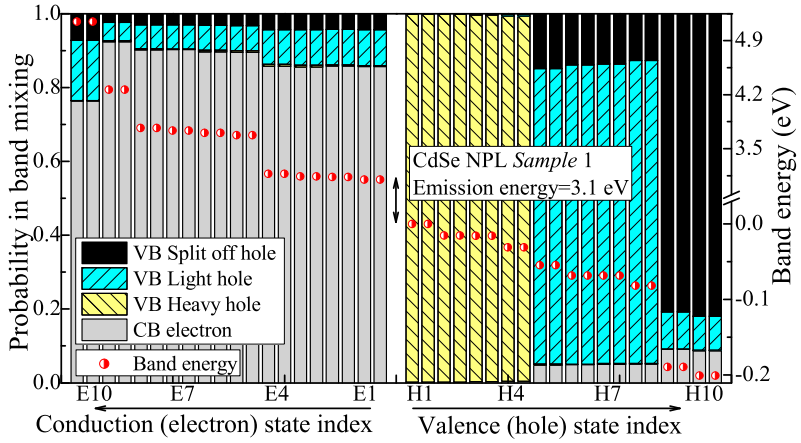

Figure E.5: For *Sample* 1: Electronic bandstructure and probability in band-mixing between conduction electrons and valence *hh*, *lh* and *so* holes showing the first ten conduction (E) states and valence (H) states.

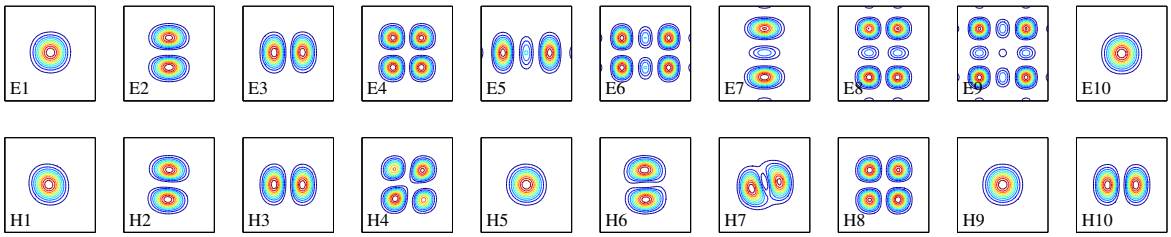

Figure E.6: For *Sample* 1: Spatial charge density distributions of the first ten conduction (E) and valence (H) states.

E.3 Conclusion and Future works

The relative strength of the *hh* and *lh*/*so* absorption largely depends on the lateral size of the ultrathin sub-nm 2ML CdSe NPLs governed by its TE and TM polarized TMEs. The narrow band-edge absorption suggests that the samples are monodisperse. Therefore, the high QY broad PL emission is the result of a multitude of surface-related trap emitting states. The significantly higher intrinsic absorption, high quantum yield and large Stokes shift make these ultrathin colloidal CdSe NPLs an ideal candidate for optoelectronic applications. Currently, we are making concerted efforts to effectively use TOA as a solvent to improve the QY, and then using them as phosphors integrated as high quality color conversion layers with blue LEDs to produce pleasant and healthy white-light.

Appendix F

Inverted Type-I CdS/CdSe Core/Crown Quantum Ring

INVERTED Type-I quantum rings (QRs) are a recently developed class of nanostructure in which a lower bandgap material is laterally grown as a crown of same thickness around a higher bandgap nanoplatelet (NPL) core [32, 35], *e.g.* core/crown CdS/CdSe as shown in Fig. F.1. Fig. F.1 (a) shows the 3D atom-by-atom view of a typical QR. It is an example showing 3 ML CdS core and CdSe crown forming a rectangular Type-I core/crown CdS/CdSe QR. Fig. F.1 (b) shows the schematic of a typical QR of dimensions $a \times b \times t$. The width of the CdSe crown (ring) is d.

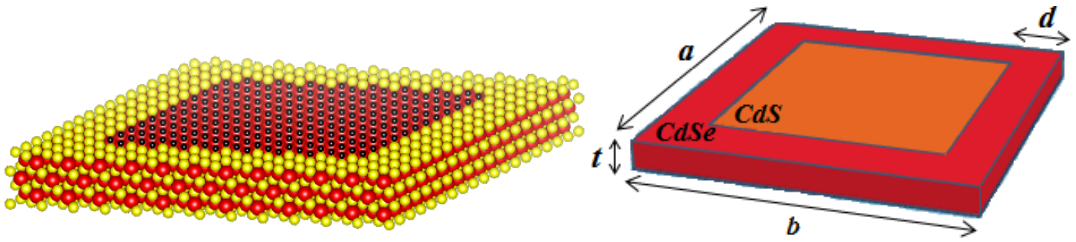

(a) (b)

Figure F.1: (a) A 3D atom-by-atom view of a typical QR (*example*: 3 ML CdS/CdSe QR – of CdS core and CdSe crown). Red spheres are Cd atoms, yellow Se atoms and dark blue S atoms; and (b) Schematic of a typical inverted Type-I core/crown CdS/CdSe quantum ring of dimensions $a \times b \times t$ and crown width d.

For this work [33], we have colloidally synthesized 3 monolayer (ML) thick CdS/CdSe QR samples using seed-mediated method, by using 3 ML CdS NPLs as the core seed [36]. Subsequently, continuous injection of Se precursor, elemental Se dissolved in octadecene (ODE), Cd precursor and $Cd(CH_3CO_2)_2$ led to the growth of CdSe crown. The ring width was controlled by tuning the injection amount to regulate the extent of the lateral size of the crown coating. A TEM image of the 3 ML CdS/CdSe QRs is shown in Fig. F.2, which suggests atomically flat lateral growth of CdSe on CdS NPLs, as it has larger average lateral size (30±10 nm) compared to the CdS core only NPLs.

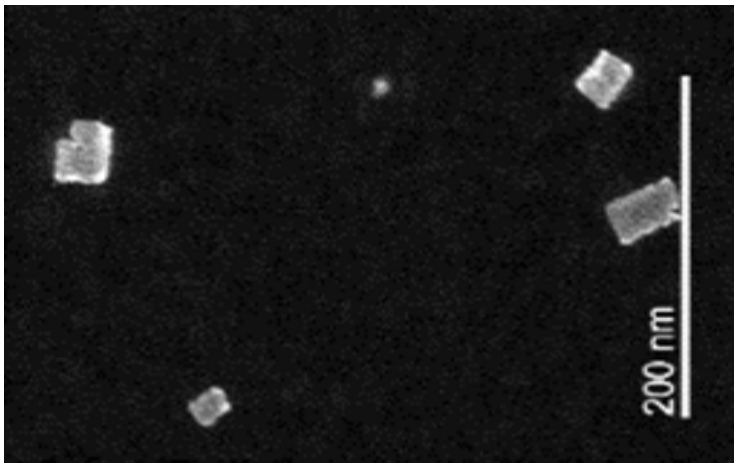

Figure F.2: Transmission Electron Microscopy (TEM) image of 3 ML thick CdS/CdSe QRs (scale: 200 nm)

We have measured the photoluminescence (PL) and absorption spectra of CdS/CdSe QRs at different phases of crown growth. Fig. F.3 shows the PL and absorption spectra for two contrasting cases having comparatively (*i*) thin, and a (*ii*) thick CdSe crown. As the crown thickness increases, there is lesser extent of lateral confinement, and thus a red-shift in the PL peak position. Also the linewidth of the emission spectra narrows down as more CdSe is deposited in the crown. This is owing to the randomly dispersed CdSe islands of varying sizes formed around the CdS NPLs at the initial phase of the CdSe crown growth resulting in a normal distribution of energy levels. For a sufficiently thick CdSe crown, the electronic structure and optical properties of CdS/CdSe QR is identical to CdSe NPLs alone, characterized by narrower linewidths. Moreover, we have verified that the emission peak of the 3 ML CdS/CdSe QRs is spectrally tunable between the peak emissions of 3 ML CdS NPL core only (382 nm) and 3 ML CdSe NPL core only (462 nm). In terms of the

absorption spectra, as we begin to grow the CdSe crown, there is a gradual emergence of the primary and secondary CdSe absorption peaks at 460 nm (electron-heavy hole) and 431 nm (electron-light hole) respectively, as can be seen in Fig. F.3 *(ii)*. On the other hand, for thin CdSe crowns, these peaks are undeterminable, while the overlapping primary and secondary absorption peaks of CdS at 382 nm (electron-heavy hole) and 373 nm (electron-light hole) are more prominent, as can be seen in Fig. F.3 *(i)*.

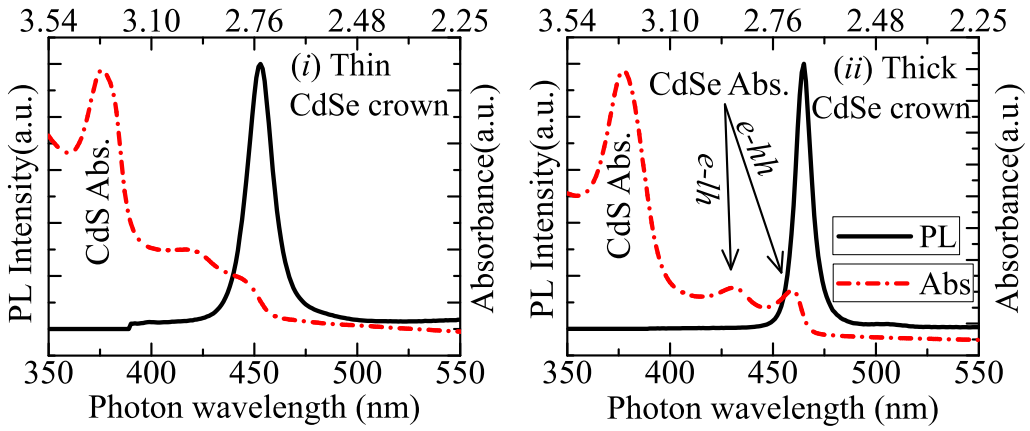

Figure F.3: PL spectra excited at 350 nm and absorption spectra for comparatively (i) thin and (ii) thick CdSe crowns. There is a redshift and fall in linewidth as ring width increases. CdSe and CdS absorption peaks are indicated.

We have also studied the 3 ML CdS/CdSe QRs theoretically using an effective mass envelope function theory approach based on the Kane's 8-band $\boldsymbol{k}\cdot\boldsymbol{p}$ method using the first basis type to construct the Hamiltonian as described in Sec. 2.3.1. Fig. F.4 shows the spatial charge density distributions of the first conduction (E1) and first valence (H1) states for thick ($d/a = 0.25$), medium-sized ($d/a = 0.15$) and thin ($d/a = 0.05$) CdSe crown for square QRs. We can comprehend the extent of quantum confinement, as the photo-generated charge carriers due to ultrafast non-radiative relaxations move to the lowest excited and emissive states in the CdSe crown near the band edge.

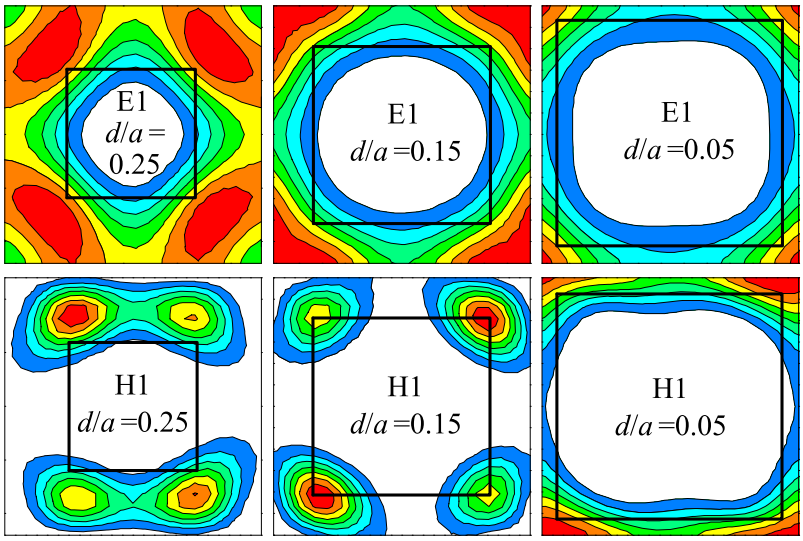

Figure F.4: Spatial charge density distributions of the first conduction (E1) and first valence (H1) states for thick ($d/a = 0.25$), medium-sized ($d/a = 0.15$) and thin ($d/a = 0.05$) CdSe crown for square QRs. Warmer (reddish) colors depict higher electron/hole occupation probability over cooler ones (bluish).

CdS/CdSe QRs have already found application as phosphor for color conversion in white light LEDs [36]. They are also potential candidates for magneto-optical device applications (using Aharonov-Bohm effect) [35].

Author's Publications and Vita[1]

Journals (relevant only, in reverse chronological order)

- Y. Liu, **S. Bose**, W. J. Fan, "Effect of Size and Shape on Electronic and Optical Properties of CdSe Quantum Dots", *Optik – International Journal for Light and Electron Optics*, **155**, 242–250, 2018.
- **S. Bose**, W. J. Fan, D. H. Zhang, "Optoelectronics of Inverted Type-I CdS/CdSe Core/Crown Quantum Ring", *Journal of Applied Physics*, **122** (16), 163102, 2017.
- Z. Song, **S. Bose**, W. J. Fan, D. H. Zhang, Y. Y. Zhang, S. S. Li, "Quantum Spin Hall Effect and Topological Phase Transition in $InN_xBi_ySb_{1-x-y}$/InSb Quantum Wells", *New Journal of Physics*, **19** (7), 073031, 2017.
- **S. Bose**, S. Shendre, Z. Song, V. K. Sharma, D. H. Zhang, C. Dang, W. J. Fan, H. V. Demir, "Temperature-dependent Optoelectronic Properties of Quasi-2D Colloidal Cadmium Selenide Nanoplatelets", *Nanoscale*, **9**, 6595-6605, 2017.
- W. J. Fan, **S. Bose**, D. H. Zhang, "Electronic Bandstructure and Optical Gain of Lattice Matched III-V Dilute Nitride Bismide Quantum Wells for 1.55μm Optical Communication Systems", *Journal of Applied Physics*, **120** (9), 093111, 2016.
- **S. Bose**, Z. Song, W. J. Fan, D. H. Zhang, "Effect of Lateral Size and Thickness on the Electronic Structure and Optical Properties of Quasi Two-dimensional CdSe and CdS Nanoplatelets", *Journal of Applied Physics*, **119**, (14), 143107, 2016.
- Z. G. Song, **S. Bose**, W. J. Fan, S. S. Li, "Electronic Bandstructure and Optical Gain of $GaN_xBi_yAs_{1-x-y}$/GaAs Pyramidal Quantum Dots", *Journal of Applied Physics*, **119** (14), 143103, 2016.

[1] As best reflected on February 26, 2018.

- **S. Bose**, W. J. Fan, D. H. Zhang, "Optoelectronics of Quasi Two-dimensional CdS_xSe_{1-x} Nanoplatelets", [*to submit*].
- **S. Bose**, S. Delikanli, V. K. Sharma, C. Dang, W. J. Fan, D. H. Zhang, H. V. Demir, "Electronic Bandstructure and Excitonic Absorption in CdSe Nanoplatelets" [*to submit*].

Conferences (relevant only, in reverse chronological order)

- **S. Bose**, W. J. Fan, D. H. Zhang, "Theoretical Investigations of Excitonic Absorption in Quasi Two-dimensional CdSe Nanoplatelets", *The 12^{th} Conference on Lasers and Electro-Optics Pacific Rim (CLEO-PR)*, Singapore, 2017.
- **S. Bose**, W. J. Fan, D. H. Zhang, "Strain Profile and Size Dependent Electronic Bandstructure of Type-I CdS/CdSe Quantum Ring", *The 12^{th} Conference on Lasers and Electro-Optics Pacific Rim (CLEO-PR)*, Singapore, 2017.
- **S. Bose**, Z. Song, W. J. Fan, D. H. Zhang, "KdotPsoft: Modelling and Simulation of Semiconductors and Device Physics", *9^{th} International Conference on Materials for Advanced Technologies*, Singapore, 2017.
- Z. Song, **S. Bose**, W. J. Fan, X. H. Tang, D. H. Zhang, S. S. Li, "Electronic Structure and Optical Gain of $InAs_{1-x-y}N_xBi_y$/InP pyramidal quantum dots", *9^{th} International Conference on Materials for Advanced Technologies*, Singapore, 2017.
- **S. Bose**, S. Delikanli, M. Z. Akgul, Y. Gao, W. J. Fan, D. H. Zhang, H. V. Demir, "Inverted Type-I CdS/CdSe Core/Crown Colloidal Quantum Ring", *Conference on Lasers and Electro-Optics (CLEO)/Europe and the European Quantum Electronics Conference (EQEC)*, Munich, 2017.
- **S. Bose**, S. Delikanli, A. Yeltik, M. Sharma, O. Erdem, C. Dang, W. J. Fan, D. H. Zhang, H. V. Demir, "Anomalous Spectral Characteristics of Ultrathin sub-nm Colloidal CdSe Nanoplatelets", *Conference on Lasers and Electro-Optics (CLEO)*, San Jose, 2017.
- **S. Bose**, W. J. Fan, J. Chen, D. H. Zhang, C. S. Tan, "Strain Profile and Size Dependent Electronic Band Structure of GeSn/SiSn Quantum Dots for Optoelectronic Application", *International Conference on Fibre Optics and Photonics*, Kharagpur, 2014.
- **S. Bose**, W. J. Fan, C. Jian, D. H. Zhang, C. S. Tan, "Strain profile, electronic band structure and optical gain of self-assembled Ge quantum dots on SiGe virtual substrate", *7^{th} International Silicon-Germanium Technology and Device Meeting*, Singapore, 2014.

Vita

Education

Nanyang Technological University (NTU) Singapore 2013 – 2018
Doctor of Philosophy (Ph.D.), Electrical and Electronic Engineering CGPA: 4.63/5.00
Advisor: Assoc. Prof. Fan Weijun and Prof. Zhang Dao Hua
Thesis: Semiconductor Quantum Nanostructures for Optoelectronic Applications

National Institute of Technology (NIT) Trichy, India 2009 – 2013
Bachelor of Technology, Electronics and Communication Engineering CGPA: 8.36/10.0
Advisor: Prof. S. Raghavan
Thesis: Mathematical modeling of a metamaterial regular polygon split ring resonator
(Graduated with First Class honors)

Research Interests

- Mathematical modeling and theoretical simulation of semiconductor quantum nanostructures.
- Application of semiconductor quantum nanostructures for optoelectronic, lighting and display technology.

Honors and Awards

- IEEE Region-10 Young Professionals Affinity Group Award in recognition and appreciation of valued services and contributions; Aug 2016.
- NTU Research Scholarship, for the duration of Aug 2013 – July 2017.
- University Graduate Scholarship, University of Glasgow, *offered* 2013.
- *Grant for Student* of EUR 750 to present a paper at the 6^{th} International Congress on Adv. Electromagnetic Materials in Microwaves & Optics, St. Petersburg,; Sept 2012.
- Govt. of India's University Grant Commission (UGC) Sponsored Fellowship for Summer Research Internship at Indian Institute of Science (IISc), Bangalore; May – July 2012.

Academic Services

Talks (*Invited*)

- "Semiconductor Quantum Nanocrystals for Optoelectronic Applications" at the 7$^{\text{th}}$ Annual World Congress of Advanced Materials 2018 in Xiamen, China; Sept 2018.
- "Semiconductor Quantum Nanocrystals for Optoelectronic Applications" at the 4$^{\text{th}}$ Annual World Congress of Smart Materials 2018 in Osaka, Japan; Mar 2018.
- "Semiconductor Quantum Nanocrystals for Optoelectronic Applications" at the 3$^{\text{rd}}$ Annual World Congress of Smart Materials 2017 in Bangkok, Thailand; Mar 2017.
- "Semiconductor Quantum Nanocrystals for Optoelectronic Applications" at the EMN Meeting on Optical Communications 2016 in Dubai; Nov 2016.

Journal Reviewer

- Institute of Electrical & Electronics Engineers (IEEE): *Journal of Lightwave Technology*.
- Institute of Physics (IOP): *Materials Research Express* and *Nanotechnology*.
- Springer Open: *Nanoscale Research Letters*.
- Multidisciplinary Digital Publishing Institute (MDPI): *Applied Sciences* and *Computation*.

Conference Reviewer

- IEEE TENCON 2016 – IEEE Region 10 Conference
- IEEE CRALT 2016 – Conference on Recent Advances in Lightwave Technology

Personal Particulars

- First Name: Sumanta
- Family Name: Bose
- Date of Birth: January 26, 1990
- Nationality: Indian
- Email: sumanta001@e.ntu.edu.sg
- Homepage: https://sumantabose.github.io/

Bibliography

[1] G. Busch, "Early history of the physics and chemistry of semiconductors-from doubts to fact in a hundred years," *European Journal of Physics*, vol. 10, no. 4, pp. 254, 1989.

[2] V. G. Lytovchenko and M. V. Strikha, "100 years of semiconductor science: The Ukrainian contribution," *Europhysics News*, vol. 45, no. 1, pp. 15–18, 2014.

[3] W. S. Gorton, "The Genesis Of The Transistor," *Proceedings of the IEEE*, vol. 86, no. 1, pp. 50–52, Jan 1998.

[4] Jaroslav Kováčč, František Uherek, Daniel Donoval, Jaroslav Kováčč Jr., and Alexander Šatka, *Optoelectronics*, pp. 203–238, Springer US, Boston, MA, 2009.

[5] Paul Harrison, *Quantum Wells, Wires and Dots: Theoretical and Computational Physics of Semiconductor Nanostructures*, Wiley, 2009.

[6] A. I. Ekimov and A. A. Onushchenko, "Quantum size effect in three-dimensional microscopic semiconductor crystals," *JETP Letters*, vol. 34, pp. 4, 1981.

[7] S. Ithurria and B. Dubertret, "Quasi 2D colloidal CdSe platelets with thicknesses controlled at the atomic level," *Journal of the American Chemical Society*, vol. 130, no. 49, pp. 16504–5, 2008.

[8] Burak Guzelturk, Yusuf Kelestemur, Murat Olutas, Savas Delikanli, and Hilmi Volkan Demir, "Amplified Spontaneous Emission and Lasing in Colloidal Nanoplatelets," *ACS Nano*, vol. 8, no. 7, pp. 6599, 2014.

[9] Zhuoying Chen, Brice Nadal, Benoit Mahler, Hervé Aubin, and Benoit Dubertret, "Quasi-2D Colloidal Semiconductor Nanoplatelets for Narrow Electroluminescence," *Advanced Functional Materials*, vol. 24, no. 3, pp. 295–302, 2014.

[10] S. Ithurria, M. D. Tessier, B. Mahler, R. P. Lobo, B. Dubertret, and A. L. Efros, "Colloidal nanoplatelets with two-dimensional electronic structure," *Nat. Mater.*, vol. 10, no. 12, pp. 936, 2011.

[11] Maria C. Tamargo, *II-VI Semiconductor Materials and their Applications*, CRC Press, New York, N.Y., 2002.

[12] R. R. Drenten, K. W. Haberern, and J. M. Gaines, "Thermal characteristics of blue-green II-VI semiconductor lasers," *J. Appl. Phys.*, vol. 76, no. 7, pp. 3988–3993, 1994.

[13] Gertrude F. Neumark, Robert M. Park, and James M. Depuydt, "Blue-Green Diode Lasers," *Phys. Today*, vol. 47, no. 6, pp. 26–32, 1994.

[14] C. B. Murray, Shouheng Sun, W. Gaschler, H. Doyle, T. A. Betley, and C. R. Kagan, "Colloidal Synthesis of Nanocrystals and Nanocrystal Superlattices," *IBM J. Res. Dev.*, vol. 45, no. 1, pp. 47–56, 2001.

[15] R. Benchamekh, N. A. Gippius, J. Even, M. O. Nestoklon, J. M. Jancu, S. Ithurria, B. Dubertret, Al L. Efros, and P. Voisin, "Tight-binding calculations of image-charge effects in colloidal nanoscale platelets of CdSe," *Physical Review B*, vol. 89, no. 3, 2014.

[16] M. D. Tessier, B. Mahler, B. Nadal, H. Heuclin, S. Pedetti, and B. Dubertret, "Spectroscopy of colloidal semiconductor core/shell nanoplatelets with high quantum yield," *Nano Letters*, vol. 13, no. 7, pp. 3321–8, 2013.

[17] L. Biadala, F. Liu, M. D. Tessier, D. R. Yakovlev, B. Dubertret, and M. Bayer, "Recombination dynamics of band edge excitons in quasi-two-dimensional CdSe nanoplatelets," *Nano Letters*, vol. 14, no. 3, pp. 1134–9, 2014.

[18] Donna McKinney, "Faster colloidal fluorescence emitters: Nanoplatelets," December 2011, [Online; posted 9-December-2011].

[19] Philipp Sippel, Wiebke Albrecht, Johanna C. van der Bok, Relinde J. A. Van Dijk-Moes, Thomas Hannappel, Rainer Eichberger, and Daniel Vanmaekelbergh, "Femtosecond cooling of hot electrons in cdse quantum-well platelets," *Nano Lett.*, vol. 15, no. 4, pp. 2409–2416, 2015.

[20] Joel Q. Grim, Sotirios Christodoulou, Francesco Di Stasio, Roman Krahne, Roberto Cingolani, Liberato Manna, and Iwan Moreels, "Continuous-wave biexciton lasing at room temperature using solution-processed quantum wells," *Nat. Nanotechnol.*, vol. 9, no. 11, pp. 891, 2014.

[21] Sunandan Sarkar, Biplab Rajbanshi, and Pranab Sarkar, "Understanding the electronic structure of CdSe quantum dot-fullerene (C_{60}) hybrid nanostructure for photovoltaic applications," *J. Appl. Phys.*, vol. 116, no. 11, pp. 114303, 2014.

[22] P. Bhattacharya, X. H. Su, S. Chakrabarti, G. Ariyawansa, and A. G. U. Perera, "Characteristics of a tunneling quantum-dot infrared photodetector operating at room temperature," *Appl. Phys. Lett.*, vol. 86, no. 19, pp. 191106, 2005.

[23] Chunxing She, Igor Fedin, Dmitriy S. Dolzhnikov, Peter D. Dahlberg, Gregory S. Engel, Richard D. Schaller, and Dmitri V. Talapin, "Red, Yellow, Green, and Blue Amplified Spontaneous Emission and Lasing Using Colloidal CdSe Nanoplatelets," *ACS Nano*, vol. 9, no. 10, pp. 9475–9485, 2015.

[24] Sudip K. Saha, Asim Guchhait, and Amlan J. Pal, "Organic/inorganic hybrid *pn*-junction between copper phthalocyanine and CdSe quantum dot layers as solar cells," *J. Appl. Phys.*, vol. 112, no. 4, pp. 044507, 2012.

[25] A. W. Achtstein, A. Schliwa, A. Prudnikau, M. Hardzei, M. V. Artemyev, C. Thomsen, and U. Woggon, "Electronic structure and exciton-phonon interaction in two-dimensional colloidal CdSe nanosheets," *Nano Letters*, vol. 12, no. 6, pp. 3151–7, 2012.

[26] Burak Guzelturk, Murat Olutas, Savas Delikanli, Yusuf Kelestemur, Onur Erdem, and Hilmi Volkan Demir, "Nonradiative energy transfer in colloidal CdSe nanoplatelet films," *Nanoscale*, vol. 7, pp. 2545, 2015.

[27] Yiming Zhao, Charl Riemersma, Francesca Pietra, Rolf Koole, Celso de Mello Donegá, and Andries Meijerink, "High-temperature luminescence quenching of colloidal quantum dots," *ACS Nano*, vol. 6, no. 10, pp. 9058–9067, 2012.

[28] Fengjia Fan, Pongsakorn Kanjanaboos, Mayuran Saravanapavanantham, Eric Beauregard, Grayson Ingram, Emre Yassitepe, Michael M. Adachi, Oleksandr Voznyy, Andrew K. Johnston, Grant Walters, Gi-Hwan Kim, Zheng-Hong Lu, and Edward H. Sargent, "Colloidal $CdSe_{1-x}S_x$ nanoplatelets with narrow and continuously-tunable electroluminescence," *Nano Lett.*, vol. 15, no. 7, pp. 4611–4615, 2015.

[29] Aydan Yeltik, Savas Delikanli, Murat Olutas, Yusuf Kelestemur, Burak Guzelturk, and Hilmi Volkan Demir, "Experimental determination of the absorption cross-section and molar extinction coefficient of colloidal cdse nanoplatelets," *J. Phys. Chem. C*, vol. 119, no. 47, pp. 26768–26775, 2015.

[30] Chunxing She, Igor Fedin, Dmitriy S. Dolzhnikov, Arnaud Demortière, Richard D. Schaller, Matthew Pelton, and Dmitri V. Talapin, "Low-threshold stimulated emission using colloidal quantum wells," *Nano Letters*, vol. 14, no. 5, pp. 2772–2777, 2014.

[31] Alexander W. Achtstein, Artsiom Antanovich, Anatol Prudnikau, Riccardo Scott, Ulrike Woggon, and Mikhail Artemyev, "Linear absorption in cdse nanoplates: Thickness and lateral size dependency of the intrinsic absorption," *J. Phys. Chem. C*, vol. 119, no. 34, pp. 20156–20161, 2015.

[32] Sébastien Lamarre, Étienne Rochette, Samuel Tremblay, and Claudine Nè. Allen, "Cdse colloidal quantum rings," 2015, arXiv:1509.07793.

[33] S. Bose, S. Delikanli, M. Z. Akgul, Y. Gao, W. Fan, D. H. Zhang, and H. V. Demir, "Inverted Type-I CdS/CdSe Core/Crown Colloidal Quantum Ring," in *2017 Conference on Lasers and Electro-Optics - European Quantum Electronics Conference*. 2017, Optical Society of America.

[34] Mickaël D. Tessier, Piernicola Spinicelli, Dorian Dupont, Gilles Patriarche, Sandrine Ithurria, and Benoit Dubertret, "Efficient Exciton Concentrators Built from Colloidal Core/Crown CdSe/CdS Semiconductor Nanoplatelets," *Nano Lett.*, vol. 14, no. 1, pp. 207–213, 2014.

[35] Igor Fedin and Dmitri V. Talapin, "Colloidal CdSe Quantum Rings," *J. Am. Chem. Soc.*, vol. 138, no. 31, pp. 9771–9774, 2016.

[36] Savas Delikanli, Burak Guzelturk, Pedro L. Hernández-Martínez, Talha Erdem, Yusuf Kelestemur, Murat Olutas, Mehmet Zafer Akgul, and Hilmi V. Demir, "Continuously Tunable Emission in Inverted Type-I CdS/CdSe Core/Crown Semiconductor Nanoplatelets," *Adv. Funct. Mater.*, vol. 25, no. 27, pp. 4282–4289, 2015.

[37] G. Vardar, S. W. Paleg, M. V. Warren, M. Kang, S. Jeon, and R. S. Goldman, "Mechanisms of droplet formation and Bi incorporation during molecular beam epitaxy of GaAsBi," *Applied Physics Letters*, vol. 102, no. 4, pp. 042106, 2013.

[38] Robert D. Richards, Faebian Bastiman, Christopher J. Hunter, Danuta F. Mendes, Abdul R. Mohmad, John S. Roberts, and John P.R. David, "Molecular beam epitaxy growth of GaAsBi using As_2 and As_4," *Journal of Crystal Growth*, vol. 390, pp. 120 – 124, 2014.

[39] F. Bastiman, A.R.B. Mohmad, J.S. Ng, J.P.R David, and S.J. Sweeney, "Non-stoichiometric GaAsBi/GaAs (100) molecular beam epitaxy growth," *Journal of Crystal Growth*, vol. 338, no. 1, pp. 57 – 61, 2012.

[40] M. K. Shakfa, D. Kalincev, X. Lu, S. R. Johnson, D. A. Beaton, T. Tiedje, A. Chernikov, S. Chatterjee, and M. Koch, "Quantitative study of localization effects and recombination dynamics in GaAsBi/GaAs single quantum wells," *Journal of Applied Physics*, vol. 114, no. 16, pp. 164306, 2013.

[41] G. Ciatto, E. C. Young, F. Glas, J. Chen, R. Alonso Mori, and T. Tiedje, "Spatial correlation between Bi atoms in dilute $GaAs_{1-x}Bi_x$: From random distribution to Bi pairing and clustering," *Phys. Rev. B*, vol. 78, pp. 035325, Jul 2008.

[42] S Mazzucato, P Boonpeng, H Carrère, D Lagarde, A Arnoult, G Lacoste, T Zhang, A Balocchi, T Amand, X Marie, and C Fontaine, "Reduction of defect density by rapid thermal annealing in GaAsBi studied by time-resolved photoluminescence," *Semiconductor Science and Technology*, vol. 28, no. 2, pp. 022001, 2013.

[43] S. J. Sweeney and S. R. Jin, "Bismide-nitride alloys: Promising for efficient light emitting devices in the near- and mid-infrared," *Journal of Applied Physics*, vol. 113, no. 4, pp. 043110, 2013.

[44] W. J. Fan, "Tensile-strain and doping enhanced direct bandgap optical transition of n^+ doped Ge/GeSi quantum wells," *Journal of Applied Physics*, vol. 114, no. 18, pp. –, 2013.

[45] S. Imhof, C. Bückers, A. Thränhardt, J. Hader, J. V. Moloney, and S. W. Koch, "Microscopic theory of the optical properties of Ga(AsBi)/GaAs quantum wells," *Semicond. Sci. Technol.*, vol. 23, no. 12, pp. 125009, 2008.

[46] S. J. Sweeney, Z. Batool, K. Hild, S. R. Jin, and T. J. C. Hosea, "The potential role of bismide alloys in future photonic devices," in *2011 13th International Conference on Transparent Optical Networks*, June 2011, pp. 1–4.

[47] Ming Su, Chong Li, Pengfei Yuan, Fengfei Rao, Yu Jia, and Fei Wang, "Electronic and optical properties of quaternary alloy GaAsBiN lattice-matched to GaAs," *Opt. Express*, vol. 22, no. 25, pp. 30633–30640, Dec 2014.

[48] Muhammad Usman, Christopher A. Broderick, and Eoin P. OReilly, "Theory of the electronic structure of dilute bismide and bismide-nitride alloys of GaAs: Tight-binding and k.p models," *AIP Conf. Proc.*, vol. 1566, no. 1, pp. 21–22, 2013.

[49] Zhi-Gang Song, Sumanta Bose, Wei-Jun Fan, and Shu-Shen Li, "Electronic band structure and optical gain of $GaN_xBi_yAs_{1-x-y}$/GaAs pyramidal quantum dots," *Journal of Applied Physics*, vol. 119, no. 14, pp. 143103, 2016.

[50] S. J. Sweeney, A. R. Adams, M. Silver, E. P. O'Reilly, J. R. Watling, A. B. Walker, and P. J. A. Thijs, "Dependence of Threshold Current on QW Position and on Pressure in 1.5 μm InGaAs(P) Lasers," *Physica Status Solidi (B)*, vol. 211, no. 1, pp. 525–531, 1999.

[51] S. Tixier, S. E. Webster, E. C. Young, T. Tiedje, S. Francoeur, A. Mascarenhas, P. Wei, and F. Schiettekatte, "Band gaps of the dilute quaternary alloys $GaN_xAs_{1-x-y}Bi_y$ and $Ga_{1-y}In_yN_xAs_{1-x}$," *Applied Physics Letters*, vol. 86, no. 11, pp. 112113, 2005.

[52] M. Beaudoin, R.B. Lewis, J.J. Andrews, V. Bahrami-Yekta, M. Masnadi-Shirazi, S.K. O'Leary, and T. Tiedje, "Bandedge optical properties of mbe grown GaAsBi films measured by photoluminescence and photothermal deflection spectroscopy," *Journal of Crystal Growth*, vol. 425, pp. 245 – 249, 2015.

[53] Chaturvedi Gogineni, Nathaniel A. Riordan, Shane R. Johnson, Xianfeng Lu, and Tom Tiedje, "Disorder and the Urbach edge in dilute bismide GaAsBi," *Applied Physics Letters*, vol. 103, no. 4, pp. 041110, 2013.

[54] R. Alaya, M. Mbarki, and A. Rebey, "Pressure and composition dependence of structural, electronic and optical properties of GaAsBi alloys," *Materials Science in Semiconductor Processing*, vol. 40, pp. 925 – 930, 2015.

[55] M.M. Habchi, A. Ben Nasr, A. Rebey, and B. El Jani, "Theoretical study of optoelectronic properties of $GaAs_{1x}Bi_x$ alloys using valence band anticrossing model," *Infrared Physics & Technology*, vol. 67, pp. 531 – 536, 2014.

[56] C A Broderick, M Usman, and E P O'Reilly, "Derivation of 12- and 14-band k· p hamiltonians for dilute bismide and bismide-nitride semiconductors," *Semicon. Sci. and Tech.*, vol. 28, no. 12, pp. 125025, 2013.

[57] C A Broderick, M Usman, S J Sweeney, and E P O'Reilly, "Band engineering in dilute nitride and bismide semiconductor lasers," *Semicon. Sci. and Tech.*, vol. 27, no. 9, pp. 094011, 2012.

[58] Christopher A Broderick, Patrick E Harnedy, Peter Ludewig, Zoe L Bushell, Kerstin Volz, Robert J Manning, and Eoin P O Reilly, "Determination of type-I band offsets in $GaBi_xAs_{1-x}$ quantum wells using polarisation-resolved photovoltage spectroscopy and 12-band k·p calculations," *Semiconductor Science and Technology*, vol. 30, no. 9, pp. 094009, 2015.

[59] Muhammad Usman, Christopher A. Broderick, Andrew Lindsay, and Eoin P. O'Reilly, "Tight-binding analysis of the electronic structure of dilute bismide alloys of GaP and GaAs," *Phys. Rev. B*, vol. 84, pp. 245202, Dec 2011.

[60] B. Breddermann and A. B "Luminescence properties of dilute bismide systems," *Journal of Luminescence*, vol. 154, pp. 95 – 98, 2014.

[61] C A Broderick, P E Harnedy, and E P O'Reilly, "Theory of the electronic and optical properties of dilute bismide quantum well lasers," *IEEE J. Sel. Top. Quantum Electron.*, vol. 21, no. 6, pp. 287–299, Nov-Dec 2015.

[62] S. L. Chuang, *Physics of Photonic Devices; 2nd ed.*, Wiley, Hoboken, NJ, 2009.

[63] V.A. Serebryakov, É.V. Boĭko, N.N. Petrishchev, and A.V. Yan, "Medical applications of mid-IR lasers. Problems and prospects," *J. Opt. Technol.*, vol. 77, no. 1, pp. 6–17, Jan 2010.

[64] M. Z. Hasan and C. L. Kane, "*Colloquium* : Topological insulators," *Rev. Mod. Phys.*, vol. 82, pp. 3045–3067, Nov 2010.

[65] Thorsten Hesjedal and Yulin Chen, "Topological insulators: Engineered heterostructures," *Nature Materials*, vol. 16, pp. 3–4, 2017.

[66] A. R. Mellnik, J. S. Lee, A. Richardella, J. L. Grab, P. J. Mintun, M. H. Fischer, A. Vaezi, A. Manchon, E.-A. Kim, N. Samarth, and D. C. Ralph, "Spin-transfer torque generated by a topological insulator," *Nature*, vol. 511, pp. 449–451, July 2014.

[67] B. Andrei Bernevig, Taylor L. Hughes, and Shou-Cheng Zhang, "Quantum Spin Hall Effect and Topological Phase Transition in HgTe Quantum Wells," *Science*, vol. 314, no. 5806, pp. 1757–1761, 2006.

[68] Markus König, Steffen Wiedmann, Christoph Brüne, Andreas Roth, Hartmut Buhmann, Laurens W. Molenkamp, Xiao-Liang Qi, and Shou-Cheng Zhang, "Quantum Spin Hall Insulator State in HgTe Quantum Wells," *Science*, vol. 318, no. 5851, pp. 766–770, 2007.

[69] Chaoxing Liu, Taylor L. Hughes, Xiao-Liang Qi, Kang Wang, and Shou-Cheng Zhang, "Quantum Spin Hall Effect in Inverted Type-II Semiconductors," *Phys. Rev. Lett.*, vol. 100, pp. 236601, Jun 2008.

[70] Ivan Knez, Rui-Rui Du, and Gerard Sullivan, "Evidence for helical edge modes in inverted InAs/GaSb quantum wells," *Phys. Rev. Lett.*, vol. 107, pp. 136603, Sep 2011.

[71] Y. Xia, D. Qian, D. Hsieh, L. Wray, A. Pal, H. Lin, A. Bansil, D. Grauer, Y. S. Hor, R. J. Cava, and M. Z. Hasan, "Observation of a large-gap topological-insulator class with a single dirac cone on the surface," *Nature Physics*, vol. 5, pp. 398–402, 2009.

[72] O. P. Sushkov and A. H. Castro Neto, "Topological insulating states in laterally patterned ordinary semiconductors," *Phys. Rev. Lett.*, vol. 110, pp. 186601, May 2013.

[73] M. S. Miao, Q. Yan, C. G. Van de Walle, W. K. Lou, L. L. Li, and K. Chang, "Polarization-driven topological insulator transition in a GaN/InN/GaN quantum well," *Phys. Rev. Lett.*, vol. 109, pp. 186803, Nov 2012.

[74] Dong Zhang, Wenkai Lou, Maosheng Miao, Shou-cheng Zhang, and Kai Chang, "Interface-induced topological insulator transition in GaAs/Ge/GaAs quantum wells," *Phys. Rev. Lett.*, vol. 111, pp. 156402, Oct 2013.

[75] Qing Lin He, Xufeng Kou, Alexander J. Grutter, Gen Yin, Lei Pan, Xiaoyu Che, Yuxiang Liu, Tianxiao Nie, Bin Zhang, Steven M. Disseler, Brian J. Kirby, William Ratcliff II, Qiming Shao, Koichi Murata, Xiaodan Zhu, Guoqiang Yu, Yabin Fan, Mohammad Montazeri, Xiaodong Han, Julie A. Borchers, and Kang L. Wang, "Tailoring exchange couplings in magnetic topological-insulator/antiferromagnet heterostructures," *Nature Materials*, vol. 16, pp. 94–100, 2017.

[76] Wanxiang Feng, Wenguang Zhu, Hanno H. Weitering, G. Malcolm Stocks, Yugui Yao, and Di Xiao, "Strain tuning of topological band order in cubic semiconductors," *Phys. Rev. B*, vol. 85, pp. 195114, May 2012.

[77] Haijun Zhang, Yong Xu, Jing Wang, Kai Chang, and Shou-Cheng Zhang, "Quantum spin hall and quantum anomalous hall states realized in junction quantum wells," *Phys. Rev. Lett.*, vol. 112, pp. 216803, May 2014.

[78] W. J. Fan, Sumanta Bose, and D. H. Zhang, "Electronic bandstructure and optical gain of lattice matched III-V dilute nitride bismide quantum wells for 1.55 μm optical communication systems," *Journal of Applied Physics*, vol. 120, no. 9, pp. 093111, 2016.

[79] Y. J. Jin, X. H. Tang, J. H. Teng, and D. H. Zhang, "Optical properties and bonding behaviors of insbn alloys grown by metal-organic chemical vapor deposition," *Journal of Crystal Growth*, vol. 416, pp. 12 – 16, 2015.

[80] Y. H. Zhang, P. P. Chen, H. Yin, T. X. Li, and W. Lu, "The effects of growth parameters on the RF-MBE growth of dilute InNSb films," *Journal of Physics D: Applied Physics*, vol. 43, no. 30, pp. 305405, 2010.

[81] X. W. Zhang, W. J. Fan, S. S. Li, and J. B. Xia, "Influence of N doping on the Rashba coefficient, semiconductor-metal transition, and electron effective mass in $InSb_{1-x}N_x$ nanowires: Ten-band $k \cdot p$ model," *Phys. Rev. B*, vol. 75, pp. 205331, May 2007.

[82] S. C. Das, T. D. Das, and S. Dhar, "Infrared absorption and Raman spectroscopy studies of InSbBi layers grown by liquid phase epitaxy," *Infrared Physics & Technology*, vol. 55, no. 4, pp. 306 – 308, 2012.

[83] D. P. Samajdar and S. Dhar, "Estimation of Bi induced changes in the direct E_0 band gap of III-V-Bi alloys and comparison with experimental data," *Physica B: Condensed Matter*, vol. 484, pp. 27 – 30, 2016.

[84] M. K. Rajpalke, W. M. Linhart, K. M. Yu, M. Birkett, J. Alaria, J. J. Bomphrey, S. Sallis, L. F. J. Piper, T. S. Jones, M. J. Ashwin, and T. D. Veal, "Bi-induced band gap reduction in epitaxial InSbBi alloys," *Applied Physics Letters*, vol. 105, no. 21, pp. 212101, 2014.

[85] Y. Z. Gao and T. Yamaguchi, "Liquid Phase Epitaxial Growth and Properties of InSbBi Films grown from In, Bi and Sn Solutions," *Crystal Research and Technology*, vol. 34, no. 3, pp. 285–292, 1999.

[86] K. Alberi, J. Wu, W. Walukiewicz, K. M. Yu, O. D. Dubon, S. P. Watkins, C. X. Wang, X. Liu, Y.-J. Cho, and J. Furdyna, "Valence-band anticrossing in mismatched III-V semiconductor alloys," *Phys. Rev. B*, vol. 75, pp. 045203, Jan 2007.

[87] N. W. Ashcroft and N. D. Mermin, *Solid State Physics*, Saunders College, Philadelphia, 1976.

[88] G. L. Bir and G. E. Pikus, *Symmetry and Strain-induced Effects in Semiconductors*, Wiley, New York, 1974.

[89] J. Bardeen, "An Improved Calculation of the Energies of Metallic Li and Na," *The Journal of Chemical Physics*, vol. 6, no. 7, pp. 367, 1938.

[90] Frederick Seitz, *Modern Theory of Solids*, McGraw New York, 1940.

[91] G. Dresselhaus, A. F. Kip, and C. Kittel, "Cyclotron Resonance of Electrons and Holes in Silicon and Germanium Crystals," *Phys. Rev.*, vol. 98, pp. 368–384, Apr 1955.

[92] E.O. Kane, "Energy band structure in p-type Germanium and Silicon," *Journal of Physics and Chemistry of Solids*, vol. 1, no. 1, pp. 82 – 99, 1956.

[93] Evan O. Kane, "Band structure of Indium Antimonide," *Journal of Physics and Chemistry of Solids*, vol. 1, no. 4, pp. 249–261, 1957.

[94] J. M. Luttinger and W. Kohn, "Motion of electrons and holes in perturbed periodic fields," *Phys. Rev.*, vol. 97, pp. 869–883, Feb 1955.

[95] J. Chen, W. J. Fan, Q. Xu, X. W. Zhang, S. S. Li, and J. B. Xia, "Shape effects on the electronic structure and the optical gain of InAsN/GaAs nanostructures: From a quantum lens to a quantum ring," *Superlattices and Microstructures*, vol. 52, no. 4, pp. 618–631, 2012.

[96] J. Chen, W. J. Fan, Q. Xu, X. W. Zhang, S. S. Li, and J. B. Xia, "Electronic structure and optical gain saturation of $InAs_{1-x}N_x$/GaAs quantum dots," *Journal of Applied Physics*, vol. 105, no. 12, pp. 123705, 2009.

[97] Craig Pryor, "Eight-band calculations of strained InAs/GaAs quantum dots compared with one-, four-, and six-band approximations," *Physical Review B*, vol. 57, no. 12, pp. 7190–7195, 1998.

[98] Mitsuru Sugawara, "Chapter 1 - Theoretical Bases of the Optical Properties of Semiconductor Quantum Nano-Structures," in *Self-Assembled InGaAs/GaAs Quantum Dots*, R.K. Willardson and Eicke R. Weber, Eds., vol. 60 of *Semiconductors and Semimetals*, pp. 1 – 116. Elsevier, 1999.

[99] Sumanta Bose, Sushant Shendre, Zhigang Song, Vijay Kumar Sharma, Dao Hua Zhang, Cuong Dang, Weijun Fan, and Hilmi Volkan Demir, "Temperature-dependent optoelectronic properties of Quasi-2D colloidal Cadmium Selenide nanoplatelets," *Nanoscale*, vol. 9, pp. 6595–6605, 2017.

[100] Kain Lu Low, Yue Yang, Genquan Han, Weijun Fan, and Yee-Chia Yeo, "Electronic band structure and effective mass parameters of $Ge_{1-x}Sn_x$ alloys," *J. Appl. Phys.*, vol. 112, no. 10, pp. 103715, 2012.

[101] S. Ng, W. Fan, Y. Dang, and S. Yoon, "Comparison of electronic band structure and optical transparency conditions of $In_xGa_{1-x}As_{1-y}N_y$/GaAs quantum wells calculated by 10-band, 8-band, and 6-band k·p models," *Physical Review B*, vol. 72, no. 11, 2005.

[102] Hui-Xiong Deng, Jingbo Li, Shu-Shen Li, Haowei Peng, Jian-Bai Xia, Lin-Wang Wang, and Su-Huai Wei, "Band crossing in isovalent semiconductor alloys with large size mismatch: First-principles calculations of the electronic structure of Bi and N incorporated GaAs," *Phys. Rev. B*, vol. 82, pp. 193204, Nov 2010.

[103] I. Vurgaftman and J. R. Meyer, "Band parameters for nitrogen-containing semiconductors," *J. Appl. Phys.*, vol. 94, no. 6, pp. 3675–3696, 2003.

[104] C. Pryor, J. Kim, L. W. Wang, A. J. Williamson, and A. Zunger, "Comparison of two methods for describing the strain profiles in quantum dots," *Journal of Applied Physics*, vol. 83, no. 5, pp. 2548–2554, 1998.

[105] P. N. Keating, "Effect of Invariance Requirements on the Elastic Strain Energy of Crystals with Application to the Diamond Structure," *Phys. Rev.*, vol. 145, pp. 637–645, May 1966.

[106] Richard M. Martin, "Elastic properties of ZnS structure semiconductors," *Phys. Rev. B*, vol. 1, pp. 4005–4011, May 1970.

[107] Joachim Piprek, "Chapter 5 - Photon Generation," in *Semiconductor Optoelectronic Devices*, Joachim Piprek, Ed., pp. 121 – 139. Academic Press, Boston, 2003.

[108] Mitsuru Sugawara, Kohki Mukai, Yoshiaki Nakata, Hiroshi Ishikawa, and Akira Sakamoto, "Effect of homogeneous broadening of optical gain on lasing spectra in self-assembled $In_xGa_{1-x}As$/GaAs quantum dot lasers," *Physical Review B*, vol. 61, pp. 7595–7603, Mar 2000.

[109] J. Minch, S. H. Park, T. Keating, and S. L. Chuang, "Theory and experiment of $In_{1-x}Ga_xAs_yP_{1-y}$ and $In_{1-x-y}Ga_xAl_yAs$ long-wavelength strained quantum-well lasers," *IEEE J. Quant. Electron.*, vol. 35, no. 5, pp. 771–782, May 1999.

[110] M. del CastilloMussot and L. J. Sham, "Excitonic effect in the optical spectrum of semiconductors," *Phys. Rev. B*, vol. 31, pp. 2092–2098, Feb 1985.

[111] J. Voigt, F. Spiegelberg, and M. Senoner, "Band parameters of cds and cdse single crystals determined from optical exciton spectra," *Physica Status Solidi (B)*, vol. 91, no. 1, pp. 189–199, 1979.

[112] Ali Naeem, Francesco Masia, Sotirios Christodoulou, Iwan Moreels, Paola Borri, and Wolfgang Langbein, "Giant exciton oscillator strength and radiatively limited dephasing in two-dimensional platelets," *Phys. Rev. B*, vol. 91, pp. 121302, Mar 2015.

[113] Joseph Micallef, E.Herbert Li, and Bernard L. Weiss, "Exciton optical absorption in disordered, strained InGaAs/GaAs single quantum wells," *Superlattices Microstruct*, vol. 13, no. 3, pp. 315, 1993.

[114] E. Herbert Li and Bernard L. Weiss, "Exciton optical absorption in a diffusion-induced nonsquare AlGaAs/GaAs quantum well," *Proc. SPIE*, vol. 1675, pp. 98–108, 1992.

[115] David A. B. Miller, "Optical physics of quantum wells," in *Quantum Dynamics of Simple Systems*, G. L. Oppo, S. M. Barnett, E. Riis, and M. Wilkinson, Eds., pp. 239–266. Institute of Physics, London, 1996.

[116] Isaac Hernandez Calderon, "Chapter 4 - Optical Properties and Electronic Structure of Wide Band Gap II-VI Semiconductors," in *Vol 12: II-VI Semiconductor Materials and their Applications*, Maria C. Tamargo, Ed. Taylor and Francis, New York, 2002.

[117] Y. P. Varshni, "Temperature dependence of the energy gap in semiconductors," *Physica*, vol. 34, no. 1, pp. 149 – 154, 1967.

[118] Weiwei Zhang, Zhiqiang Su, Ming Gong, Chuan Feng Li, Guang Can Guo, and Lixin He, "Giant optical anisotropy in cylindrical self-assembled InAs/GaAs quantum rings," *EPL (Europhysics Lett.)*, vol. 83, no. 6, pp. 67004, 2008.

[119] Y. Arakawa and H. Sakaki, "Multidimensional quantum well laser and temperature dependence of its threshold current," *Appl. Phys. Lett.*, vol. 40, no. 11, pp. 939–941, 1982.

[120] E. W. Weisstein, "Ellipsoid," From MathWorld–A Wolfram Web Resource. http://mathworld.wolfram.com/Ellipsoid.html.

[121] O. Madelung, *Semiconductors: Data Handbook*, Springer, Berlin/ Heidelberg, 2004.

[122] W. Shan, J. J. Song, H. Luo, and J. K. Furdyna, "Determination of the fundamental and split-off band gaps in zinc-blende CdSe by photomodulation spectroscopy," *Phys. Rev. B*, vol. 50, no. 11, pp. 8012, 1994.

[123] J. B. Jeon, Yu. M. Sirenko, K. W. Kim, M. A. Littlejohn, and M. A. Stroscio, "Valence band parameters of wurtzite materials," *Solid State Commun.*, vol. 99, no. 6, pp. 423 – 426, 1996.

[124] H. Riane, F. Hamdache, S. Bahlouli, and N. Benharrats, "Alloy composition effects on the gain and the differential gain for CdZnTe based II-VI semiconductor lasers," *Superlattices Microstruct.*, vol. 40, no. 1, pp. 19 – 28, 2006.

[125] S. A. Anson, J. T. Olesberg, Michael E. Flatté, T. C. Hasenberg, and Thomas F. Boggess, "Differential gain, differential index, and linewidth enhancement factor for a 4 μm superlattice laser active layer," *J. Appl. Phys.*, vol. 86, no. 2, pp. 713–718, 1999.

[126] Richard S. Quimby, "Chapter 23 - Survey of Laser Types, Fiber Lasers," in *Photonics and Lasers: An Introduction*, pp. 425 – 434. Wiley-Interscience, New Jersey, 2006.

[127] Changyin Ji, Yu Zhang, Tieqiang Zhang, Wenyan Liu, Xiaoyu Zhang, Hongzhi Shen, Yu Wang, Wenzhu Gao, Yiding Wang, Jun Zhao, and William W. Yu, "Temperature-Dependent Photoluminescence of Ag_2Se Quantum Dots," *J. Phys. Chem. C*, vol. 119, no. 24, pp. 13841–13846, 2015.

[128] Pengtao Jing, Jinju Zheng, Micho Ikezawa, Xueyan Liu, Shaozhe Lv, Xianggui Kong, Jialong Zhao, and Yasuaki Masumoto, "Temperature-Dependent Photoluminescence of CdSe-Core CdS/CdZnS/ZnS-Multishell Quantum Dots," *J. Phys. Chem. C*, vol. 113, no. 31, pp. 13545–13550, 2009.

[129] Q. Le-Van, X. Le Roux, T. V. Teperik, B. Habert, F. Marquier, J.-J. Greffet, and A. Degiron, "Temperature dependence of quantum dot fluorescence assisted by plasmonic nanoantennas," *Phys. Rev. B*, vol. 91, pp. 085412, Feb 2015.

[130] S. Logothetidis, M. Cardona, P. Lautenschlager, and M. Garriga, "Temperature dependence of the dielectric function and the interband critical points of CdSe," *Phys. Rev. B*, vol. 34, pp. 2458–2469, Aug 1986.

[131] L. I. Burov, E. V. Lebedok, V. K. Kononenko, A. G. Ryabtsev, and G. I. Ryabtsev, "Interband transition matrix element and temperature dependence of the lasing threshold for GaN laser structures," *J. Appl. Spectroscopy*, vol. 74, no. 6, pp. 878–883, 2007.

[132] S.-H. Wei and Alex Zunger, "Role of metal d states in II-VI semiconductors," *Phys. Rev. B*, vol. 37, pp. 8958–8981, May 1988.

[133] Sumanta Bose, Zhigang Song, W. J. Fan, and D. H. Zhang, "Effect of lateral size and thickness on the electronic structure and optical properties of quasi two-dimensional CdSe and CdS nanoplatelets," *J. Appl. Phys.*, vol. 119, no. 14, pp. 143107, 2016.

[134] Murat Olutas, Burak Guzelturk, Yusuf Kelestemur, Kivanc Gungor, and Hilmi Volkan Demir, "Highly efficient nonradiative energy transfer from colloidal semiconductor quantum dots to wells for sensitive noncontact temperature probing," *Adv. Funct. Mater.*, vol. 26, no. 17, pp. 2891–2899, 2016.

[135] Guillaume H. V. Bertrand, Anatolii Polovitsyn, Sotirios Christodoulou, Ali Hossain Khan, and Iwan Moreels, "Shape control of zincblende CdSe nanoplatelets," *Chem. Commun.*, vol. 52, pp. 11975–11978, 2016.

[136] Benoit Mahler, Brice Nadal, Cecile Bouet, Gilles Patriarche, and Benoit Dubertret, "Core/Shell Colloidal Semiconductor Nanoplatelets," *J. Am. Chem. Soc.*, vol. 134, no. 45, pp. 18591–18598, 2012.

[137] Mickaël D. Tessier, Piernicola Spinicelli, Dorian Dupont, Gilles Patriarche, Sandrine Ithurria, and Benoit Dubertret, "Efficient exciton concentrators built from colloidal core/crown cdse/cds semiconductor nanoplatelets," *Nano Letters*, vol. 14, no. 1, pp. 207–213, 2014.

[138] Yusuf Kelestemur, Burak Guzelturk, Onur Erdem, Murat Olutas, Kivanc Gungor, and Hilmi Volkan Demir, "Platelet-in-Box Colloidal Quantum Wells: CdSe/CdS@CdS Core/Crown@Shell Heteronanoplatelets," *Adv. Funct. Mater.*, vol. 26, no. 21, pp. 3570–3579, 2016.

[139] Murat Olutas, Burak Guzelturk, Yusuf Kelestemur, Aydan Yeltik, Savas Delikanli, and Hilmi Volkan Demir, "Lateral size-dependent spontaneous and stimulated emission properties in colloidal cdse nanoplatelets," *ACS Nano*, vol. 9, no. 5, pp. 5041–5050, 2015.

[140] Burak Guzelturk, Onur Erdem, Murat Olutas, Yusuf Kelestemur, and Hilmi Volkan Demir, "Stacking in colloidal nanoplatelets: Tuning excitonic properties," *ACS Nano*, vol. 8, no. 12, pp. 12524–12533, 2014.

[141] Eline M. Hutter, Eva Bladt, Bart Goris, Francesca Pietra, Johanna C. van der Bok, Mark P. Boneschanscher, Celso de Mello Donegá, Sara Bals, and Daniël Vanmaekelbergh, "Conformal and atomic characterization of ultrathin cdse platelets with a helical shape," *Nano Lett.*, vol. 14, no. 11, pp. 6257–6262, 2014.

[142] Joseph R. Lakowicz, *Principles of Fluorescence Spectroscopy*, Springer US, Boston, 2006.

[143] Onur Erdem, Murat Olutas, Burak Guzelturk, Yusuf Kelestemur, and Hilmi Volkan Demir, "Temperature-dependent emission kinetics of colloidal semiconductor nanoplatelets strongly modified by stacking," *J. Phys. Chem. Lett.*, vol. 7, no. 3, pp. 548–554, 2016.

[144] O. Halder, A. Pradhani, P. K. Sahoo, B. Satpati, and S. Rath, "Highly luminescent two dimensional excitons in atomically thin cdse nanosheets," *Appl. Phys. Lett.*, vol. 104, no. 18, pp. 182109, 2014.

[145] C. H. Chia, C. T. Yuan, J. T. Ku, S. L. Yang, W. C. Chou, J. Y. Juang, S. Y. Hsieh, K. C. Chiu, J. S. Hsu, and S. Y. Jeng, "Temperature dependence of excitonic emission in cubic CdSe thin film," *Journal of Luminescence*, vol. 128, no. 1, pp. 123 – 128, 2008.

[146] S. Rudin, T. L. Reinecke, and B. Segall, "Temperature-dependent exciton linewidths in semiconductors," *Phys. Rev. B*, vol. 42, pp. 11218–11231, Dec 1990.

[147] G. Perna, V. Capozzi, and M. Ambrico, "Structural properties and photoluminescence study of CdSe/Si epilayers deposited by laser ablation," *J. Appl. Phys.*, vol. 83, no. 6, pp. 3337–3344, 1998.

[148] T. Takagahara, "Electron-phonon interactions and excitonic dephasing in semiconductor nanocrystals," *Phys. Rev. Lett.*, vol. 71, pp. 3577–3580, Nov 1993.

[149] D. Valerini, A. Cretí, M. Lomascolo, L. Manna, R. Cingolani, and M. Anni, "Temperature dependence of the photoluminescence properties of colloidal CdSe/ZnS core/shell quantum dots embedded in a polystyrene matrix," *Phys. Rev. B*, vol. 71, pp. 235409, Jun 2005.

[150] M. Leroux, N. Grandjean, B. Beaumont, G. Nataf, F. Semond, J. Massies, and P. Gibart, "Temperature quenching of photoluminescence intensities in undoped and doped GaN," *J. Appl. Phys.*, vol. 86, no. 7, pp. 3721–3728, 1999.

[151] Xichen Cai, James E. Martin, Lauren E. Shea-Rohwer, Ke Gong, and David F. Kelley, "Thermal Quenching Mechanisms in II-VI Semiconductor Nanocrystals," *J. Phys. Chem. C*, vol. 117, no. 15, pp. 7902–7913, 2013.

[152] Tian-Cai Liu, Zhen-Li Huang, Hai-Qiao Wang, Jian-Hao Wang, Xiu-Qing Li, Yuan-Di Zhao, and Qing-Ming Luo, "Temperature-dependent photoluminescence of water-soluble quantum dots for a bioprobe," *Anal. Chim. Acta*, vol. 559, no. 1, pp. 120 – 123, 2006.

[153] Su-Huai Wei, S. B. Zhang, and Alex Zunger, "First-principles calculation of band offsets, optical bowings, and defects in CdS, CdSe, CdTe, and their alloys," *J. Appl. Phys.*, vol. 87, no. 3, pp. 1304–1311, 2000.

[154] Eugen Merzbacher, *Quantum Mechanics, 3rd Ed.*, Wiley, 1998.

[155] Sumanta Bose, Savas Delikanli, Aydan Yeltik, Manoj Sharma, Onur Erdem, Cuong Dang, Weijun Fan, Dao H. Zhang, and Hilmi V. Demir, "Anomalous spectral characteristics of ultrathin sub-nm colloidal cdse nanoplatelets," in *Conference on Lasers and Electro-Optics*. 2017, p. SM1K.2, Optical Society of America.

[156] G. Bastard, J.A. Brum, and R. Ferreira, "Electronic states in semiconductor heterostructures," *Solid State Physics*, vol. 44, pp. 229 – 415, 1991, Semiconductor Heterostructures and Nanostructures.

[157] S. Tomic, E. P. O'Reilly, R. Fehse, S. J. Sweeney, A. R. Adams, A. D. Andreev, S. A. Choulis, T. J. C. Hosea, and H. Riechert, "Theoretical and experimental analysis of 1.3 μm InGaAsN/GaAs lasers," *IEEE J. Sel. Top. Quantum Electron.*, vol. 9, no. 5, pp. 1228–1238, 2003.

[158] J. Wu, W. Walukiewicz, and E. E. Haller, "Band structure of highly mismatched semiconductor alloys: Coherent potential approximation," *Phys. Rev. B*, vol. 65, pp. 233210, Jun 2002.

[159] A. Ben Nasr, M.M. Habchi, C. Bilel, A. Rebey, and B. El Jani, "Theoretical calculations of absorption spectra of GaNAsBi-based MQWs operating at 1.55 μm," *J. Alloys Compd.*, vol. 647, pp. 159 – 166, 2015.

[160] M. Gladysiewicz, R. Kudrawiec, and M. S. Wartak, "8-band and 14-band *kp* modeling of electronic band structure and material gain in Ga(In)AsBi quantum wells grown on GaAs and InP substrates," *J. Appl. Phys.*, vol. 118, no. 5, 2015.

[161] G. A. Rozgonyi and M. B. Panish, "Stress compensation in $Ga_{1x}Al_xAs_{1y}P_y$ LPE layers on GaAs substrates," *Appl. Phys. Lett.*, vol. 23, no. 10, pp. 533–535, 1973.

[162] N. Tansu and L. J. Mawst, "Low-threshold strain-compensated InGaAs(N) (λ = 1.19-1.31 μm) quantum-well lasers," *IEEE Photonics Tech. Lett.*, vol. 14, no. 4, pp. 444–446, April 2002.

[163] Masao Kawaguchi, Tomoyuki Miyamoto, Atsushi Saitoh, and Fumio Koyama, "Photoluminescence and Lasing Characteristics of GaInNAs/GaAsP Strain-Compensated Quantum Wells," *Jpn. J. Appl. Phys.*, vol. 43, no. 2B, pp. L267, 2004.

[164] S. Hausser, G. Fuchs, A. Hangleiter, K. Streubel, and W. T. Tsang, "Auger recombination in bulk and quantum well InGaAs," *Appl. Phys. Lett.*, vol. 56, no. 10, pp. 913–915, 1990.

[165] L. Chiu and A. Yariv, "Auger recombination in quantum-well InGaAsP heterostructure lasers," *IEEE J. Quant. Electron.*, vol. 18, no. 10, pp. 1406–1409, Oct 1982.

[166] A. F. Phillips, S. J. Sweeney, A. R. Adams, and P. J. A. Thijs, "The temperature dependence of 1.3- and 1.5-μm compressively strained InGaAs(P) MQW semiconductor lasers," *IEEE J. Sel. Top. Quantum Electron.*, vol. 5, no. 3, pp. 401–412, May-Jun 1999.

[167] W. J. Fan, S. F. Yoon, T. K. Ng, S. Z. Wang, W. K. Loke, R. Liu, and A. Wee, "Comparison of nitrogen compositions in the as-grown GaN_xAs_{1-x} on GaAs measured by high-resolution x-ray diffraction and secondary-ion mass spectroscopy," *Appl. Phys. Lett.*, vol. 80, no. 22, pp. 4136–4138, 2002.

[168] E.C. Young, S. Tixier, and T. Tiedje, "Bismuth surfactant growth of the dilute nitride GaN_xAs_{1-x}," *J. Cryst. Growth*, vol. 279, no. 3-4, pp. 316 – 320, 2005.

[169] P. Ludewig, N. Knaub, N. Hossain, S. Reinhard, L. Nattermann, I. P. Marko, S. R. Jin, K. Hild, S. Chatterjee, W. Stolz, S. J. Sweeney, and K. Volz, "Electrical injection Ga(AsBi)/(AlGa)As single quantum well laser," *Appl. Phys. Lett.*, vol. 102, no. 24, 2013.

[170] Hiroshi Okamoto and Kunishige Oe, "Structural and Energy-Gap Characterization of Metalorganic-Vapor-Phase-Epitaxy-Grown InAsBi," *Japanese Journal of Applied Physics*, vol. 38, no. 2S, pp. 1022, 1999.

[171] P. T. Webster, N. A. Riordan, S. Liu, E. H. Steenbergen, R. A. Synowicki, Y.-H. Zhang, and S. R. Johnson, "Measurement of InAsSb bandgap energy and InAs/InAsSb band edge positions using spectroscopic ellipsometry and photoluminescence spectroscopy," *Journal of Applied Physics*, vol. 118, no. 24, pp. 245706, 2015.

[172] P. T. Webster, A. J. Shalindar, N. A. Riordan, C. Gogineni, H. Liang, A. R. Sharma, and S. R. Johnson, "Optical properties of InAsBi and optimal designs of lattice-matched and strain-balanced III-V semiconductor superlattices," *Journal of Applied Physics*, vol. 119, no. 22, pp. 225701, 2016.

[173] Christopher A Broderick, Muhammad Usman, and Eoin P O'Reilly, "Derivation of 12- and 14-band k·p hamiltonians for dilute bismide and bismide-nitride semiconductors," *Semiconductor Science and Technology*, vol. 28, no. 12, pp. 125025, 2013.

[174] Christopher A Broderick, Patrick E Harnedy, Peter Ludewig, Zoe L Bushell, Kerstin Volz, Robert J Manning, and Eoin P O'Reilly, "Determination of type-I band offsets in $GaBi_xAs_{1-x}$ quantum wells using polarisation-resolved photovoltage spectroscopy and 12-band k·p calculations," *Semiconductor Science and Technology*, vol. 30, no. 9, pp. 094009, 2015.

[175] D G Rothe, R W Reinthaler, C-X Liu, L W Molenkamp, S-C Zhang, and E M Hankiewicz, "Fingerprint of different spin-orbit terms for spin transport in hgte quantum wells," *New Journal of Physics*, vol. 12, no. 6, pp. 065012, 2010.

[176] Supriyo Datta, *Electronic Transport in Mesoscopic Systems:*, Cambridge University Press, Cambridge, 009 1995.

[177] J. Nitta S. M. Frolov A. Manchon, H. C. Koo and R. A. Duine, "New perspectives for rashba spin-orbit coupling," *Nature Materials*, vol. 14, pp. 871–882, 2015.

[178] Dario Bercioux and Procolo Lucignano, "Quantum transport in rashba spin-orbit materials: a review," *Reports on Progress in Physics*, vol. 78, no. 10, pp. 106001, 2015.

[179] Markus König, Hartmut Buhmann, Laurens W. Molenkamp, Taylor Hughes, Chao-Xing Liu, Xiao-Liang Qi, and Shou-Cheng Zhang, "The quantum spin hall effect: Theory and experiment," *Journal of the Physical Society of Japan*, vol. 77, no. 3, pp. 031007, 2008.

[180] Wikipedia, "Nanoparticle," https://en.wikipedia.org/wiki/Nanoparticle.

[181] H. Zahra, D. Elmaghroui, I. Fezai, and S. Jaziri, "II–VI colloidal quantum-dot/quantum-rod heterostructures under electric field effect and their energy transfer rate to graphene," *Journal of Applied Physics*, vol. 120, no. 20, pp. 205702, 2016.

[182] Xiaoming Wen, Amit Sitt, Pyng Yu, Yon-Rui Toh, and Jau Tang, "Temperature dependent spectral properties of type-I and quasi type-II CdSe/CdS dot-in-rod nanocrystals," *Phys. Chem. Chem. Phys.*, vol. 14, pp. 3505–3512, 2012.

[183] Ferruccio Pisanello, Luigi Martiradonna, Godefroy Leménager, Piernicola Spinicelli, Angela Fiore, Liberato Manna, Jean-Pierre Hermier, Roberto Cingolani, Elisabeth Giacobino, Massimo De Vittorio, and Alberto Bramati, "Room temperature-dipolelike single photon source with a colloidal dot-in-rod," *Applied Physics Letters*, vol. 96, no. 3, pp. 033101, 2010.

[184] Aaron E. Albers, Emory M. Chan, Patrick M. McBride, Caroline M. Ajo-Franklin, Bruce E. Cohen, and Brett A. Helms, "Dual-Emitting Quantum Dot/Quantum Rod-Based Nanothermometers with Enhanced Response and Sensitivity in Live Cells," *Journal of the American Chemical Society*, vol. 134, no. 23, pp. 9565–9568, 2012.

[185] Maksym Yarema, Yunhua Xing, Rainer T. Lechner, Lukas Ludescher, Nikola Dordevic, Weyde M. M. Lin, Olesya Yarema, and Vanessa Wood, "Mapping the Atomistic Structure of Graded Core/Shell Colloidal Nanocrystals," *Scientific Reports*, vol. 7, no. 1, pp. 11718, 2017.

[186] Wan Ki Bae, Lazaro A. Padilha, Young-Shin Park, Hunter McDaniel, Istvan Robel, Jeffrey M. Pietryga, and Victor I. Klimov, "Controlled Alloying of the Core-Shell Interface in CdSe/CdS Quantum Dots for Suppression of Auger Recombination," *ACS Nano*, vol. 7, no. 4, pp. 3411–3419, 2013.

[187] Jaehan Jung, Chun Hao Lin, Young Jun Yoon, Sidney T. Malak, Yaxin Zhai, Edwin L. Thomas, Valy Vardeny, Vladimir V. Tsukruk, and Zhiqun Lin, "Crafting Core/Graded Shell-Shell Quantum Dots with Suppressed Re-absorption and Tunable Stokes Shift as High Optical Gain Materials," *Angewandte Chemie International Edition*, vol. 55, no. 16, pp. 5071–5075, 2016.

[188] Klaus Boldt, Nicholas Kirkwood, Gary A. Beane, and Paul Mulvaney, "Synthesis of Highly Luminescent and Photo-Stable, Graded Shell CdSe/$Cd_xZn_{1-x}S$ Nanoparticles by In Situ Alloying," *Chemistry of Materials*, vol. 25, no. 23, pp. 4731–4738, 2013.

[189] S. A. Empedocles and M. G. Bawendi, "Quantum-Confined Stark Effect in Single CdSe Nanocrystallite Quantum Dots," *Science*, vol. 278, no. 5346, pp. 2114–2117, 1997.

[190] Clare E. Rowland, Kimihiro Susumu, Michael H. Stewart, Eunkeu Oh, Antti J. Mäkinen, Thomas J. O'Shaughnessy, Gary Kushto, Mason A. Wolak, Jeffrey S. Erickson, Alexander L. Efros, Alan L. Huston, and James B. Delehanty, "Electric Field Modulation of Semiconductor Quantum Dot Photoluminescence: Insights Into the Design of Robust Voltage-Sensitive Cellular Imaging Probes," *Nano Letters*, vol. 15, no. 10, pp. 6848–6854, 2015.

[191] Samuel D. Stranks and Henry J. Snaith, *Perovskite Solar Cells*, pp. 277–291, John Wiley & Sons, Ltd, 2016.

[192] Michael D. McGehee, "Perovskite solar cells: Continuing to soar," *Nature Materials*, vol. 13, pp. 845, Aug 2014.

[193] J. Even, L. Pedesseau, M.-A. Dupertuis, J.-M. Jancu, and C. Katan, "Electronic model for self-assembled hybrid organic/perovskite semiconductors: Reverse band edge electronic states ordering and spin-orbit coupling," *Phys. Rev. B*, vol. 86, pp. 205301, Nov 2012.

[194] Jacky Even, Hsinhan Tsai, Wanyi Nie, Jean-Christophe Blancon, Amanda J Neukirch, Laurent Pedesseau, Soline Boyer-Richard, Boubacar Traore, Mikael Kepenekian, Jean-Marc Jancu, Constantinos Stoumpos, Sergei Tretiak, Mercouri G Kanatzidis, Aditya D Mohite, and Claudine Katan, "Physical properties of 3D and 2D Ruddlesden-Popper halide perovskite semiconductors," in *Compound Semiconductor Week 2017 - 44th International Symposium on Compound Semiconductors (ISCS 2017)*, Berlin, Germany, May 2017.

[195] Jacky Even, Laurent Pedesseau, Jean-Marc Jancu, and Claudine Katan, "DFT and k·p modelling of the phase transitions of lead and tin halide perovskites for photovoltaic cells," *physica status solidi (RRL) – Rapid Research Letters*, vol. 8, no. 1, pp. 31–35, 2014.

[196] Hong-Hua Fang, Raissa Raissa, Mustapha Abdu-Aguye, Sampson Adjokatse, Graeme R. Blake, Jacky Even, and Maria Antonietta Loi, "Photophysics of Organic–Inorganic Hybrid Lead Iodide Perovskite Single Crystals," *Advanced Functional Materials*, vol. 25, no. 16, pp. 2378–2385, 2015.

[197] Jacky Even, Laurent Pedesseau, and Claudine Katan, "Understanding Quantum Confinement of Charge Carriers in Layered 2D Hybrid Perovskites," *ChemPhysChem*, vol. 15, no. 17, pp. 3733–3741, 2014.

[198] Daniel Sapori, Mikael Kepenekian, Laurent Pedesseau, Claudine Katan, and Jacky Even, "Quantum confinement and dielectric profiles of colloidal nanoplatelets of halide inorganic and hybrid organic-inorganic perovskites," *Nanoscale*, vol. 8, pp. 6369–6378, 2016.

[199] Jasprit Singh, *Physics of Semiconductors and Their Heterostructures*, McGraw-Hill College, 1993.

[200] *CRC Handbook of Chemistry and Physics*, CRC Press, 53rd edition, 1972.

[201] Matthew L. Landry, Thomas E. Morrell, Theodora K. Karagounis, Chih-Hao Hsia, and Chia-Ying Wang, "Simple Syntheses of CdSe Quantum Dots," *J. Chem. Educ.*, vol. 91, no. 2, pp. 274–279, 2014.

[202] Y. Wang, X. Yang, T. C. He, Y. Gao, H. V. Demir, X. W. Sun, and H. D. Sun, "Near resonant and nonresonant third-order optical nonlinearities of colloidal InP/ZnS quantum dots," *Applied Physics Letters*, vol. 102, no. 2, pp. 021917, 2013.

[203] S Zh Karazhanov and LC Lew Yan Voon, "Ab initio studies of the band parameters of III-V and II-VI zinc-blende semiconductors," *Semiconductors*, vol. 39, no. 2, pp. 161–173, 2005.

[204] V. Kumar, "Interatomic force constants of semiconductors," *J. Phys. Chem. of Solids*, vol. 61, no. 1, pp. 91 – 94, 2000.

[205] S. Logothetidis, M. Cardona, P. Lautenschlager, and M. Garriga, "Temperature dependence of the dielectric function and the interband critical points of CdSe," *Phys. Rev. B*, vol. 34, pp. 2458–2469, Aug 1986.

[206] A. Al Salman, A. Tortschanoff, M. B. Mohamed, D. Tonti, F. van Mourik, and M. Chergui, "Temperature effects on the spectral properties of colloidal CdSe nanodots, nanorods, and tetrapods," *Appl. Phys. Lett.*, vol. 90, no. 9, pp. 093104, 2007.

[207] X.W. Zhang, Y.H. Zhu, and J.B. Xia, "Optical properties and g factors of GaAs quantum rods," *Physica E: Low-dimensional Systems and Nanostructures*, vol. 33, no. 2, pp. 376 – 380, 2006.

[208] Zhi-Gang Song, Sumanta Bose, Wei-Jun Fan, and Shu-Shen Li, "Quantum Spin Hall Effect and Topological Phase Transition in $InN_xBi_ySb_{1-x-y}$/InSb Quantum Wells," *New Journal of Physics*.

[209] E. B. Elkenany, "Optoelectronic and Mechanical Properties of InSb Semiconductor Under the Effect of Temperature," *Silicon*, vol. 8, no. 3, pp. 391–396, 2016.

[210] R. Muthukrishnan and D. G. Seiler, "Deformation Potential Parameters of n-InSb," *Physica Status Solidi (B)*, vol. 54, no. 2, pp. K83–K86, 1972.

[211] Sergey Gaponenko, Hilmi Volkan Demir, Christian Seassal, and Ulrike Woggon, "Colloidal nanophotonics: the emerging technology platform," *Opt. Express*, vol. 24, no. 2, pp. A430–A433, Jan 2016.